MUSE's privileged look at the sources of cosmic reionization

Geoffroy De La Vieuville

Université Fédérale
Toulouse Midi-Pyrénées

THÈSE

En vue de l'obtention du

DOCTORAT DE L'UNIVERSITÉ DE TOULOUSE

Délivré par : *l'Université Toulouse 3 Paul Sabatier (UT3 Paul Sabatier)*

Présentée et soutenue le *21/10/2019* **par :**

GEOFFROY DE LA VIEUVILLE

Le regard privilégié de MUSE sur les sources de la réionisation cosmique

---

JURY

PRÉSIDENTE DU JURY	Geneviève Soucail	IRAP, Toulouse
RAPPORTEUR	David Elbaz	CEA, Saclay
RAPPORTEUR	Olivier Le Fèvre	LAM, Marseille
EXAMINATEUR	Johan Richard	CRAL, Lyon
EXAMINATEUR	Jean-Paul Kneib	EPFL, Lausanne
DIRECTRICE DE THÈSE	Roser Pelló	IRAP, Toulouse

École doctorale et spécialité :
SDU2E : Astrophysique, Sciences de l'Espace, Planétologie
Unité de Recherche :
Institut de Recherche en Astrophysique en Planétologie (IRAP, UMR 5277)
Directeur de Thèse :
Roser Pelló
Rapporteurs :
David Elbaz et *Olivier Le Fèvre*

Abstract

Reionization is the last change of state of the Universe which made its entire hydrogen content transition from a neutral to a completely ionized state. This rapid transition and heating of the gas content had major consequences on the formation and evolution of structures which makes of reionization a key element to understand the present day Universe.

In our current understanding, reionization was mostly done by $z \sim 6$ and the sources responsible for this transition are likely faint, low mass and star-forming galaxies (SFGs). One way to study this population is to determine the Luminosity Function (LF) of galaxies selected from their Lyman-alpha emission and assess their ionizing flux density. However, most recent studies and their conclusions are in general limited by the lowest flux that can be reached with the current observational facilities.

One of the major goals of the work presented in this manuscript is the study of the Lyman-alpha emitters (LAE) LF using deep observations of strong lensing clusters with the VLT/MUSE instrument. MUSE is a large field of view Integral Field Unit (IFU) ideal to work on the galaxy LF since it allows a complete and blind selection of LAEs without any photometric preselection. In addition, MUSE provides a continuous redshift range of $2.9 < z < 6.7$ for LAEs that just overlaps with the end of the reionization era, making MUSE well suited to provide constraints on the contribution of LAEs to reionization.

The combined usage of large IFU data cubes and lensing fields makes this analysis computationally challenging. To get around this difficulty, we have developed new methods to account for the contribution of each individual LAE, including the effective-volume and completeness determinations. The volume computation is based on the simulation of the detection process of individual LAEs in the source plane reconstruction of MUSE cubes to account for both the lensing effects and the individual spatial and spectral profiles of LAEs. Throughout this work special care was given to faint and highly magnified LAEs since they are the key to access the very faint end of the LAE LF. To the cost of a significant increase in complexity and a lower volume of Universe explored, both due to the lensing effect, we build the LAE LF using a Monte-Carlo process to account for all possible sources of uncertainties, for a population of 152 LAEs with $39 \lesssim \log L_{\mathrm{Ly}_\alpha}[\mathrm{erg\ s^{-1}}] \lesssim 43$ selected across four MUSE fields of view.

The LFs resulting form this analysis set an unprecedented level of constraint on the shape of the faint end and reached down to $\log L = 40.5$. We conclude, making no assumption on the escape fraction of Lyα emission, that the LAE population has a similar level of contribution to the total ionising emissivity as the UV-selected galaxies (LBGs) at $z \sim 6$. Depending on the relative intersection of these two populations, the SFGs could produce enough ionising flux to fully ionise the Universe by $z \sim 6$.

In the continuity of this work on the LAE LF, we investigate the effect of the selection method on the conclusions mentioned above. A better characterisation of the bias intrinsic to the LAE and LBG selection processes is needed to reach a more robust assessment of the complete population of high redshift SFGs. To this end, we implemented a blind and systematic search of both LAEs and LBGs behind lensing field A2744 using the deep MUSE observations in combination with public data of the Hubble Frontier Fields (HFF) program. The results have shown that the observed proportion of LAEs increases significantly among UV-faint galaxies and at increasing redshift.

Resumé

La réionisation est le dernier changement d'état de l'Univers qui a fait passer la totalité du contenu en hydrogène d'un état neutre à un état complètement ionisé. Cette transition rapide et le réchauffement de la phase gazeuse ont eu des conséquences majeures sur la formation et l'évolution des structures qui font de la réionisation un élément clé pour comprendre l'Univers actuel.

Dans notre compréhension actuelle, la réionisation était principalement finie autour $z \sim 6$ et les sources responsables de cette transition sont probablement les galaxies peu lumineuses, de faible masse et à formation d'étoiles (SFG). Une façon d'étudier cette population consiste à déterminer la fonction de luminosité (LF) des galaxies choisies grâce à leur émission Lyman-alpha et à évaluer leur densité de flux ionisant. Cependant, les études les plus récentes et leurs conclusions sont en général limitées par la limite en flux qui peut etre atteinte par les instruments actuels.

L'un des principaux objectifs du travail présenté dans ce manuscrit est l'étude des émetteurs Lyman-alpha (LAE) LF à l'aide d'observations profondes d'amas de galaxies à effet de lentilles fortes avec l'instrument VLT/MUSE. MUSE est un "Integral Field Unit" (IFU) à grand champ de vision idéal pour travailler sur la LAE LF puisqu'il permet une sélection complète et aveugle de LAEs sans aucune présélection photométrique. De plus, MUSE offre une plage de redshift continu de $2.9 < z < 6.7$ pour les LAE qui coïncide avec la fin de la réionisation, ce qui rend MUSE très pertinent pour fournir des contraintes sur la contribution des LAEs à la réionisation.

L'utilisation combinée de grands cubes de données IFU et de champs lentillés rend cette analyse difficile sur le plan informatique. Pour contourner cette difficulté, nous avons mis au point de nouvelles méthodes pour tenir compte de la contribution de chaque LAE, y compris la détermination du volume effectif et de la complétude. Le calcul du volume est basé sur la simulation du processus de détection des LAEs individuelles dans la reconstruction du plan source des cubes MUSE, pour tenir compte à la fois des effets de lentille et des profils spatiaux et spectraux individuels des LAEs. Tout au long de ce travail, un soin particulier a été apporté aux LAEs de faible luminosité et fortement lentillés car ils sont la clé d'accès à l'extrémité à faible luminosité de la LAE LF. Au prix d'une augmentation significative de la complexité et d'une diminution du volume de l'Univers exploré, tous deux dus à l'effet de lentille, nous construisons la LAE LF en utilisant un processus de Monte-Carlo pour tenir compte de toutes les sources possibles d'incertitudes, pour une population de 152 LAEs avec $39 \lesssim \log L_{\mathrm{Ly}\alpha}[\mathrm{erg\ s^{-1}}] \lesssim 43$ sélectionnés parmi quatre champs de vision MUSE.

Les résultats de cette analyse ont établi un niveau de contrainte sans précédent sur l'allure à faible luminosité de la LF jusqu'à $\log L = 40.5$. Nous concluons, sans faire d'hypothèse sur la fraction d'échappement de l'émission Lyα, que la population de LAE a un niveau de contribution à l'émissivité ionisante totale similaire à celui des galaxies sélectionnées par imagerie UV (LBG) à $z \sim 6$. En fonction de l'intersection relative de ces deux populations, les SFG pourraient produire suffisamment de flux ionisants pour ioniser complètement l'Univers à $z \sim 6$.

Dans la continuité de ce travail sur la LAE LF, nous étudions l'effet de la méthode de sélection sur les conclusions mentionnées ci-dessus. Une meilleure caractérisation du biais intrinsèque aux processus de sélection LAE et LBG est nécessaire pour parvenir à une évaluation plus robuste de l'ensemble de la population des SFGs à haut redshift. À cette fin, nous avons effectué une recherche aveugle et systématique des LAEs et des LBGs derrière l'amas de galaxies A2744 en utilisant les observations MUSE en combinaison avec les données publiques du programme Hubble Frontier Fields (HFF). Les résultats ont montré que la proportion observée de LAEs augmente de manière significative parmi les galaxies à faible continu UV et et parmi les galaxies à haut redshift.

Contents

Remerciements

Mes premiers remerciements vont évidemment à Roser qui m'a encadré pendant ces trois années. Lorsque j'ai finalement décidé de venir faire ma thèse à Toulouse sur MUSE et les sources de la reionisation, nous ne nous connaissions pas du tout, mais pendant ces trois ans j'ai pu découvrir quelqu'un que j'apprécie sincèrement. Elle a su me laisser une liberté et autonomie dans mon travail que j'ai beaucoup apprécié, tout en me poussant à faire mieux et en sachant me remotiver dans les moments les plus difficiles. Merci pour ta confiance, ton entrain et ta disponibilité malgré ton emploi du temps inhumain !

Je remercie également chaleureusement Johan Richard (ainsi que toute l'équipe lensing du CRAL à Lyon) et Franz Bauer pour leur aide, leurs encouragements, leur disposnibilité et leur accueil, avec une attention spéciale pour Franz chez qui je suis resté deux semaines lors de mon séjour à Santiago. Ils font pour moi parti des personnes qui montrent que faire de l'astrophysique peut être amusant et épanouissant, et qui m'ont fortement fait hésiter à continuer un peu plus longtemps dans cette voie. Je remercie également Thierry et Geneviève avec qui j'ai eu l'occasion de discuter plus longuement pendant les "Busy Week", et qui m'ont écouté et encouragé lorsque j'étais dans le dilemne classique du doctorant : "post-doc ou pas post-doc ?". Et plus généralement, je remercie toutes les personnes de l'IRAP et de l'équipe MUSE GTO avec qui j'ai pu interagir pendant ces trois années de thèse et qui ont pu m'aider sur une vaste panoplie de problèmes.

Mais une thèse ne peut pas se résumer au travail et la science, c'est aussi l'occasion de se faire des amitiés solides. Je pense tout particulièrement à mes deux co-bureau du B137 qui m'ont supporté pendant deux ans : Louise et Baptiste. J'estime avoir eu de la chance car j'aurais facilement pu tomber sur pire. Mon seul regret est que vous fassiez des exo-planètes, mais nul n'est parfait... ! Merci d'avoir rendu supportable par votre bonne humeur et votre entrain quotidien les phases les moins drôles et les moments difficiles de la thèse ! Merci également à Adrien, Edoardo, Damien, Gaylor et Etienne pour le tarot le midi, les discussions, les soirées, le vélo et plus généralement pour avoir été d'excellents amis et compagnons de thèse.

Je remercie également Amaury, qui m'a aidé pour un grand nombre de soucis informatique sur lesquels je suis tombé, et qui petit à petit m'a permis d'etre plus efficace et plus rapide dans mon travail. Merci d'avoir passé du temps à m'envoyer des lignes de code et de script, des conseils d'organisation, d'architecture, configuration, et bien d'autres choses encore, aux heures ou tu travaillais également !

Je terminerai en remerciant Mélissa pour son soutient inconditionnel, ses encouragements et sa présence à mes cotés malgré la distance.

Foreword

One important driver for the development of astronomy and cosmology is the will to constantly see further and especially further back in time, to understand the very beginning of the Universe. In this long lasting hunt for distant and high redshift objects, a lot of the observational efforts have been directed towards investigating the reionization era and the sources responsible for this cosmic reionization.

Reionization is the last major change of phase of the Universe. After recombination, the hydrogen content of the Universe was mostly neutral, and as the Universe expanded, this neutral gas cooled down and the first stars and galaxies formed. The ionizing lights emitted during this period made the Universe transition from a mostly cold and neutral state towards a mostly warm and ionized state. This reheating of the Universe had significant impact on the formation of structures at all spatial scales. As such, reionization is a key element to understand the evolution of the Universe and present-day observations.

To date, little is known about the sources responsible for reionization. It was established over the years that quasars, gamma-ray bursts, X-rays binaries were not numerous enough to drive this transition, leaving normal star forming galaxies (SFGs) as the most likely candidates. However, there is not direct observational evidence of this fact. Previous studies of the galaxy Luminosity Function (LF), which is the distribution of galaxy numerical density per magnitude/luminosity bin, revealed that for SFGs to drive the reionization, the contribution of faint and low mass galaxies has to be decisive. But by essence, low mass and intrinsically faint SFGs are challenging to observe, especially at high redshift. To reach more definitive conclusions, deeper (and larger) observations are required, and for that reason progresses made in understanding reionization are closely related to the development of new and more efficient telescopes and instruments.

Another matter of interest in this search for SFGs is the question of the selection mean. Two methods are commonly used to select high redshift SFGs: the drop-out selection based on multi band rest-frame UV observations, and the Lyman-alpha (Lyα) selection based on spectroscopic identification of Lyα emission line. As each of them have their own observational biases, it remains challenging to have a complete assessment of SFGs without a better understanding and characterization of the intersection between the populations selected with these two methods. To date the UV selected population (LBG) and Lyman-alpha emitters (LAEs) have mostly been studied as separate population with no attempt to unify them. And the same goes for the galaxy LF which is usually separated in either the UV/LBG LF or the LAE LF.

This thesis manuscript summarizes the three years of work done at the Institut de Recherche en Astrophysique et Planétologie (IRAP) on investigating the sources of cosmic reionization using strong lensing clusters and the VLT/MUSE instrument. MUSE is an ideal instrument for the detection of faint line emitters, and being an IFU it allows a complete selection of LAEs in the range $2.9 < z < 6.7$ in a $1' \times 1'$ Field of View (FoV). The main goal of this work was to set constraints on the contribution of the LAE population to cosmic reionization by computing their

LF. Using MUSE observation of strong lensing clusters, acting as gravitational telescope, we were able to detect and select intrinsically fainter LAEs compared to deep blank fields.

Because working with strong lensing is (CPU-)time consuming, the main difficulty of this project was to find and efficient method to process large spectroscopic cubes in a lensing context, while treating each LAE individually to account for their own specificities (namely spatial and spectral profile).

A lot of of the work done during this thesis was therefore very technical and involved a lot of coding to implement a method as automated as possible for the LF computation. This process involved a lot of trial and errors and it took much more time than initially expected, to finally reach something satisfactory.

A lot of efforts were made to make this code as automated as possible, to ease the process of adding future MUSE cubes to the lensing sample. Working in the frame of the MUSE Guaranteed Time Obsevations (GTO), we suffered no shortage of data, but only the results obtained with four lensing fields (namely A1689, A2390, A2667, A2744) are presented in this thesis.

Some preliminary work using additional lensing fields part of the GTO program or data available through external collaborators has been done, but was not included in this manuscript for lack of time. A new analysis using a larger sample will be the focus of a future publication in preparation.

Regarding the layout of this manuscript, Chapter 1 provides a large introduction to the problematics linked to reionization and the observation and selection of high redshift galaxies. In Chapter 2 we present the VLT/MUSE instrument, from its technical features and science goals to its data and noise structure. In Chapter 3, we describe the lensing sample used for this work, and explain the basics of strong lensing required to understand the methods developed in this work. Chapter 4 presents the method adopted for the effective volume computation as well as the motivations for its development. Being the most difficult and technical chapter of this thesis, many examples and illustrations are provided, and some guideline is given to ease the read. In Chapter 5 we present the different steps required to compute the LAE LF from the MUSE cubes. This includes the Lyα flux computation and the final LAE sample selection, a brief summary of the effective volume computation, the computation of a completeness correction and the final step to actually compute the LF with proper error transfer. The analysis of the LF is presented in Chapter 6 together with the conclusion regarding the contribution of the observed LAE population to reionization. Finally in Chapter 7 we present a brief comparison between the LAE and LBG population selected within a same volume, behind the A2744 lensing cluster. A conclusion and summary of all the work done during this thesis can be found together with a brief overview of possible future perspectives can be found in Chapter 8.

Avant propos

Un moteur important du développement de l'astronomie et de la cosmologie est la volonté de voir toujours plus loin et surtout plus loin dans le temps, afin de comprendre le tout début de l'Univers. Dans cette chasse de longue haleine aux objets éloignés et à grand redshift, une grande partie des efforts d'observation ont été orientés vers l'étude de la réionisation et des sources responsables de cette réionisation cosmique.

La réionisation est le dernier changement majeur de phase de l'Univers. Après la recombinaison, le contenu en hydrogène de l'Univers était en grande partie neutre et, à mesure que l'Univers se développait, ce gaz neutre s'est refroidi et les premières étoiles et galaxies se sont formées. Les lumières ionisantes émises durant cette période ont fait passer l'Univers d'un état essentiellement froid et neutre à un état essentiellement chaud et ionisé. Ce réchauffement de l'Univers a eu un impact significatif sur la formation des structures et à toutes les échelles spatiales. La réionisation est donc un élément clé pour comprendre l'évolution de l'Univers et les observations actuelles.

Jusqu'à présent, on sait peu de choses sur les sources responsables de la réionisation. Il a été établi au fil des ans que les quasars, les sursaut gamma et les binaires X n'étaient pas assez nombreux pour entraîner cette transition, laissant les galaxies "normales" à formant des étoiles (SFG) comme les plus probables candidats. Cependant, il n'y a pas de preuve d'observation directe de ce fait. Des études antérieures sur la fonction de luminosité (LF) des galaxies, qui est la distribution de la densité numérique des galaxies par intervalle de magnitude/luminosité bin, ont révélé que pour que les SFG dominent la réionisation, la contribution des galaxies peu brillantes et faible masse doit être décisive. Mais par essence, il est difficile d'observer des SFGs de faible masse et de faible intensité intrinsèque, surtout à haut redshift. Pour parvenir à des conclusions plus définitives, des observations plus profondes (et plus étendues) sont nécessaires, et c'est pourquoi les progrès réalisés dans la compréhension de la réionisation sont étroitement liés au développement de nouveaux télescopes et instruments, sans cesse plus efficaces.

Un autre sujet d'intérêt dans cette recherche des SFGs est la question de la méthode de sélection. Deux méthodes sont couramment utilisées pour sélectionner les SFG à grand redshift : la sélection dite "drop out" basée sur des observations UV multi bandes, et la sélection Lyman-alpha (Lyα) basée sur l'identification spectroscopique de la raie d'émission Lyα. Étant donné que chacune de ces deux méthodes a ses propres biais d'observation, il demeure difficile d'avoir une évaluation complète des SFGs sans une meilleure compréhension et caractérisation de l'intersection des populations sélectionnées par ces deux méthodes. Jusqu'à présent, les populations sélectionnées à partir d'image UV (LBG) et les émetteurs de Lyman-alpha (LAE) ont surtout été étudiées en tant que populations distinctes, sans aucune tentative de les unifier. Et il en va de même pour la LF qui est habituellement séparée entre d'un coté la fonction de luminosité UV/LBG et de l'autre celle des émetteurs Lyα.

Ce manuscrit de thèse résume les trois années de travail effectuées à l'Institut de Recherche en Astrophysique et Planétologie (IRAP) sur l'étude des sources de la réionisation cosmique à l'aide d'amas de galaxies agissant comme lentille gravitationnelle et de l'instrument VLT/MUSE. MUSE est un instrument idéal pour la détection de raies d'émission faibles, et étant un IFU, il permet

une sélection complète de LAEs dans le domaine de redshift $2.9 < z < 6.7$ dans un champ de vue de $1' \times 1'$. L'objectif principal de ce travail est de contraindre la contribution de la population des LAE à la réionisation cosmique en calculant leur LF. En utilisant les observations MUSE d'amas de galaxies agissant comme télescope gravitationnel, nous avons pu détecter et sélectionner des LAEs intrinsèquement plus faibles que dans les champs vides profonds les plus profonds.

Comme l'analyse dans le cadre des lentilles gravitationnelles est très gourmande en terme de temps de calcul, la principale difficulté de ce projet a été de trouver une méthode efficace pour traiter les grand cubes spectroscopiques, tout en traitant chaque LAE individuellement pour tenir compte de leurs propres spécificités notamment le profil spatial et spectral ainsi que leur grandissement.

Une grande partie du travail effectué pendant cette thèse fut donc très technique et impliquait beaucoup de code pour implémenter une méthode aussi automatisée que possible pour le calcul des LFs. Ce processus a nécessité beaucoup d'essais et d'erreurs et il a fallu beaucoup plus de temps que prévu pour arriver à quelque chose de satisfaisant.

Beaucoup d'efforts ont été faits pour rendre ce code aussi automatisé que possible, afin de faciliter le processus d'ajout de futurs cubes MUSE à l'échantillon presenté dans ce travail. Dans le cadre du "MUSE Guaranteed Time Obsevations" (GTO), nous n'avons pas manqué de données, mais seuls les résultats obtenus avec quatre champs (A1689, A2390, A2667, A2744) sont présentés dans cette thèse.

Certains travaux préliminaires utilisant des champs de lentilles supplémentaires faisant partie du programme GTO ou des données disponibles auprès de collaborateurs externes ont été effectués, mais n'ont pas été inclus dans ce manuscrit faute de temps. Une nouvelle analyse utilisant un échantillon plus large fera l'objet d'une future publication en préparation.

En ce qui concerne la mise en page de ce manuscrit, le chapitre 1 fournit une grande introduction aux problématiques liées à la réionisation et à l'observation et la sélection des galaxies à haut redshift. Dans le chapitre 2 nous présentons l'instrument VLT/MUSE, ses caractéristiques techniques et objectifs scientifiques ainsi que la structure de ces données et la structure du bruit à l'intérieur des cubes. Dans le chapitre 3, nous décrivons l'échantillon de lentilles utilisé pour ce travail, et expliquons les bases de la lentille gravitationnelle nécessaires pour comprendre les méthodes développées dans ce travail. Le chapitre 4 présente la méthode adoptée pour le calcul effectif du volume ainsi que les motivations de son développement. Étant le chapitre le plus difficile et le plus technique de cette thèse, de nombreux exemples et illustrations sont fournis, et quelques lignes directrices sont données pour en faciliter la lecture. Dans le chapitre 5 nous présentons les différentes étapes nécessaires pour calculer la LAE LF à partir des cubes MUSE. Ceci inclut le calcul du flux Lyα et la sélection finale de l'échantillon LAE, un bref résumé du calcul du volume effectif, le calcul d'une correction de complétude et l'étape finale pour calculer la LF avec un transfert d'erreur correct. L'analyse de la LF est présentée au chapitre 6 ainsi que la conclusion concernant la contribution de la population LAE observée à la réionisation. Enfin, dans le chapitre 7, nous présentons une brève comparaison entre la population de LAE et de LBG sélectionnée dans un même volume, derrière l'amas-lentille A2744. Vous trouverez au chapitre 8 une conclusion et un résumé de tous les travaux réalisés dans le cadre de cette thèse ainsi qu'un bref aperçu des perspectives futures possibles.

1 Introduction

Contents

1.1 The early Universe

1.1.1 First structure and galaxy formation

Just after the beginning of inflation (Guth, 1981), the energy content of the Universe was dominated by baryonic matter, radiation and collisionless Dark Matter (DM). During this time, the temperature and density of the Universe were so high that matter and radiation coexisted in a thermal equilibrium, meaning that photons were coupled with baryonic matter and followed the black-body radiation law. In these first instants, these extreme conditions only allowed the existence of baryonic matter as ionized nuclei, or free electrons. The electric charges in these particles made the interaction with photons very frequent therefore preventing them from travelling freely and in straight line.

One of the effect of such a rapid expansion of the Universe is the reduction of the local cosmological horizon thus preventing gravitation to act upon spatial scales larger than this cosmological horizon. An other side-effect of rapid expansion was the expansion to cosmic sizes and the smoothing of the initial overdensities caused by quantum fluctuations. Both DM and baryonic matter were affected in the same way by the Universe expansion. However, the proper motion of DM not being supported by photon pressure, velocity dispersion and collisions as it was the case for baryonic matter, its gravitational collapse could began at an earlier stage of the evolution of the Universe. Therefore as soon as the expansion rate allowed it, and prior to baryonic matter, the DM began its purely gravitational collapse around local overdensities to form filaments and halos.

Around $z \sim 1\,100$ (i.e. $\sim 300\,000$ years after the beginning of the inflation) and as the Universe continued its expansion, the temperature and density reached low enough values to allow matter to form the first atoms of hydrogen ($\sim 75\%$) and helium ($\sim 25\%$), with only traces of light elements. This recombination of matter ended the coupling between baryonic matter and radiation and the Universe was therefore made transparent, meaning that photons were able to travel freely in straight lines and with minimal interaction with matter. Because this shift to neutral state happened quickly, the photons emitted just before the decoupling are perfectly representative of the overdensities at this epoch of the Universe. And since the light now propagates freely, these photons are still travelling across the Universe to this day. For any observer, this Last Scattering Surface (LSS) appears as a sphere whose radius is perpetually increasing at the speed of light. The redshifted fossil emission of this LSS has been observed for the first time in 1965 (Penzias & Wilson, 1965) and is called the Cosmic Microwave Background (CMB). The measurement of the temperature fluctuations of the CMB has been the object of several spatial missions, the last to date being Planck. Measurements of these temperature/density variations (see Fig. 1.1) are of crucial importance to put constraints on certain cosmological parameters (Planck Collaboration et al., 2016c) or models (Planck Collaboration et al., 2016b) and to understand the initial conditions that allowed the formation of the first structures.

After the dissipation of the LSS, the Universe entered the so-called dark-ages. As matter was no longer coupled to radiation, there were no sources of light and the Universe remained dark until the formation of the first stars and galaxies. Not being supported by internal radiation pressure anymore, the baryonic matter began its gravitational collapse around the previously formed dark-matter halos and filaments. Unlike DM which can only interact through gravitation, baryonic matter can take advantage of various mechanisms (e.g., radiative cooling) to quickly dissipate its kinematic energy and facilitate its collapse at the smaller scales. Once the gas was cool enough, this collapse led to the formation of the first star and quickly after the first galaxies.

The gas being still warm after the recent inflation and recombination, it was relatively easy to

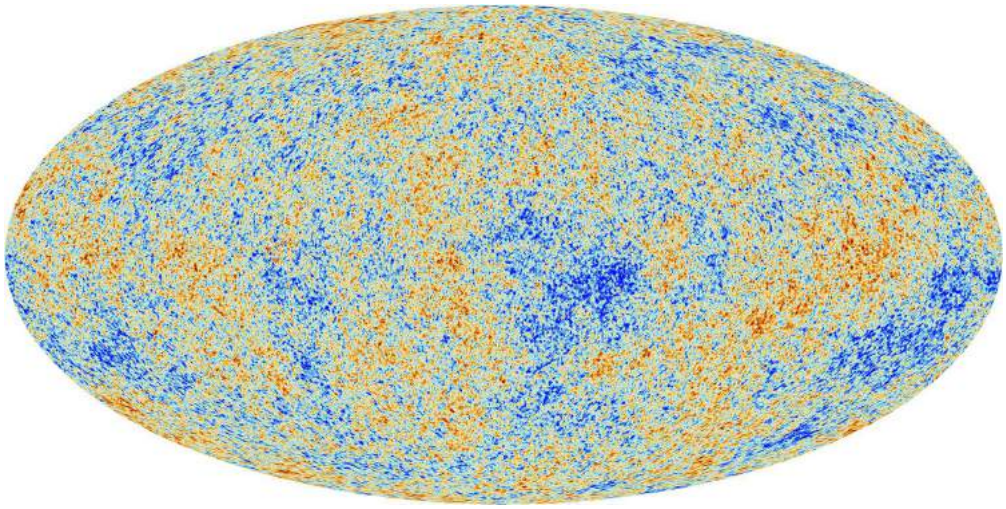

Figure 1.1: Temperature fluctuation of the CMB as observed by the Planck mission.

form heavy stars (around 100 $M_{\odot}$ and above) at this early stage of the Universe. Even though these massive stars, called population III (pop III) stars have never been observed directly, there are some indications for their existence, one of which being the very low metallicity star population observed in primordial galaxies. The presence of such population in very high redshift galaxies argues in favour of a rapid chemical evolution of the medium which is consistent with the existence of (very) massive stars with a short life span (see e.g., Tornatore et al., 2007; Wise et al., 2012; Frebel et al., 2015; de Bennassuti et al., 2017, and the references therein). The exact mechanisms involved in the formation of these first stars, and the relative proportion of stars is still matter of debate and is still being investigated. As these first stars lighted up around $z \sim 20$ in the DM and large gas halos, the first galaxies began to form shortly after at $z \sim 10$ - 15. Here again some uncertainties remain and the exact epoch of the first galaxy formation depends on the exact definition used for the word galaxy. From that point, a succession of structures mergers (galaxies, filaments, DM halos etc...) ensues along the dark matter filaments and halos (see Fig. 1.2 for an example of simulated filaments and halos).

One of the first work to propose a satisfying theoretical depiction of this hierarchical clustering and of the mechanisms intervening at the different scales was published White & Rees (1978). This study also showed the need for efficient dissipative mechanisms to collapse the gas, and the need for a cold dark matter collapse prior to recombination. Nowadays this hierarchical formation of structure is well accepted to describe the global picture of evolution and formation of galaxies. The filaments predicted by such a theory are indirectly observed in the SDSS survey using galaxies as a tracer of structure (see e.g., Sousbie et al., 2011; Tempel et al., 2014) and are also successfully reproduced by numerical simulations (see e.g., Miralda-Escudé et al., 1996; De Lucia et al., 2004; Vogelsberger et al., 2014; Schaye et al., 2015). Nowadays, the difficulty has shifted towards a finer understanding of the dissipative mechanisms involved in star formation and therefore galaxy formation and chemical enrichment.

Such investigations are currently limited by the computational power available. Hydrodynamical simulations (see e.g. Springel et al., 2005; Vogelsberger et al., 2014; Schaye et al., 2015) are extremely demanding in terms of CPU resources, which makes virtually impossible to have a spatial resolution fine enough to include small scale effects such as stellar feedback or radiative transfer, in a volume large enough to include cosmological effects. Even though some progress are introduced with continuously increasing CPU power, these simulations cannot properly study how the small

scale effects may or may not impact the evolution of cosmological volumes. To get around this difficulty, an alternative approach was developed: Semi-Analytic Models (SAM). These models use a mix of N-body simulations and parameterized effects to describe as precisely as possible the physics of baryons (see e.g., Somerville & Primack, 1999; Garel et al., 2012) and are therefore able to study effects which are usually out of reach of purely hydrodynamical simulations. But they are nonetheless limited by the (sometimes strong) assumptions needed to describe the physics of baryons.

An example of the results of the EAGLE simulation (Schaye et al., 2015), one of the most recent and detailed hydrodynamical simulation coupled with sub-grid physics is provided in Fig. 1.2. The two panels show the gas distribution and temperature (left panel) and the underlying DM distribution (right panel). In this snapshot at z = 0 of the simulation, the cosmic web structure predicted by the hierarchical formation is clearly visible for both the DM and gas distribution.

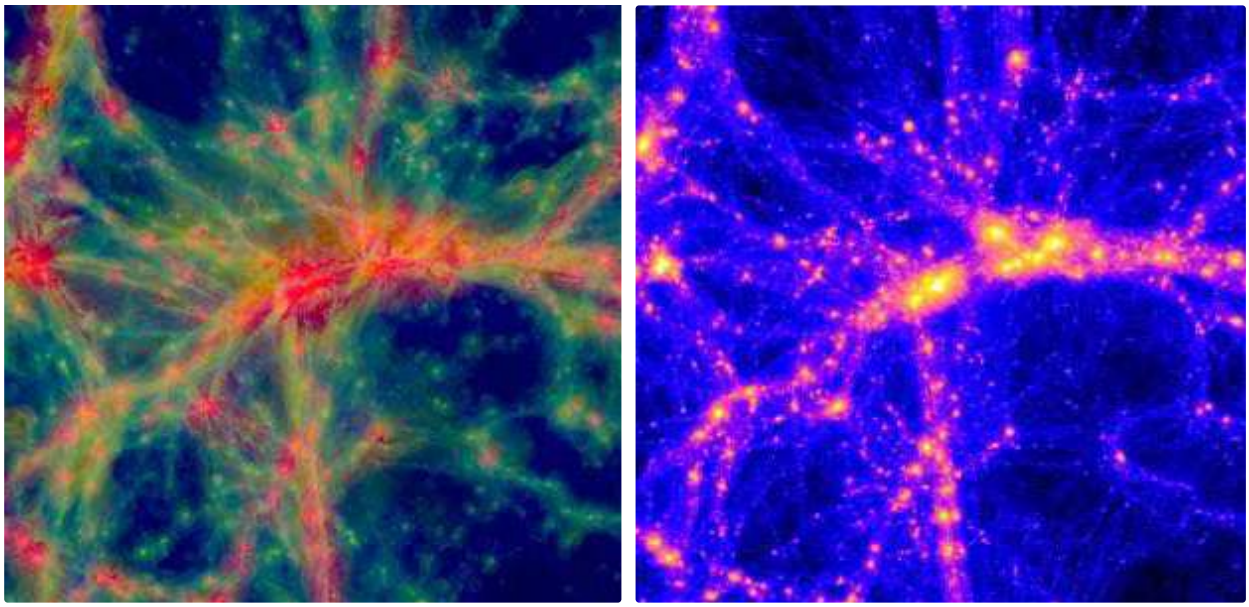

Figure 1.2: Left panel: slice of the EAGLE simulation at $z = 0$. The intensity color encodes the gas density while the color itself encodes the temperature of the gas. Blue is for $T \leq 10^{4.5}$, green for $10^{4.5} \leq T \leq 10^{5.5}$ and red for $T \geq 10^{5.5}$. Right panel: underlying dark matter distribution in the same simulation slice
Credits: figure taken from the EAGLE website (Schaye et al., 2015)

1.1.2 Epoch of reionization

As the first structures appeared in the early Universe, they emitted the first light and in the same time ended the dark-ages and began reionization. Reionization is the last transition of state of the Universe and happened when the neutral hydrogen (HI) was ionized by the UV photons emitted by the first ionizing sources. As these first sources and structures grew and formed, they emitted more and more UV-photons leading to bubbles of ionized hydrogen (HII regions) forming and expanding around these ionizing sources. As the density of UV photons continued its increase, these HII regions continued their growth until the entire neutral hydrogen of the Universe was ionized. A schematic representation of this is provided in Fig. 1.3. A more complete description of this process can be found e.g. in Barkana et al. (2001).

According to theory and simulations, this entire change of state happened between redshift z$\sim$ 20 and z $\sim$ 6. However, there is growing evidences for an in-homogeneous end of reionization,

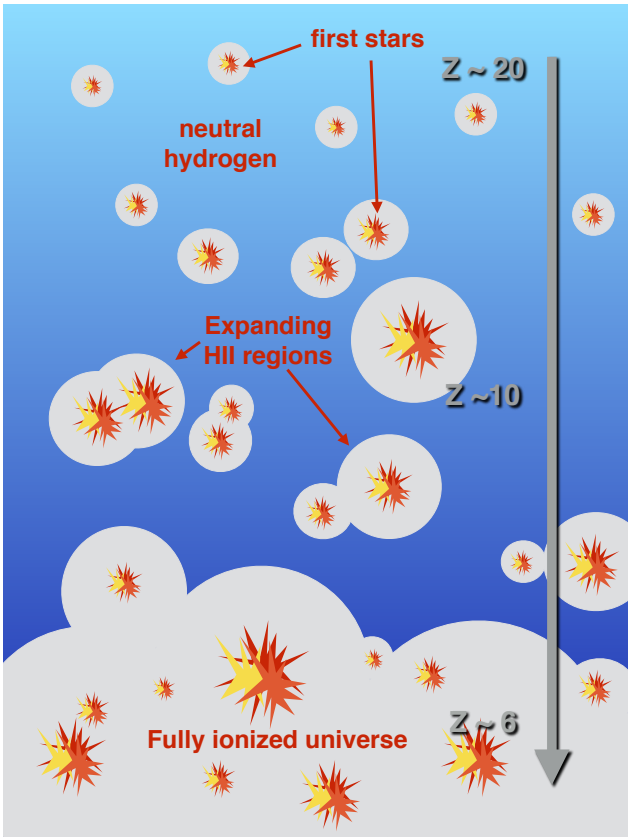

Figure 1.3: Schematic of the reionization of the Universe. AS the fist stars and structures appeared, expanding HII regions began to from around ionizing source, until the entire Universe was completely reionized around z$\sim$ 6.

meaning that some regions in the Universe went through this transition later than others (Pentericci et al. (see e.g. 2014); Becker et al. (see e.g. 2015) or Sect. 1.3).

The energy required to ionize a neutral atom of hydrogen is of 13.6 eV, which corresponds to a photon wavelength of 912 Å. As a consequence, any photon with a wavelength shorter than this limit would end up absorbed by neutral hydrogen. This phenomenon can be observed in spectra of high redshift galaxies, where photons with $\lambda \leq 912$Å (called UV photons hereafter) are absorbed (in various ways depending on redshift effects and gas kinematics) by the surrounding neutral medium (more on that in Sect. 1.2). The transition to a completely ionized state can only happen under the condition that the ionizing rate is higher than the recombination rate. Since the ionizing rate is the emission rate of UV photons in a given volume, the condition for reionization translates into a need for enough ionizing flux density to reionize the Universe and maintain that ionized state. Therefore, one of the most prominent points in the study of reionization is the search for a population that would provide enough ionizing flux density at such an early stage of the Universe. Up to now, several types of objects have been investigated as potential sources of reionization as discussed in Sect. 1.1.3. Simulations are also very important to understand the reionization timeline, in addition to the direct detection of the sources responsible for this process.

As mentioned in previous section, we now have a good global understanding of the structure formation process through hierarchical clustering and prior dark-matter assembly and halos formation. However the precise details of the baryonic collapse are still unclear. Notably, observations have revealed the existence of massive black holes at high redshift (see e.g., the one at z= 7.1 in

Mortlock et al. (2011), or the quasar with $z \geq 6.4$ in Venemans et al. (2013)), but current models and theories still struggle to explain their formation at such an early stage of the Universe. The most likely theories supported by simulations involve direct collapse black holes and very high and continuous accretion rate (see e.g., Volonteri, 2010; Agarwal et al., 2014; Volonteri et al., 2016, and the references therein) but definitive observational evidences for this are not available.

Reionization had an impact on the evolution of the Universe as the gas content of the Universe transitioned from a cold to a warm phase. Such a transition could have had repercussions on structure and galaxy formation in numerous ways and various scales. Being warmer, gas halos and gas clouds become partly supported by velocity dispersion and can even start to photoevaporate depending on their mass (Okamoto et al., 2008). This effect combined with the radiative pressure and processes starting to build around bright sources can impact stellar formation and trigger many complex feedback mechanisms (see e.g. Ocvirk et al., 2016)

In addition, by studying the first light and reionization era, we push our observations towards the frontier of possible observation since by definition, nothing was visible before these first lights. Studies of these first sources and structure therefore serve as a link between the initial condition at the recombination stage and the observations of the lower redshift Universe.

1.1.3 Identifying the sources of reionization

Over the past years, various type of ionizing sources have been investigated in an effort to find the primary sources of reionization.

Following the chronological order, the first candidates that were considered were the massive pop III stars. However, because of their short life-span and because they were quickly replaced by a new generation of metal poor stars, they could not have contributed to reionization during an extended period of time (see e.g., the simulation results from Ricotti & Ostriker, 2004a; Paardekooper et al., 2013). The X-ray emission from hard X-ray sources such as binaries and Active Galactic Nuclei (AGN) were also considered as ionizing sources. Even though these populations are poorly constrained at high redshift, it seems that they are not numerous enough to produce a significant fraction of the ionizing flux required for reionization (see e.g. Ricotti & Ostriker, 2004b; Willott et al., 2010; McQuinn, 2012; McGreer et al., 2013).

Nowadays, these two populations have been mostly set aside in this search for the sources of reionization. It is not excluded that they contribute to a somewhat significant level to the overall ionizing flux density budget ($\lesssim 10\%$), but a consensus is beginning to appear in the sense that none of them are driving the reionization process. More recently, the search for ionizing sources has therefore shifted towards galaxies as they are the most likely candidates remaining. And more specifically the low mass and star forming galaxies, as their high numerical density and their hard spectra produce a large amount of ionizing flux. However, a definitive proof has yet to be made that this population do indeed drive the reionization process.

We provide below a description of these high redshift and star forming galaxies and explain how to quantify the contribution of this galaxy population with the Luminosity Function (LF) in Sect. 1.2. We then present the recent progresses and developments regarding the reionization timeline and the assessment of the contribution of SFGs to reionization in Sect. 1.3 and Sect. 1.4. Finally, we explain in Sect. 1.5 the strategy used in this present work and show how it can contribute to answer to some of the remaining questions about reionization.

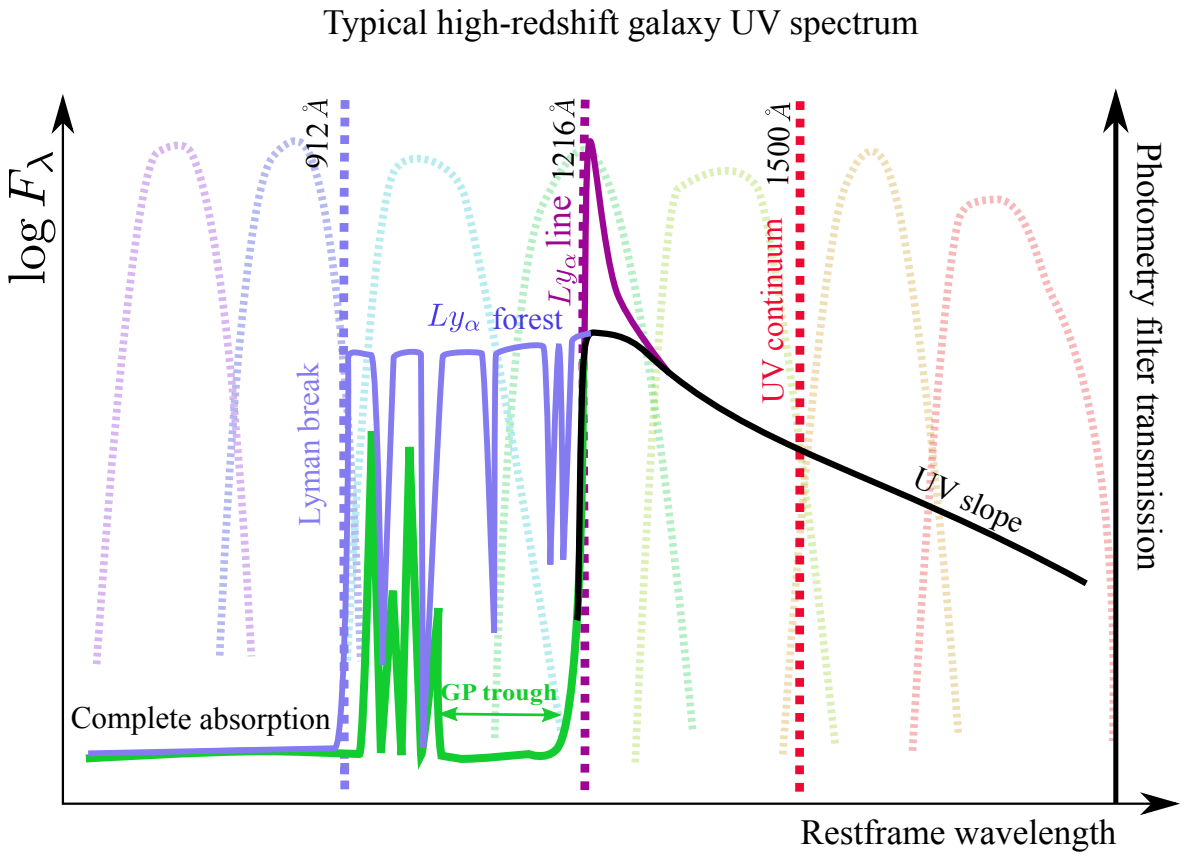

Figure 1.4: Simplified spectrum of a high redshift star forming galaxy in its rest frame wavelength with the different possible observed features. The transmission of photometry filters is shown in the background as dotted colored lines. Individual galaxies can be selected as both LAE and LBGs. The Gunn Peterson trough is observed for galaxies at $z > 6$ when surrounded by a large amount of HI.

1.2 High redshift and star forming galaxies

The first challenge of studying high redshift galaxies, is to find and observe them. Because the rest-frame emission of these galaxies is typically dominated by the spectra of star forming regions and young stellar population, they have a bright UV continuum associated with a steep UV slope together with a characteristic break (GP trough and Lyα forest, see Sect. 1.2.2) that helps identifying them. In addition they can also have recombination and forbidden emission lines representative of star forming regions.

To select sources from this population, two methods are commonly used: the drop-out selection based on multi-band photometry or the Lyα selection based on either Narrow-Band (NB) photometry or IFU observations. These two selection methods and the underlying physical processes traced by these methods are presented in Sect. 1.2.2 and Sect. 1.2.1 respectively. An idealized representation of such a high redshift galaxy spectrum is presented in Fig. 1.4 to illustrate the following sections.

1.2.1 Lyman-Alpha emitters

1.2.1.1 Description and observational features

The Lyα is a resonant emission line of hydrogen at $\lambda_{Ly_\alpha} = 1216$Å and is intrinsically the brigthest line of the hydrogen emission line spectrum. It can be emitted by atom collision and recombination of ionized hydrogen and as such is often used a tracer for star forming galaxies and star-forming regions. It is also commonly used a a signature for high redshift and young galaxies (Partridge & Peebles, 1967; Malhotra & Rhoads, 2002). Galaxies observed with this Lyα emission are called Lyman-Alpha Emitters (LAEs).

Models of stellar populations predict that normal star forming galaxies cannot produce Lyα emission lines with an Equivalent Width (EW) $\mathrm{EW_{Ly\alpha}} \gtrsim 240$Å (Charlot & Fall, 1993). Exceptions to that rule can be observed in case of significant absorption of the continuum by dust, extremely poor metallicity, young galaxy ages or non standard Initial Mass Function (IMF), the three latest being indicative of primitive galaxies (Schaerer, 2003; Raiter et al., 2010). The Lyα emission of galaxies with rest-frame $\mathrm{EW_{Ly\alpha}}$ much greater than 240 Å is therefore likely to be powered by AGN rather than a normal stellar population and as such is tracing a completely different population.

Being a resonant emission, a Lyα photon can be absorbed by an atom of hydrogen and re-emitted at the exact same wavelength. Regarding high redshift galaxies, this has major consequences that can be observed in the spectra of LAEs.

Spatially extended emission. The Lyα emission tends to be more extended than the UV continuum emission provided that a large amount of neutral gas can be found in the Circum-Galactic Medium (CGM) (Leclercq et al., 2017; Wisotzki et al., 2018). Therefore galaxies observed in Lyα can have varying morphologies with respect to rest-frame UV observations.

Escape fraction. The complex radiative transfer of a Lyα in the surrounding CGM leads to low escape fractions (Verhamme et al., 2017). Photons can only escape the influence of the surrounding CGM once they have travelled far enough to be redshifted out of resonance. This process can be very long since the repeated scattering can lead a Lyα photon to randomly wander in neutral halos for millions of years. This long timescale means that even a very low fraction of dust in the medium is likely to absorb a Lyα photon and that we expect the escape fraction of a Lyα photon to be very different from the escape fraction of a typical UV photon.

Line profile. The kinematic of the surrounding CGM impact significantly the observed profiles of Lyα lines. Radiative transfer simulations have shown that a static shell of gas (i.e. neutral HI) around a LAE would create a double peak emission. In that situation the velocity dispersion within the cloud absorbs the photons in the line center. At each step of the radiative transfer, the re-emitted photons have their frequency shifted by a small amount depending on the angle between the velocity of the atom and the direction of re-emission of the photon. Eventually, during this process, the photon will be shifted out of resonance, either on the blue or red side of the central emission, leading to the observed double peak emission.

Following a very similar mechanisms, an outflow of gas would redshift the peak of the line and create an asymmetry with an extended wing on the red side of the lines. This asymmetry can be caused by gas outflows driven by a rapid expansion of space or by regions with intense star formation.

The exact geometry considered and kinematics of the gas can lead to a wide range of Lyα profiles as shown in Fig. 1.5. For high redshift galaxies, the most common profiles are the one caused by outflow and the double peak emission caused by static shells (or a combination of the two). Typical profiles like these are quite common in observations and makes easier the identification of

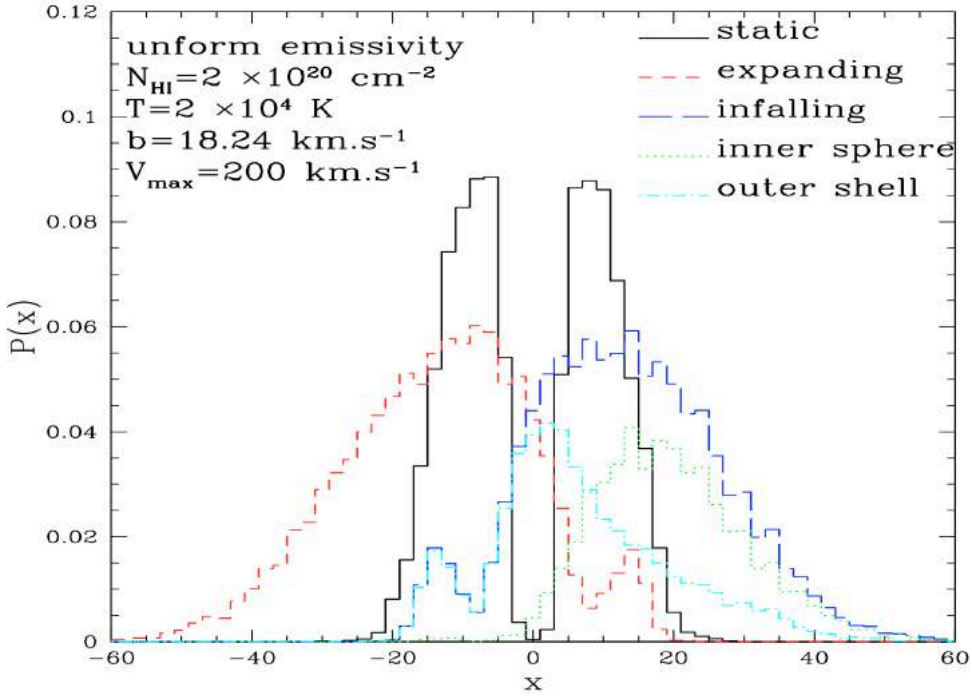

Figure 1.5: Simulated observed Lyα line profiles assuming different scenarios for the surrounding gas. The x-axis is the frequency shift and the y-axis the probability distribution resulting from the simulations (i.e. the line profile).
Figure taken from Verhamme et al. (2006)

the Lyα lines when no other spectral features can be seen. For a more complete introduction to this complex subject, we refer the reader to the simulations and analysis presented in Verhamme et al. (2006) and Laursen et al. (2011).

The complex physics of Lyα emission is a blessing for observers, as it allows to learn much about galaxy properties and the CGM, but it also introduces biases in the observations that are difficult to overcome. The first one is obviously the low escape fraction that dims the Lyα emission (see e.g. Verhamme et al., 2017) and the second one is the apparent clustering of LAEs at high redshift. Both effects are described latter in Sect. 1.3.2.

1.2.1.2 Selection methods

To select LAEs, two methods are commonly used:

- Using NB imaging to detect an excess of flux indicating the presence of an emission line. This technique can only be used to select LAEs in narrow redshift ranges and by construction, is only efficient to select LAEs with a high enough $EW_{Ly\alpha}$. When using NB imaging, a spectroscopic follow-up can be done to confirm the likely candidates (see e.g. Rhoads et al., 2000; Ouchi et al., 2010; Sobral et al., 2018).
- Serendipitous detections in slit spectroscopy observations (see e.g. Cassata et al., 2011).
- Complete blind spectroscopic selection with Integral Fields Units (IFUs). In that case, the process is simpler and leads to a higher level of completeness compared to NB imaging (see e.g. Blanc et al., 2011; Drake et al., 2017b).

Since the Lyα is at the core of the method described in this present work, these three approaches are tackled in more details in Sect. 2.3 when talking about the issue of the completeness of Lyα

selection process.

1.2.2 Lyman-Break Galaxies

1.2.2.1 Absorption features in Lyman-break galaxies

The Lyman-Break Galaxies (LBGs) are the galaxies selected with the drop-out technique (Steidel et al., 1996, 1999) using multi-band rest frame UV photometry. As such the term "LBG" refer only to a selection method using the spectral features described in this section. Individual galaxies can be selected as both LAE and LBGs and whether there is an intrinsic physical difference between LBGs and LAEs is not fully understood yet. The LBG selection relies on the identification of integrated spectral features that can be visible on broad-band photometry. Three features (shown in Fig. 1.4), or a combination of these, can be used for this exercise:

The Lyman break. The neutral hydrogen present in large amount in the Inter-Stellar Medium (ISM) of star forming regions causes the absorption of the photons with $\lambda \leq 912$Å. As a result, this signature appears as a break since no (or very weak) emission can reach the observers below this rest-frame wavelength. This is called the Lyman break or the Lyman limit.

The Lyman-alpha absorption forest. This feature is caused by HI clouds placed on the line of sight (LoS) causing a series of narrow absorption lines. UV photons with $912\text{Å} \leq \lambda \leq \lambda_{Ly_\alpha} = 1216\text{Å}$ are continuously redshifted as they travel and at a given point some of them will be seen by their local surrounding as photons with $\lambda = \lambda_{Ly_\alpha} = 1216$Å. At this exact location of space they enter a resonant state and if they also happen to encounter a cloud of neutral hydrogen, these photons can be scattered as described in Sect. 1.2.1. Such random scattering will cause these resonant photons to leave the LoS trajectory and to create an absorption line in the observed spectrum. These absorption lines appear as many times and at as many different wavelengths as there are clouds along the LoS (hence the name Lyman-alpha forest). The observed wavelength of these absorption lines depends on the redshift of the various clouds with respect to the SFG. The higher the redshift the denser the Lyman forest, as the amount of neutral hydrogen increases with redshift. The same stands for Ly$_\beta$. At $\lambda < 1216$Å, both the Lyα and Ly$_\beta$ forests are responsible for the dimming on the spectral continuum

Historically, this mechanism was first observed in the spectra of high-redshift quasars (see e.g. Lynds, 1971) as they are the brightest objects, but the same applies to normal star forming galaxies. This phenomenon was precisely modeled to evaluate its impact on the color of high redshift galaxies in Madau (1995).

The Gunn-Peterson Trough. This spectral feature is a complete suppression of all emission for rest frame wavelengths with $(1 + z_{\text{eor}})1215\text{Å} \leq \lambda \leq 1216$Å, where z_{eor} is the redshift of the end of the reionization process. This absorption can only be observed for sources with $z > z_{\text{eor}}$. It was first described in Gunn & Peterson (1965) and observed for the first time much later in Becker et al. (2001). This effect can be seen as an extreme and continuous Lyman-alpha absorption forest:

- All photons with $\lambda \leq 912$Å are completely absorbed when ionizing the neutral Inter-Galactic Medium (IGM).
- All photons with $912\text{Å} \leq \lambda \leq 1216$Å are not energetic enough to ionize the hydrogen but as they propagate, the longest wavelength are progressively redshifted into Lyα resonance. These resonant photons are progressively scattered by the neutral IGM, causing a complete and large absorption just bluewards of Lyα. Eventually, photons with high enough wavelength will travel until the end of reionization without having been redshift into resonance.however,

these photons remain affected by traces of neutral hydrogen present on the LoS for $z > z_{\rm eor}$, and remain therefore subjected to the Lyα forest phenomenon.

High redshift galaxies showing this GP trough show a complete absorption for $(1+z_{\rm eor})1216\text{Å} \leq \lambda \leq 1216\text{Å}$, Ly$\alpha$ absorption forest for $912\text{Å}\lambda \leq (1+z_{\rm eor})1216\text{Å}$ and a complete absorption for $\lambda \leq 912\text{Å}$.

Each of these three phenomenon are shown and summarized on the schematic spectra in Fig. 1.4. Depending on the columns density of hydrogen, the observed spectra can be a combination of several of the effect described here. The quasars spectra published in Fan et al. (2006) showing the evolution of their observed spectral features with redshift are shown in Fig. 1.6. The spectra at $z = 5.93, 6.01$ and $z > 6.13$ can be labelled as GP troughs. The difference with respect to the other spectra is that the higher redshift lead a complete absorption between the Lyα line and a Lyα absorption forest.

1.2.2.2 Selection method and photometric redshifts

Two examples of rest frame UV photometric observations with HST and leading to LBG selection are shown in Fig. 1.7. Both sources are not detected in the filters centred on the shortest wavelengths. This is explained by the fact that these filters are sampling rest frame wavelengths bluewards of Lyα emission (see transmission bands in Fig. 1.4), where either of the three absorption phenomena mentioned above play a role to suppress the continuum. For the galaxy shown in the top panel, the break is observed at lower wavelengths (between F435w and F606w) than for the bottom panel galaxy (between F814w and F105w), indicating that its redshift is lower.

The position of the integrated breaks can be used to give more reliable constraints on the redshift through color-color selection (as done originally in Steidel et al. (1996) or more recently in Bouwens et al. (2015b)), or with SED-fitting techniques to compute more precise photometric redshift (see e.g. HyperZ presented in Bolzonella et al. (2000) and used in e.g., Pelló et al. (2018)).

The color-color selection is a simple and fast method relying on the direct comparison of magnitudes in different filters, in order to identify a break combined with a steep UV slope (i.e. a rest frame "very blue" galaxy). A set of rules and conditions can be given to assess in a consistent way the colors of galaxies and sort them in different pre-defined redshift ranges.

The SED-fitting (Spectral Energy Distribution) techniques are a bit more complex and heavy to implement. From photometric observations and measurements, the procedure fits the observed SED using a library of template spectra spanning a parameter space given by e.g. star formation type and age (with or without e-line contribution), metallicity, IMF, Lyman forest prescriptions, with redshift being one of the parameters.

Photometric redshift measured are obviously less precise than spectroscopic measurements but the agreement with true redshifts is of the order of $\sigma(z_{\rm phot} - z_{\rm true}) \sim 0.05(1+z_{\rm true})$ for a deep broad band survey. In addition to the best photometric redshift, SED-fitting procedures also provide the best fit across the parameter space. An example of SED-fitting made with HyperZ is provided in Fig. 1.8. In this figure, the photometric observations are best fitted by HyperZ when using a photometric redshift of $z_{\rm phot} = 4.1$.

Color-color diagram and photometric redshifts used to select drop-out galaxies are prone to make errors on the redshift determination. The only way to avoid this is to use narrower and more numerous photometry filters to break some of the degeneracies between low and high redshift solutions. This is of course not feasible in most cases because of the difficulty to obtain telescope time and for other technical limitations (e.g. the S/N is degraded when using narrow filters and longer exposures are need to reach equivalent depth). A comparison between narrow and broad band photometry results within the same field can be found in Arrabal Haro et al. (2018).

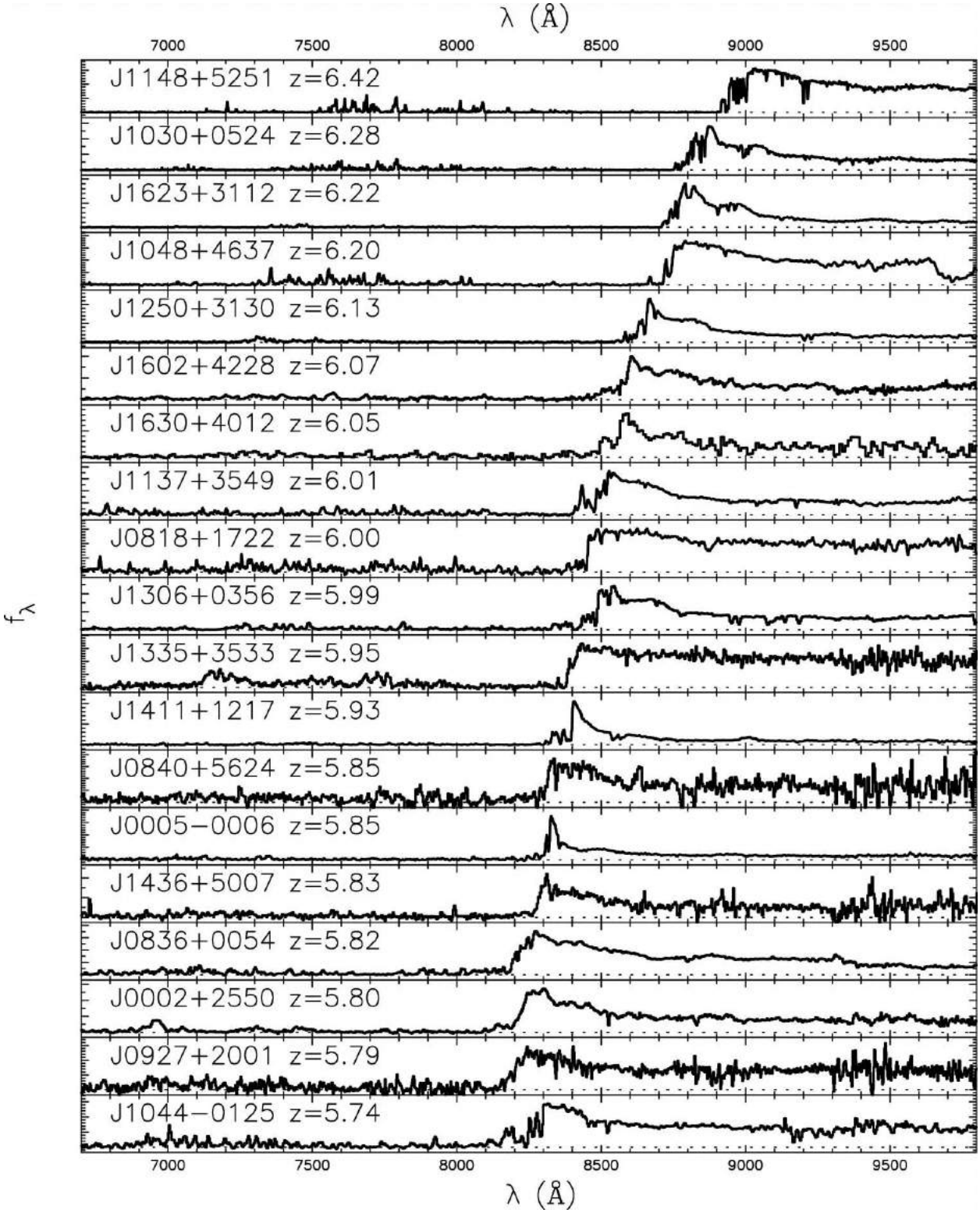

Figure 1.6: Quasar spectra showing the evolution of their spectral features with redshift. The spectra at $z = 5.93, 6.01$ and $z > 6.13$ can be labelled as GP troughs.
Figure taken form Fan et al. (2006)

.

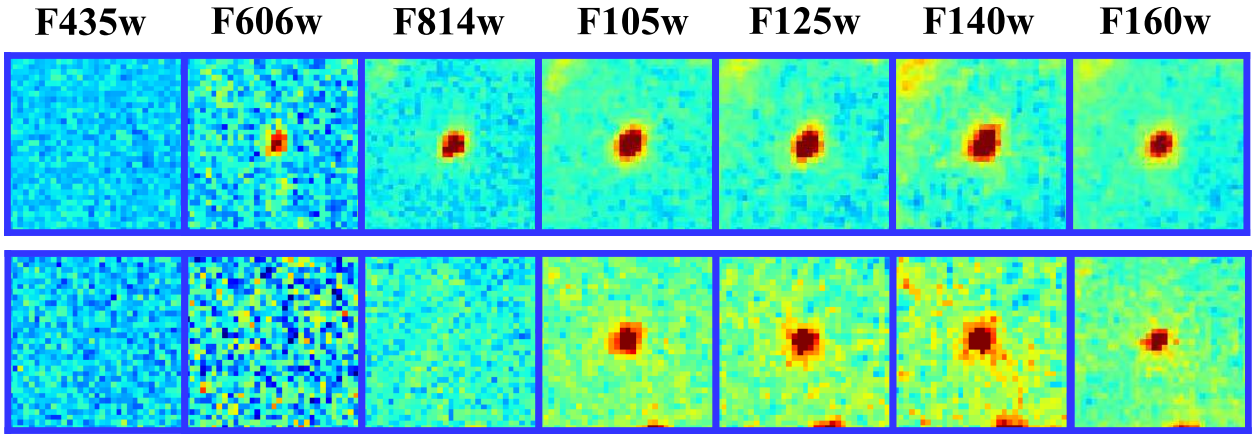

Figure 1.7: Example of two drop-out selected galaxies using HST filters in the A2744 frontiers field Lotz et al. (2017). The galaxy in the top panel has a photometric redshift at $z_{\rm phiot} \sim 4.4$, and the one in the bottom panel has a photometric redshift around $z_{\rm phot} \sim 7.0$.

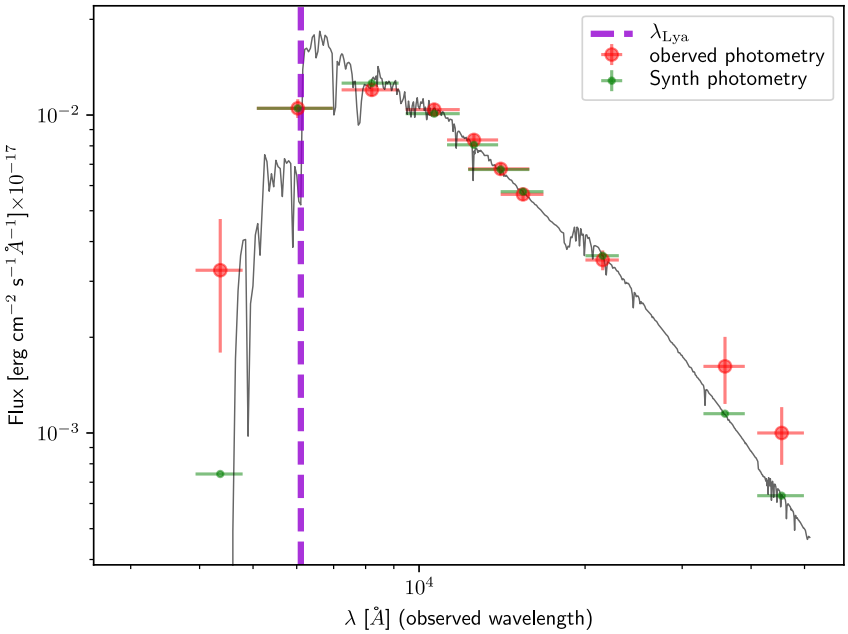

Figure 1.8: Example of SED fitting results with HyperZ using the Hubble Space Telescope (HST) photometry displayed in the top panel of Fig. 1.7 and additional photometry from Hawk-I K band and Irac 1 and 2 bands for the longest wavelength filters. The best photometric redshift as computed by HyperZ is $z_{\rm phot} = 4.1$. The red points are the photometric measurements, the black line is the best galaxy spectra template and the green points are photometric points measured from the template (synthetic photometry) using the same filter transmissions as for the original photometry. The best fit spectra shows both a Lyman-break and a Lyman-alpha absorption forest bluewards of λ_{Ly_α}.

1.2.3 The galaxy luminosity function

In the previous section it was explained how to observe and select high-redshift star forming galaxies. In this section we explain how to study these galaxies as a population and how this can be used for the study of reionization.

One of the main strategy to quantify the abundance of galaxies in a given volume is to measure their Luminosity Function (LF). The LF is simply a number density of galaxies per (co-)volume units and magnitude (or luminosity) bins. Since it aims at giving a complete assessment of a given population but observations are limited by their depth and volume, the determination of the LF is therefore limited to a restricted range of magnitude (Luminosity). Three steps are needed to derive a luminosity function:

- Select a galaxy population. The method used for selection has to be consistent and reliable (in the sense of "reproducible") to properly assess the completeness of the sample. This means that galaxies selected as a result of visual inspection or irregular selection procedures are not suited for the derivation of the LF. For galaxies in the redshift domain of interest, the selection criteria commonly used are are the LBG or LAE selections (as explained in Sect. 1.2.2 or Sect. 1.2.1, respectively).
- Do a completeness correction, or alternatively, cut the sample to the magnitude range where the sample is 100% complete. The goal of this completeness correction is to account for the sources missed in the detection process in the final statistic of the LF. Rigurously speaking, the sample used for LF computation should be complete both in terms of luminosity and volume.
- Determine the distribution of galaxies from the completeness corrected sample. This can be done by deriving the most likely parametric form given the data set or simply using a magnitude (luminosity) binned representation.

When the LF is expressed as a numerical density per magnitude (luminosity) bin, it is called the differential LF. This term is used in opposition to the cumulative LF which gives a numerical density of galaxies up to a given absolute magnitude (or luminosity). Both forms of the LF can be derived from each other and give the same information. In the rest of this work, only the differential LF is considered, unless specified otherwise.

Many different methods can be used to compute a LF but will not be detailed in this work. A short overview of the main methods and a comparison of the results obtained with some of them can be found in Herenz et al. (2019). Most methods vary in their use of the selection function and in the underlying hypothesis regarding the distribution of galaxies. The most commonly used methods are variations of a maximum likelihood estimator or variations of the the $1/V_{\rm max}$ methods. For more details on these methods and the use of the selection function, see the introduction of Sect. 4. In the following sections, we introduce a convenient parameterization of the LF to facilitate the discussion and the comparison with previous studies (Sect. 1.2.3.1), and explain what can be learned from the study of the galaxy luminosity function (Sect. 1.2.3.2).

1.2.3.1 Schechter parameterization

A widely used parameterization for the study of the LF is the Schechter function (Schechter, 1976) which writes as:

$$\Phi_M(M)dM = 0.4 \ln 10 \times \Phi_* 10^{0.4(M_*-M)(\alpha+1)} \exp(-10^{(M_*-M)})dM. \tag{1.1}$$

when expressed as a function of absolute magnitude. When using luminosities instead (and in particular Lyα luminosity) a similar Schechter parameterization can be used and takes the following form:

$$\Phi(L)dL = \frac{\Phi_*}{L_*}\left(\frac{L}{L_*}\right)^{\alpha} \exp\left(-\frac{L}{L_*}\right) \tag{1.2}$$

Because the second form is easier to read and is the one used in this work for LAEs, only this last one is commented, but the same can be transposed to the parameterization with magnitudes instead of luminosity. The term $\Phi(L)dL$ is the expected density of galaxy within the luminosity range $[L, L + dL]$, Φ_* is a normalization parameter, L_* regulates the position of the transition between the exponential law at higher luminosity and the power law at low luminosity (often called the knee of the LF). The parameter $\alpha \leq 0$ is the slope of the faint end: as the Schechter function is almost always plotted in Log space, the power law of the faint end transposes as a line of slope α. An example of Schechter functions is shown in Fig. 1.9 where the impact of the value of the three parameters are also shown. Observed LFs with the best Schechter parameterization are shown in Fig. 6.5.

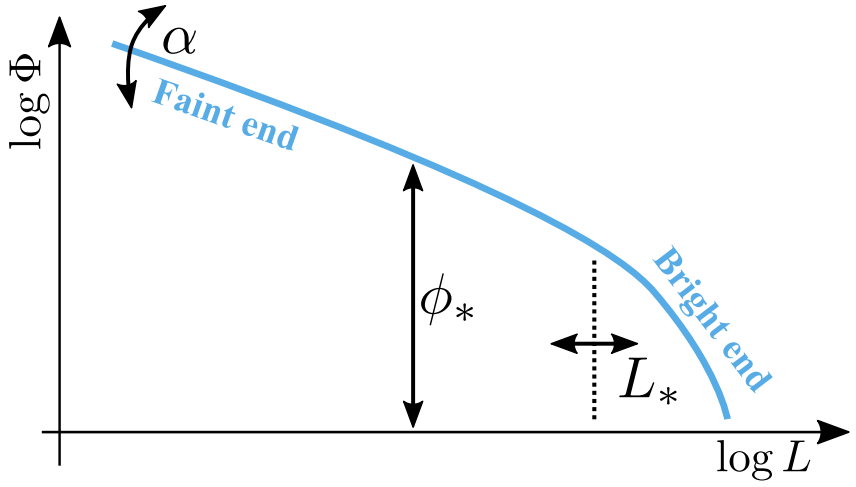

Figure 1.9: Example of Schechter function expressed in luminosity.

The motivation for such a function is that its form derives from the Press-Schechter formalism for the halo mass function developed in Press & Schechter (1974) and that it provides a good approximation for the observed LF. This formalism uses a linear perturbation theory to describe the growth of structures at the larger scales only. As specified in Press & Schechter (1974), using only the larger scales is needed to avoid as much as possible the non linear effects that are inherent to the N-body problems. The authors also do not exclude the idea that the non linear perturbations could transfer to larger scales and produce effects non predicted by their formalism.

There is therefore no strong physical evidence or guarantee that this function should correctly describe the galaxy LF at all luminosity ranges. The main reason for the use of this function is that up to now, it has been proven to work reasonably well (once again this is clearly stated by the author in Schechter (1976)) to describe the observations. In addition, it provides an easy way to compare the results obtained in different studies, and the three parameters α, L_* and Φ_* make it easier to discuss possible evolution of the LF shape. And finally, using a parametric form can be useful to extrapolate results to luminosity ranges that are out of reach of present observations.

The use of the Schechter function is therefore quite convenient, the main interrogation remaining is whether it can continue to accurately describe the LF as we reach lower and lower luminosity regimes, or if there is some effective turnover luminosity under which the Schechter function is no longer a good representation of the data.

1.2.3.2 What can we learn from the study of the LF ?

The galaxy LF is one of the most fundamental observables regarding galaxy physics and evolution. It has been studied for decades and continues to be a subject of interest. This brings the question,

what can we still learn from the study of the galaxy LF ?

The first and most important answer is that the study of the LF allows us to learn much about galaxy evolution. Being an observed quantity, it can easily be compared to results from the most recent simulations. This constant back and forth between observations and more powerful simulations is essential to reach a better understanding of all the fine details of galaxy formation and disentangle between possible scenarios. And with the constant increasing depth of surveys, we can reach luminosity and redshift regimes that were previously out of reach, therefore slowly extending our understanding towards the formation of the first galaxies.

In itself, and by splitting a galaxy population in several redshift bins, the LF can give an overview of the galaxy population at a given redshift. One of the area of interest is the evolution of faint end slope of the LF with redshift. A steeper slope means an increase in the proportion of faint galaxies. Such an evolution is expected at higher redshift because of the hierarchical formation of galaxies. At lower redshift, because of the numerous galaxy mergers, one expects a flatter slope and maybe a shift towards higher luminosity of the LF knee (L_*) as the galaxies tend to grow brighter.

The second point is that by computing the LF, we can estimate average or integrated properties of a galaxy population such as Star Formation Rate Density (SFRD), integrated luminosity density, ionizing flux density and many more.

The ionizing flux density is especially interesting when investigating the sources of reionization and allows to estimate the contribution of a given population to the total ionizing flux at a given redshift. By definition, these integrated properties are dependant on the lowest luminosity probed by the LF and therefore the depth that can be reached in a given survey. The LF can also be used for investigating the effect of selection methods in integrated measurements. For example, the integrated ionizing flux density measured from a LF may no be the same depending on whether the galaxies considered were selected as LAE or LBGs, even though these two selection methods are designed to select star forming galaxies. Such a discrepancy indicates a difference between the physical properties of the two populations.

The last point is that the LFs can be used to make extrapolated predictions regarding the expected number of galaxies in a given volume. These predictions can be injected in numerical simulations or used for preparing future surveys and/or instruments.

1.3 Constraints on the timeline of reionization

Reionization began as soon as the first ionizing sources formed in the primordial Universe. For now, these first galaxies are mostly out of reach until the commissioning of the future James-Web Space Telescope (JWST), which is expected to detect these first galaxies up to $z \sim 15$. While direct observational constraints on the properties of the primary sources of reionization will remain challenging for a long time, it is already possible to get constraints on the timeline of reionization through observations. Various models and simulations tend to place the beginning of reionization at redshifts higher than $z \sim 12$ (see e.g. Fig. 1.11), but a lot more is known about the end of the reionization. We address below the main constraints presently available on the timeline of reionization.

1.3.1 Quasar observations

Historically, the first observational constraints on the End of Reionization (hereafter EoR) were derived from the evolution of absorption features in high redshift quasars spectra (see Sect. 1.2.2

and Fig. 1.6 for more details on these absorption features).

Gunn-Peterson Trough. At $z > z_{\rm eor}$, one expect to observe a Gunn-Peterson Trough. Therefore when accumulating several quasars spectra around $z_{\rm eor}$, the presence of this feature in some of them and not in others allows to constrain the value of $z_{\rm eor}$. This was first done in Becker et al. (2001) with the study of three quasars at z = 5.82, 5.99 and 6.28 (see also Fan et al. (2000, 2001)). Since a complete Gunn-Peterson Trough was only observed in the highest redshift quasar, the study concluded that the Universe was approaching reionization by $z \sim 6$. A few years later, with a sample of 19 quasars with $5.74 \leq z \leq 6.42$ it was shown in Fan et al. (2006) that the fraction of neutral hydrogen (note $\bar{x}_{\rm HI}$) had decreased by a factor greater than 10 in this redshift interval and was around 1 - 4 % at $z \sim 6.2$. This confirmed that a rapid transition phase was occurring and that the IGM was mostly neutral by $z \gtrsim 6$. The authors also noted that the absorption features showed some large line of sight variations in their sample, even among quasar with $z > 6$. They concluded that this was indicative of fluctuations of the UV background, or in simpler terms, that reionization is inhomogeneous and that HII spheres develop faster in certain regions. Since then there has been growing evidence for this phenomenon which is now called "patchy" reionization (see e.g., Pentericci et al., 2014; Becker et al., 2015; Bosman et al., 2018). More studies using quasar observations have been successful in placing constraints on $z_{\rm eor}$ since then, and an all of them tend to agree that the Universe was reionized by z $\sim$ 6 (see e.g., Maselli et al., 2007; McGreer et al., 2015).

Damping wings. Even after consistent and reliable constraints were set on $z_{\rm eor}$, bright and high redshift quasar were still proven useful to probe optical depth and the evolution of the IGM before $z_{\rm eor}$. The difficulty is that for quasars well above $z_{\rm eor}$, the usual Lyα absorption features are completely saturated and can only give upper limits on IGM optical depth. By looking at the extent of the damping wings of the Lyα absorption on the red side of the Lyα emission, it remains possible to derive constraints on the optical depth of the medium as explained in the model introduced in Miralda-Escude (1998). To simplify, the width of this absorption can be observed as its red wing remains visible and can also be parameterized with redshift. An adjustment of this model to observed spectra gives constraints on the optical depth of the surrounding medium. This method was used in Mortlock et al. (2011) who reported the discovery of a quasar at z = 7.08, the highest redshift QSO at the time of discovery. The derived transmission revealing the Lyα damping is shown in Fig. 1.10. The conclusion was that the extent ionization front of these QSO was significantly lower than QSO of the same intrinsic luminosity around $z = 6$, indicating a denser IGM. The neutral fraction was estimated to be $0.1 \leq \bar{x}_{\rm HI} \leq 1$ on the region surrounding the quasar. In 2018 Bañados et al. (2018) reported the discovery of a QSO at z = 7.54, the most distant QSO known to date, and only the second QSO discovered at z $\geq$ 7. $\bar{x}_{\rm HI} \geq 0.3$ at a 68% level of confidence. More in depth studies of these two quasars, combining a proper spectra reconstruction with results of reionization simulations to marginalize over line of sights variations were made in Greig et al. (2017) and Greig et al. (2019) and derived neutral fractions of respectively $\bar{x}_{\rm HI} = 0.4^{+0.21}_{-0.19}$ and $\bar{x}_{\rm HI} = 0.21^{+0.17}_{-0.19}$ at z = 7.08 and z = 7.54.

Quasar observations have proven to be very useful regarding the study of reionization, but are limited to probe the higher redshift Universe. Due to the young age of the Universe, high redshift quasars are rare as they did not have a lot of time to form (see e.g., Shankar et al., 2010; Jiang et al., 2016; Parsa et al., 2018): at the time of the redaction of this thesis, only two QSO have been fount at z $\geq$ 7. In addition to this, it has been shown that quasars observations tend to be biased towards over dense regions (Utsumi et al., 2010; Shankar et al., 2010; Husband et al., 2013) which is likely to affect the measurement of $\bar{x}_{\rm HI}$.

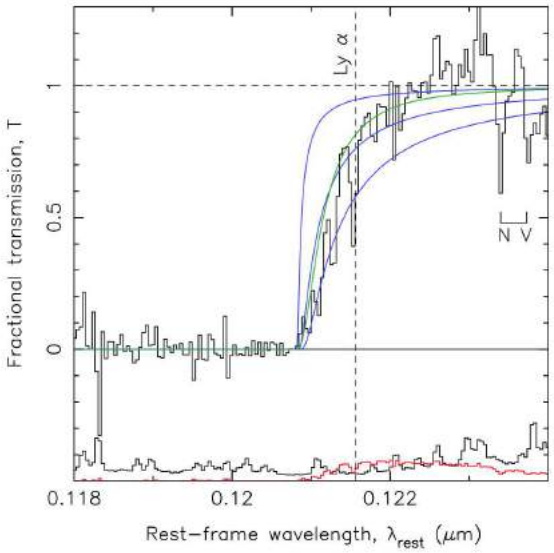

Figure 1.10: Example of damping wing feature on the red side of the Lyα emission taken from Mortlock et al. (2011). The presence of dense neutral hydrogen in the medium leads to a wide absorption feature whose red side remains visible even in the case of complete Gunn-Peterson absorption. The blue lines correspond to parameterization of this absorption feature with, starting from the top, $\bar{x}_{\rm HI} = 0.1$, 0.5 and 1. For more details, see the original publication.

In an attempt to reach more general conclusions about the timeline of reionization, observations turned toward very high redshift galaxies and other indicators such as the fraction of LAEs among UV selected galaxies.

1.3.2 High redshift LAEs

As extensively shown in the previous section, the Lyα emission is very sensitive to even a tiny fraction of HI along the line of sight. In this regard, studying the LAE population and the evolution of its detected number counts with redshift, or line of sight can give constraints on $z_{\rm eor}$ and its variations. LAEs do have the same spectral signature as quasars, but since they are not as bright, they are less suited for detailed spectra analysis and are in general used to measure statistical properties.

LAE fraction. The observed fraction of LAEs among UV selected galaxies is the simplest probe of end of reionization that can be used with LAEs. For $z > z_{\rm eor}$, it is expected that the number of detected LAEs drops significantly since most of Lyα emission would be absorbed. By extrapolating the trend observed at $z < z_{\rm eor}$ to $z > z_{\rm eor}$, and comparing this to the actual measurements obtained at $z > z_{\rm eor}$, it is possible to estimate $\bar{x}_{\rm HI}$. Using this technique, Caruana et al. (2014) reported $\bar{x}_{\rm HI} \sim 0.5$ at $z \sim 7$ and Pentericci et al. (2014) concluded that $\bar{x}_{\rm HI} \geq 0.51$ for $z \sim 7$ was needed to explain the observations, assuming that the evolution was only caused by an evolving IGM. More recently, more precise measurements of $\bar{x}_{\rm HI} = 0.59^{+0.11}_{-0.15}$ at $z \sim 7$ and $\bar{x}_{\rm HI} \geq 0.76$ at $z \sim 8$ (68% lower limit) were obtained in respectively Mason et al. (2018) and Mason et al. (2019), through improved modeling of the IGM and the use of reionization simulations. These results are consistent between themselves, and it can be noted that the average estimate of $\bar{x}_{\rm HI}$ derived from galaxy observation tend to be higher than the one derived from quasar observations at the same redshift. This argues

in favor of the fact that quasar do tend to probe over dense regions of the IGM where ionizing fronts progress faster.

Escape fraction. Another approach is to study the evolution Lyα photons escape fraction. Under normal star forming condition, f_{Ly_α} can be computed by comparing the SFR obtained from measurments of the dust corrected monochromatic UV continuum (L_{1500}) to the one estimated from $L_{\mathrm{Ly}\alpha}$. The idea behind that, is that using L_{1500} we can recover the intrinsic SFR and assuming that the Lyα emission is only powered by star forming regions (i.e., no AGN), the observed discrepancy between $\mathrm{SFR_{UV}}$ and $\mathrm{SFR_{Ly\alpha}}$ can only be explained by an increased absorption of Lyα photons. Using a Hα to Lyα line ratio of 8.7, assuming a case B recombination (Osterbrock & Ferland, 2006), a Salpeter IMF and the prescription for SFR computation in Kennicutt, Jr. (1998), the following formula can be used to estimate f_{Ly_α}:

$$f_{\mathrm{Ly}_\alpha} = \frac{\mathrm{SFR}_{\mathrm{Ly}_\alpha}}{\mathrm{SFR_{UV}}} = 7.9 \times 10^{42} \frac{L_{\mathrm{Ly}\alpha}}{8.7} \times \frac{1}{10^{-28} L_{1500}} \propto \frac{L_{\mathrm{Ly}_\alpha}}{L_{1500}} \tag{1.3}$$

where $L_{\mathrm{Ly}\alpha}$ and L_{1500} are expressed in respectively $\mathrm{erg\,s^{-1}}$ and $\mathrm{erg\,Hz^{-1}\,s^{-1}}$. This simple prescription does not allow to differentiate between the effect of dust, neutral hydrogen in the ISM of star forming regions, or neutral hydrogen present in the IGM. In addition, it is only valid assuming a stationary regime of star formation has been established for longer than $\sim$ 100Myr. In a transition regime of star formation, the typical timescale of escape of a Lyα photon being much longer (possibly several millions of years) than the one of a UV photon, the SFR measured from $L_{\mathrm{Ly}\alpha}$ is lagging behind the SFR measured from L_{1500} which provides a better "instantaneous" measurement.

Observations have shown that f_{Ly_α} is increasing from $z = 0$ to $z \sim 6$, and drops for $z \gtrsim 6$. This can be explained by a lower dust content at higher redshift and an increasing amount of neutral hydrogen at $z > 6$ (see e.g., Ono et al., 2010; Blanc et al., 2011; Hayes et al., 2011) which once again, places z_{eor} around 6. Since it is not possible to differentiate between the effects of dust, ISM and IGM in the observation of f_{Ly_α}, study of lower redshift galaxies are needed to disentangle between these effects.

A good introduction to this approach is provided in Matthee et al. (2016); Sobral et al. (2017); Sobral & Matthee (2019) presenting the CALYMHA program (CAlibrating LYMan-α with H_α), a survey of H_α selected galaxies at $z \sim 2$ designed to investigate the impact of galaxy properties on observed Lyα related quantities such as flux, $\mathrm{EW_{Ly\alpha}}$ or f_{Ly_α}. It has been observed in Matthee et al. (2016) that f_{Ly_α} tends to be anti correlated with SFR, and that while it is naively expected that high mass galaxies would have lower f_{Ly_α} due to higher dust content, this is not seen in this work. These two observations suggest that the kinematics of the gas and dust content may have a greater impact on f_{Ly_α} than previously thought, and that therefore f_{Ly_α} can show great variations from one galaxy to another.

The translation of the conclusions developed in these studies to higher redshift and the study of reionization is non trivial, and some progress are yet to be made on the understanding of the selection bias affecting such work. However, this offers a promising line of work to understand and estimate the escape fraction of high redshift galaxies. As illustration of this statement, it has been shown that the strong correlation that exists between f_{Ly_α} and $\mathrm{EW_{Ly\alpha}}$ could be used to estimate f_{Ly_α} Verhamme et al. (2017); Sobral & Matthee (2019). In addition, this correlation does not show significant evolution over the redshift range $z = 0 - 5$ (Harikane et al., 2018), which justifies the study of low redshift analogs to understand the physics of high redshift galaxies.

LAE clustering. At the very beginning of reionization, only the brightest galaxies could create an HII region large enough for their Lyα photons to be redshifted out of resonance before reaching the

neutral medium (see the "toy model" presented in Matthee et al., 2015). As reionization made its progress, these HII regions expanded, progressively unveiling more LAEs within the denser regions. In terms of observations this means that for $z \gtrsim z_{\rm eor}$, LAEs appear more clustered compared to UV selected galaxies (see e.g. Orsi et al., 2008; Sobacchi & Mesinger, 2015; Ouchi et al., 2018). The fact that ionizing fronts progress faster along over-dense regions has not always been the general understanding since these regions also attract more neutral gas in their surrounding, which has the opposite effect.

As such, the clustering effect can be used to probe and quantify the inhomogeneity of the end of reionization, and can be compared to the different measurements of $z_{\rm eor}$ (see e.g., the slight differences between $z_{\rm eor}$ measured from quasar spectra and $z_{\rm eor}$ derived from the evolution of LAE fraction mentioned at the beginning of this section). But the measurement of this clustering can also be compared to theoretical predictions and used to constrain $\bar{x}_{\rm HI}$. This was done for example, in Ouchi et al. (2018) who measured $\bar{x}_{\rm HI} = 0.15 \pm 0.15$ using the clustering signal of LAEs at $z \sim 6.6$.

LAE spectral profile. The last probe of end of reionization with LAEs is the spectral profile of the Lyα line itself. Hu et al. (2016) reported the discovery of a double peak LAE at $z = 6.59$, which remains at this time, the only double peaked LAE at $z > 6$. This observation was unexpected since the transmission of the blue part of the Lyα emission is often very low (Dijkstra et al., 2007; Laursen et al., 2011), especially at high redshift where the Lyα radiation is easily absorbed by the surrounding neutral hydrogen.

The original publication states that the detection of this blue wing could be a indicative of either a highly ionized region created by an extremely UV bright source (as suggested by the model in Matthee et al. (2015)), or a high velocity shift with respect to the IGM. The improved analysis in Matthee et al. (2018) confirms this discovery and investigates various possible scenarios to explain this observed profile. The conclusion is that the large velocity offset scenario seems to be unlikely, leaving the large HII region as a reasonable explanation for this observed profile.

Since this galaxy is not identified as an AGN which typically have broader Lyα lines, this could be one of the first direct evidence of a star forming galaxy actively ionizing its surrounding medium. This discovery potentially opens the door to a new approach for the study of reionization if more objects like this are found in the future.

1.3.3 Thomson optical depth and summary

The last constraint on reionization detailed in this manuscript can be derived from observation of the CMB itself, through the study of the Thomson scattering optical depth. The Thompson scattering is the elastic scattering of radiation by charged particles. After recombination, around $z \sim 1100$, photons were no longer affected by it as the Universe was mostly neutral, but as soon as reionization began Thomson scattering was effective again on the CMB photons. By careful modeling of this effect through the reionization era, it is possible to estimate this optical depth from observations of the power spectrum of the CMB. This modeling is quite complex and is not detailed here. We refer the reader to the book chapter Zaroubi (2013) and the references therein for a better introduction to this subject. The optical depth of Thomson scattering was estimated using Planck data in Planck Collaboration et al. (2016c), an can be used to constrain the evolution of ionizing emissivity during reionization (see results of Bouwens et al., 2015a).

Nowadays, there is a general agreement on the patchy reionization scenario. All the different probes listed in this section and the previous one converge towards $z_{\rm eor} \sim 6$. The large panel of

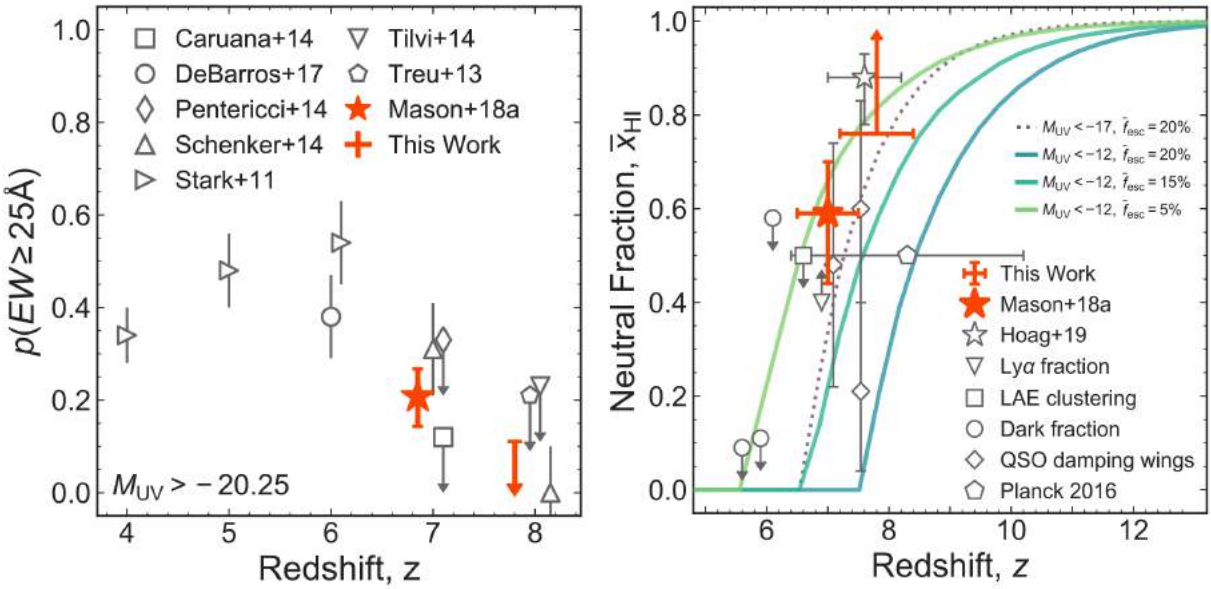

Figure 1.11: **Left panel:** Evolution of the fraction of LAEs with $\mathrm{EW}_{\mathrm{Ly}\alpha} > 25$Å among UV-faint galaxies. A slight redshift offset is applied for clarity. **Right panel:** Evolution of neutral fraction of hydrogen, $\bar{x}_{\mathrm{HI}}$, with redshift. The green and dashed lines correspond to predictions coming from the UV luminosity functions presented in Mason et al. (2015), for different integration limits ($M_{\mathrm{UV}} > -12$ and $M_{\mathrm{UV}} > -17$) and for different values of ionizing photons escape fractions (f_{escp}). For more details on the underlying hypothesis, see the original publication. A small redshift offset is applied to some points for clarity.
Both figures are taken from Mason et al. (2019)

observational techniques described above are needed to get a coherent picture of the end of reionization as each of them provide different observables that are relevant by themselves, and that can be used to improve our understanding through simulations. The various results on the measurements or estimation of $\bar{x}_{\rm HI}$ are coherent, and the slight differences can easily be explained by an inhomogeneous end of the reionization (e.g. quasars tend to probe over dense regions and give slightly higher $z_{\rm eor}$).

Figure 1.11 taken from Mason et al. (2019) summarizes the different measurements of the fraction of LAEs and of $\bar{x}_{\rm HI}$ using many of the methods explained above. The goal of this figure is not to compile all results obtained to date, but to the illustrate the observed trends and provide a support for the following discussions. Left panel of Fig. 1.11 shows the evolution of the fraction of LAEs with $\mathrm{EW}_{\mathrm{Ly}\alpha} > 25$Å among UV-selected galaxies. A steady increase of this fraction is observed up to $z = 6$, which can be explained by a lower dust content at higher redshift and therefore a higher escape fraction f_{Ly_α}. From $z = 6$, and above, the decrease can be explained by an increasingly neutral medium that absorbs the Lyα radiation, especially for low luminosity galaxies that may not have enough ionizing emissivity to create their own ionized spheres. Right panel of Fig. 1.11 shows the measurements of $\bar{x}_{\rm HI}$ and prediction derived from observed UV LFs (see caption for more details). This panel shows that reionization was a relatively rapid phenomenon: it was mostly completed by $z \sim 6$, but half done (i.e., $\bar{x}_{\rm HI} \sim 0.5$) by $z \sim 7$ which argues in favour of a rapid evolution of $\bar{x}_{\rm HI}$. All predictions shown in this figure also coincide in placing the beginning of reionization around $z \sim 12$. Since the redshift domain is mostly out of reach of current observation facilities, most constraints on the beginning of reionization can only come from models, and simulations.

1.4 Investigating SFGs as main drivers of reionization

1.4.1 The UV and LAE LF

As mentioned in the beginning of this Introduction, SFGs are the most likely candidates as main driver of reionization, as all previous candidates were dismissed one by one (see Sect. 1.1.3). But a definitive observational proof of this fact has yet to be made. To investigate the SFGs as potential sources of reionization, the method often used is to derive the LF and to infer the ionizing flux density of the selected population. As explained in Sect. 1.2, two methods are used to select SFGs, the UV selection (LBGs) or selection from the Lyα line (LAEs).

The underlying biases introduced by these selection methods are not completely clear and whether there are intrinsic physical differences between galaxies selected as LAEs or LBG (or both) remains to be determined. Up to now the study of the LF of SFGs has been divided in two: the UV LF for the LBG selected galaxies, and the LAE LF for the Lyα selected galaxies. Progresses on the LF of SFGs have been made in parallel as it is not known how to combine/reconcile the results obtained with LAEs and LBGs.

Based on LBG studies, the LF is well represented by the Schechter function and evolves significantly for $z > 4$ with a depletion of bright galaxies and an a steepening of faint end slope as illustrated in Fig. 1.12 taken from Bouwens et al. (2015b). This indicates that the proportion of faint UV galaxies increases at higher redshift, as it is expected and predicted by the hierarchical scenario of galaxy formation. The same trend had already been observed prior to this work and is now considered a well established fact (see e.g. Bouwens et al., 2007; Oesch et al., 2014; Finkelstein et al., 2015, and the references therein).

Nowadays the mains interrogation about the UV LF is whether it continues to be well repre-

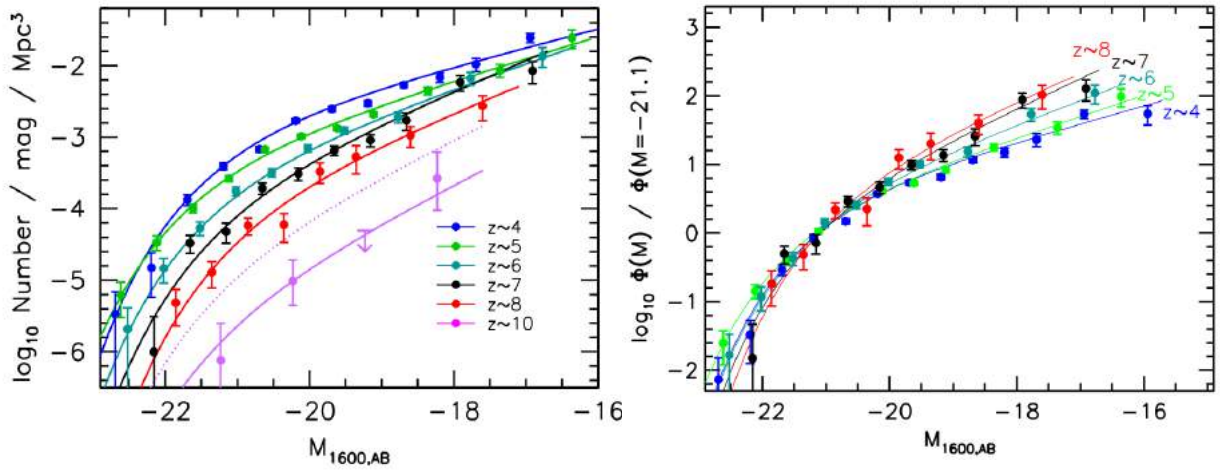

Figure 1.12: **Left panel:** observed UV LFs in different redshift bins. **Right panel:** observed UV LFs normalised to have the same density at $M_{1600,\mathrm{AB}} \sim -21$.
Both figures are taken form Bouwens et al. (2015b)

sented by the Schechter function for extremely faint galaxies, or whether a turn around is observed. As for now, no sign of such turn around has been observed, but this conclusion remains limited by the depth that can be achieved in current surveys.

Regarding reionization, it was estimated in Bouwens et al. (2015a) using the LFs derived in Bouwens et al. (2015b), that the faint end slope would have to be extrapolated down to $M_{1600,\mathrm{AB}} \sim -13$ to allow LBGs to match the ionizing cosmic emissivity and therefore drive reionization. However, the corresponding observations only extend down to $M_{1600,\mathrm{AB}} \sim -16$, and only for the lowest redshift bin at $z = 4$, which leaves a consequent gap of 4 dex with no reliable information.

The study of the LAE LF is not as "straightforward" as for the LBG LF. The main reason behind that is that the LAE population is affected by more observational biases:

- The difficulty to scan large volumes. Using large band photometry combined with photometric redshift for LBG selection, allows to probe a continuous redshift range within the area surveyed. This is not the case with imaging, since the narrow filters only allow LAEs within very restricted redshift ranges. Furthermore, spectroscopic confirmations are (telescope-)time consuming making it difficult to achieve large samples of LAEs over large volumes. When using serendipitous detections in slit spectroscopy, the volume is even lower and introduce additional biases regarding the measured flux (see Sect. 2.3.2).
- The more complex selection process can lead to higher incompleteness. For example, using NB imaging allows only to detect LAEs with $\mathrm{EW}_{\mathrm{Ly}\alpha}$ above a certain threshold.
- Potential systematic loss of flux which can happen when using NB imaging (if the line profile is larger than the filter) or slit spectroscopy (if the source is extended).
- Escape fraction of Lyα photons and apparent clustering, especially when probing redshift approaching z_{eor} (see previous sections of this introduction).

Historically the first LAE samples were selected using NB imaging (see Cowie & Hu, 1998; Ouchi et al., 2003; Hu et al., 2004; Dawson et al., 2007; Ouchi et al., 2008, and more). With progresses made in observational techniques and instrumentation, these techniques became more and more efficient over the past years to survey larger areas of the sky (see e.g. SILVERRUSH survey, Ouchi et al. (2018); Shibuya et al. (2018b,a) which covers 14 and 21 square degrees at respectively $z = 6 - 7$). Narrow-band imaging is therefore becoming essential to survey large areas, which is required to study the brightest and rarest LAEs. Nonetheless, recent NB surveys remain affected by

the biases described above. To avoid these, it is possible to use a blind spectroscopic selection. Such selection can be achieved with serendipitous detections in slit spectroscopy observations (Cassata et al., 2011), but the ideal way to go is to use IFUs, which produce complete spectra for each spatial pixel of their FoV (see Chpt. 2). The advantage of this type of instrument, in addition to the large quantity of information, is that they allow an as unbiased as possible selection of all LAEs within a given volume.

The very first attempt of LAE selection with IFU was made in van Breukelen et al. (2005) and a few years later in Adams et al. (2011). However, these first pioneer studies were severely limited by either a small FoV, low spectral resolution or low sensitivity.

More recently the VLT/MUSE instrument Bacon et al. (2014) was commissioned. It is a large field of view ($1' \times 1'$) IFU allowing a continuous redshift selection between $2.9 < z < 6.7$ for LAEs and a spectral resolution varying between $R = 2000$ and $R = 4000$ (see Chpt. 2 dedicated to the MUSE instrument). The primary science goal of MUSE is to detect LAEs taking advantage of its increased sensitivity, high spectral resolution and large FoV. The first results of the LAE LF with MUSE in blank fields are presented in Drake et al. (2017b,a); Herenz et al. (2019) and proved the efficiency of this new generation instrument to detect extremely faint LAEs with minimal biases.

Studies of the LAE population find a deficit of bright Lyα emitting galaxies at $z \geq 6$ which can be attributed to either an increase in the fraction of neutral hydrogen in the IGM or an evolution of the parent population (or both). For lower redshift, while some studies report an evolution similar to the one described for the LBG population, this evolution seems to be less significant and is not always seen (Kashikawa et al., 2006; Pentericci et al., 2014; Tilvi et al., 2014; Drake et al., 2017b; Herenz et al., 2019). In the same way as for the UV LF, the study of the LAE LF has been limited by available observations and depth. And the uncertainties are much larger since the LAE population is intrinsically more biased. In order to get around the depth limitation that is currently affecting both the study of the UV and LAE LF, recent work have turned towards strong lensing clusters to increase their reach.

1.4.2 Using strong lensing clusters

Since the first observation of a lensed galaxy in Soucail et al. (1988), strong lensing clusters have been used for various purposes. Specific and highly magnified objects can be used to perform detailed analysis taking advantage of the increased signal-to-noise (S/N) ratio and/or the increased spatial resolution (see e.g. Patricio et al., 2018). Alternatively, galaxy clusters can be used as gravitational telescopes while surveying the entire background of the cluster looking for fainter – but magnified – galaxies (Pelló et al., 1998; Richard et al., 2006). Such technique can be used to either select intrinsically fainter galaxies or galaxies at higher redshift. Recently, the Hubble Space Telescope (HST) Frontier Fields program (HFF) (Lotz et al., 2017) observed six of the most massive galaxy clusters. Each of the six clusters were observed for a total of 103 hours, pushing the observations to the limits of what can be achieved with HST.

Encouraged by the unprecedented depth of these new observations, many studies started working on the UV LF of the galaxies detected behind these clusters (see e.g. Livermore et al., 2017; Bouwens et al., 2017; Atek et al., 2018). At the cost of increased uncertainties, smaller volumes probed and more complex data processing, these studies managed to further constrain the shape of the UV LF. As an illustration, Bouwens et al. (2015b) only reached down to $M_{\mathrm{UV,AB}} \sim -17$ at $z = 6$ using a combination of deep HST blank fields, whereas using similar methods and the HFF observation, the three studies mentioned above managed to set reasonable constraints down to to $M_{1600,\mathrm{AB}} \sim -15$ at the same redshift (see Fig. 1.14). For fainter magnitudes, the LFs derived start to show large uncertainties and some disagreement between them. These large error bars are caused

Figure 1.13: Lensed galaxy in the A370 galaxy cluster observed with HST. This arc was historically the first confirmed observation of a galaxy lensed by a galaxy cluster (Soucail et al., 1988).
credits: NASA, ESA, Jennifer Lotz and the HFF Team (STScI)

by the uncertainty on both the magnification of individual galaxies and the choice of specific mass model(s). A more detailed presentation of all lensing effects and of the methods used in the frame of lensing fields is provided in Chpt. 3. Even though significant progress was achieved, all three studies concluded that no turn over was visible within the magnitudes probed by the observations. And the large uncertainties on the faint end transpose into larger uncertainties on the integrated ionizing flux.

To date, strong lensing fields have only been used once in Bina et al. (2016) as a proof of concept using MUSE, to set constraints on the LAE LF. The small sample (17 LAEs only) and the extremely small volume probed seriously limited the conclusion of this work, leaving a large margin of progression on the determination of the faint end shape of the LAE LF.

By essence, lensing fields surveys are exploring a different population than blank fields. The increased depth in these fields comes at the cost of a smaller volume explored, and since faint galaxies are much more numerous than bright ones (see LFs in Fig. 1.12, it is extremely unlikely to find bright galaxies in the background of lensing fields. For that reason, it is challenging to derive a single and coherent LF that would be well constrained on both the faint and the bright end. This is clearly visible in Fig. 1.14, where the LFs derived in both Bouwens et al. (2017) and Livermore et al. (2017) could almost be adjusted by a single straight line showing that they are very inefficient to select even moderately bright sources. On the contrary, it can be seen in Fig. 1.12 that LFs computed in blank fields are obviously less sensitive to the shape of the faint end. Lensing fields are therefore very important to probe the faint end of the LF, whereas larger blank-fields surveys are needed to probe the bright end. Regarding the Schechter parameterization, this means that it is very challenging to have a simultaneous and consistent determination of the three parameters, unless combinning very large volumes with extreme depth.

1.4.3 Total SFGs contribution to reionization

As explained all along this Introduction, LAEs and LBG are just reflecting a selection method, and the separation of the SFGs in these two populations is not necessarily representative of any

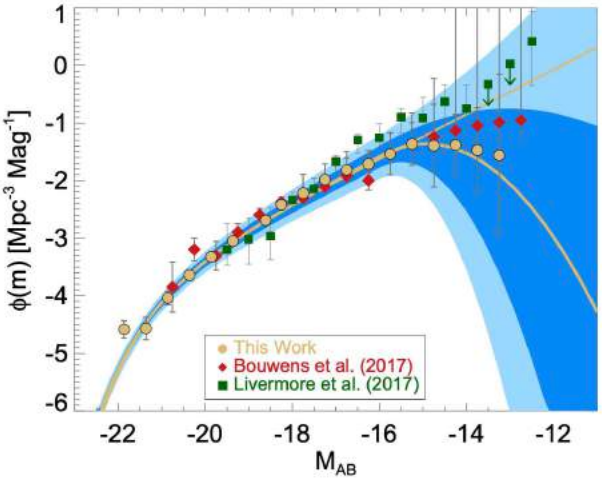

Figure 1.14: UV LFs derived at $z = 6$ using HFF observations.
Figure taken from Atek et al. (2018)

physical differences between them. However, regarding reionization and the study of the LF, these two populations have most of the time been studied in parallel with no attempt to unify them or to further characterize their interrelation. This raises the questions: how much of the SFGs are we missing when looking at only the LAEs or the LBGs ? Do we need to unify these two population to see SFGs producing enough ionizing flux to drive and maintain reionization ?

The interrelation between these two populations is studied in Arrabal Haro et al. (2018), where a simultaneous search for LAEs and LBGs is undertaken using the narrow band photometry of the SHARDS survey (Pérez-González et al., 2013) and public HST data. The large field of view (130 arcmin^2) combined with the use of narrow band filters allows for a good statistic and very secure photometric redshift in the range $3.35 \leq z \leq 6.8$. However, and as stated by the authors these observations are not suited to detect sources with wither faint Lyα emission or faint continuum (unfortunately the range explored in both $M_{\rm UV}$ and $L_{\rm Ly\alpha}$ are not discussed in this work). The interesting point of this work, is that for once, both LAE and LBGs are detected using the exact same set of observation, making the comparison between these populations extra relevant. As seen in Fig. 1.15 (taken from Arrabal Haro et al. (2018)), it appears that within the volume explored, the fraction of observed galaxies showing Lyα emission increases with redshift. And more precisely, the fraction of LAE without continuum detection also increases with redshift.

Following the same line of inquiry, Maseda et al. (2018) combined the Hubble Ultra-Deep Field (HUDF) observations with the MUSE HUDF and UDF-10 observations (see Bacon et al., 2017) to investigate the LAEs detected with MUSE without optical counterparts on HST images. This type of sources appears to be numerous (see e.g., Bacon et al., 2015, 2017; Herenz et al., 2017) and are expected to play a significant role in the reionization, yet they remain invisible in the deep photometric observations of the HUDF. The same type of population has been observed in Mahler et al. (2018), by comparing again MUSE observations to the even deeper HFF images of the A2744 lensing field. These LAEs have intrinsically high equivalent widths, but since no UV continua can be measured, only (high) lower limits of $\rm EW_{Ly\alpha}$ can be derived. However these limits are sufficient to see that some LAEs are detected with $\rm EW_{Ly\alpha} > 240$Å with no sign of AGN activity, therefore reinforcing the claim that this can be a sign of either a young age or very low metallicity (see Sect. 1.2.1). As suggested in Hashimoto et al. (2017) such high $\rm EW_{Ly\alpha}$ can be explained without

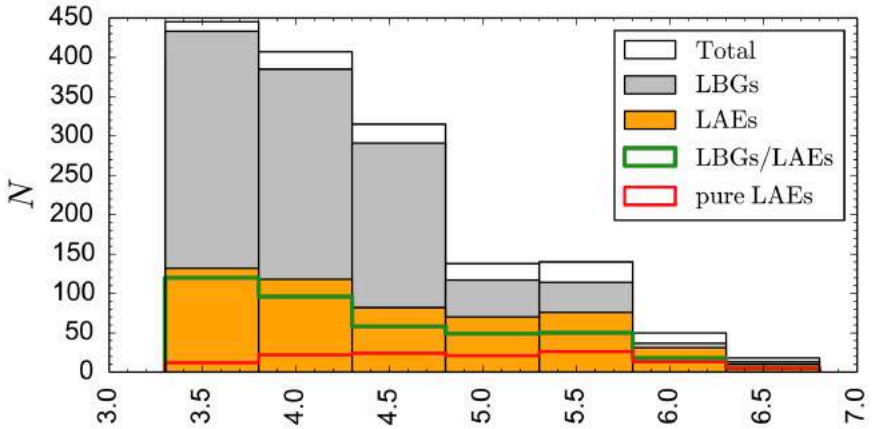

Figure 1.15: Interrelation between the LAE and LBG population in the SHARDS survey. Figure taken from Arrabal Haro et al. (2018)

invoking population III stars or irregular top-heavy IMFs and is therefore not necessarily indicating galaxies of first generation, strictly speaking.

By stacking HST images in different redshift bins, Maseda et al. (2018) showed that LAEs detected in the MUSE HUDF with no optical continuum detection have a typical UV magnitude of $M_{\rm UV} \sim -15$, which makes them the faintest "UV-objects" with spectroscopic confirmation. The large discrepancy between the expected number of these UV-faint galaxies, obtained by extrapolation of the current UV LFs, and the actual number of detection suggests that only those with the highest $\rm EW_{Ly\alpha}$ are detected with HST. In other words, only LAEs with an emission bright enough show on observations as their signal is not completely drown in the large width of the HST filters. In this regards, using IFUs such as MUSE allows to indirectly probe a new population of UV-faint galaxies.

From the work of Arrabal Haro et al. (2018) and Maseda et al. (2018) it appears that LAEs and LBGs cannot be treated as two completely independent populations, and that the LAE selection is probably more suited to select intrinsically UV-faint galaxies out of the reach of deep large band photometry surveys. This picture has emerged during the last years, and it is presently urgent to adress the intersection between the different populations of SFGs. When this thesis started, no specific study had been made to compare the LBG-UV and LAE populations within the same volume of the Universe, in particular regarding the faintest galaxies responsible for cosmic reionization.

1.5 This work

In the previous sections reviewing reionization, we have seen that while the end of reionization is quite well constrained, many aspects of this last state transition of the Universe remain elusive. The study of reionization is of great interest as it made the Universe shift from a cold to a mostly warm state, and therefore had a great impact the ongoing formation of stars and galaxies. A better understanding of reionization is therefore needed to get a coherent picture of the early Universe. The main remaining questions on the reionization era are listed below by order of importance:

1- By elimination, star forming galaxies are likely to drive reionization, but this has yet to be confirmed by observations. Can star forming galaxies produce enough UV flux density thanks to a large (but mostly invisible) contribution of extremely faint galaxies, to ensure the

reionization of the Universe ?

2 - What is the exact timeline of reionization ? There is evidence for a rapid transition between $6 < z < 7$, but our observational constraints stops at $z \sim 7.5$ for now, leaving the questions of the pace and beginning of reionization open.

3 - What is the shape of the very faint end of the luminosity function of star forming galaxies ? How does it evolve with redshift ? Is there a turn-over magnitude / luminosity ?

4 - Are we missing a significant portion of star forming galaxies when committing to either the LAE or the LBG selection process ? Is it possible to achieve a better empirical assessment of the star forming galaxies by understanding better the interrelation between the LAE and LBG population ?

5 - Are LAEs and LBGs essentially the same population and we are just affected by observational biases inherent to these two selection methods ?

This present work addresses these questions by focusing on a better understanding of the sources responsible for cosmic reionization. To this aim, we are using the incredible capabilities of the VLT/MUSE instrument combined with the power of strong lensing clusters to select intrinsically faint LAEs. This combined approach allows us to focus on the determination of the very faint end of the LF and to set unprecedented constraints on both its shape and the ionizing emissivity of the selected population.

The layout of this thesis is as follows. In Chpt. 2, we provide an overview of the capabilities and specificities of the VLT/MUSE instrument and explain why this instrument is so efficient (compared to other techniques) in detecting faint line emitters in an unbiased manner. A detailed presentation of the complex MUSE data structure is also provided in this chapter. In Chpt. 3, we provide a more thorough introduction to strong-lensing clusters, including a general overview of the mass models and mass-model construction as well as illustrations of various lensing effects relevant for this study. Finally we describe the strong lensing clusters observations and the detection process for LAEs used in this work. Chapter 4 presents the method implemented to compute effective volumes for individual LAEs across several MUSE cubes, as well as the physical and technical motivations for the development of such a complex method. Chapter 5 presents the various steps needed to compute the LAE LF, including the selection of one LAE per multiple-image system, flux computation, completeness correction and Monte Carlo (MC) iterations to account for all possible sources of uncertainties. The results and interpretation that can be derived from the LF computed in previous chapter are presented in Chpt. 6 focusing on the evolution of the LAE LF with redshift, the estimation of the ionizing flux density produced by the selected population and the possible impact of the choice of mass model on the conclusions. In Chpt. 7, we tackle the question of the selection method and we discuss on the intersection between the LAE and LBG populations and the implications for the contribution to the ionizing flux. Finally Chpt. 8 present respectively a summary a conclusion and possible future prospects.

The main results of this this have been presented in a refereed paper de La Vieuville et al. (2019) given in Annex B. Additional results presented in the discussion sections are also presented in a paper in preparation.

Throughout this work, we adopt a standard dark-matter cosmology with $\Sigma_m = 0.3$, $\Sigma_\Lambda = 0.70$ and $H_0 = 70 \mathrm{km\,s^{-1}\,Mpc^{-1}}$. All magnitudes are given in the AB system (Oke & Gunn, 1983) and all redshifts are quoted based on the vacuum rest frame wavelengths.

2 | The VLT/MUSE instrument

Contents

2.1 General overview and technical features

MUSE (Multi Unit-Spectroscopic Explorer) is a large field of view Integral Field Unit (IFU) placed on UT4, one of the four VLTs at the ESO Paranal observatory, in Chile. Most of the information provided in the following sections come from the ESO MUSE user manual or the ESO MUSE pipeline user manual [1]. The MUSE project was initiated by its current PI, R. Bacon in the early 2000s and the instrument itself was commissioned in 2014. It operates with the 8 m mirror of UT4 in the optical domain, between $\lambda = 4750$Å and $\lambda = 9350$Å. Its spectral sampling is of 1.25Å and its resolving power varies between $R = 2000$ and $R = 4000$ at higher wavelength. MUSE has two observation modes: the Wide-Field Mode (WFM) and the Narrow-field Mode (NFM) which respectively have and angular Field of View (FoV) of $1' \times 1'$ and of $7.5'' \times 7.5''$ and a spatial pixel size of $0.2''$ and $0.025''$. The spatial resolution of the NFM is typically of $0.05 - 0.08''$ whereas that of the WFM is typically of $0.2 - 0.3''$ (both figures quoted are without adaptive optics, see Fig. 2.3 for a comparison between the spatial resolution of NFM and WFM).

Because of its higher spatial resolution, the NFM it well suited for more detailed studies of brighter objects. On the contrary, the WFM is more suited for surveys and for probing larger cosmological volumes. All observations used in this work were conducted using the WFM and unless specified otherwise, all examples and discussions are made assuming the use of the WFM .

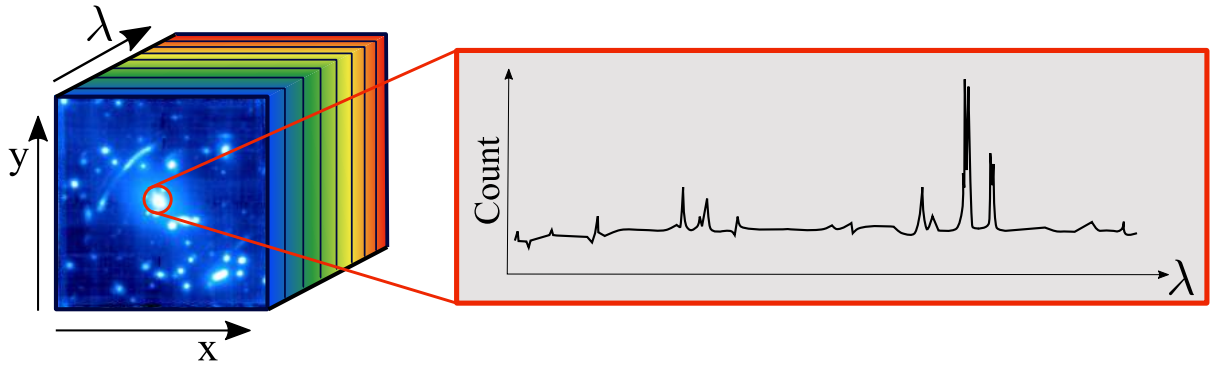

Figure 2.1: MUSE cube structure, for each spatial pixel, a full spectrum is available.

Being an IFU, the final data products are data cubes (hereafter just cubes; see Fig. 2.1): all spatial pixels of the FoV have a complete spectrum with the features mentioned in the previous paragraph. Another way to say this is that MUSE produces 3681 images every 1.25Å between $\lambda = 4750$Å and $\lambda = 9350$Å. Hereafter, these monochromatic images will be referred to as layers or spectral layers. A single MUSE cube weights around 3Gb with a variance cube extension. Several MUSE cubes can be combined together to form a single mosaic cube (see e.g., the A2744 mosaic in Sect. 3.2.1 which is more than 10 Gb of data).

As of mid 2017, MUSE WFM also uses Adaptive Optics (AO) to correct the front-wave distortions caused by turbulence in the high layers of the atmosphere. This system can be used for both the WFM and the NFM. The four sodium lasers (see Fig. 2.2) have a wavelength of λ5890Å which falls in the middle of the MUSE spectral range. Because the laser are powerful and create scattered light, all exposures taken with AO have the spectral range centred on the sodium emission masked. This mask is applied to the entire FoV and spans a spectral range of at least 150Å depending on

[1] Both documents can be found online at `https://www.eso.org/sci/facilities/paranal/instruments/muse/doc.html`

Figure 2.2: UT4 telescope on which MUSE is mounted, with the four adaptive optics lasers in action.
Credit ESO/F. Kamphues

what exact filter is used.

The reduction of MUSE cubes is an entire subject in itself and is not addressed in details in this work. More information on the MUSE ESO reduction pipeline can be found in Weilbacher et al. (2012, 2014) or on the ESO website[2]. The basic feature of this reduction process are bias subtraction, flat-fielding, wavelength and flux calibration, basic sky subtraction and astrometry. All exposures are reduced individually before being combined into a final data cube.

2.2 Main science goals of MUSE

The combined use of a very large light collecting area, adaptive optics with the possibility to use WFM of NFM makes MUSE a very versatile instrument. It has been used in a lot of different science fields since its commissioning, from planetary and small body science to stellar population in nearby galaxies and high redshift studies. This section aims at providing a wide but non exhaustive overview of the motivations at the origin of the MUSE project as well as a glimpse of the various work that have been conducted taking advantage of the various abilities of the instrument. The different thematic fields are listed below by order of priority as exposed in the original science goals of the instrument[3].

The study of evolution and formation of galaxies and of the early Universe was the main driver for the development of MUSE. Most of the design of the instrument is therefore optimized for this specific kind of science. In this field, as often a detailed spatial resolution is not an absolute necessity, the WFM is most often used to probe larger volumes of Universe.

Distant galaxies are difficult to detect as they appear faint. An efficient and reliable way to

[2] `https://www.eso.org/sci/software/pipelines/muse/`

[3] The original science goals as determined at the beginning of the MUSE project in 2004 are can be found online at `http://muse.univ-lyon1.fr/spip.php?rubrique2`

select high redshift star forming galaxies is through their Lyα emission line (see Sect. 1.2.1 for details on the Lyα line). One of the main focus of MUSE is the detection of this line between $2.9 < z < 6.7$ to reliably select faint and high redshift galaxies. The Lyα selection is not an end on itself, but gives access to a new faint population of galaxies that was mostly out of reach before the advent of MUSE. The identification of these low luminosity low mass galaxies is for example, a crucial point to set constraints on the hierarchical scenario of galaxy formation (see e.g., Ventou et al., 2017, which studies the galaxy merger fraction), to study the sources of reionization(see e.g., Drake et al. (2017a); Hashimoto et al. (2017); Japelj et al. (2017); Caruana et al. (2018) and de La Vieuville et al. (2019)) or the star formation rate history. In addition to these, the peculiar line profile of the Lyα line can be used to look for possible inflow or outflow of neutral hydrogen in high redshift galaxies (see e.g., Verhamme et al. (2006); Swinbank et al. (2015); Guaita et al. (2017) or Sect. 1.2.1)

According to the Λ-CDM theory of cosmology, one of the first structures to form in the Universe is the cosmic web (see Sect. 1.1.1). This cosmic web structure can be indirectly observed and traced with a 3D mapping of galaxies provided that we have their redshift. Such work has been done with the galaxies of the SDSS survey in Sousbie et al. (2011) and Tempel et al. (2014). Since MUSE allows the detection of very faint LAEs (see Sect. 2.3.1) compared to previous facilities, it can provides new observational constraints on this structure as a by-product of any observation. Direct observation of these filamentary structures through diffuse Lyα emission of the gas remain very challenging due to the extremely low surface brightness of such an emission. It has been attempted in (see e.g., Gallego et al., 2018; Cantalupo et al., 2019), and while the diffuse Lyα emission can be seen in the close neighborhood of galaxies, nothing really conclusive can be seen at intergalactic scales.

At lower redshift (mostly $z < 1$) one of MUSE goals was to produced detailed analysis of the galactic environment and its mechanisms including studies of the inter-galactic medium, galactic winds, feedback and galaxy kinematics. Taking advantage of the higher spatial resolution on these closer galaxies, MUSE allows a more in depth study and understanding of the mechanisms playing a possible role in the evolution of galaxies. The conclusion of such studies can also be transposed to the study of higher redshift galaxies for which such work is not possible. This can be done using for example, spatially resolved spectroscopy in QSO line of sights to probe the possible presence of circumgalactic gas or galactic winds (see e.g., Schroetter et al., 2016; Bouché et al., 2016; Zabl et al., 2019) or studying gas or stellar kinematic by mapping the Doppler effect of emission lines across spatially resolved galaxies (see e.g., Contini et al., 2016; Guérou et al., 2016, 2017). At these lower redshift, MUSE can also be used to study punctual and rarer events such as the on-going merger in the Antennae galaxy (see .e.g., Weilbacher et al., 2018; Monreal-Ibero et al., 2018) or specific studies of the strangest galaxies found in the SDSS survey (see Baron & Poznanski (2017) and Monreal-Ibero in prep.)

The IFU capabilities of the instruments comes in handy when studying crowded fields as it allows to capture a very large number of spectra within a single observation. Conducting massive spectroscopy in globular clusters can help understanding the evolution of star population in such environments and allows comprehensive studies of the velocity field and dispersion (see e.g., Husser et al., 2016; Kamann et al., 2016, 2018a,b). This observational work contributes (among many other things) to the investigation of the formation mechanisms of globular clusters and the search for possible black-holes at their center.

In dense stellar fields MUSE observations allows to produce several thousands of stellar spectra (Roth et al., 2018) which in itself represents a legacy value for the community and can be used for many different applications including the study of the chemical evolution of galaxies, the study of

star formation history and the possibility to complete previous stellar libraries with un-biased and complete blind spectroscopic selection.

For such observations, and especially when looking at the core of globular clusters, the use of the NFM with AO can give the necessary spatial resolution needed to dissociate individual stars form their neighbours. Figure 2.3 provides an illustration of the resolution reached with the NFM with AO in the center of a globular cluster, and a comparison of the resolution reached with HST on Neptune.

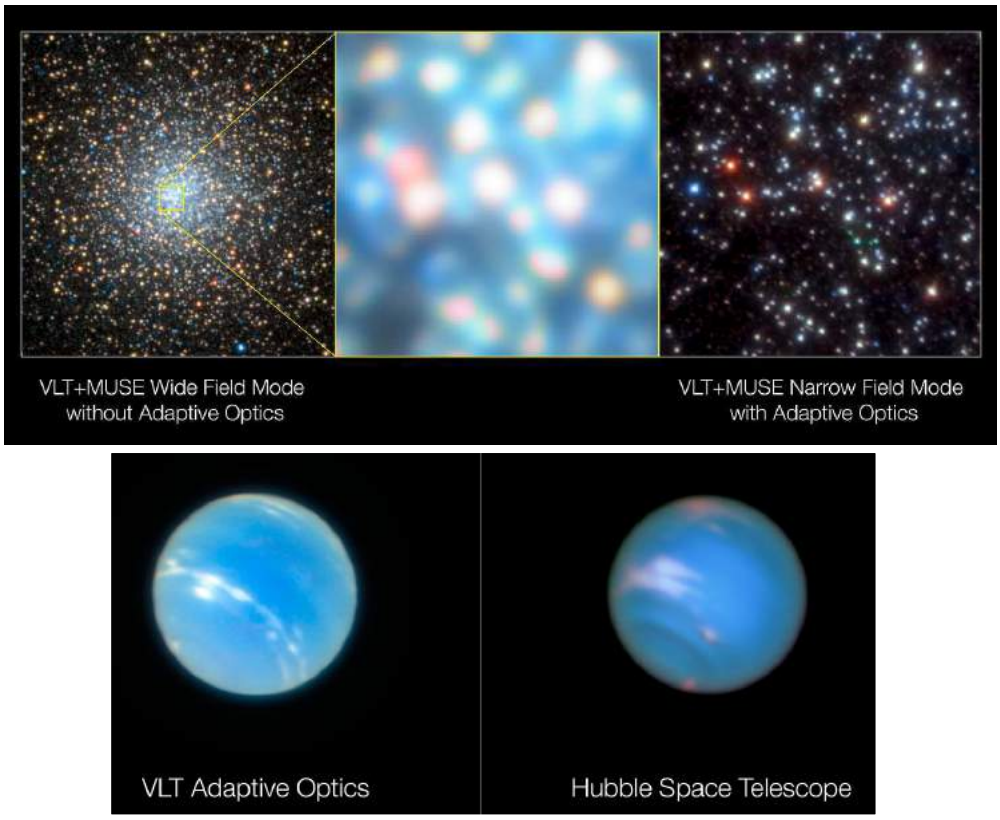

Figure 2.3: Top: comparison of the spatial resolution reached with MUSE WFM without AO and with MUSE NFM with AO. Bottom: Comparison of the spatial resolution reached with MUSE NFM with AO, with HST.
Credits: ESO/S. Kamann (LJMU) (top), ESO/P. Weilbacher (AIP)/NASA, ESA, and M.H. Wong and J. Tollefson (UC Berkeley)(bottom)

With the use of the NFM, MUSE was also intended to be used in the study of small bodies and planets in the solar system. While some observations were made during various commissioning runs (See e.g„ Neptune in Fig. 2.3), almost no literature can be found on the subject.

In this Section we have shown that due to its very wide abilities, MUSE can be (and has been) used in virtually any field of astrophysics. However, up to now, most science products and publications come from the MUSE deep and very deep surveys (with a special focus on the LAEs), since the telescope time has been divided according to the priority of the different science cases exposed in this section. In the following sections, we focus on the use of MUSE to study the population of SFGs at $2.9 < z < 6.7$ based on their Lyα emission. In Sect. 2.3.1 we explain why MUSE is so efficient to detect emission line objects compared to other instrumental techniques and we show that its capabilities makes it an ideal instrument to study the galaxy LF in Sect. 2.3.2.

2.3 MUSE to study the galaxy population

2.3.1 Detection of faint emission line objects

The main motivation for the conception of MUSE was to study faint and distant galaxies, with a focus on the detection of hydrogen emission lines associated with the presence of young star populations and the formation of stars. It has been shown on several occasions that MUSE is indeed most efficient to detect emission lines objects (see e.g., Bacon et al., 2015, 2017; Herenz et al., 2017; Mahler et al., 2018; Maseda et al., 2018, where a lot of emission line emitters have been detected without any identified counterpart on very deep HST images). The efficiency of MUSE resides in the optimization of the signal to noise around emission lines thanks to its IFU capabilities.

One of the classical approach to select emission line emitters is the use of Narrow-Band imaging. A preliminary selection is done by looking for a flux excess in certain band that would be compatible with the presence of an emission line at a certain redshift. The use of NB makes this technique only sensitive to a flux excess in a reduced redshift range, depending on the spectral width of the NBs. This exercise can be repeated to select emission-line emitters centered on different narrow redshift ranges. The use of broader filters obviously enlarges the redshift range of the selection, but broader filters are also less sensitive to a potential flux excess caused by an emission line which is by nature, quite narrow. As a second step, a spectroscopic follow up of the sources that passed the first selection can be done. This technique, or some variations of it have often been used to select a LAE population in order to study its LF (see e.g., Rhoads et al., 2000; Westra et al., 2006; Dawson et al., 2007; Hu et al., 2010; Ouchi et al., 2010; Matthee et al., 2015; Santos et al., 2016; Sobral et al., 2018, and many more) but is not only limited to the selection of the Lyα line.

As an alternative to the NB imaging techniques, a blind spectroscopic search for line emitters has been developed by looking for serendipitous detections in slits of multi-slits instruments (see e.g., Martin & Sawicki, 2004; Rauch et al., 2008; Cassata et al., 2011, 2015; Dressler et al., 2015). In this method, the regions of slits free from the presence of target sources are used for "blind" detection of line emitters. The term "blind" is used as contrary to the NB imaging with spectroscopic follow-ups, no photometric priors are used to spectroscopically identified line emitters. The main advantage of such method is that it is less biased in its selection than NB surveys and allows for the detection of fainter line emitters. However, and as detailed in next section, it suffers from a systematic loss of flux for extended sources.

By construction, narrow-band imaging techniques are sensitive to an integrated flux on a given spectral range, which make them very efficient to measure the continuum of faint galaxies, as the spectral integration increases the signal-to-noise of the continuum. On the contrary, and as mentioned in the previous paragraph, the excess flux caused by the presence of an emission line, can easily be lost in the continuum integration. MUSE is the opposite of NB imaging: it is efficient to detect emission lines, but not so to measure and detect faint continua. Being an IFU, the signal of a galaxy continuum is divided on many spectral pixels which results in an increase of both the photon noise and the relative contribution of the read-out noise of the CCDs. The signal of the continuum is therefore divided and the noise increased, making the detection and measurement of faint continua difficult with MUSE. On the contrary, the signal of emission lines is spectrally compact and brighter than the continuum. As the emission lines are not diluted in a spectral integration, and because of the large light collecting area, they easily rise above the noise in MUSE cubes. Blind spectroscopic search for line emitters are quite similar to IFUs in terms of detection abilities but do not provide complete spatial information nor do they allow to precisely measure the flux.

2.3.2 Advantages of a blind spectroscopic selection for the LAE LF

While the NB imaging and blind search with slit spectroscopy techniques have been proven to work quite well and have been widely used, they both have certain flaws that can be avoided when using an IFU. In this section we discuss the advantages of the MUSE selection and measurements with respect to other instrumental techniques to show that MUSE is the ideal instrument to study the faint end of the LAE LF and the sources responsible for reionization.

The first and maybe the most important default of NB surveys is the potential loss of flux when the emission line is cut by the border of the NB filter or when spatially extended galaxies do not fit entirely in the slit used for the spectroscopic follow up. A systematic underestimation of the flux of LAE results in a shift of the entire LF towards lower luminosity. Such systematic loss is studied in Cassata et al. (2011) for LAEs. This study shows that in average 15% of the flux is lost, with variations ranging from 10% to 30% depending on the seeing conditions. In addition to the luminosity shift, there are also some systematic effects on the shape of the LF: lower luminosity or higher redshift galaxies are less affected by the loss of flux, as in average they appear smaller on the sky. Using MUSE, we systematically recover a greater fraction of the total flux as we recover the entire spectral and spatial profile of any emission line emitter. For LAEs, this aspect is especially important as it has been shown in Wisotzki et al. (2016),Leclercq et al. (2017) and Wisotzki et al. (2018) that LAEs tend to have extended halos.

The second point is the completeness of the selection. Using NB imaging, the LAEs are selected by detecting an excess of flux with respect to the continuum detection which automatically remove the objects with non detectable continuum that are nevertheless LAEs. In addition, this technique is only reliable to select bright line emitters, and fails to identify the faintest objects. A significant fraction of the LAE population is therefore missed using NB surveys only. Using blind spectroscopic search with slit spectroscopy provides more complete samples, but as mentioned in the previous paragraph, this type of selection is affected by systematic loss of flux. Using MUSE, we have a truly blind spectroscopic selection of all line emitters in a given volume and systematic effects are expected to be small. This allows to properly assess the completeness of the selection, measure the volume probed during the observations and compute accurate flux estimates for all LAEs. All these three elements are key steps when computing a LF. As a side note, this complete blind spectroscopic selection of sources is also a huge advantage for the mass modelling of galaxy clusters since it allows the discovery and confirmation of new multiple images systems that are essential for these precise needs (see e.g., Richard et al., 2015; Bina et al., 2016; Caminha et al., 2016; Mahler et al., 2018; Lagattuta et al., 2017, 2019, and many more).

The third and last point is the continuous redshift selection of LAEs between $2.9 < z < 6.7$ with MUSE. This wide redshift range is interesting to study the sources of reionization as it just overlaps with the end of the reionization era at $z \sim 6$, and allows to study a possible evolution of the LAE LF over a wide range of redshift.

To sum up this section, MUSE allows a complete and as unbiased as possible selection of a LAEs in a single observation. It probes a wide range of luminosity and redshift while offering the possibility of systematically recovering a larger fraction of the LAE flux. The large collecting area combined with the IFU structure makes it possible to detect faint LAEs whose continuum would not have been detected otherwise with NB imaging. All of these points combined makes MUSE the ideal instrument to work with to probe the faint end of the LAE LF.

To further extend the sensitivity to the low luminosity LAEs, strong lensing clusters are used in this work. Because of the volume contraction induced by lensing effects (see Chpt. 3) the volume probed in such FoV drastically shrinks which makes it more difficult to get a statistically

relevant sample of LAEs. Even without the presence of galaxy clusters in the line of sight, the volume probed by MUSE cannot compete with the large volume probed with large NB surveys. For example the MUSE HUDF the total covolume between $2.9 < z < 6.7$ probed on the 3×3 MUSE mosaic is around 9.4×10^4Mpc^3 which is far more than can be reached in the high magnification regions of lensing fields: the total covolume probed in this work with 4 cubes is around 1.6×10^4 Mpc^3. For comparison, in Sobral et al. (2018) the total covolume probed within the 2 square degree of the COSMOS field using a collection of broad and narrow bands to look for LAEs is about 6.2×10^7Mpc^3. This shows that even though MUSE is a nice instrument to look in depth in a given volume, large NB surveys are still much needed to probe large cosmological volumes. And more specifically in the study of the LF, faint galaxies being much more numerous than bright ones, such large volumes are required to study the bright end of the LF.

2.4 Noise structure in MUSE cubes

In this section we pay close attention to the noise in cubes to better understand its structure because it can affect the source detection. What we define as noise in this work is the range of random variation from pixel to pixel with respect to a "true value". A higher level of noise means a higher dispersion of pixel value with respect to this true value, and a lower noise level means a lower dispersion. Because any noise measurement relies on the measurement of pixel variations, it is necessarily averaged on a local area (i.e., we cannot measure any variations on a single pixel). In astronomical data, the main sources of noise can be grouped under three broad categories: the photon noise, the noise caused by the instrument itself and the read-out noise caused by the electronics of the instrument.

Following the definition above, the presence of a source locally increases the noise. Indeed, assuming that the photon count of a source follows a Poissonian distribution (as it is often assumed) the photon count is proportional to F, the flux of the source and the variations (or uncertainty) are proportional to $\sqrt{F}$. This simply shows that the absolute photon noise increases with an increasing flux, even though the signal-to-noise ratio of the source increases as $\frac{F}{\sqrt{F}} = \sqrt{F}$.

In addition to this phenomenon, there are at least three constant noise components in MUSE cubes that are always present regardless of the observation being carried out. Some of them are intrinsic to the instrument and caused by its design, and some are external to the instrument itself. All these different components play an important role in the understanding of the volume computation described in Chpt. 4. For this reason they are detailed in Sect. 2.4.1, Sect. 2.4.2 and Sect. 2.4.3, and some illustrations are provided.

2.4.1 Structure of the instrument

When the light enters the instrument, it is split in 24 by a field separator that redirects the light towards the 24 spectroscopic units of MUSE. Before reaching each of these units, each beams is split again into 48 smaller beams by slicers that rearrange each beams on the 24 CCDs, in a complex combination of spatial and spectral positions (see Fig. 2.4). During the reduction process, the data is collected across the 24 CCDs and is combined into a single data cube. Even after the end of the reduction process, the architecture and organisation of these field separators and slicers remain visible on some of the spectral slices of the cubes as illustrated in the right panel of Fig. 2.4. These patterns are especially visible in cubes with long exposure time, since the relative contribution of photon noise decreases with exposure time.

There are several possible explanations for this effect, starting from different sensitivities on different part of a same CCD or different sensitivity from one CCD to another, or from a slight misalignment when combining all spectra into a cube. To minimize the slicer patterns on the

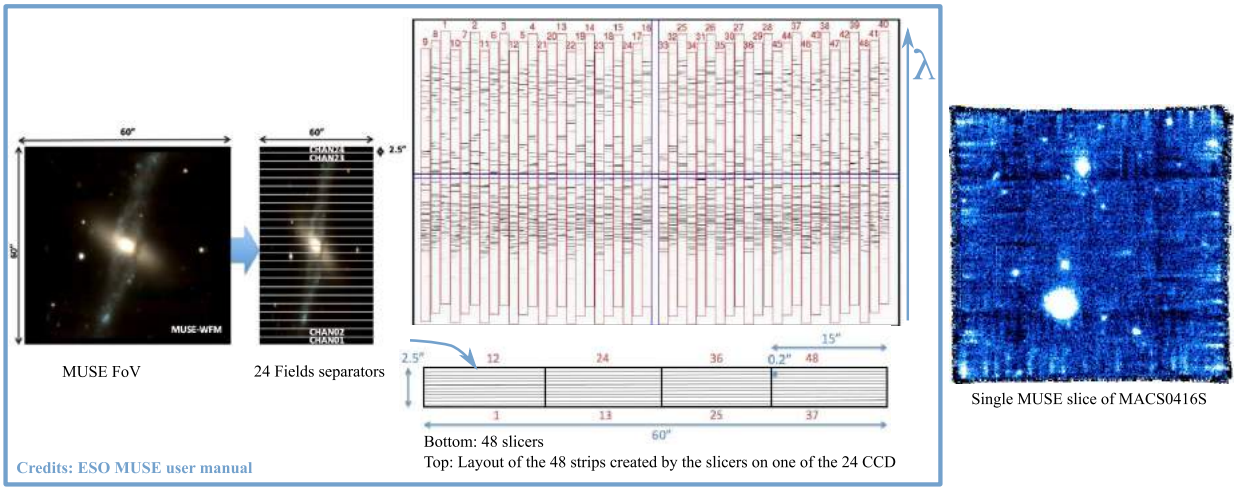

Figure 2.4: Left panel: the 24 field separators and the 48 slicers on the MUSE FoV and layout of the 48 spectral strip on one of the 24 CCDs of the instrument. Each strip is about 3600 spectral pixels long and has in average a width of $\sim$ 76.5 spatial pixels according to the MUSE pipeline User Manual.

final cubes, a 90° rotation is often used between each individual exposure of a same field. In this situation, the patterns appear as squares as seen in right panel of Fig. 2.4.

These differences are accounted for during the reduction and added into the variance extension of each cube. They nonetheless remain visible in the main data cube and affect the detection of sources and therefore play an important role when computing the effective volume as described in Sect. 4.4. The effects of the structure described in this section are not visible on all slices of a cube. However, the patterns and their spatial layout are almost identical on all slices where they are visible.

2.4.2 Sky emission lines

Because MUSE is an instrument based on Earth working in the optical domain, it is subjected to bright sky emission consisting of a slowly varying continuum and bright emission lines. The wavelengths of each possible sky lines are well known and affect certain spectral layers of the cubes with various intensities. The sky lines can be further removed after reduction, with the use of ZAP (Zurich Atmosphere Purge, Soto et al. (2016)). This software uses a principal component analysis to characterize the sky lines residuals and further subtracts them. If most of the line flux is removed, the increased Poissonian variance caused by the bright sky emission remains on the affected layers. For each of those spectral layer, this results in and increased but constant level of noise across its entire spatial extent. Some of the sky lines are so bright that they leave MUSE almost blind in certain layers, leaving only the brightest sources to be possibly detected there. Sky lines are not homogeneously distributed (see Fig. 2.5 for an example) and most of them fall in the redder part of MUSE wavelength coverage making it harder to detect high redshift emission line emitters.

2.4.3 Sensitivity of the instrument and final combination

The last component, is the sensitivity of the instrument itself. During commissioning, it has been established through the computation of the throughput of the instrument that MUSE is most efficient at around 7000Å. This increased efficiency automatically translates into a reduced noise

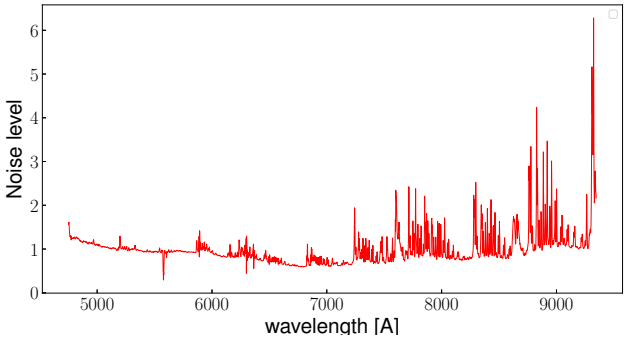

Figure 2.5: Relative variation of the average background noise computed from every layer of the A2390 cube. More details on this specific computation are provided in Sect. 4.4.1.

as the photon count is more precise. When measuring the relative averaged background noise for every wavelength step of a MUSE cube as it is done in Fig. 2.5, we in fact measure the added noise contribution of the instrument sensitivity, the continuum sky emission and the sky emission lines. From this figure, we indeed see that the relative noise reaches a minimum around 7 000Å. The slow continuum variation are mostly guided by the sensitivity of the instrument and the sky continuum emission. The spikes, mostly seen in the redder part of the MUSE wavelength coverage, at $\sim$ 7 200Å and above, are caused by the sky-emission lines. In addition to these relative and average variation of noise along the spectral axis of a MUSE cubes, for each layer, there is a spatial variation of noise governed by the layout of the slicers and field separators as shown in right panel of Fig. 2.4 (and possibly the rotation of the FoV during the data acquisition).

2.5 Cataloging sources in a MUSE FoV

Because of the 3D structure of the data, visualisation becomes quite challenging, and manual inspection of large numbers of sources or large sections of cubes quickly becomes very limited. For that reason specific tools have been developed within the MUSE collaboration to facilitate common, repetitive and or complex tasks.

A specific python module, MPDAF (Piqueras et al., 2017), was developed to make easier the analysis of MUSE cubes. It allows among other things, to handle MUSE cubes, images and spectra with dedicated classes and functions. For source detection, several alternatives have been developed including CubExtractor (Cantalupo et al., 2019), based on an connecting-labelling component algorithm, LSDCat based on a three-dimensional matched filter approach (Herenz & Wisotzki, 2017), Origin (Bacon et al., 2017) based on 3D filter matching and finally Muselet which is part of the MPDAF package and is based on SExtractor (Bertin & Arnouts, 1996). In this work, only Muselet is used, and because this software plays an important role in the method developed in this thesis, a more detailed description of it is provided in Sect. 4.2.

When cataloging a certain area of the sky, the goal is to be as complete as possible. However, as explained in Sect. 2.3.1, MUSE is not the most efficient to detect continuum sources and is therefore likely to miss some of them. To have an as complete as possible list of sources in a given area, the best strategy is to cross match the MUSE detections with HST detections. This process yields three categories of sources:

- Line emitters only (MUSE detection only)
- Line emitters with detected continuum (MUSE + HST detection)

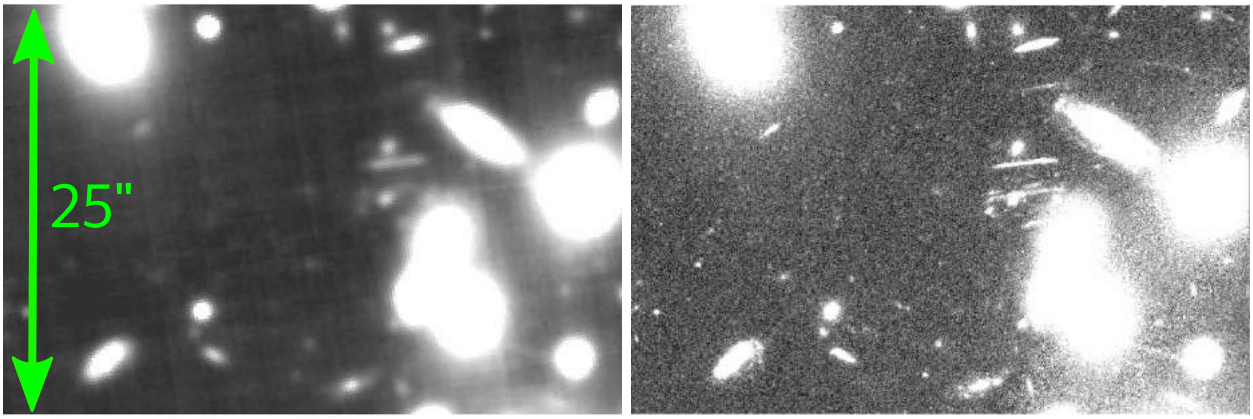

Figure 2.6: Comparison of the spatial resolution of MUSE (Left) and HST(right) on a region of the A2744 lensing cluster. The MUSE image is a white light image (i.e., the sum of all spectral layers into a single image). The comparison of the two images is obviously a bit limited since by nature MUSE data are cubes, and HST data are single images.

◦ Continuum only (HST detection only)

In addition to the complete assessment of sources in a volume, the cross matching is necessary to get photometric information and more precise spatial information for the MUSE detections that are successfully matched to an HST detection. The higher spatial resolution of HST is also useful to improve the source segmentation, and therefore to optimize the spectrum extraction in MUSE cubes. When working in lensing clusters, it can also help for the identification of multiple images. Even though some part of the cross match can be automated trough a simple coordinate matching procedure, the identification of an HST counterpart sometimes remains tricky as the spatial resolution of MUSE and HST are so different. Figure 2.6 provides a comparison of the spatial resolution seen by MUSE and HST. To avoid as much as possible doing any mis-match, it is therefore needed that all sources of both catalogs are manually reviewed, which can be tedious work for a single person depending on the depth of the observations and the area surveyed. For that reason, some collaborative tools have been developed within the MUSE collaboration to make it easier to go quickly through a large number of sources and to share the work load between different groups of people.

To give an example of the numbers at stake, in the MUSE HUDF and UDF-10 (Bacon et al., 2017) mosaic, more than 1 500 candidate emission lines objects have been identified. Each of these candidates were manually inspected to assess the robustness of the detection, validate or not the corresponding HST detection (if any was found), assess the quality of the spectrum extraction and whether the sources is being contaminated by nearby neighbours and measure the redshift. The entire process is very tedious and is described in Inami et al. (2017). At the end of the process, a secure redshift was measured for 1 338 galaxies.

3 | Lensing clusters: methodology and MUSE observations

Contents

Galaxy clusters are among the most massive structures of the Universe (typically $10^{14-15}M_{\odot}$). Following the prediction of general relativity, the high concentration of mass warps the surrounding space-time and prevents the light from propagating in "straight" lines causing the optical effects that can be seen in Fig. 1.13 or Fig. 3.3. In a very similar way to a simple converging lens, gravitational lensing can amplify the background and is therefore often used as gravitational telescope.

To do any quantitative measurements on the background galaxies using this technique, it is necessary to characterize precisely the deformation suffered by each of them. Such a task is only possible provided we are able to trace the observed photons back to the source plane, behind the gravitational lens. Inverting the trajectory of light can be done using predictions of general relativity but requires the knowledge of the distribution of mass. In perfectly symmetrical cases such as black holes, this is relatively easy as the only unknown is the mass of a punctual mass. However, in a galaxy cluster this is not the case, and to add to the complexity, about 80% of the mass budget resides in dark matter halo(s) and is not directly observable. It is nonetheless possible to reconstruct this distribution of mass using various observational techniques.

The goal of the following sections on gravitational lensing is not to give a detailed review of lensing phenomena, techniques and equations, but to give the reader the minimum required to understand the analysis developed in the following chapters. For a thorough introduction to strong lensing and mass model reconstruction, we refer the reader to the excellent (and relatively easy to read) work of G. Mahler or D. J. Lagattuta who both tackle mass modelling with MUSE data (see Mahler et al. (2018) or his thesis manuscript which is in french, and Lagattuta et al. (2017, 2019)). A more general review can be found in Kneib & Natarajan (2011) or Schneider et al. (1992). In Sect. 3.1, we present an overview of the method for mass modelling with gravitational lensing and introduce the Lenstool software. In Sect. 3.2, we present the observations used in this work and explain the source detection and cataloging. The large number of spectroscopic redshifts and the discovery of new multiple image systems allows to build improved mass models which are presented in Sect. 3.3. This section also illustrates how the mass model can be used to correct the observations from the lensing effects.

We also emphasize that even though the mass modelling aspect was not part of the work done during this thesis, summarizing this process is of interest to fully understand the logic of the approach, from the initial observations with MUSE leading to improved mass models, to the final selection of the LAEs used for the computation of the LF. As a side note, this chapter illustrates very well the variety and amount of work that had to be done by other people to allow this present thesis to exist.

3.1 Mass modelling methodology

3.1.1 Constraining the mass distribution with gravitational lensing

There exist several ways to constrain the mass distribution of galaxy clusters with observations. It is possible to derive constraints on the DM distribution using X-rays observation of the hot gas, assuming that it traces DM (Merten et al., 2015, see e.g.,). Another method is to use the Sunyaev-Zeldovich (SZ) effect which is the inverse Compton scattering of the CMB photons with hot electrons of the intra-cluster gas. This effect induces a frequency shift in the photons of the CMB and the strength of this signature can be used to weight galaxy clusters or simply to detect them (see e.g., Planck Collaboration et al., 2016a,d). However, both methods require to make assumptions on the dynamic state of the gas within the cluster to use them as tracers of DM. As illustrated in the now famous case of the Bullet cluster shown in Fig. 3.1, such assumptions cannot always be made. The Bullet cluster is in fact two colliding clusters. During this process, the hot

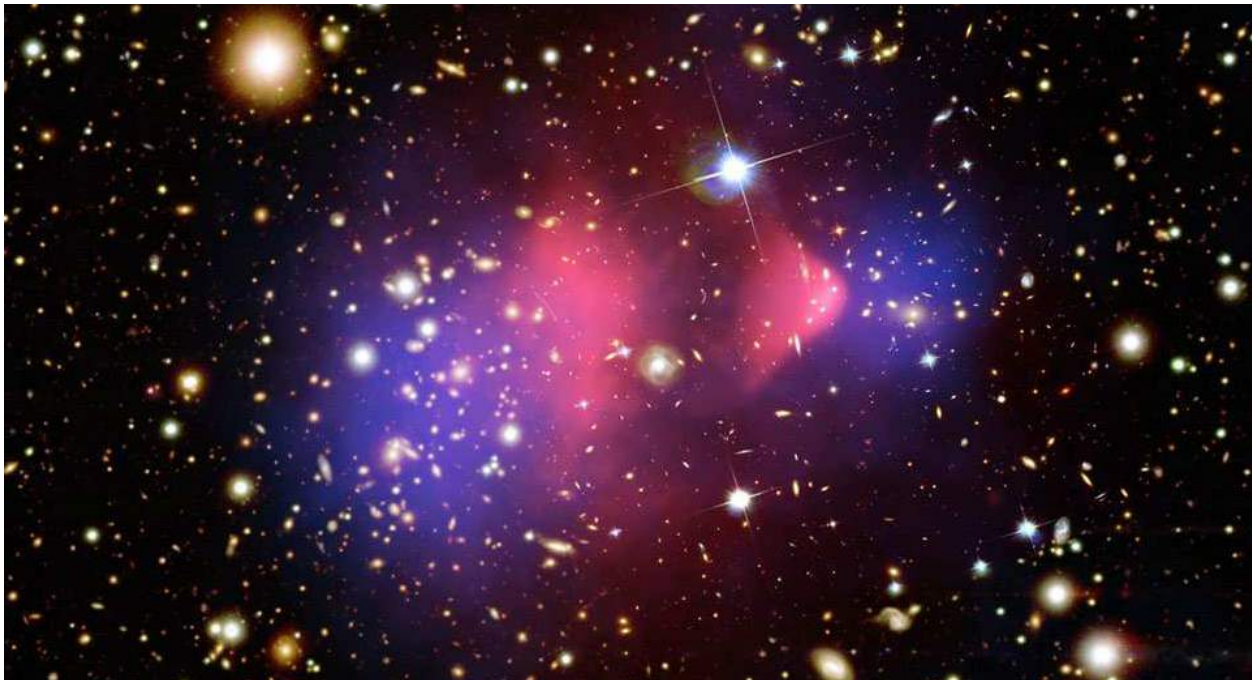

Figure 3.1: Bullet cluster seen by HST with dark matter halo component (Clowe et al., 2006) and hot gas (Markevitch, 2006) overlaid in respectively blue and pink. It can be seen that there is a large offset between these two components showing that gas is not necessarily a good tracer of DM.

gas of the two clusters collided and was stopped "in the middle", whereas DM being collisionless, simply went through causing the large offset seen in Fig. 3.1. This is an obvious example of the fact that X-rays emission cannot always be used to trace DM.

Unlike the SZ effect or the X-rays emission of the gas, strong gravitational lensing offers the possibility to constraint the distribution of DM without making any assumptions on the gas. The general idea of the method is to use the background galaxies that are multiply imaged to constraint the mass distribution. These multiples images of a same background galaxies appear when the wave fronts are so deformed by gravitation that they overlap with themselves as seen in Fig. 3.2. They can be used for mass modelling following the iterative process described in a very simplistic manner below:

- Assume a set of multiple systems, each of the systems with their own redshift or at least their constraints on the redshift.
- Assume a somewhat realistic mass distribution using the visible baryonic matter and making a guess about the DM distribution. The mass distribution is assumed to be thin in the lens plane since the depth of the "real" distribution is negligible with respect to the distances between the observer and the lens or the observer and the background sources.
- Lens back each image of the multiple systems to their own source plane using the current mass model. If the model is not too bad, their position should coincide or almost coincide.
- Lens each image again, from the source to the image plane using the current mass model. If the mass model is off, the positions predicted from the back and forth through the lens will be significantly different from the observed ones. On the contrary, if the model is good, the predicted positions should once again coincide with the observed positions. The mean squared difference between each predicted and observed position is called the RMS and is often used as the value to minimize when optimizing mass models.
- Improve the mass model and iterate once more.

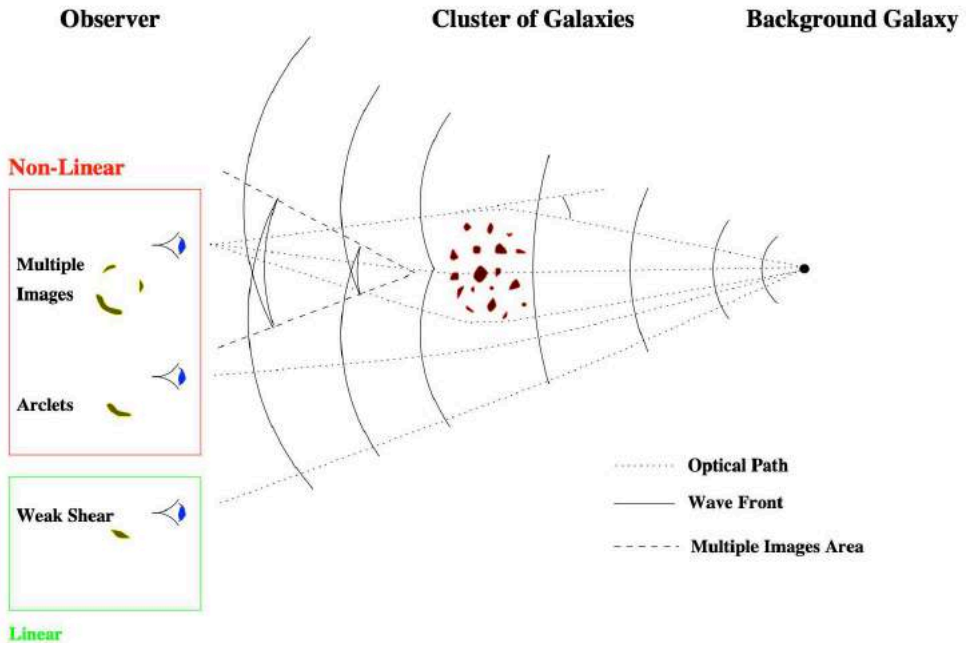

Figure 3.2: Schematic view of the wave front deformation around a galaxy cluster.
Figure taken from Kneib & Natarajan (2011)

The difficulty of mass modelling resides in the large dimensionality of the problem, and the entire process can not always be completely automated. For example, as the identification of multiple images is not always straightforward, it is not uncommon to use this iterative process to test whether a given image belongs or not to a certain multiple system. If the image does indeed belong to the system, the resulting RMS should decrease. An in addition, it is also common to divide the multiple system according to the level of constraints they provide and compare the mass models derived using each set of multiple system (see e.g., Mahler et al., 2018; Lagattuta et al., 2019).

The quality of the final mass models really depends on the amount of multiple systems found: provided that enough of them are found, most of the possible degeneracies can be broken. Having secure spectroscopic redshifts (as opposed to photometric redshifts) is of great help in this process. It helps identifying the image parts of a multiple system and removes one free parameter from the problem.

For this reason, MUSE is also an ideal instrument for mass modelling. It provides a complete assessment of source within the FoV, with a high number of spectroscopic redshifts. Each time MUSE observed a lensing fields, it discovered new sets of multiple systems (see e.g. Richard et al., 2015; Bina et al., 2016; Caminha et al., 2016; Karman et al., 2016; Lagattuta et al., 2017; Mahler et al., 2018; Lagattuta et al., 2019), it is therefore a great asset to produce mass models of improved quality, especially when working in parallel with deep HST observations which provide high spatial resolutions. Other constraints beside multiple systems can be used to reconstruct the mass distribution: for example it is possible to compare the intrinsic flux of images part of the same multiple system to locally constrain the magnification and therefore the mass distribution, or to use the velocity dispersion of resolved lensed galaxies (here again we refer the reader to the thesis work of G. Mahler).

In practice, there are two families of models: parametric and non-parametric reconstructions (also called free-form). In parametric reconstructions, the overall potential is modelled as the sum

of sub-potentials, and each of them is parameterized with a given position, shape, set of axis and density profile. Some parameters can be fixed and the rest is optimized. With the free form approach, no shape is assumed and the mass distribution is reconstructed within and (adaptive) grid, using various lensing constraints. As such, free-forms methods are well suited for the detection of DM halos or filaments with irregular forms.

Parametric reconstructions are useful as they greatly decrease the dimensionality of the problem: each component is simplified to a finite series of simple parameters. As a result, this approach performs better when only a few constraints are available, and for extrapolations outside of the multiple-image area where no strong lensing constraints are found. On the contrary, free-form methods require a larger number of constraints to perform well and are therefore less efficient for extrapolation. In the next section we present LENSTOOL, the strong lensing software used to optimize the parametric mass models of this work and to compute source plane projections or individual galaxy magnification.

A more thorough comparison of various mass modelling methods is provided in Meneghetti et al. (2017) where different teams were given simulated observations of simulated galaxy clusters to try to reconstruct the original mass distribution. To understand better the possible biases in mass modelling, the existing degeneracies and how to break them we refer the reader to the work of Priewe et al. (2017).

3.1.2 Parametric modelling with Lenstool

The mass models were constructed with LENSTOOL, using the parametric approach described in Kneib et al. (1996), Jullo et al. (2007) and Jullo & Kneib (2009). This parametric approach relies on the use of analytical dark-matter (DM) halo profiles to describe the projected 2D mass distribution of the cluster. Two main contributions are considered by LENSTOOL: one for each large-scale structure of the cluster, and one for each massive cluster galaxy. The parameters of the individual profiles are optimized through a Monte Carlo Markov Chain (MCMC) minimization. Lenstool aims at reducing the cumulative distance in the parameter space between the predicted position of multiple images obtained from the model, and the observed ones (see RMS introduced in previous section). In the following paragraph we describe the general method used to build parametric models with LENSTOOL.

Because of the large number of cluster members, the optimization of each individual galaxy-scale clump cannot be achieved in practice. Instead, a relation combining the constant mass-luminosity scaling relation described in Faber & Jackson (1976) and the fundamental plane of elliptical galaxies is used by LENSTOOL. This assumption allows us to reduce the dimensionality of the problem leading to more constrained mass models (and fastest convergence), On the opposite, individual parameterization of clumps would lead to extremely degenerate results and therefore poorly constrained mass model. The analytical profiles used are double pseudo-isothermal elliptical potentials (dPIEs) as described in Elíasdóttir et al. (2007). The ellipticity and position angle of each elliptical profiles are measured for the galaxy-scale clumps with SEXTRACTOR from high spatial resolution images of HST. Because the Brightest Cluster Galaxies (BCGs) lie at the center of clusters, they are subjected to numerous merging processes and are not expected to follow the same light-mass scaling relation. They are modeled separately in order to not bias the final result. In a similar way, the galaxies that are close to the multiple images or critical lines can sometimes be manually optimized because of the significant impact they have on the local magnification and the local geometry of the critical lines (the theoretical lines with infinite magnification in the image plane).

3.2 Observations

3.2.1 MUSE observations

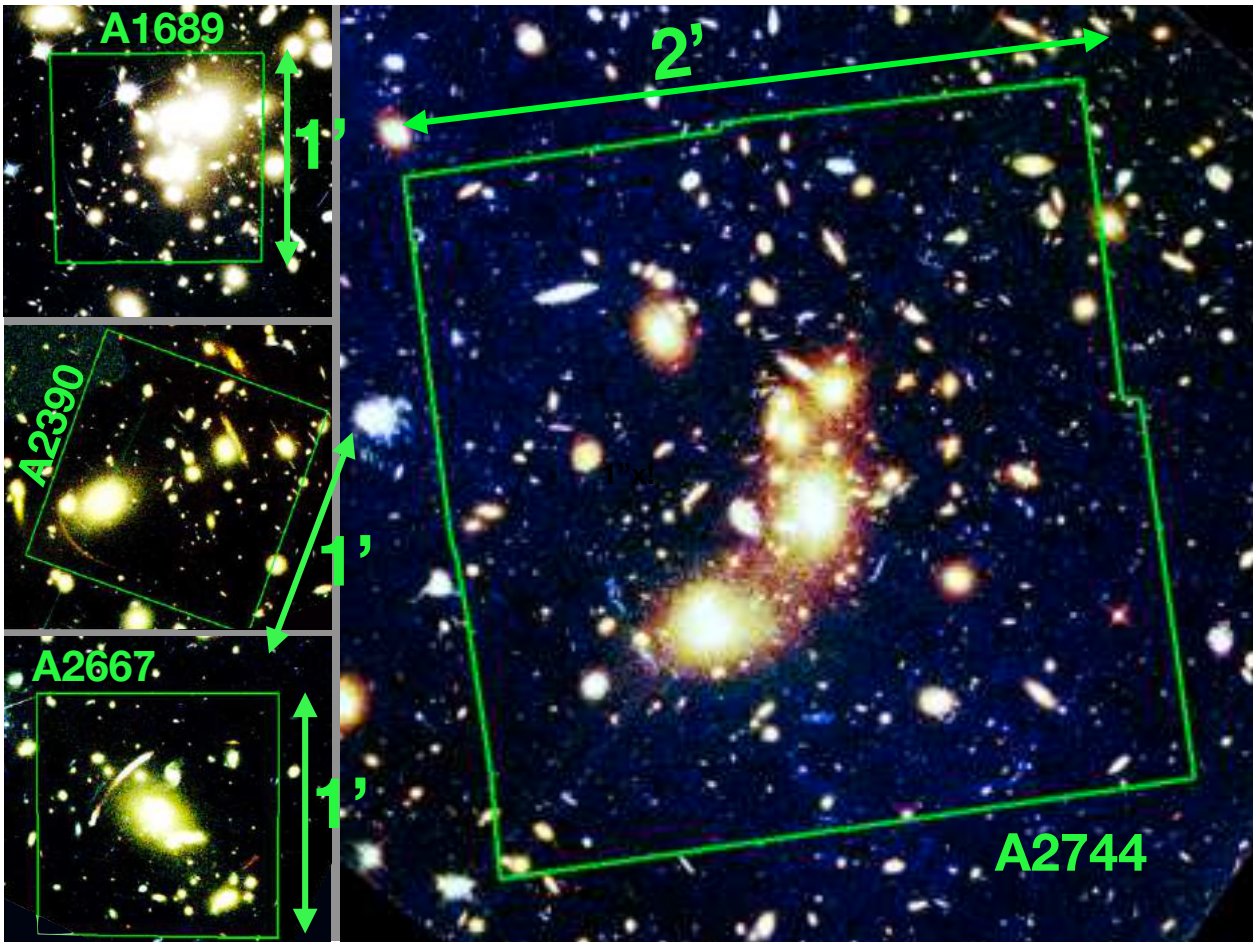

Figure 3.3: HST colour composite image overlaid with MUSE footprint. North is up and East is to the left.

The sample used in this study consists of four MUSE cubes of different sizes and exposure times, covering the central regions of well-characterized lensing clusters: Abell 1689,Abell 2390, Abell 2667 and Abell 2744 (resp. A1689, A2390, A2667 and A2744 hereafter). These four clusters already had well constrained mass models before the MUSE observations, as they benefited from previous spectroscopic observations. The reference mass models can be found in Richard et al. (2010) (LoCuSS) for A2390 and A2667, in Limousin et al. (2007) for A1689 and in Richard et al. (2014) for the Frontier Fields cluster A2744. These observations were obtained as part of the MUSE GTO program and commissioning run (for A1689). All the observations were conducted in the nominal WFM-NOAO mode of MUSE. The main characteristics of the four fields are listed in Table 3.1. The geometry and limits of the four FoVs are shown on the available HST images, in Fig. 3.3.

A1689: Observations were already presented in Bina et al. (2016) from the first MUSE commissioning run in 2014. The total exposure was divided into six individual exposures of 1100 s. A small linear dither pattern of 0.2″was applied between each exposure to minimize the impact of the

Table 3.1: Main characteristics of MUSE observations. The A2744 field was splitted in two (part a and part b) because of the additional pointing covering the center of the 2×2 MUSE mosaic. For A1689 and A2390, the seeing was measured on the white light image obtained from the final datacube. For A2667 and A2744, the seeing was obtained by fitting a MUSE reconstructed F814W image with a seeing convolved HST F814W image (see Patricio et al. (2018) for A2667 and Mahler et al. (2018) for A2744).

	FoV	Seeing	Integration(h)	RA (J2000)	Dec (J2000)	ESO Program
A1689	$1' \times 1'$	$0.9'' - 1.1''$	1.8	$197°52'39''$	$-1°20'42''$	60.A-9100(A)
A2390	$1' \times 1'$	$0.75''$	2	$328°23'53''$	$17°41'48''$	094.A-0115(B)
A2667	$1' \times 1'$	$0.62''$	2	$357°54'50''$	$-26°05'03''$	094.A-0115(A)
A2744 (a)	$2' \times 2'$	$0.58''$	16.5	$3°35'14''$	$-30°23'54''$	094.A-0115(B)
A2744 (b)	$1' \times 1'$	$0.58''$	2	$3°35'14''$	$-30°23'54''$	094.A-0115(B)

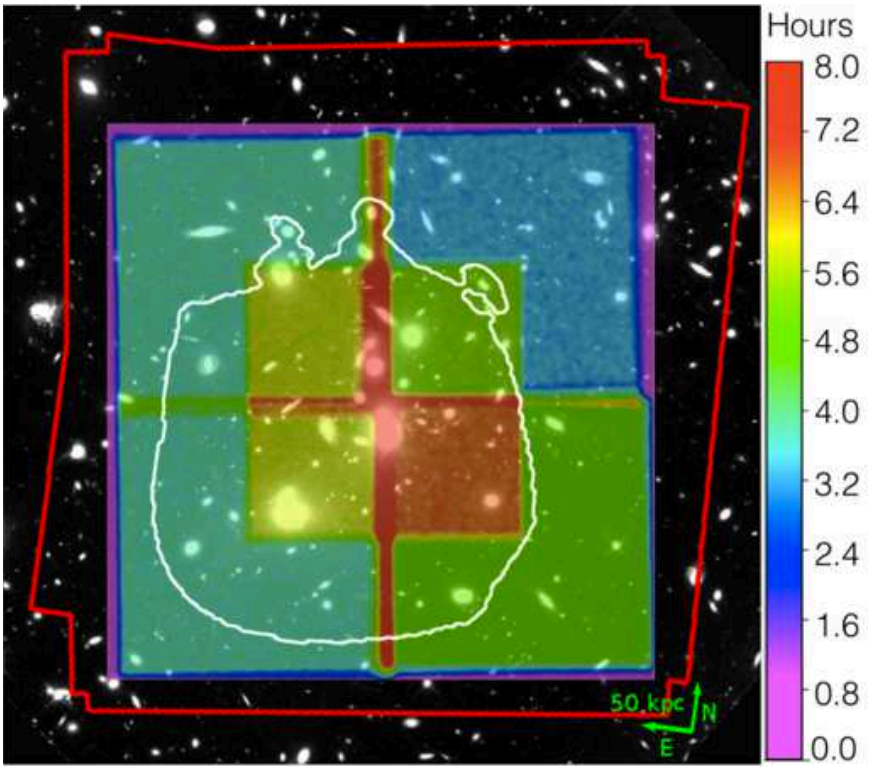

Figure 3.4: Exposure time of the MUSE mosaic of A2744 overlaid on HST F814w image. The region enclosed within white line is where multiple images are expected.
Figure taken from Mahler et al. (2018)

structure of the instrument (see example of slicer pattern in Fig. 2.4)on the final data. No rotation was applied between individual exposures

A2390, A2667 and A2744: The same observational strategy was used for all three cubes: the individual pointings were divided into exposures of 1800 sec. In addition to a small dither pattern of 1″, the position angle was incremented by 90°between each individual exposure to further minimize the striping patterns caused by the slicers of the instrument. A2744 is the only mosaic included in the present sample. The strategy was to completely cover the multiple-image area. For this cluster, the exposures of the four different FoVs are as follows : 3.5, 4, 4, 5 hours of exposure plus an additional 2 hours at the centre of the cluster (see Fig. 3.4). For A2390 and A2667, the centre of the FoV was positioned on the central region of the cluster as shown in Table 3.1 and Fig. 3.3.

All the MUSE data were reduced using the MUSE ESO reduction pipeline Weilbacher et al. (2012, 2014). This pipeline includes: bias subtraction, flat-fielding, wavelength and flux calibrations, basic sky subtraction, and astrometry. The individual exposures were then assembled to form a final data cube or a mosaic. An additional sky line subtraction was performed with the ZAP software (see Sect. 2.4 for more details on the sky-line subtraction and how this affects the data). Even though the line subtraction is improved by this process, the variance in the wavelength-layers affected by the presence of sky-lines remains higher, making the source detection of faint sources more unlikely on these layers.

3.2.2 Complementary HST observations

For all MUSE fields analysed in this paper, complementary deep data from HST are available. They were used to help the source detection process in the cubes but also for modelling the mass distribution of the clusters (see Sect. 3.1). A brief list of the ancillary HST data used for this project is presented in Table 3.2. For A1689 the data are presented in Broadhurst et al. (2005). For A2390 and A2667, a very thorough summary of all the HST observations available are presented in Richard et al. (2008) and more recently in Olmstead et al. (2014) for A2390. A2744 is part of the HFF for which the details of the observations are presented in Lotz et al. (2017). All the raw data and individual exposures are available from the Mikulski Archive for Space Telescopes (MAST), and the details of the reduction are addressed in the articles cited above.

3.2.3 Source detection

As established in Sect. 2.3.1, MUSE is most efficient to detect line emitters whereas deep photometry is well suited for detection of weak continua. To build a complete catalog of the sources in a MUSE cube, we combined a continuum-guided detection strategy based on deep HST images (see Table 3.2 for the available photometric data) with a blind detection in the MUSE cubes. Many of the sources end up being detected by both approaches and the catalogs are merged at the end of the process to make a single master catalog. The detailed method used for the extraction of sources in A1689 and A2744 can be found in Bina et al. (2016) and Mahler et al. (2018) respectively. The general method used for A2744 (which contains the vast majority of sources in the present sample) is summarized below and follows the general guidelines presented in Sect. 2.5.

The presence of diffuse Intra-Cluster Light (ICL) makes the detection of faint sources difficult in the cluster core, in particular for multiple-images located in this area. A running median filter computed in a window of 1.3″was applied to the HST images to remove most of the ICL. The ICL-subtracted images were then weighted by their inverse variance map and combined to make

Table 3.2: Ancillary HST observations. From left to right: HST instrument used, filter, exposure time, Programme ID (PID) observation epoch and reference(s).

–	Instrument	Filter	Exp(ks)	PID	Date	Refs.
A1689	ACS	F475W	9.5	9289	2002	Broadhurst et al. (2005)
	ACS	F625W	9.5	9289	2002	
	ACS	F775W	11.8	9289	2002	
	ACS	F850LP	16.6	9289	2002	
A2390	WFPC2	F555W	8.4	5352	1994	Richard et al. (2008)
	WFPC2	F814W	10.5	5352	1994	Olmstead et al. (2014)
	ACS	F850LP	6.4	1054	2006	
A2667	WFPC2	F450W	12	8882	2001	Richard et al. (2008)
	WFPC2	F606W	4	8882	2001	Olmstead et al. (2014)
	WFPC2	F814W	4	8882	2001	
	NICMOS	F110W	18.56	10504	2006	
	NICMOS	F160W	13.43	10504	2006	
A2744	ACS	F435W	45	13495	2013-14	Lotz et al. (2017)
	ACS	F606W	25	13495	2013-14	
	ACS	F814W	105	13495	2013-14	
	WFC3	F105W	60	13495	2013-14	
	WFC3	F125W	30	13495	2013-14	
	WFC3	F140W	25	13495	2013-14	
	WFC3	F160W	60	13495	2013-14	

a single deep image. The final photometric detection was performed by SExtractor (Bertin & Arnouts, 1996) on the weighted and combined deep images.

For the blind detection on the MUSE cubes, the Muselet software was used (MUSE Line Emission Tracker [1]). This tool is based on SExtractor to detect emission-line objects from MUSE cubes and its precise operation is detailed in Sect. 4.2. It produces NB images for each layer of the cubes and a SExtractor detection is run on each of them. At the end of the process, sources with several detections across the layers of the cube are merged together to form a single master catalog.

Following the master catalog, all spectra were extracted for redshift measurement. For A1689, A2390 and A2667, the 1D spectra were extracted using a fixed 1.5″aperture. For A2744 the extraction area is based on the SExtractor segmentation maps obtained from the deblended photometric detections described above. At this stage, the extracted spectra are only used for the redshift determination. The precise measurement of the total line fluxes requires a specific procedure, described later in Sect. 5.1. Extracted spectra were manually inspected to identify the different emission lines and accurately measure the redshift.

A system of confidence levels was adopted to reflect the uncertainty in the measured redshifts, following Mahler et al. (2018). The reader can find in this paper some examples that illustrate the different cases. All the LAEs used in this thesis belong to the confidence category 2 and 3, meaning that they all have fairly robust redshift measurement. For LAEs with a single line and no continuum detected, the wide wavelength coverage of MUSE, the absence of any other line and the asymmetry of the line were used to validate the identification of the Lyα emission. For A1689, A2390 and A2667 most of the background galaxies are part of multiple-image systems, and are

[1]Publicly available as part of the python package MPDAF (Piqueras et al., 2017).

therefore confirmed high redshift galaxies based on lensing considerations.

In total 247 LAEs were identified in the four fields: 17 in A1689, 18 in A2390, 15 in A2667 and 197 in A2744. The important difference between the number of sources found in the different fields results from a well-understood combination of field size, magnification regime and exposure time, as explained in Sect. 3.3.3. The complete catalog of source of A2744 can be found in Mahler et al. (2018) and an online version is available[2].

At this stage of the analysis, it is not possible to fully describe the final LAE sample used for computing the LAE LF as the magnification of each of these LAEs is unknown and the LAE multiply imaged by the cluster are not identified yet. Both these aspects require the use of an accurate mass model to estimate their intrinsic properties. The characteristics of the final sample used for the LF are presented in Sect. 6.1 where it is also compared to the sample of the MUSE HUDF (deepest MUSE blank field to date).

3.3 Correcting for lensing

3.3.1 Description of the models used

The present MUSE survey has allowed us to improve the reference models available in previous works. Table 3.3 summarizes their main characteristics. For A1689, the model used is an improvement made on the model of Limousin et al. (2007), previously presented in Bina et al. (2016). For A2390, the reference model is presented in Pello et al. (1991), Richard et al. (2010). For A2667, the original model was obtained by Covone et al. (2006), and was updated in Richard et al. (2010). For A2744, the gold model presented in Mahler et al. (2018) is used, including as novelty the presence of NorthGal and SouthGal, two background galaxies included in the mass model as they could have a local influence on the position and magnification of multiple images.

3.3.2 Image plane

Now that the mass models have been improved thanks to the new MUSE multiple systems and spectroscopic redshifts, the mass models can be used to "unlens" the Universe. One of the first values of interest for this work is the magnification (or amplification) noted μ. This magnification can be empirically defined as the ratio between the observed flux and the intrinsic flux of a given source. But the original definition is the ratio between the image surface and source surface, as gravitational lensing conserves the surface brightness (see Schneider et al., 1992).

With Lenstool and a mass model, it is possible to compute predicted magnification maps in the image plane, at a given redshift. Examples of such magnification maps at $z = 3.5$ for each cluster of our sample are provided in Fig. 3.5. The theoretical lines with infinite magnification in the image plane, called critical lines, can be seen in this figure. Two main components can be seen: the large scales high magnification lines which are surrounding the DM halos, and the smaller scale lines surrounding the cluster galaxies. This shows the importance of properly modelling the individual galaxies in a cluster as they have an important impact on the local magnification. It also becomes visible from this figure that the gradient of the magnification field becomes much higher around the high magnification regions. This is the reason why highly magnified galaxies have a much higher uncertainty attached to their magnification: a small displacement of the critical lines can have a huge impact on their measured magnification.

This type of maps can be used to measure central magnification by simply taking the magnification value at a given sky coordinate, or to compute more complex estimates such as the flux

[2] http://muse-vlt.eu/science/a2744/

Cluster	Clump	$\Delta\alpha(''$)	$\Delta\delta(''$)	e	θ	$r_{\rm core}$(kpc)	$r_{\rm cut}$(kpc)	σ_0(km s^{-1})	Ref
A1689	DM1	$0.6^{+0.2}_{-0.2}$	$-8.9^{+0.4}_{-0.4}$	$0.22^{+0.01}_{-0.01}$	$91.8^{+1.4}_{-0.8}$	$100.5^{+4.6}_{-4.0}$	[1515.7]	$1437.3^{+20.0}_{-11.1}$	(1)
rms = 2.87″	DM2	$-70.0^{+1.4}_{-1.5}$	$47.9^{+2.3}_{-4.1}$	$0.80^{+0.04}_{-0.05}$	$80.5^{+2.7}_{-2.5}$	$70.0^{+8.0}_{-5.3}$	[500.9]	$643.2^{+0.5}_{-4.5}$	
$n_{\rm const}$ = 128	BCG	$-1.3^{+0.2}_{-0.3}$	$0.1^{+0.4}_{-0.5}$	$0.50^{+0.03}_{-0.05}$	$61.6^{+9.6}_{-4.0}$	$6.3^{+1.2}_{-1.2}$	$132.2^{+42.0}_{-31.5}$	$451.6^{+11.6}_{-12.1}$	
$n_{\rm free}$ = 33	Gal1	[49.1]	[31.5]	$0.60^{+0.07}_{-0.16}$	$119.3^{+6.2}_{-10.0}$	$26.6^{+3.4}_{-4.1}$	$179.6^{+2.5}_{-27.8}$	$272.8^{+4.5}_{-21.5}$	
	Gal2	$45.1^{+0.2}_{-0.9}$	$32.1^{+0.6}_{-1.1}$	$0.79^{+0.05}_{-0.03}$	$42.6^{+2.3}_{-1.9}$	$18.1^{+0.3}_{-3.4}$	$184.8^{+1.2}_{-11.1}$	$432.7^{+16.6}_{-33.4}$	
	L^* Gal					[0.15]	$18.1^{+0.7}_{-2.2}$	$151.9^{+7.0}_{-0.3}$	
A2390	DM1	$31.6^{+1.8}_{-1.3}$	$15.4^{+0.4}_{-1.0}$	$0.66^{+0.03}_{-0.02}$	$214.7^{+0.5}_{-0.3}$	$261.5^{+8.5}_{-5.2}$	[2000.0]	$1381.9^{+23.0}_{-17.6}$	(2)
rms = 0.33″	DM2	[-0.9]	[-1.3]	$0.35^{+0.05}_{-0.03}$	$33.3^{+1.2}_{-1.6}$	$25.0^{+1.8}_{-1.1}$	$750.4^{+100.2}_{-65.5}$	$585.1^{+20.0}_{-9.7}$	(3)
$n_{\rm const}$ = 45	BCG1	[46.8]	[12.8]	$0.11^{+0.10}_{-0.01}$	$114.8^{+26.8}_{-31.5}$	[0.05]	$23.1^{+3.0}_{-1.6}$	$151.9^{+5.9}_{-7.5}$	(4)
$n_{\rm free}$ = 18	L^* Gal					[0.15]	[45.0]	$185.7^{+5.3}_{-3.3}$	
A2667	DM1	$0.2^{+0.5}_{-0.4}$	$1.3^{+0.5}_{-0.4}$	$0.46^{+0.02}_{-0.02}$	$-44.4^{+0.2}_{-0.3}$	$79.33^{+1.1}_{-1.1}$	[1298.7]	$1095.0^{+5.0}_{-3.7}$	(5)
rms = 0.47″	L^* Gal					[0.15]	[45.0]	$91.3^{+4.5}_{-4.5}$	(3)
$n_{\rm const}$ = 47									
$n_{\rm free}$ = 9									
A2744	DM1	$-2.1^{+0.3}_{-0.3}$	$1.4^{+0.0}_{-0.4}$	$0.83^{+0.01}_{-0.02}$	$90.5^{+1.0}_{-1.1}$	$85.4^{+5.4}_{-4.5}$	[1000.0]	$607.1^{+7.6}_{-0.2}$	(6)
rms = 0.67″	DM2	$-17.1^{+0.2}_{-0.3}$	$-15.7^{+0.4}_{-0.3}$	$0.51^{+0.02}_{-0.02}$	$45.2^{+1.3}_{-0.8}$	$48.3^{+5.1}_{-2.2}$	[1000.0]	$742.8^{+20.1}_{-14.2}$	
$n_{\rm const}$ = 134	BCG1	[0.0]	[0.0]	[0.21]	[-76.0]	[0.3]	[28.5]	$355.2^{+11.3}_{-10.2}$	
$n_{\rm const}$ = 30	BCG2	[-17.9]	[-20.0]	[0.38]	[14.8]	[0.3]	[29.5]	$321.7^{+15.3}_{-7.3}$	
	NGal	[-3.6]	[24.7]	[0.72]	[-33.0]	[0.1]	[13.2]	$175.6^{+8.7}_{-13.8}$	
	SGal	[-12.7]	[-0.8]	[0.30]	[-46.6]	[0.1]	$6.8^{+93.3}_{-3.2}$	$10.6^{+43.2}_{-3.6}$	
	L^* Gal					[0.15]	$13.7^{+1.0}_{-0.6}$	$155.5^{+4.2}_{-5.9}$	

Table 3.3: Sumary of the main mass components for the lensing models used for this work. The values of RMS indicated are computed from the position of multiply imaged galaxies in the image plane. $n_{\rm const}$ and $n_{\rm free}$ correspond respectively to the number of constraints passed to LENSTOOL and the number of free parameters to be optimized. The coordinates $\Delta\alpha$ and $\Delta\delta$ are in arcsec with respect to the following reference points: **A1689:** $\alpha = 197°52'23''$, $\delta = -1°20'28''$, **A2390:** $\alpha = 328°24'12''$, $\delta = 17°41'45''$,**A2667:** $\alpha = 357°54'51''$, $\delta = -26°05'03''$ **A2744:** $\alpha = 3°35'11''$, $\delta = -30°24'01''$. The ellipticity e, is defined as $(a^2 - b^2)/(a^2 + b^2)$ where a and b are the semi-major and the semi-minor axes of the ellipse. The position angle θ, provides the orientation of the semi-major axis of the ellipse measured counterclockwise with respect to the horizontal axis. Finally, $r_{\rm core}$, $r_{\rm cut}$ and σ_0 are respectively the core radii, the cut radii and the central velocity dispersion. References are as follows: (1) Limousin et al. (2007), (2) Pello et al. (1991), (3) Richard et al. (2010), (4) Pello et al. (in prep.), (5) Covone et al. (2006) and (6) the gold model from Mahler et al. (2018).

weighted magnifications presented in Sect. 5.1.

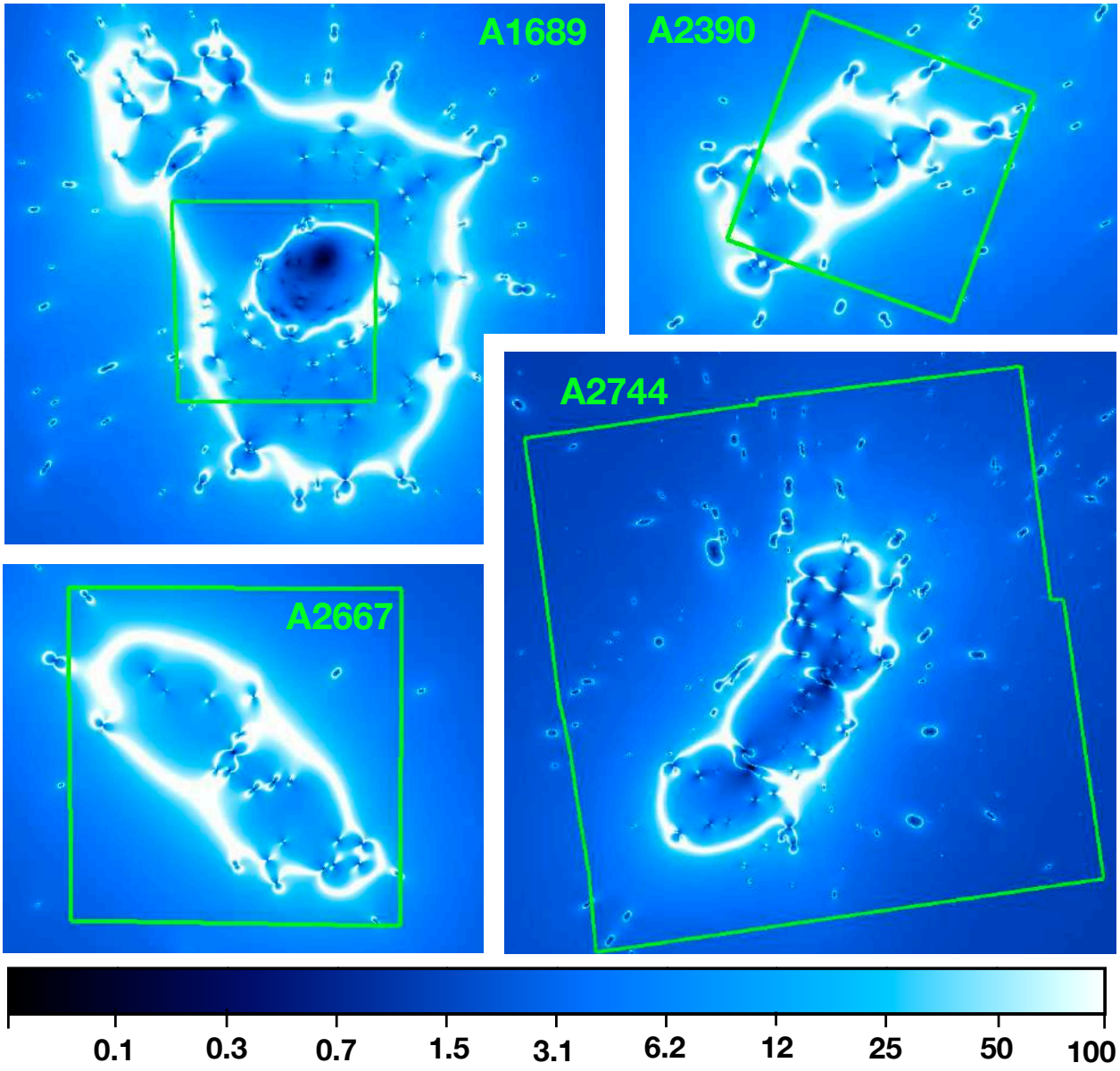

Figure 3.5: Magnification maps computed by LENSTOOL at $z = 3.5$ with the MUSE footprint in green. The spatial scale varies from one panel to the other. One MUSE FoV is $\sim 1'$ wide and the A2744 field is a 2×2 MUSE mosaic.

3.3.3 Source plane projection

As already mentioned in the introduction of this thesis, one of the major downside of using lensing is the reduction of the explored volume of Universe. One simple way to explain this is that the volume enclosed within each pixel (in the image plane) is inversely proportional to the average magnification within this pixel. Therefore, as we get closer to the high magnification regions, the density of volume (volume per angular area) decreases. This effect is illustrated in Fig. 3.6 showing source plane reconstruction of the four MUSE FoVs at $z = 3.5$ combined with magnification maps. For pixels multiply imaged, only the highest magnification is shown. On the left side of the figure

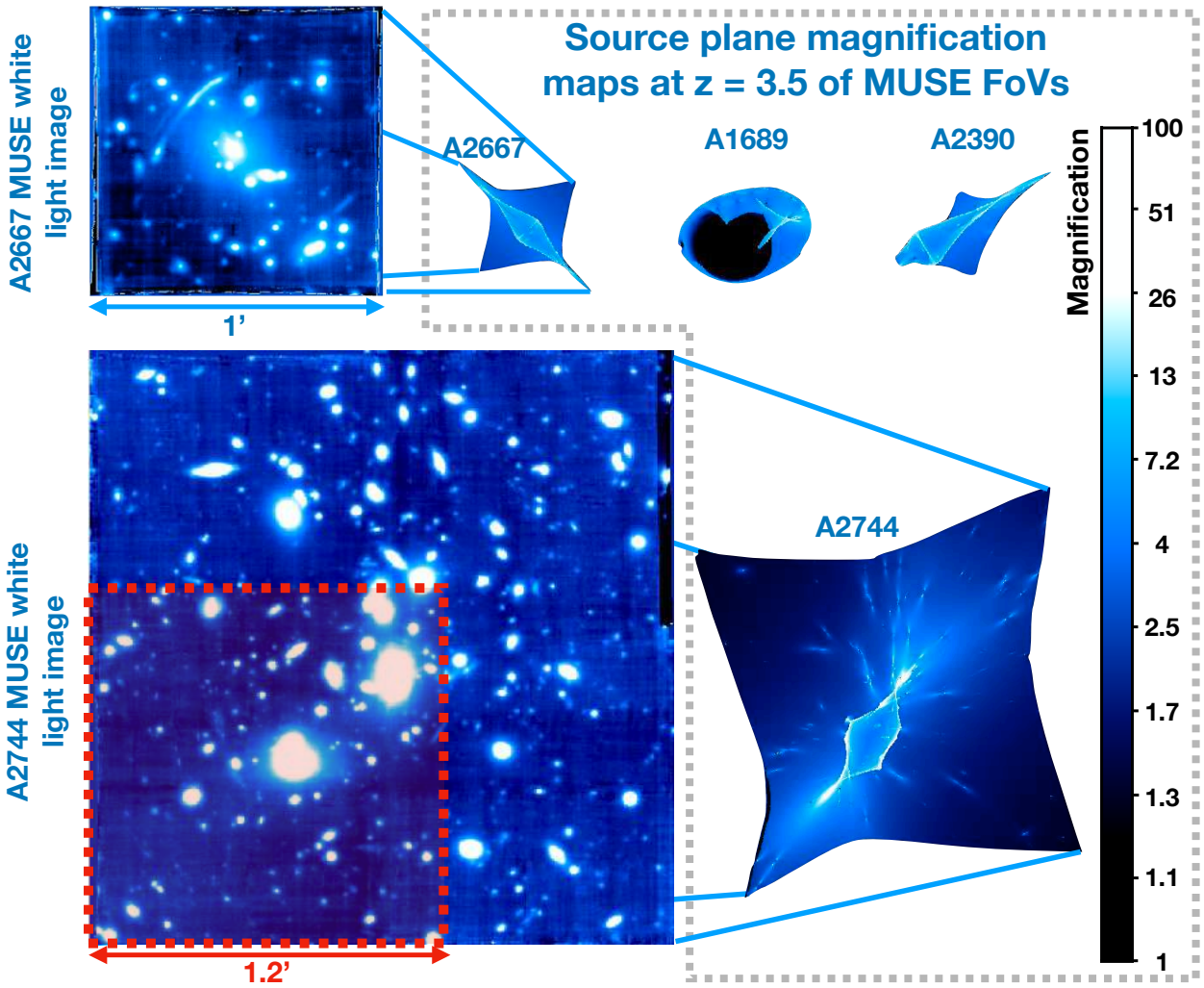

Figure 3.6: MUSE white light images of A2667 and A2744 on the left, and source plane projection of all 4 MUSE FoVs combined with magnification maps on the right. All images are shown using the same angular scale.

are also shown white light images of the A2667 and A2744 MUSE cubes to compare the area seen on the sky to the effective area probed. The same angular scale is used for all images of this figure. For A1689, A2390 and A2667, the MUSE observations are centered on the core of the clusters where the magnification is maximal (see Fig. 3.5), and therefore the decrease of volume is huge and about the same order of magnitude for these three clusters. For A2744, being a 2×2 MUSE mosaic, the observed area is able to reach a lower magnification regime where the dilution effect is less. For this reason, the large majority of the detected LAEs are seen in the A2744 mosaic (see LAE detected count in 3.2.3)

When combinning the effective area probed in the four clusters, we get an effective FoV of $1.2'' \times 1.2''$, which is represented as a red square on top of the A2744 white light image. Since these observations are composed of 7 MUSE pointings (3 for A1689, A2390, A2667 and 4 for A2744), this effective area is to be compared to the $\sim 7'' \times 1''$ surveyed area.

One of the main interests of these source plane reconstructions, is that it allows to have more precise estimate of the effective area or volume. While such computation can still be done in the image plane by taking into account the magnification of each pixel, doing so does not allow to

account for the areas of the survey that are multiply imaged. On the contrary, when working in the source plane such biases are not present, and the computation of the effective area is as simple as counting pixels on these source plane reconstructions. In addition given how much the FoVs of the three clusters A1689, A2390 and A2667 fold over themselves (see Fig. 3.6) it becomes clear that this effect would be the predominant source of error if computing their effective area or volume in the image plane.

4 | Luminosity Function of LAEs: Computing effective volumes from MUSE data cubes

Contents

4.1 Motivations

Because of the combined use of lensing clusters and spectroscopic data cubes, it is extremely challenging to adopt a parametric approach to determine a selection function. By construction, the sample of LAEs used in this paper includes sources coming from very different detection conditions, from intrinsically bright emitters with moderate magnification to highly magnified galaxies that could not have been detected far from the highly magnified areas of the survey. To properly take into account these differences when computing the LF, we adopt a non-parametric approach allowing us to treat the sources individually: the $V_{\rm max}$ method (Schmidt, 1968; Felten, 1976).

This chapter is dedicated to the computation of $V_{\rm max}$. By definition, $V_{\rm max}$ is the volume of the survey where an individual source could have been detected. By taking the inverse, $1/V_{\rm max}$, we get the contribution of one source to a numerical density of galaxies. This $V_{\rm max}$ is the core of the method used to build the LAE LF in Chapter 5, and is therefore of primordial importance for a proper computation of the LF.

The $V_{\rm max}$ computation has usually been answered through the computation of a parametric selection function. The selection function, $f_s(L, z)$, is the probability of finding a source at a given redshift and luminosity in the survey. By integration of this selection function, we can get the $V_{\rm max}$ values associated to a certain luminosity and redshift:

$$V_{\rm max}(L, z) = \omega \int_{z_{\rm min}}^{z_{\rm max}} f_s(L, z) \frac{dV}{dz} dz \tag{4.1}$$

where $z_{\rm min}$ and $z_{\rm max}$ are the redshift selection limits of the survey and ω is the angular area of the survey and $\frac{dV}{dz}$ is the density of volume of Universe explored by redshift interval and steradian. This technique, or some variations of it, was commonly used to compute volumes in NB surveys for either UV selected galaxies (see e.g. Ouchi et al., 2004; Stark et al., 2009) or LAE selected galaxies (see e.g. Dawson et al., 2007; Cassata et al., 2011).

To compute the selection function, the most common method is to perform Monte Carlo (MC) source recovery simulations, injecting fake (and often point-like) sources at a random position in the survey, and for different luminosities and redshifts. The fraction of source successfully recovered at a given redshift and luminosity directly gives the value of the selection function $f_s(L, z)$.

This type of approach can also be used for computing the selection function of LAEs in spectroscopic cubes. One of the first attempt was made in Adams et al. (2011), again using point like sources and the resulting LAE LF was published in Blanc et al. (2011). More recently with MUSE, the same approach was used in Drake et al. (2017a) and in Herenz et al. (2019). In these two blank fields studies the mock sources are modelled as a single emission line, as the detection – or not – of a continuum is completely independent of the detection of an emission line in the procedure used in these studies. While the usual MC approach used for UV images can still be used, it becomes more complex and more computationally expensive because of the larger and continuous redshift range to explore.

In Drake et al. (2017a), the selection function is computed for the LAEs of the MUSE HUDF (Bacon et al., 2017). In an effort to account for the extended nature of the LAEs, the mock LAE sources are modelled with two components: a point like component which is representative of the UV continuum and an exponentially declining profile representative of the extended emission. The mock LAEs are assigned a luminosity value, a redshift, and a halo length scale, and are injected at a random spatial position in the survey. This operation is repeated many times until the selection function is properly sampled in both luminosity and redshift.

In Herenz et al. (2019), the selection is computed for the LAEs of the MUSE-Wide survey (Herenz et al., 2017), using 10 real LAEs from the MUSE HUDF with a range of surface brightness

profiles. These real LAEs are scaled to different luminosity values and inserted at five wavelength positions that are representative of the different level of noise in the MUSE cubes. This simplification is necessary as at the time of this work, the MUSE-Wide survey already consisted of 24 cubes out of more than a hundred when the program is finalized. For such a large data set, simulations on the entire cubes as in (Drake et al., 2017a) are not realistic. The results of these five source recovery experiment are then adapted to account for the variation of noise along the spectral axis, to obtain a selection function for the full redshift range.

One of the conclusions also developed in Herenz et al. (2019) is that the use of point like sources is not an acceptable solution to compute the selection function, especially for LAEs which are known to have extended emissions (see e.g. Wisotzki et al., 2016; Leclercq et al., 2017). Using them in source recovery simulations leads to a serious over-estimation of the selection function and therefore an over-estimation of $V_{\max}$, especially at lower luminosities.

The two examples detailed above show that the task of computing the selection function is complex and easily becomes computationally expensive: precise simulations with a fine resolution in both redshift and luminosity do not scale well with an increasing number of data cubes.

Working with lensing clusters adds an extra level difficulty. The images of the sources found in the background of lensing clusters are magnified and frequently distorted. In that case, properly accounting for extended spatial profiles is even more necessary than for blank fields. In addition, parts of the field are multiply imaged (see how the image plane folds over itself in the source plane reconstruction shown in Fig. 3.6), and the magnification introduces a variable depth meaning that the faintest sources can only be detected in highly magnified areas. These two additional effects have to be accounted for an accurate $V_{\max}$ computation and make the computation of a parameterized selection function very tricky. We summarized below, the main difficulties one would have to face to compute a parametric selection function of sources detected behind lensing clusters in MUSE cubes:

- The same difficulties as for MUSE blank fields surveys: a large volume of data, a lengthy detection process and properly accounting for the extended halos of LAEs.
- The necessity to work in the source plane to avoid counting several times areas of the survey that are multiply imaged. Going back and forth between the source and image plane is technically possible but computationally expensive.
- An additional parameter to account for in the simulations: the magnification induced by the cluster. Random luminosities and redshift can be assigned to mock sources, which can then be injected in the sources plane. By making these mock catalog of sources go through the lens, we can compute their magnification and their (multiple) position in the image plane. The source recovery can then begin on these mock galaxies in the image plane. The difficulty of such an exercise is that it requires constant and numerous back and fort between the source and image plane to compute $f_s(L, z, \mu)$ (or $f_s(F(\mu), z)$).
- The use of the selection function would not be efficient to account for the multiply images areas of the survey, as the source recovery experiment are conducted on the image plane. This shows that the very concept of selection function becomes blurry in strong lensing fields.
- The need to combine constant back and forth between image and source plane with simulations done on thousands of MUSE slices when performing simulations on full MUSE cubes (and this is already challenging in blank fields).

For all these reasons, it was decided to use a different approach that allows the computation of $V_{\max}$ on a source to source basis. This approach relies on mocking the detection process of individual LAEs, to create one 3D detectability map (or mask) of the survey in the image plane for each LAE. These survey masks are then projected in the source plane where the volume integration

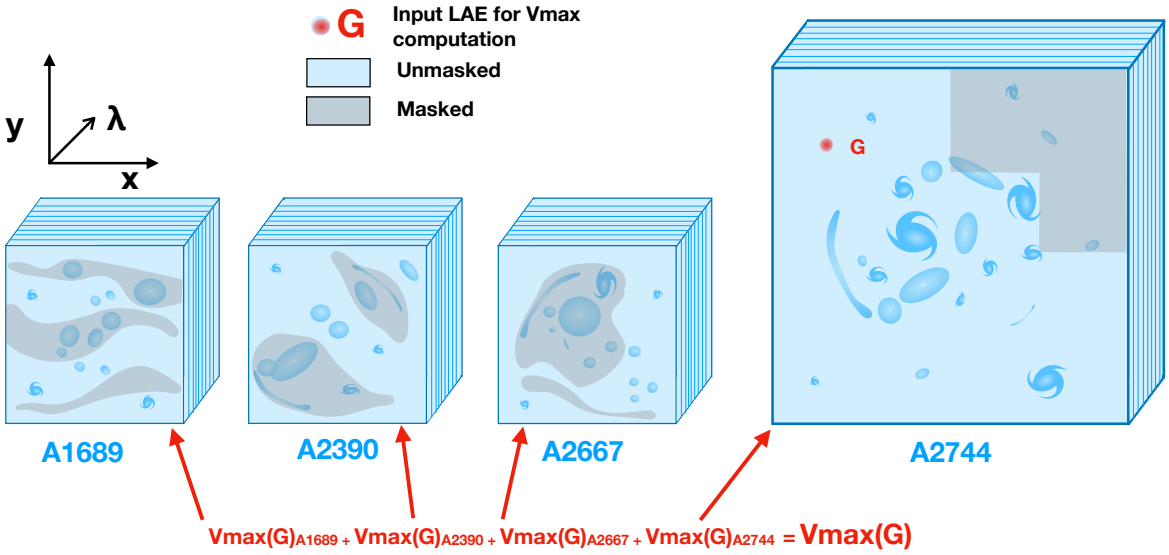

Figure 4.1: Simple schematic of the strategy adopted to compute $V_{\rm max}$ for individual LAE. All clusters part of the survey must be accounted for. Because of the strong spectral and spatial variations of noise in the cubes, the morphologies of the 2D masks (grey areas on the figure) used to mask layers of the cubes may change drastically from one layer to the next. The final $V_{\rm max}$ computation requires the projection of these 3D image plane masks in the source plane.

is done on the unmasked pixels. These individual masks are computed for each LAE, through a comparison of the source to the local noise level, for all spectral and spatial positions in the cubes. A simple representation of the strategy adopted is shown in Fig. 4.1.

To implement and understand this method, it is essential to understand how the detection process works and what affects the detectability of individual sources. This aspect is detailed in Sect. 4.2. Because in this work, the detection process of MUSE LAEs is based on 2D Narrow-Band images, Sect. 4.3 presents the first step of the $V_{\rm max}$ computation method: evaluating the detectability of individual source from a single image accounting for its spatial profile. In Sect. 4.4 we show how the main difficulties of building 3D survey masks can be circumvented and explain in details the final method adopted. Finally, in Sect. 4.5 the results of the $V_{\rm max}$ computation are presented and the different steps of the method are discussed.

4.2 Source detection in MUSE cubes with Muselet

All the LAEs detected in the lensing sample presented in Chapter. 3, were detected using the Muselet detection software. This tool is based on SExtractor (Bertin & Arnouts, 1996) detections and is part of the MPDAF python package [1](Piqueras et al., 2017), developed to help analyzing the MUSE specific data. Muselet allows blind detections (i.e., without any photometric prior) of emission line objects in MUSE cubes by performing a series of 2D detections on continuum subtracted NB images constructed from each layer of the data cube. These NB images are the weighted average of 5 wavelength planes, corresponding to a spectral width of 1.25Å. The

[1]The MPDAF package documentation can be found here `https://mpdaf.readthedocs.io/en/latest/index.html`

entire set of NB-images form a NB cube, in which only the emission-line objects remain. SExtractor is then applied to each of the NB images, reducing the detection process to a series of consecutive 2D detections along the wavelength axis. In parallel Muselet also performs the same detection process on 3 broad band continuum images to identify the sources linked to a continuum. At the end of the process, the individual detections catalogs are merged together, and sources with several detected emission lines are assembled as one single source. Muselet returns separately the sources with a continuum detection and the emission-line only objects.

For the complete SExtractor detection process, we refer the reader the reader to the SExtractor manual [2] and will only provide a very short description. To detect sources, SExtractor produces two images: the background RMS image (shortened to only RMS image hereafter), and a background subtracted and convolved image, called the filtered image. The RMS image provides an estimation of the local level of noise for each pixel of the original image. Each pixel of the filtered image is then compared to this RMS image to determine whether a group of pixels is sufficiently above the local noise level to be considered as a detection.

For this process, SExtractor uses 2 parameters: `MIN_AREA` and `DETECTION-THRESH` which respectively refer to a minimum number of connected pixels and to a detection threshold in relative units with respect to the RMS image. All pixels values of the filtered image are compared to the corresponding pixel of the RMS image, and if the value is above the detection threshold, it is treated as a potential detection. For the detection to be confirmed, there must be at least `MIN_AREA` connected pixels above the threshold. When speaking of MUSE detections, because the sources are detected on the NB images, the RMS images refer to the RMS images computed by SExtractor, from the Muselet NB images. We also refer to these images as RMS cube as one RMS image can be produced for each layer of the NB cube. An example of the different images used during the detection process and that are computed from the original layer of a MUSE data cube is provided in Fig. 4.2.

Since the volume computation aims at reproducing the detection process, it is also important to understand what can affect the detectability of individual sources:

- The flux of the source. For a given spatial profile and noise level, the higher the flux the higher the source will rise above the local noise.
- The spatial profile of the source or surface brightness. At a given flux and noise level, a spatially compact source has a higher signal-to-noise and is more likely to be detected than a very diffuse source.
- The spectral profile of the source. Assuming constant flux and noise level, a wider spectral profile results in less flux on individual layers of the cube, reducing the signal-to-noise and making the detection harder.
- The seeing conditions. The seeing tends to blur the observations and therefore directly affects the observed spatial profile of the sources. This point is important when simulating the detectability of a source in a cube with a different seeing. A source clearly detected in a cube with good seeing would be harder to catch in a bad seeing cube.
- The noise level. It is affected by mainly three components: the integration time, the patterns caused by the imperfections of the instrument and the presence of bright sources (see Sect. 2.4 for a description of the noise structure in MUSE cubes). A longer exposure reduces the average noise level on a large spatial scale, making the detection of faint sources easier. The effect of exposure time can easily be seen on MUSE mosaics where the average noise level follows the geometry of the different pointings. The presence of bright sources locally increases the noise because of a higher number count on the detectors following the Poisson shot noise. The defaults and structure of the instrument mostly affect the level of noise on

[2] The SExtractor manual can be found here: `https://www.astromatic.net/software/sextractor`

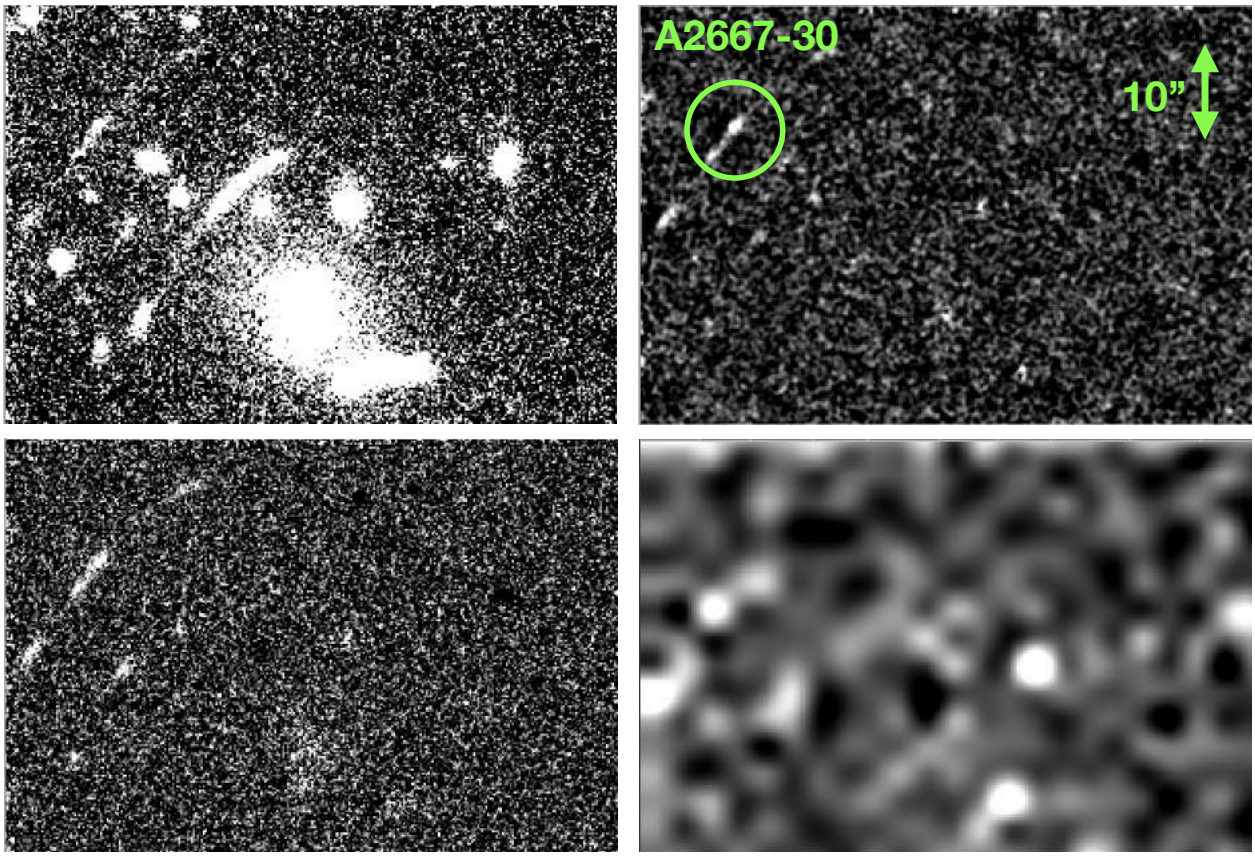

Figure 4.2: Example of the different images that are used during the detection process. In this figure we are focusing on the Lyα emission of the source A2667-30 detected on layer 1041 of the MUSE cube. **Upper left panel:** layer 1041 of the MUSE data cube. **Lower left panel:** NB image produced by MUSELET and centered on layer 1041. **Upper right panel:** filtered image produced by SEXTRACTOR from the MUSELET NB image. The convolution kernel used here is the default 3x3 kernel used by SEXTRACTOR. **Lower right panel:** RMS image produced by SEXTRACTOR from the MUSELET NB image.

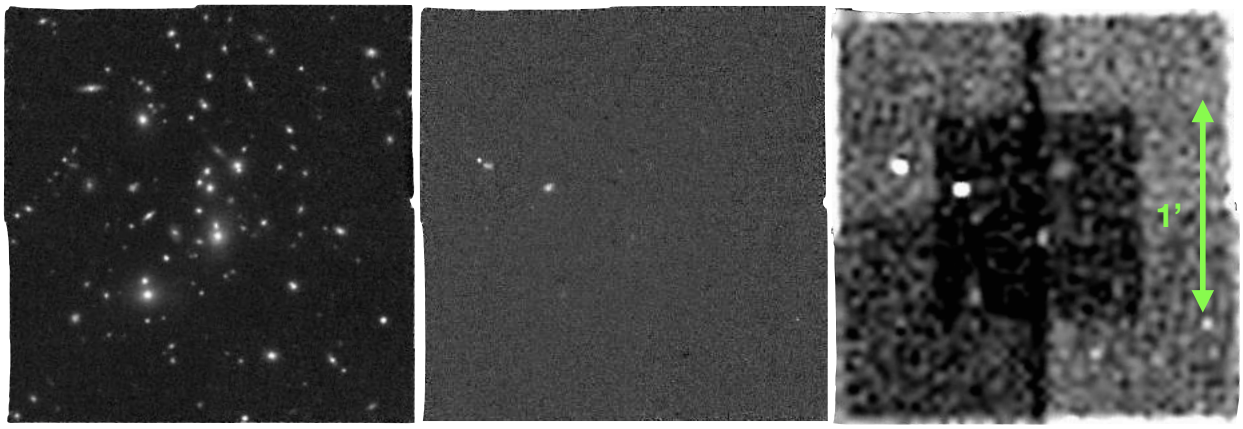

Figure 4.3: **Left panel:** Layer 2000 of the A2744 data cube. **Middle panel:** Layer 2000 of the A2744 NB cube produced by MUSELET. Only emission line object remains visible **Right panel:** RMS image produced from the middle panel by SEXTRACTOR. All images have the same spatial scale and are shown in logarithmic colorscale.

the smaller spatial scales (see Fig. 2.4). An example of these three phenomena is shown on Fig. 4.3 with different images of the A2744 field. On the left and middle panels, the different pointings cannot be identified, whereas the rightmost panel reproduces almost exactly the exposure maps shown in Fig. 3.4. This also shows that the highest value of the RMS image are reached at the position of bright emission line object. All the smaller scale variations of RMS values are either random or caused by the imperfections and slicers of the instrument.

- The redshift of the source. Because MUSE is an earth based instrument in the optical domain, it is affected by sky lines. The layers affected by these sky lines are a subjected to higher noise levels (see Sect. 2.4.2 for more details) and as a consequence, only the brightest sources can be seen in these layers. Regarding the LAEs selection, this means that we expect to find very few LAEs with a redshift that would place the Lyα emission on the same layers as these sky lines.
- In the case of lensing clusters, the magnification also has an impact: the faintest sources can only be detected in the highly magnified regions.

For a precise computation of the volume of detection in MUSE cubes, the method developed must account for all of the points described above in a realistic way. The first step toward this goal is to find a way to evaluate the detectability of sources on 2D images.

4.2.1 Definitions

In the following sections of this chapter, we will only be speaking about the Lyα emission in MUSE cubes for clarity, but most of it can be applied to any other emission line. All LAEs have been detected using `MIN_AREA = 6` and `DETECTION-THRESH = 1.3`. These parameter values are the default values for all computation/simulation done in this chapter. Below some of the technical terms used in this Chapter are listed.

- The term NB image refers to the NB images produced by MUSELET,
- The term detection image refers to the NB image on which the Lyα emission of the source was detected.
- The term filtered (or RMS) image refers to the filtered (or RMS) image produced by SEXTRACTOR from the MUSELET NB images. The RMS images, and filtered images are computed

using the `-CHECKIMAGE_TYPE` option provided by SExtractor. Because a RMS image can be produced for each NB image, they form a cube – referred to as the RMS cube – with the same indexing as the NB cube or the raw data cube. We do not construct a filtered cube, as the filtered images only need to be computed from the detection image of each LAE, to retrieve the spatial information (see Sect. 4.3.1).

- The term layer refers to a spectral layer of a MUSE cube and can be applied indifferently to the RMS cube, the NB cube or the raw data cube, as they all have the same indexing. The term parent cube refers to the cube in which a given source was actually detected and by opposition, the term external cube refers to a cube the source does not belong to. For example, for the source A2390-96, the native cube is A2390, and A1689, A2667 and A2744 are the external cubes.

4.3 Computing 2D detection masks

4.3.1 Presentation of the algorithm

In this section, we describe the generic method used to create a 2D detectability map from a input image and a given source. This generic method is not restricted to MUSE data and could be applied to any photometric data. Mocking the SExtractor detection process across the input image, we are able to produce binary masks: on masked pixels, the input source could not have been detected, whereas on the unmasked pixels, it could have. This result is achieved by comparing the local noise to the signal of the brightest pixels of the input source.

The inputs needed by this procedure are: an input image, the Bright Pixel profile (Bp) of the source and the values of `DETECT_THRESH` and `MIN_AREA` used for the original detection. The input image can be the detection image of the input source, but it is also possible to use any other image. For example, it is possible to compute the detectability of the input source on any layer of any MUSE cube. The profile Bp is simply the list of brightest-pixel values of the input source, ordered by decreasing intensity (see Fig. 4.12 for example of bright pixel profiles). This profile is determined from the filtered image as SExtractor uses this same image to do the pixel-to-pixel comparison with the RMS image. To recover the values of Bp, we look for the maximum value in a circle of radius $r = 1''$ around the position of the source. Once the first value is determined, we look for the highest value among the eight connected pixels and add that second value to Bp. We repeat the same process iteratively and look for the maximum value among the pixels connected to the pixel already included in the Bp list. The process stops when 9 values are recovered. This simple algorithm is efficient to follow the exact morphology of the source with no priors on its shape. This is especially important for heavily distorted or elongated sources. Figure 4.4 presents examples of bright pixels recovered from the filtered image. This profile is not a spatial profile, as two consecutive values in Bp could not be directly spatially connected. However, Bp nonetheless detain information about the spatial profile of the sources: compact sources have most of their flux concentrated in a few pixels and would have sharply decreasing Bp profiles. On the contrary extended sources have flatter Bp profiles.

The information enclosed in the Bp profile is then used to mock the SExtractor detection process through the entire detection image to produce a 2D mask. This is done using the following steps:

- For each pixel `[x,y]` of the RMS map, a list of 9 RMS pixels is created, the list contains the central RMS pixel as well as the 8 connected RMS pixel values. This list is called `local_noise[x,y]`.

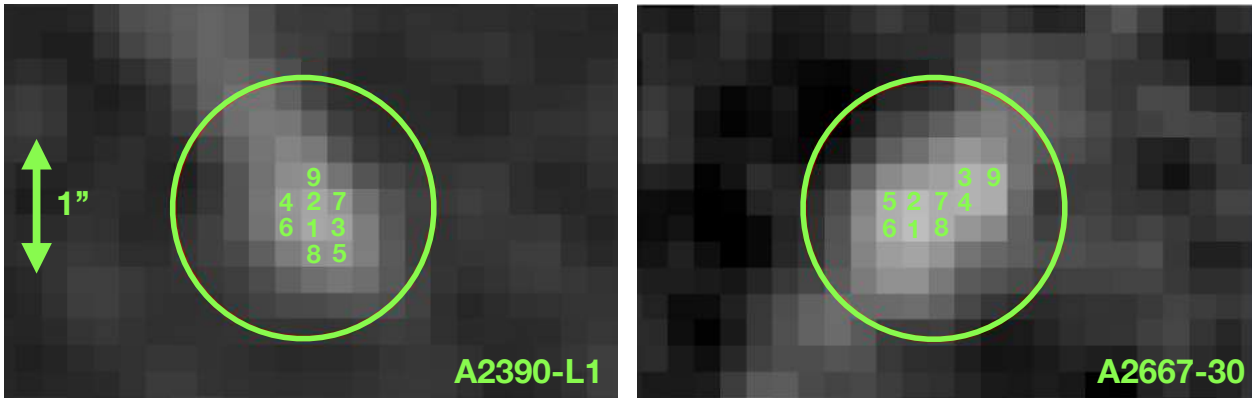

Figure 4.4: Example of the determination of the *Bp* list for two LAEs. The images shown are filtered images and both are represented with a linear colorscale. The green circle represents the area where we look for the maximal pixel value of the source. After the first value is fixed, the process look iteratively among the connected pixel for the following values.

- We consider the `MIN_AREA`-th value of the *Bp* list (i.e., `Bp[MIN_AREA-1]` with an indexing starting from 0). Only this value is used for the comparison to `local_noise`. To determine whether the pixel `[x,y]` is masked, the following rule is applied: if any value in `local_noise[x,y]` fulfills the condition:

  `Bp[MIN_AREA-1] / DETECT_THRESH < local_noise[x,y]`

  then the pixel `[x,y]` is masked. In all of the other cases, the central pixel remains unmasked. This criterion is a bit looser than the one used by SExtractor as the comparison is only done for `Bp[MIN_AREA-1]` and not for all the pixels. However assuming that the noise in a small area is not too drastically different, the SExtractor criterion and the one in use here remain very close. If `Bp[MIN_AREA-1]` fulfills the criterion, it is very likely that the other bright pixels, who all have higher signal values, will also fulfill the same criterion at some point on the 9 pixels area where `local_noise` is defined.
- Repeat this operation for all pixels of the RMS image.

A practical example of the application of this criterion is given on Fig. 4.5. The results and masks produced by this method are discussed in the next section.

4.3.2 Results, examples and tests

A sample of masks produced by the method detailed in the previous section is given in Fig. 4.6. In all these figures, the masked pixels are shown in white. The term ”covering fraction of a mask” refers to the proportion of masked pixels. A covering fraction of 1 means that the input source would not be detected anywhere on the image, and a covering fraction of 0 means that the detection would be possible anywhere on the image. Between 0 and 1, the source can be detected on only some part of the image. The masks presented in this figure are computed using the detection image of the input source.

From these examples, it can be seen that the method is efficient to mask the brightest cluster members. For A1689-1404, A1689-LN18 and A2744-11806 the shape of the mask follows closely the brightest sources of the cluster (see Fig. 3.3). We can also see that fainter sources tend to have a mask with a higher covering fraction, but part of this can also be caused by a variation of the average noise level from one input image to another. On the mask with a higher covering fraction (e.g., A1689-LN22, A2744-12026), we see that small spatial scale patterns are masked. These examples show that the method is well suited to account for the local variations of noise

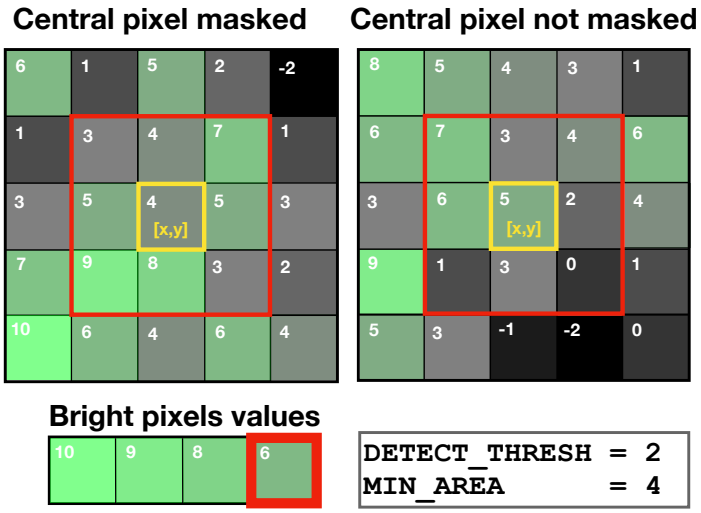

Figure 4.5: Illustration of the criterion used to create a mask. The grid represents part of an RMS map. To determine whether the central pixel `[x,y]` is masked or not, the bright pixels values shown on the bottom left are used; only the `MIN_AREA`-th pixel with a value of 6 is used for the comparison to the local noise. This comparison is only done for the 9 pixels centred on `[x,y]` (i.e red square on this figure). The values used for the detection threshold and the minimal area in this example are respectively 2 and 4. On the left, none of the pixels in the red area have values that are strictly less than `min(Bp) / DETECT_THRESH = 3` which results in the central pixel being masked. On the right panel, three pixels fulfill the condition and the central pixel is not masked.

caused by the combination of the structure of the instrument and random photon noise. This figure also shows that the method is efficient to account for the difference in exposure time. Considering the masks produced for A2744-5488 or A2744-12026, we can identify five clearly delimited areas, representative of different average levels of noise and exposure times. The geometry of these larger spatial scale patterns follows exactly the geometry of the different pointings of this 2x2 MUSE mosaic (See Fig. 3.4). Looking only at these masks, it can be determined that the upper right corner of the mosaic is the shallowest and that the center of the field is the deepest. It appears that we are therefore more sensitive to emission lines in the center of the field despite the presence of the Intra-Cluster Light (ICL). However, because of the extremely low volume probed in this central and high magnification area, only a few LAEs were actually detected.

On Fig. 4.6, we have only shown masks created from the detection layer of the input source. However, the same method can be applied to evaluate the detectability of a given source at any spectral position in any cube.

This is what we do to test the effects of surface brightness on the covering fraction of masks. Two pairs of LAEs with a similar detection flux and different spatial profiles have been selected to illustrate the point. To isolate the spatial profile component the test has to be done at a constant level of noise. Therefore, the two masks are computed using the same input image. The results of this test are shown in Fig. 4.7. We see that for the most compact LAEs, the covering fraction of the mask is close to zero whereas for the one with a diffuse profile, the covering fraction is much higher. This shows that the method developed is efficient to account for the spatial profile of individual sources, using only the information stored in the Bp list.

To test the effects of sky lines on the detectability of individual sources, we have computed some detection masks for two input sources, on a series of layers that are progressively being affected by the increased variance caused by a sky line. The masks resulting from this test are shown in Fig. 4.8. It can be seen that the masks undergo drastic changes on a very reduced spectral range in the cube (here 15Å) and that the covering fraction increases as the images are more and more affected by the sky line. This example demonstrates that the method is well suited to account for the strong variations of noise in the MUSE cubes. In this figure, the two LAEs used as input have the same flux and a very similar spatial profile. They are among the 20% of sources with the faintest detection flux in the A2744 sample. However, because they have different redshifts, their Bp profile was retrieved on different layers of the A2744 cube that are affected by different levels of noise. Because the series of masks are extremely similar for the two sources, this example tends to show that we do not include too much noise in the Bp profiles when retrieving the pixel values, even for faint sources.

4.3.3 Direct application to mask 3D cubes in the source plane

In this section we show how the method to compute 2D masks (see Sect. 4.3.1) would ideally be applied to compute $V_{\max}$ for individual sources. We also explain why the computation time (CPU time) of such a straightforward application does not scale well with an increasingly large number of sources and data cubes.

It is conceptually easy to produce 3D masks of the survey in the image plane for one given source. We can simply produce a 2D mask for each layer of the NB cubes using the method described above in Sect. 4.3. However, as the volume computation has to be done in the source plane, each layer of this 3D mask has to be reconstructed in the source plane and combined with a magnification map using Lenstool (see Fig. 3.6 for examples of source plane magnification maps). The magnification map can be used to reject the areas of the survey where the magnification would

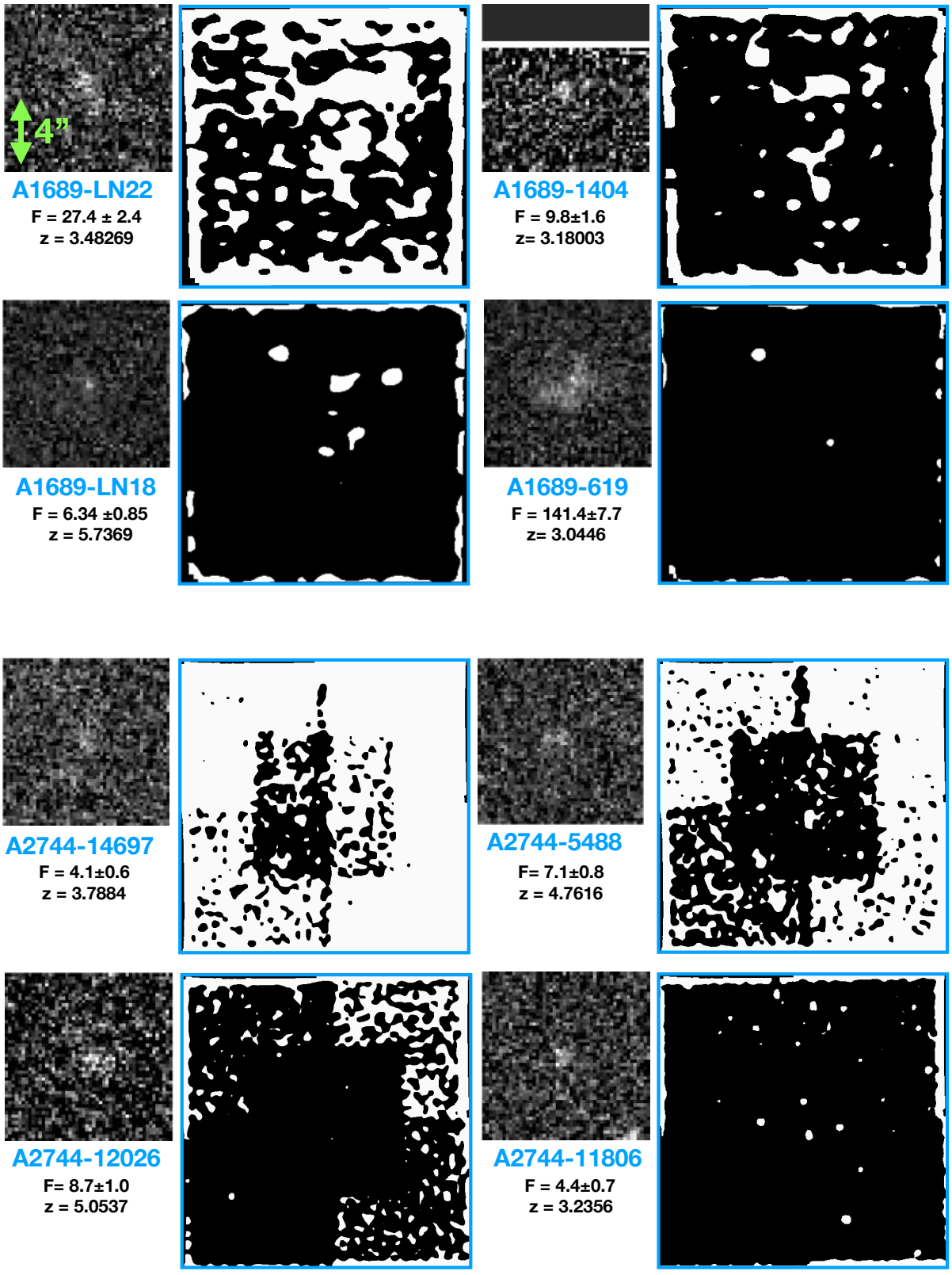

Figure 4.6: Some example of masks created with the 2D masks method. The masked pixels are in white. The masks were computed on the detection layer of each source, i.e. at their actual spectral positions in the cubes. The spatial profile of the input source used for each mask, as seen on the MUSELET NB image, is shown on the left of each mask. The flux values are detection fluxes expressed in 10^{-18} erg cm^{-2} s^{-1} units.

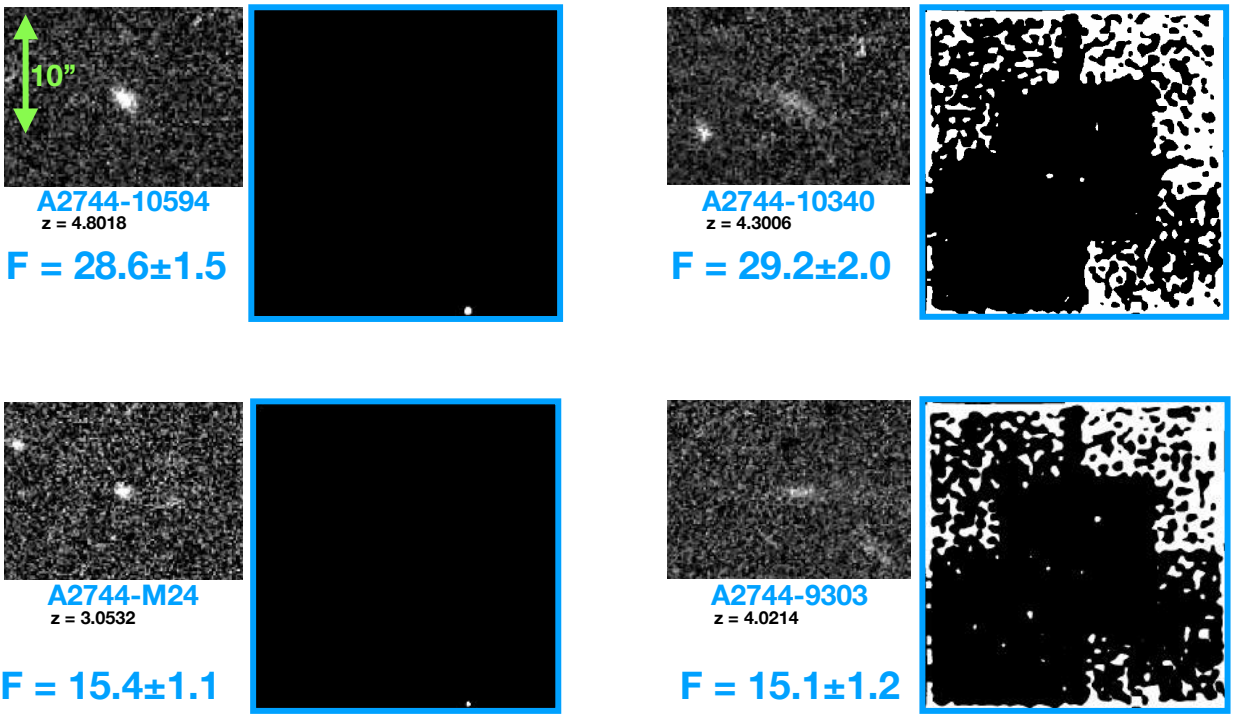

Figure 4.7: The flux values are detection fluxes expressed in 10^{-18} erg cm^{-2} s^{-1} units. For the pair A2744-10594, A2744-10340, the masks were computed for the layer 3256, and for the pair A2744-M24, A2744-9303, the masks were computed for the layer 3252.

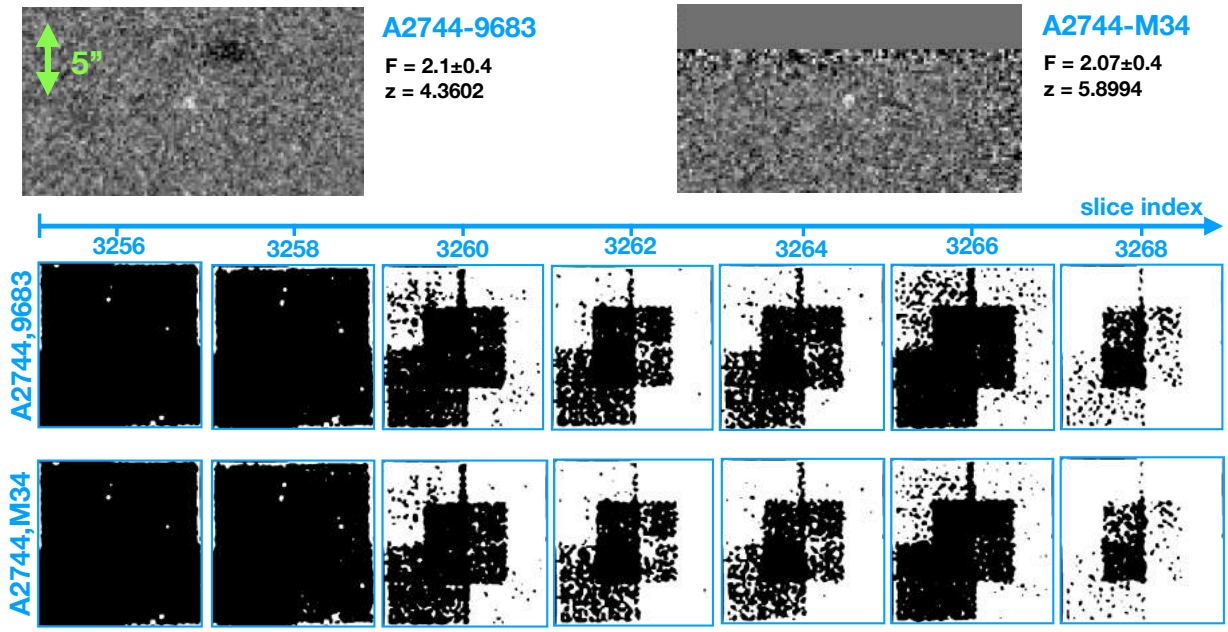

Figure 4.8: Illustration of the effect of sky lines on the morphology of the masks. The masks are computed for two LAEs on slices of a MUSE cubes that are increasingly affected by sky line noise (from left to right). The flux values are detection fluxes expressed in 10^{-18} erg cm^{-2} s^{-1} units. The two detection images are shown in the exact same colorscale.

be too low to allow the detection of the source (this aspect is detailed in the next section).

This direct application of the method, is accurate to account for the specificities of individual sources, and for the rapid variations of noise, both spatial and spectral, in the cubes. However, it is extremely long. For a single source, with a survey consisting of 4 MUSE cubes, we would need to make $3600^3 \times 4$ LENSTOOL source plane projections. This would take $\sim$ 20 days for only one source, on a 60 CPU computer. Or alternatively a bit more that 8 years and a half of computation for a full sample of $\sim$ 150 LAEs across 4 MUSE data cubes. Even creating one mask for only one layer in a hundred, the computation would take a whole month. And for a precise volume computation, we would need a much higher sampling of the rapid spectral noise variations to properly account for the sky line effects (see Fig. 4.10 for an example of the spectral noise variations inside a MUSE cube).

This simple example shows, that a direct application of the 2D mask method developed in this section would give the best results but cannot realistically be applied to large (and increasingly expanding) sample. For that reason, we developed a method, that allows a fine sampling of the spectral noise variations using only a fixed and limited number of source plane projections. This final method adopted for the volume computation is presented in the next section.

4.4 Adopted method to efficiently mask 3D cubes in the source plane

An overview of the different steps of the method developed in this section is shown in Fig. 4.9. We suggest that the reader follows the text using this figure to keep a global view of how the different steps are interrelated. The main idea, is to build a set of precomputed 2D masks for a wide range of S/N values. Linking the S/N used to create the set of masks to the S/N value computed for one source at a given layer of one cube, a precomputed mask can be assigned. Repeating this operation at different positions in a cube, it effectively produces a 3D mask. This operation can be done in the image plane or in the source plane. The advantage of this approach is that the number of LENSTOOL source plane reconstructions only depends on the range and sampling of S/N values that is used to build the initial set of 2D masks. The definition of noise level and S/N used in this chapter are presented in Sect. 4.4.1, and the main assumptions needed to apply this method are presented and discussed in Sect. 4.4.2. Finally the core of the method and the details of the volume computation are given in Sect.4.4.3.

4.4.1 Definition of noise levels and S/N

In the frame of the method developped here, the noise level refers to the average noise level of a given layer. It is computed from the RMS image of this layer using a normalization factor that reflects the average level of noise in the entire cube. For a layer i in a cube, the noise level is defined as:

$$\text{Noise level}_i = \text{Noise level}(RMS_i) = \frac{< RMS_i >_{x,y}}{< RMS_{\text{median}} >_{x,y}} \tag{4.2}$$

where $< .. >_{x,y}$ is the spatial median operator, and RMS_{median} is the median RMS image, obtained by taking the median of the entire RMS cubes along the spectral axis. Because $< RMS_{\text{median}} >$ is used as a normalization, the values of noise level are not directly comparable between cubes, and are only reflective of the relative variations of noise levels inside a given cube. An example of the noise variations in MUSE cubes as defined in this equation is given in Fig.

[3]Number of slices in a MUSE cube

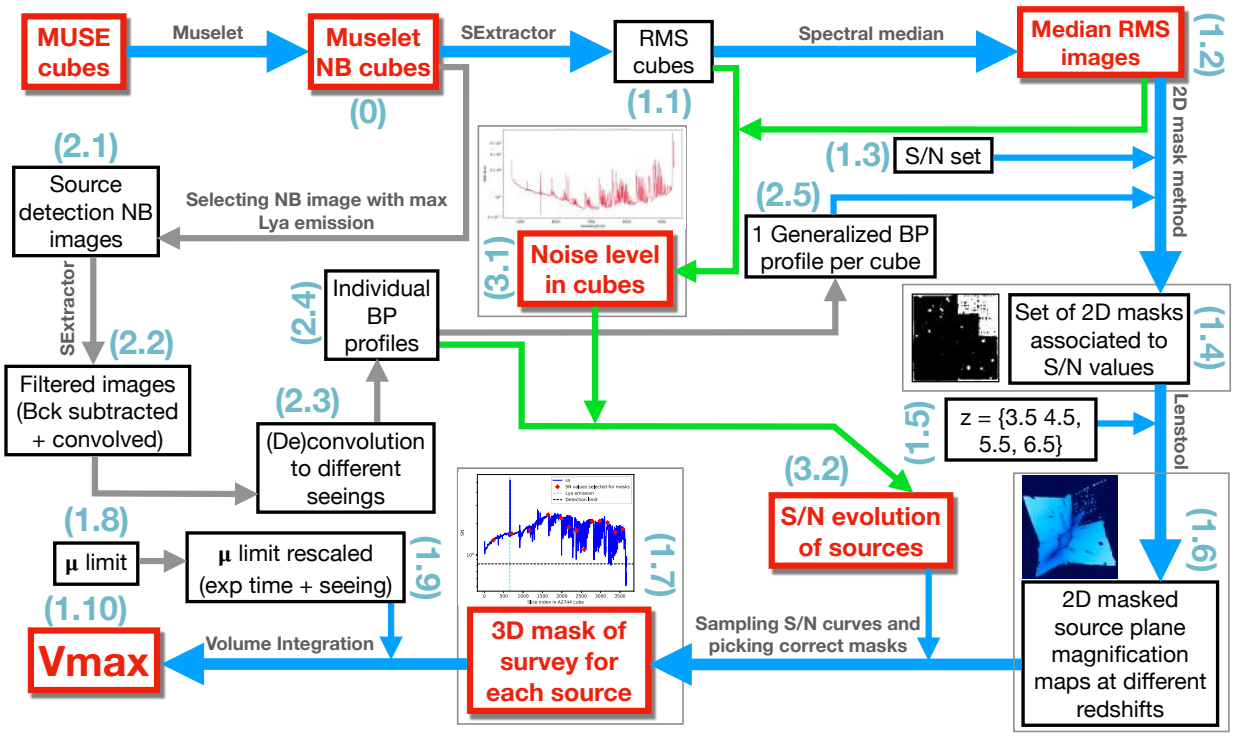

Figure 4.9: Flow chart of the method used to produce the 3D masks and to compute $V_{\rm max}$. The main path followed by the method is in blue. All the steps related to the determination of the bright pixels are in grey. The steps related to the computation of the S/Ns of each source are in green.
(0) The NB cubes consist of all the NB images produced by MUSELET. All LAEs were detected on those NB images. (1.1) Background RMS maps produced separately by SEXTRACTOR and assembled into a RMS cube. The RMS cube are cubes of noise that are used to track the spectral evolution of noise levels in cubes. (1.2) Median of the RMS cubes along the spectral axis. One median RMS image is obtained per cube. They are used to mock the 2D SEXTRACTOR detection process. (1.3) Set of S/N values designed to encompass all possible values in the LAE sample. The definition used for S/N is provided in Eq. 4.2. (1.4) Using a generalized bright-pixels profile (see Fig. 4.12) and the median RMS maps, a 2D detection mask is built for each value of the S/N set and for each cube. (1.5) Redshift values used to sample the evolution of the source plan projections and magnification maps (1.6) Source plan projection of the set of 2D masks combined with magnification maps for different redshift. (1.7) For each LAE, the final 3D survey masks are assembled from the set of source plane projections. The procedure browse the S/N curves (see Fig. 4.14), and picks the pre-computed 2D source plane projection computed from the correct S/N value and the appropriate redshift value. (1.8) Minimal magnification to allow the detection of a given LAE in its parent cube. This first value is computed from the error on the flux detection, which is indicative of the local noise level. See definition in Eq. 4.6 (1.9) A rescaled limit magnification (see definition in Eq. 4.7) is computed for each LAE and for the three additional cubes. This is done to account for the differences in both seeing and exposure time. For each LAE, the four $\mu_{\rm lim}$ values are used to restrict the volume computation to the areas of the source plane projection with a magnification high enough to allow the detection of this LAE. (1.10) Volume of the survey where a given source could have been detected. For one LAE, this volume is computed from the source plane projected 3D masks, on the pixels with a high enough magnification. (2.1) For each LAE, the NB containing the max of its Lyman-alpha emission is selected. The cleanest detection was obtained on this slice of the NB cube. (2.2) Filtered map produced with SEXTRACTOR. (2.3) From the original filtered map produced for each LAE in the parent cube, three additional images are produced to the resolution of the additional cubes the LAE does not belong to using convolution or deconvolution. (2.4) Individual bright-pixel profiles are retrieved for the four different seeing conditions from the filtered images and the three additional images produced in the previous step. The bright-pixel profiles contain the information related to the spatial profile of the LAEs. (2.5) The four generalized bright-pixel profiles are the median of the individual bright-pixel profiles computed for each seeing condition (see Fig. 4.12). These generalized profiles are used to limit the number of mask computed and simplify the production of 3D masks. (3.1) The noise level in cubes is an average measure of noise in a given slice of a cube. It is defined in Eq. 4.2 and examples are provided in Fig. 4.10. (3.2) Combining the definition of noise levels and the individual bright-pixels profiles, the evolution of S/N for individual sources is computed through the cubes with Eq. 4.3.

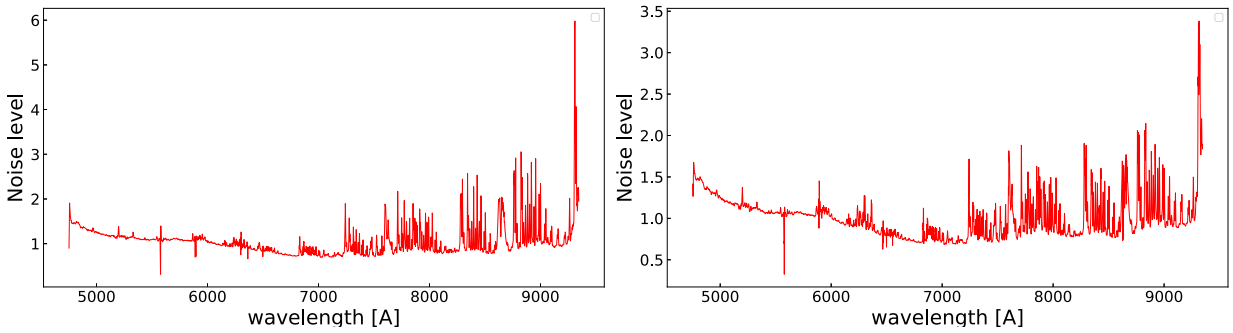

Figure 4.10: Evolution of noise level computed for A2667 on the left and for A2744 on the right. All Muse cubes follow a similar evolution

4.10. It can be seen that these noise levels are extremely similar from one cube to another. This is expected, as the effect of increased exposure (i.e., reduced absolute noise level) are not visible owing to the normalization in use.

Using this definition of noise level, we define the S/N of a given source by comparing its bright pixel profile to the noise level of a given layer. For a given source, the S/N can be computed for any layer i of a cube and is defined as follows:

$$S/N_i = \frac{\max(Bp)}{\text{Noise level}(RMS_i)} \tag{4.3}$$

This definition is not a proper signal-to-noise value but only a proxy as the normalization used depends on the cube considered. For the sake of simplicity, we will continue using the term signal-to-noise (or S/N) to refer to this proxy. For a given source, S/N_i can be used to track how the Lyα emission compares to average noise level of layer i. This evolution of S/N was computed for each LAE of the sample through all cubes part of the survey. We will refer to them as the S/N evolution curves of LAEs hereafter (see Fig. 4.14 for examples of S/N evolution curves, more details on this later).

4.4.2 Main simplifications

To limit the number of masks created, and the number of source plane reconstructions, two simplifications are made. As explained in Sect 4.3.1, to produce a 2D mask, two inputs are needed: Bp, and an image from which a RMS map is computed. The two simplifications introduced here are the use of a general bright pixel profile and median RMS images instead of individual inputs for each LAE. Below, the validity of these two assumptions and the effects on the production of 2D masks are discussed.

The first assumption is that all RMS maps of a same cube present roughly the same pattern down to a certain normalization factor. This is equivalent to say that all individual layers of the RMS cube can be approximately modeled and reproduced by a properly rescaled version of a median RMS map. An example of RMS maps at different wavelengths and the corresponding median RMS maps is provided in Fig. 4.11 for A2390 and A2744. This figure shows that the RMS images at different spectral positions in the cubes look very similar and show roughly the same spatial patterns. The main difference come from foreground and bright galaxies that have different morphologies at different wavelengths (e.g. bright emission line emitters), or random fluctuations of

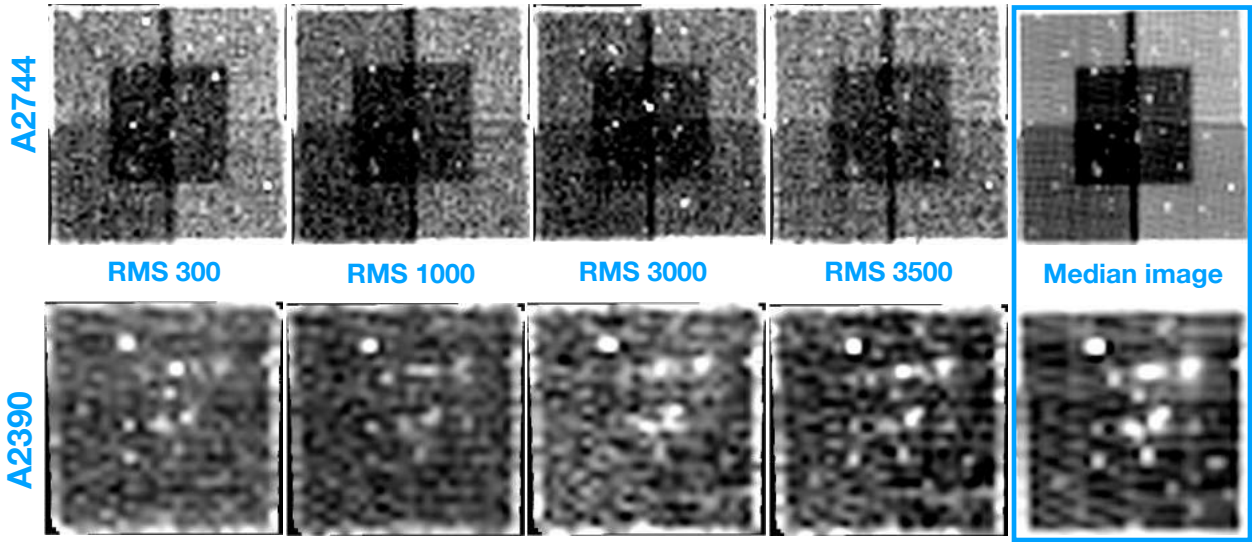

Figure 4.11: All images are shown with a logarithmic colorscale. Several RMS images are shown for different layers of the A2390 and A2744 cube. On the right, the median RMS maps computed from the entire cubes are shown. This figure shows that no matter the layer considered, the RMS images display roughly the same type of patterns, on both small and large spatial scales, and can therefore be approximated using rescaled median RMS images.

noise that affect the local noise level. The structure of the instrument and the effect of different exposure times are still clearly apparent on the median RMS images. From now on, it is therefore considered that the median RMS images provide a good approximation for all layers of the RMS cubes and can be used to compute 2D masks.

The second simplification is the use of a several generalized bright-pixel profile (hereafter $Bp_{\rm g}$, not to be confused with the individual profiles noted Bp): one for each cube part of the sample. To be consistent with the variations of seeing from one cube to another, the Bp profiles of individual LAEs are computed four times: one time in the parent cubes and three times in the three external cubes. The three additional measurements are done convolving or deconvolving the detection image of the LAE to the seeing value of the three external cubes. The deconvolution algorithm used is the supervised python implementation of a Weiner filter described in Orieux et al. (2010) and part of the Python Scikit-image package (van der Walt et al., 2014). The $Bp_{\rm g}$ are the median of all the individual Bp computed for one cube. These profiles are normalized in such a way that $\max(Bp_{\rm g}) = 1$ and are computed by taking the median of all individual brigth-pixel profiles in a given cube. The median profile and the individual profiles are shown on Fig. 4.12 for A2744 and A1689. As explained in Sect. 4.3.1, only the `MIN_AREA`-th value of Bp is needed to compute a mask. In this figure it can be seen that, comparing only the `MIN_AREA = 6` first pixels of the individual profiles, they are reasonably similar to each other, which justifies the use of such a median profile.

Using these two simplifications, we can use the four median RMS images and the four $Bp_{\rm g}$ to produce masks for a given cube at any given S/N values, instead of producing them for individual sources. According to the definition in Eq. 4.3, S/N is just a comparison of a bright pixel profile to the average noise level of a single RMS image. To fit a certain arbitrary S/N value s/n, using the median RMS maps and $Bp_{\rm g}$, we can rescale $Bp_{\rm g}$ as follows:

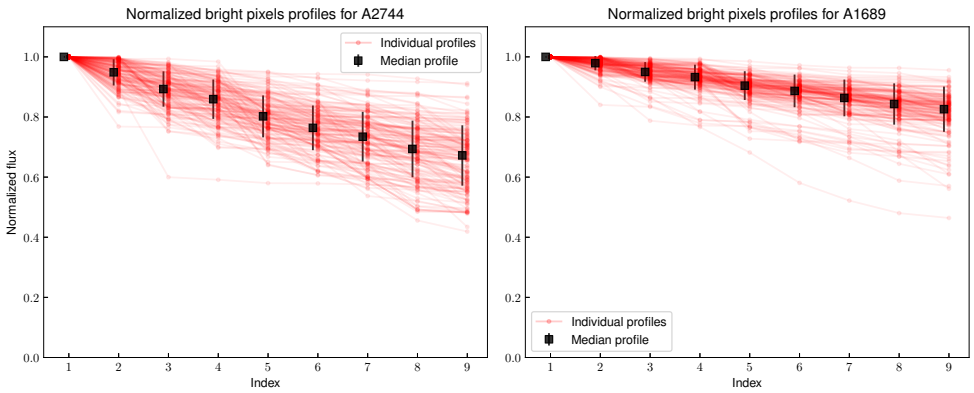

Figure 4.12: Individual and bright pixels profiles all normalized so that $\max B_p = 1$ for representation purposes. The profiles are computed for the seeing value of A2744 (left) and A1689 (right). The seeing being higher for A1689 than for A2744, the individual and median profiles are flatter.

$$s/n = \frac{\max(C \times Bp_g)}{\text{Noise level}(RMS_{\text{median}})} = C \times \max(Bp_g) = C \tag{4.4}$$

where C is a scaling factor. Using the definition of noise level in Eq. 4.2, we have:

$$\text{Noise level}(RMS_{\text{median}}) = 1 \tag{4.5}$$

and by definition of Bp_{g}, we also have $\max(Bp_g) = 1$. Therefore to produce a mask for a S/N value s/n, and for a given cube, we can use as inputs its median RMS image and the corresponding $s/n \times Bp_{\text{g}}$ as bright pixel profile. We explain in Sect. 4.4.3 how this can be used to efficiently mask 3D cubes for individual sources with only a limited number of individual 2D masks. In the rest of this section we discuss the effects of the assumptions presented here on the accuracy of the masks.

Figure 4.13 presents some masks produced using various S/N values as input for the cluster A2744. When comparing these masks to the one in Fig. 4.6, Fig. 4.7 or Fig. 4.8, it can be seen that their aspect is smoother and that the smaller spatial scale patterns are more regular. The masks produced using the median RMS images are less efficient to account for the exact spatial variations of noise. For example, the bright sources are still masked, but the sources that are only visible through their emission line are no longer masked, as they do not appear on the median RMS images. In a similar way, the exact random variation of noise on the smaller spatial scales are lost in the median RMS images, and therefore this information does not appear on these new masks causing the smoother aspect observed.

Using these two simplifications, the 2D masks are still representative of the average noise level on the different parts of the mosaic, and their structure is very similar to the more precise masks computed and shown in Sect. 4.3. It can be seen in the four leftmost panels of Fig. 4.13 that the method remains well suited to account for the different exposure regimes of the A2744 FoV. In the next section we present how these generic masks can be used to assemble 3D masks for individual sources in both the image and the source plane.

4.4.3 assembling 3D masks in image and source plane

To produce 3D survey mask for individuals sources, two steps are performed separately:

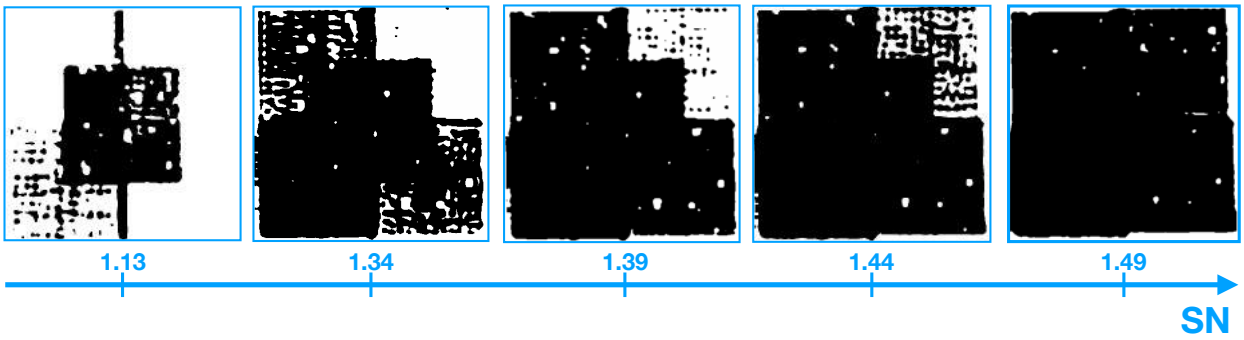

Figure 4.13: 2D masks produced using a median RMS image and $Bp_{\rm g}$ rescaled to fit different S/N values for the cluster A2744.

1 - We define S/N_s, a set of S/N values designed to include all possible values in the LAE sample. S/N_s is defined between an inferior limit $S/N_{\rm s,inf}$ and a superior limit $S/N_{\rm s,sup}$, with a constant step in logarithmic space. Applying the process explained in Sect. 4.4.2, a 2D mask is computed for each cube and for each value of this set using the four $Bp_{\rm g}$. These are the only 2D masks needed to produce 3D masks in the image plane for the full sample.
We measure the covering fraction for each of the 2D masks, and remove from the process all the masks computed from a S/N value leading to a covering fraction of 1 (or 0), except for the one with the higher (lower) S/N value. Another way to say that is that only one mask with a covering fraction of respectively 1 and 0 is kept. This step is necessary to avoid projecting many times the exact same mask in the source plane and allows for a very loose definition of S/N_s as the values $S/N_{\rm s,inf}$ and $S/N_{\rm s,sup}$ will not impact the computation time in any way.

2 - For each LAE, the S/N is computed for each cube and on every layer according to Eq. 4.3. For each cube, the individual bright pixel (i.e. not $Bp_{\rm g}$) measured at the seeing of the cube is used. Examples of these S/N evolution curves are shown in Fig. 4.14.

After the completion of these two steps, the final 3D detection masks can be assembled for each LAE individually in the image plane. For this purpose, a subset of wavelength values (or equivalently, a subset of layer index) drawn from the wavelength axis of a MUSE cube is used to resample the S/N curves of individual sources. For each source and each entry of this wavelength subset, the procedure fetches the value in S/N_s that is the closest to the measured one, and returns the associated 2D mask, effectively assembling a 3D mask. The important point being that, to increase the sampling density, we do not need to increase the number of masks computed. At this stage, the information about the individual surface brightness of sources is passed to the $V_{\rm max}$ computation: for a given detection flux, a compact source has more flux enclosed in its brightest pixel compared to and extended one, and has therefore a higher S/N.

A similar method is applied to produce individual 3D masks in the source plane. Every 2D mask is projected in the source plane at different redshifts and combined with the magnification maps at that same redshift (see example in Fig. 3.6). For the projections, we used PyLenstool[4] that allows for an automated use of Lenstool. Reconstruction of the source plane were performed for different redshift values to sample the variation of both the shape of the projected area and the magnification. In practice, the variations are very small with redshift, and we reduce the redshift sampling to z_s =3.5, 4.5, 5.5 and 6.5. Using the almost same method described in the previous paragraph, 3D masks are assembled and combined with magnification maps, in the source plane.

[4]Python module written by G. Mahler, publicly available at `http://pylenstool.readthedocs.io/en/latest/index.html`

The only difference is that in addition to the closest S/N value, the procedure also looks for the closest redshift value in z_s. For a given point $(\lambda_k, S/N_k)$ of the resampled S/N curve, the redshift of the projection selected is the closest to $z_k = \frac{\lambda_k}{\lambda_{Ly_\alpha}} - 1$. Thanks to the use of S/N instead of individual source inputs, the number of source plane reconstructions only depends on the definition of S/N_s, the length of z_s and the number of MUSE cubes included in the survey. It depends neither on the number of sources in the sample nor the accuracy on the sampling of the S/N curves.

An example of the resampling of the S/N curves used for the production of 3D masks in both the image and the source plane is presented in Fig. 4.14. The S/N curves are plotted in blue. To each of the red points, a pre-computed 2D detection mask is associated. The higher the density of the wavelength sampling (red points), the higher the precision on the final reconstructed 3D masks. The position of the Lyα emission is represented by a dashed cyan line in the native cube. The two horizontal dashed lines represents the S/N values for which the associated mask have a covering fraction of 0 and 1. As explained at the beginning of this section, all the masks with a S/N value out of the range defined by these two limits were removed from the process. For this reason, when the S/N curve goes above this range, the procedure looks for the mask with the higher S/N value that is still available. This effect can be seen for example on the upper left panel of the figure where many of the red points stop following the S/N curve when it reaches high enough S/N values. The same is also observed when the S/N curves reaches very low S/N values, as seen for example on the lower left panel.

The S/N curves presented in these plots are computed in different cubes for three different LAEs ranging from bright to faint and diffuse, representative of different detection conditions. Each curve is resampled with 300 points. The plots shown in this figure are helpful to have a simple representation of the 3D survey masks computed for each LAE, and to see how they are impacted by the average exposure of the different cubes or the presence of sky lines. A2744-M1 being a bright source easy to detect, we can see on the top right panel that the masks are barely affected by the presence of sky lines in the red part of the cube. Only a few masks have a covering fraction that is less than one. On the top left panel, the same curve was computed for the same source, but in the A1689 cube which is much shallower than the A2744 one (see Table 3.1). For this reason we see that the impact of the sky lines is greater on selection of the masks. From these two plots, we can deduce that covering fractions of the 3D masks built for this specific source would be very close to one, and that both clusters would contribute significantly to $V_{\max}$. On the two middle panels, it can be seen that A2744-3424 is harder to detect. For the S/N curve computed in the A1689 data cube, all the 2D masks selected have a wide range of covering fraction between 0 and 1, meaning that on (almost) each layer of the 3D mask, A2744-3424 could have been detected on at least some part of the field but never on the entire field. It is almost the same for the A2744 cube, except that many of the 2D masks have a covering fraction of 1. For a faint and diffuse source as A2744-9303, we see that the shallower cube A1689 almost do not contribute to $V_{\max}$, as the source can barely be detected on the layer of the cube with the lowest level of noise. Only the deepest part of the A2744 remain unmasked and can contribute to the $V_{\max}$ value for this LAE.

4.5 Volume integration and results

The last aspect to account for in the volume computation is the magnification. To remove from the $V_{\max}$ computation the areas of the survey where the magnification would be too low to make the detection of a given source possible, we introduce the limit magnification noted $\mu_{\lim}$. This limit magnification is computed for each LAE and for each cube. In the parent cube, it is computed

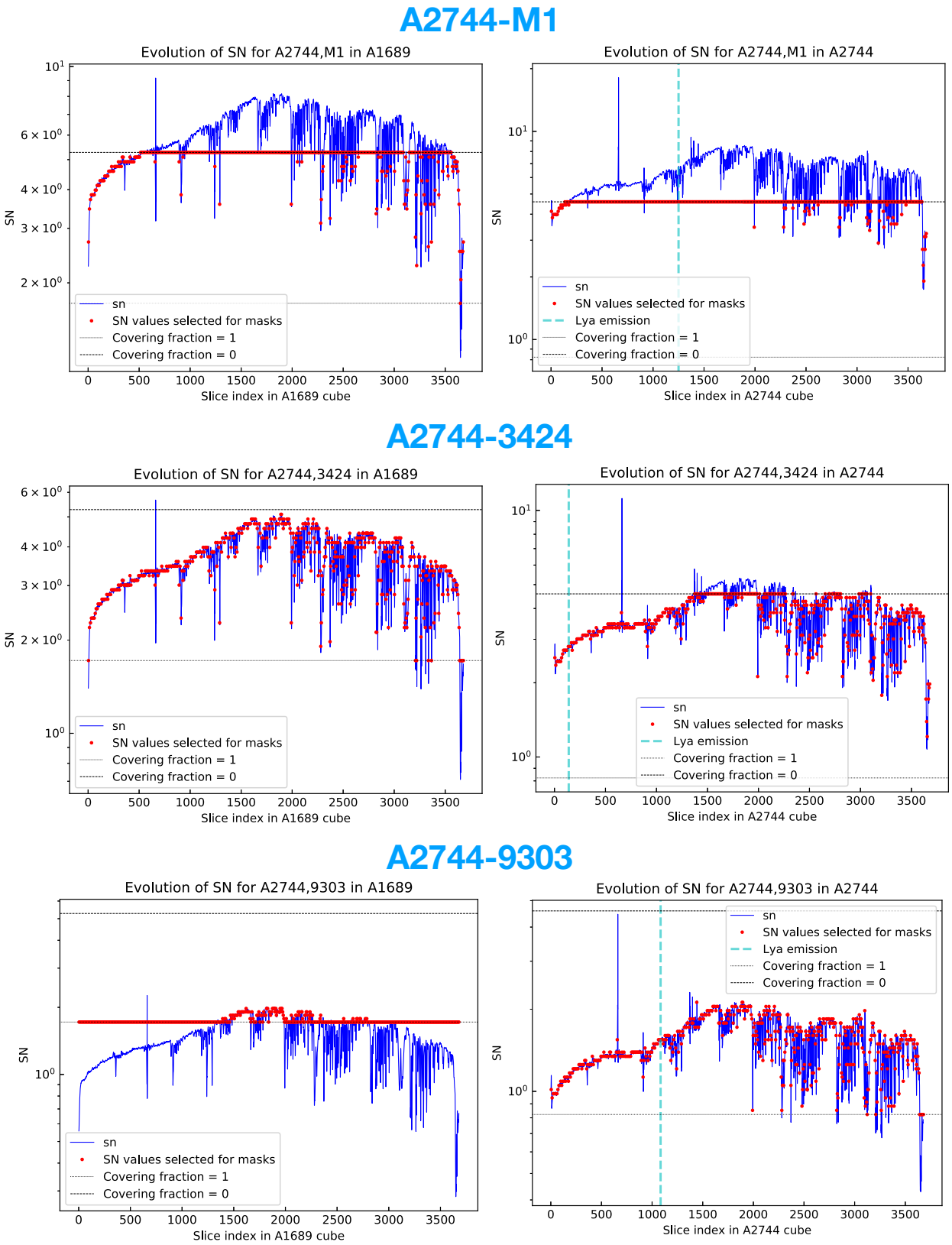

Figure 4.14: S/N curves computed for three different LAEs representative of the different detection conditions. For each LAE, the S/N curve presented in this figure is computed from the A2744 and A1689 data cube. On this figure, 300 points are used to resample the blue curves.

using:

$$\frac{\mu_{\rm lim}}{\mu}\frac{F_{\rm d}}{\delta F_{\rm d}} = 1 \tag{4.6}$$

where μ is the flux weighted magnification and $F_{\rm d}$ and $\delta F_{\rm d}$ are respectively the detection flux and the uncertainty on the detection flux as given by SExtractor. This condition simply states that for $\mu < \mu_{\rm lim}$ the signal would be too weak and the detection impossible. It is complex to find signal-to-noise criterion to use here that would be coherent with the way Muselet works on the detection images, since the images used for the flux computation are different and of variable spectral width compared to the Muselet NBs. Therefore, this criterion for the computation of the limit magnification is intentionally quite conservative to not systematically underestimate $V_{\rm max}$ and therefore overestimate the steepness of the faint end slope of the LF.

To be consistent with the different seeing values and exposure times, the value computed for the parent cube has to be rescaled for the external cubes. A source only detected because of high magnification in a shallow cube (bad seeing), does not need such a high magnification to be detected in a deeper (good seeing) cube. The scaling used to compute the limit magnification in external cubes is given by :

$$\mu_{\rm lim,ext} = \frac{< RMS_{\rm ext} >_{x,y,\lambda}}{< RMS_{\rm p} >_{x,y,\lambda}}\frac{s_{\rm ext}^2}{s_{\rm p}^2} \times \mu_{\rm lim,p} \tag{4.7}$$

where the subscript $_{\rm ext}$ and $_{\rm p}$ refer to the external and parent cubes, $< RMS >_{x,y,\lambda}$ is the median operator over the three axis of a MUSE RMS cube and s is the seeing. This simple rescaling is sufficient as only the $V_{\rm max}$ values of the few LAEs with very high magnification are dominated by the effects of the limit magnification.

The volume is then integrated by summing the contributions of individual layers of the 3D survey source plane masks and counting only the pixels with $\mu > \mu_{\rm lim}$. The contribution of one layer k to $V_{\rm max}$ is given by:

$$dV_k = N(\mu_{\rm lim}, k) \times \omega \frac{c}{H_0}\int_{z_{\rm min}(k)}^{z_{\rm max}(k)} \frac{D_L^2(z')}{(1+z')^2 E(z')} dz' \tag{4.8}$$

$$E(z) = \sqrt{\Omega_{\rm m}(1+z)^3 + (1-\Omega_{\rm m}-\Omega_\Lambda)(1+z)^2 + \Omega_\Lambda} \tag{4.9}$$

where ω is the angular size of one MUSE pixel and $D_L(z)$ is the luminosity n distance, $z_{\rm min}(k)$ and $z_{\rm max}(k)$ are the redshift limits of the layer k corresponding to its spectral width and $N(\mu_{\rm lim}, k)$ is the number of unmasked pixels on layer k, with $\mu > \mu_{\rm lim}$. The same computation can be applied to compute $V_{\rm max}$ for the entire redshift range $2.9 < z < 6.7$ or for reduced redshift ranges when studying the evolution of the shape of the LF with redshift (see Sect. 5.4).

Scatter plots showing the $V_{\rm max}$ values computed for the LAEs of the lensing sample versus detection flux, magnification and luminosity are shown in Fig. 4.15. The $V_{\rm max}$ values discussed in this section are all computed between $2.9 < z < 6.7$ and using 300 points to sample the S/N curves.

This figure illustrates well the effects of lensing on the $V_{\rm max}$ computation. On the leftmost panel, we can see that as expected, $V_{\rm max}$ tends to increase with the detection flux. However, we also see sources with a high detection flux and a small $V_{\rm max}$. These are sources that could only be detected because of their high magnification. By definition these sources have a high $\mu_{\rm lim}$ value, which reduces the area of the survey integrated in $V_{\rm max}$. On the middle panel, we see that the sources detected with a high magnification tend to have a lower $V_{\rm max}$ and on the rightmost panel, we see that sources with a lower luminosity have a lower $V_{\rm max}$. These two trends are expected as it is extremely unlikely to find a high luminosity source with a high magnification. Given the current state

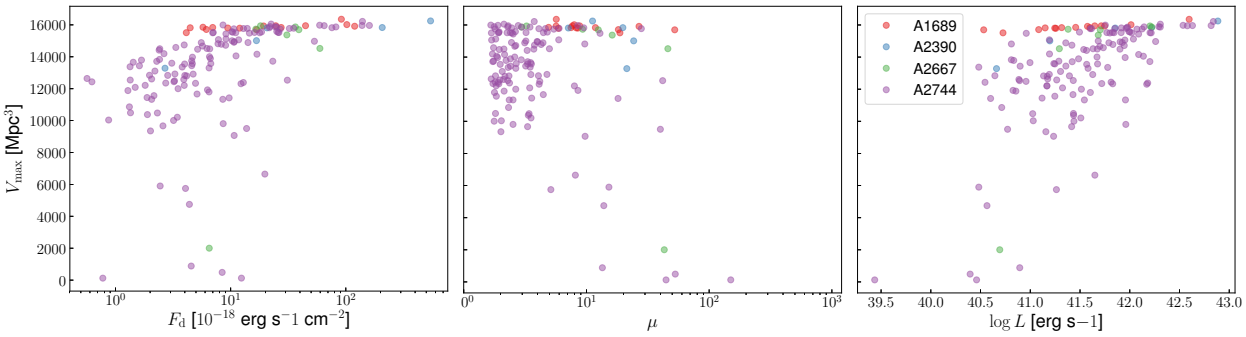

Figure 4.15: Scatter plot of the $V_{\max}$ values of each LAE of the lensing sample. The values displayed here are computed for $2.9 < z < 6.7$. **Left panel:** $V_{\max}$ versus Lyα detection flux, **middle panel:** $V_{\max}$ versus magnification **right panel:** $V_{\max}$ versus Lyα luminosity in log.

of the studies of the LAE luminosity function (e.g., Dawson et al., 2007; Cassata et al., 2011; Santos et al., 2016; Drake et al., 2017a, and many others), it appears clear that the faint LAEs are much more numerous than the high luminosity ones. As the volume probed decreased sharply around the highly magnified regions, it is extremely unlikely to find a high luminosity LAE in these regions.

4.5.1 Effect of S/N sampling

Five test have been performed (test 1 to test 5), each of them with respectively 15, 50, 100, 300 and 1 000 points used to resample the S/N curves. Test 5 having the higher sampling is considered to produce the most reliable $V_{\max}$ values. Figure 4.16 shows the relative deviation of the different tests with respect to the values obtained in Test 5.

The LAEs were sorted from lower (on the left) to higher $V_{\max}$ values (on the right) according to the results obtained in Test 5. Each point along the x-axis of this figure corresponds to a different LAE. We see that for the sources with high $V_{\max}$ values (on the right), the values are almost constant when increasing the sampling density. These are the brightest LAEs, that are virtually detectable anywhere in the cubes and therefore the result does not depend on the sampling used. On the contrary, the LAE with a smaller $V_{\max}$ are harder to detect. For these sources the density of the sampling used is expected to have a greater impact as their $V_{\max}$ is more sensitive to the exact noise variations. The plot shows that we tend to overestimate the volume with a lower sampling density, especially for the sources with low $V_{\max}$. The reason for this, is that using only a few points, it is more likely to sample the S/N curves at wavelengths non affected by the sky lines (see Fig. 4.14 for example). Since very little difference is observed between Test 4 (300 points) and Test 5 (1 000 points), we decided to adopt a 300 points sampling to save computation time. However, the sampling needs to be dense enough to allow the masks to be representative of the accumulated presence of sky lines on a local domain of wavelength. All $V_{\max}$ values used for the computation of the luminosity function were computed using a sampling of 300 points.

4.5.2 Discussion on the method

Several assumptions and simplifications were made at different levels to make the implementation of this $V_{\max}$ computation possible. In this section, we detail the possible sources of error and investigate the possible systematic effects and how they could affect the $V_{\max}$ values or the shape of

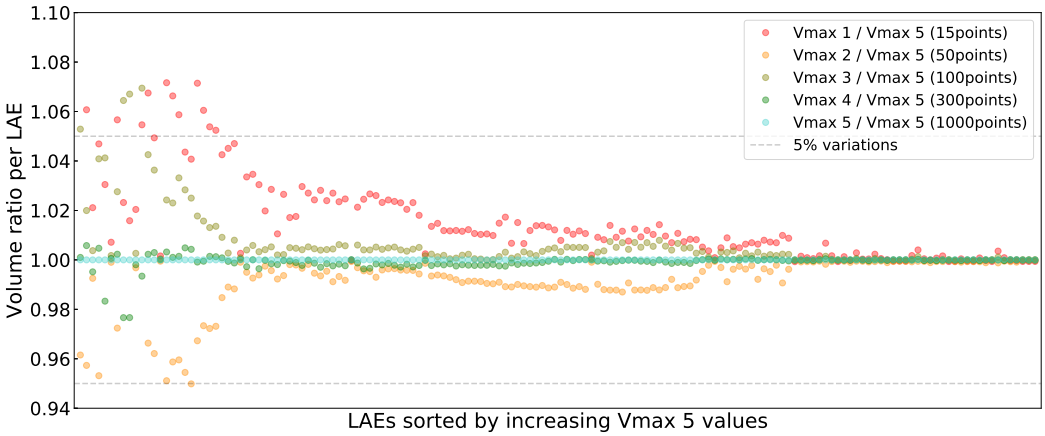

Figure 4.16: Ratio of $V_{\rm max}$ values computed from various series of tests using a different number of points to resample the S/N curves. Test 5 having the higher resampling density is used as a reference. The $V_{\rm max}$ ratios are computed for individual LAEs, and the LAEs are sorted from left to right by increasing order of $V_{\rm max}$ values, as computed during test 5.

the resulting LFs. The assumptions made are numerous and only the main ones are listed here by order of appearance in this chapter.

Noise in the bright pixel measurements. One of the first source of error is that we may include some noise when we retrieve the pixel values of the individual bright pixel profiles. As only the brightest pixel of Bp is used to compute the individual S/N curves, the inclusion of noise in this aspect of the method is minimal. And for the computation of the 2D masks most of the random noise is removed as a median profile computed from all the individual profiles is used. Therefore in average this should have only a minimal impact on the volume computation, and does not bias the results of the $V_{\rm max}$ computation.

General bright pixel profiles. The use of $Bp_{\rm g}$ instead of individual source profiles for the creation of the masks and was already partly discussed in Sect. 4.4.2. For sources with extended profiles the use of $Bp_{\rm g}$ leads to an overestimation of $V_{\rm max}$ and for compact sources, it leads to an underestimation of $V_{\rm max}$. However, in average this should not bias the distribution of $V_{\rm max}$ values as $Bp_{\rm g}$ is still representative of the distribution of spatial profiles in the LAE sample. For the sources for which $V_{\rm max}$ was overestimated, the value can be somehow corrected by the computation of the completeness correction since the simulations are done on masked layers (see completeness computation in Sect. 5.3.1 for which we use the real spectral and spatial source profile, and the discussion in Sect. 5.3.3). Indeed, if the volume is overestimated, the covering fraction of the mask used for the completeness simulations is also underestimated. This leads to a higher noise level in the layer used for the simulation and therefore a lower completeness for this source that tend to compensates the overestimated $V_{\rm max}$.

Furthermore, when using generalized profiles, part of the information about spatial profiles of LAEs is lost when creating the masks. However, this information remains stored within the individual Bp profiles used for the computation of the S/N curves and for picking the correct 2D mask.

In that sense, the final 3D mask still accounts for the surface brightness of individual LAEs.

Median RMS maps. The use of the median RMS images does not impact the $V_{\rm max}$ computation in any significant way when it is performed through the entire spectral axis of the cubes, that is to say when $V_{\rm max}$ is computed for $2.9 < z < 6.7$. However, for reduced redshift intervals, the use of a median RMS image may have an impact on the result. This computation is needed when the LAE population is split in redshift bins to investigate the evolution of the shape of the LF with redshift (see Sect. 5.4). For example, when computing $V_{\rm max}$ for $5.0 < z < 6.7$, the volume is only computed from the layers of the cubes that corresponds to the wavelength of the Lyα emission in this redshift range, whereas the median RMS is computed from the full cube. In that situation, the median RMS image is not as representative of the individual RMS images in that spectral range. The possible effects of this is difficult to assess, since it would require to do the volume computation using different median RMS images for the different redshift bins used to compute the LFs. As seen on Fig. 4.11, the use of a single median RMS image doesn't not seem to be a far-fetched approximation.

Simpler SExtractor criterion. When actually producing the 2D masks, we use a simpler criterion to mock the SExtractor detections. It is hard to know whether this impacts the covering fraction of the masks and if this has any effects on the resulting $V_{\rm max}$ computation. There are no obvious reasons that would lead to think that the use of this simpler criterion is biasing the volumes towards higher or lower values.

Limit magnification. In the definition of the limiting magnification in Eq. 4.6 and Eq. 4.7 we only define one average value per source per cube, when strictly speaking there should be one per source for each layer of each cube. The difficulty here again is the computation time and the difficulty to find a simple criterion that would be coherent with the Muselet detection process without having to do complex and lengthy simulations. As already specified in Sect. 4.5, only a few LAEs (the highly magnified ones) have their $V_{\rm max}$ values completely dominated by the effects of the limiting magnification. For these sources, a small difference in $\mu_{\rm lim}$ would not significantly impact $V_{\rm max}$ since around the highly magnified area, the magnification gradient is strong. On the opposite, for the LAE in the intermediate/lower magnification regime, a small change in $\mu_{\rm lim}$ has a greater impact on the volume computation because of the much smaller magnification gradient in the low magnification areas (see Fig. 3.5 and Fig. 3.6). For all these reasons, and lacking better options, the criteria used to compute these limit magnifications are intentionally conservative to not artificially over-estimate the steepness of the faint-end slope of the LF.

We have not identified any obvious bias or systematic effects that would have a major impact on the $V_{\rm max}$ computation and therefore on the determination of the LF. The following chapter presents the remaining steps required to build the LF.

5 | Determination of the Luminosity Function of LAEs at $3 \lesssim z \lesssim 7$

Contents

In this Chapter, we present the method used to compute LFs from the LAEs detected behind lensing clusters in MUSE cubes. As it was already discussed in Chapter 4, the combination of MUSE data with lensing fields makes this analysis quite challenging. The main difficulty to get around is the computation time.

By construction, the sample of LAEs includes sources coming from very different detection conditions, from intrinsically bright emitters with moderate magnification to highly magnified galaxies that could not have been detected far from the critical lines. To properly take into account these differences it was decided to implement a new version of the $1/V_{\rm max}$ method (Schmidt, 1968; Felten, 1976) that allows to treat all sources individually, from the volume computation to the completeness simulations. The main novelties introduced by this method is an individual $V_{\rm max}$ computation through the MUSE cubes, and completeness simulations using the real spatial and spectral profiles of the sources. The original method developed in this thesis has been published in de La Vieuville et al. (2019).

The organization of this chapter follows the four main steps of the method. Each of these four steps are as automated as possible with minimal input to be injected by the user during the computation to make it easier to add new data cubes to the sample presented in this thesis. The steps are as follows:

1 - The Lyα flux computation and source selection (one per multiple system) are detailed in Sect. 5.1

2 - The $V_{\rm max}$ computation. This volume computation is already presented in details in Chapter 4 and here we only produce a brief summary in Sect. 5.2 in order to make this chapter self-consistent and easier to follow for readers not interested in the technical details.

3 - The completeness estimation is presented in Sect. 5.3. It is computed on a source to source basis and complements the procedure for volume computation in Sect. 5.2

4 - Using the results of the three previous steps, an extensive Monte Carlo (MC) process is implemented for error transfer of Lyα flux, magnification values and completeness. In addition to these errors, an estimate of cosmic variance and of Poissonian error is added to complete the error budget. These aspects are detailed in Sect. 5.4

5.1 Lyα flux computation and final selection of lensed sources

The flux computation is the easiest step of the LF computation, yet it is a crucial point to have luminosity estimates as precise as possible. The flux measurement is made from continuum subtracted Narrow-Band (NB) images containing the entire Lyα flux. For each source, three subcubes are built: a central one containing the entire Lyα signal, and two adjacent ones that are used to estimate the continuum on the blue and red side of the central cube. All three cubes have the same spatial extent of $10'' \times 10''$ and are centered on the same spatial position of the LAE. The two adjacent cubes have a spectral width of 20 Å. The spectral width of the central cube is determined for each source specifically through prior manual inspection of the LAEs. The reason for that is that the width of the Lyα line may differ significantly from one LAE to another and we want to include as little noise as possible while still getting the entire signal of the line. This spectral width may vary from ~ 5 Å for the faintest LAEs to more than 25 Å for the brightest ones. From the two adjacent subcubes, an average continuum image is computed, which is then subtracted pixel-to-pixel to the NB image obtained from the central subcube. The Lyα flux is measured on this resulting image using SExtractor with `FLUX_AUTO`.

The NB images used here are not designed to maximize the signal-to-noise ratio, but rather to contain the entire Lyα emission. And since the sample contains very faint and low surface brightness galaxies, all the LAEs are not successfully extracted on the first try. An iterative and automated

procedure is implemented to extract the reluctant LAEs. At each new iteration, the main SExtractor parameters are loosened (decrease of `DETECT_THRESH` and `MIN_AREA`, see Sect. 4.2 in Chpt. 4 or the SExtractor manual for more details) until a successful extraction is achieved. The precise values of the SExtractor parameters used for the extraction have little to no impact on the flux measurement, and an extraction is considered successful when a source is recovered at less than $1''$ from its original position in the input catalog. Such a coordinate offset can be observed if the Lyα emission has a different morphology than the UV-continuum, or when the morphology of the emission in the NB image used for flux computation is too different from the one in the Muselet NB image used for the initial detection. Using this method, we are effectively forcing the flux measurement at the expected position of the source. Once all the sources are extracted, a careful review is done to ensure that no mis-match is made.

The choice of using SExtractor with `FLUX_AUTO` is made for several reasons:

- SExtractor has been proven to provide robust estimates of the total flux of sources to the 5% level (See for example Sect. 10.4 Fig. 8 of the SExtractor manual). This aspect is important for this work as it has been shown that many LAEs have an extended halo, especially at high redshift (see Wisotzki et al., 2016; Leclercq et al., 2017; Wisotzki et al., 2018).
- The automated computation of both the aperture shape and size is very useful to properly measure the flux of distorted sources that are frequent in lensing fields.
- Finally, `FLUX_AUTO` has a module that performs a very basic correction for sources contaminated by closeby neighbours.

Other possibilities exist for the flux measurement but are less suited or more complex to implement in lensing fields (e.g.,NoiseChisel in Akhlaghi & Ichikawa (2015) LDSCat in Herenz et al. (2017) or the curve-of-growth implementation presented in Drake et al. (2017b)).

5.1.1 Source selection and flux weighted magnification

Section 3.2.3 presented the intial detection of the entire galaxy sample, including the LAEs in MUSE cubes. This step was detailed earlier to underline the importance on the new MUSE detections to build improved mass models. However, regarding the need of the LF computation, a new source selection is required to keep only one image per multiple system. This new selection is done after the flux measurement of all possible LAEs as the robustness of the flux measurement is a relevant element to guide the decision of which image to keep. Another important aspect is the accuracy of the magnification factor. No written rule is used for this image selection: all images of each multiple system are manually inspected to determine which one is the more robust and reliable for the need of the LF calculation. The decision is arbitrary but some important aspects are systematically looked at to estimate the robustness of multiples images:

- The S/N of the images. Multiples images can be detected on different part of a MUSE mosaic with varying depth. This effect is important in A2744 where the difference in exposure time for the different parts of the mosaic is significant.
- The reliability of the flux measurement: whether the image might be contaminated by a close-by neighbour.
- Consistency of the flux measurements among the images part of a same multiple system. An image whose intrinsic flux (i.e., corrected from magnification) would be significantly different from the intrinsic flux derived with the other images, is not reliable. Obviously, in the case of a multiple system with only two images, this test cannot be done.
- The magnification estimate. The higher the magnification, the higher the uncertainty on the

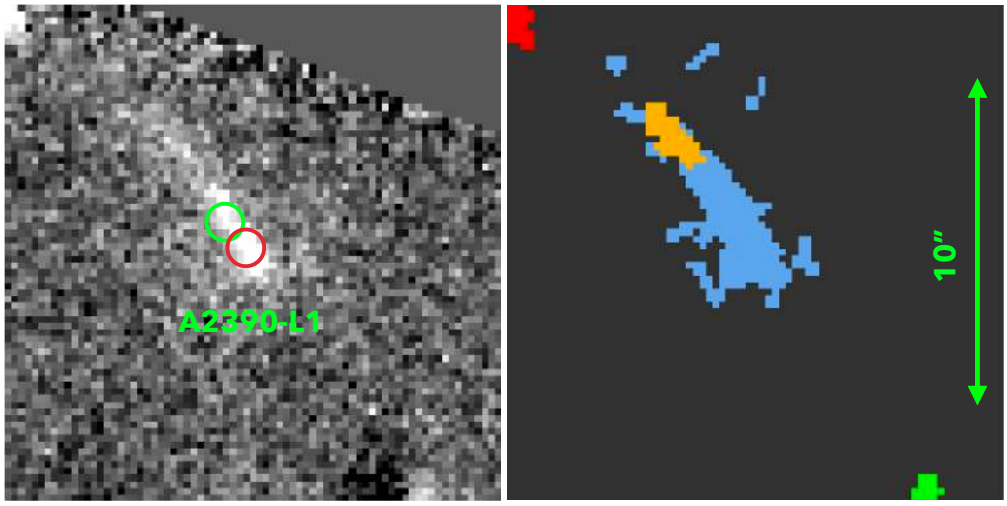

Figure 5.1: Example of segmentation (right panel) from the NB image used for the flux computation (left panel). The arc here is A2390-L1. Its flux weighted amplification is $\mu = 19.8$. The position of the source in the input catalog is shown with the red circle, and the position extracted with the flux measurement is shown in green. The segmentation is not ideal for this arc, as part of the orange object is in the aperture used to measure the flux of the blue object.

magnification.

- Multiple images merging together or blended introduce biases in the flux measurement as the magnification of each image cannot be properly related to the extracted flux in the Lyα line.
- The surface brightness. Images with very low surface brightness tend to behave badly during completeness determinations.

For example, an image part of a gravitational arc is often not the best choice. Even though the S/N may be high due to high magnification, the segmentation is often uncertain or at least difficult to achieve. The likelihood of making a mismatch when forcing the flux extraction is higher, and the resulting segmentation is less reliable (and may not be coherent with the segmentation used in 5.3 for the completeness simulations). As shown in Fig. 5.1, doing precise and automated photometry on these sources is difficult as a proper segmentation of these arcs is not always easy to achieve. The only parameter that can be tuned to optimize the extractions is the width of the NB image.

To measure the flux weighted amplification of each LAEs, the `Object` check-image produced by SExtractor is used for each LAE. This image is a combination of the two images shown in Fig. 5.1 but with a prior background subtraction. In other words, this image contains the flux of the detected object and nothing else. The `Object` image is then projected on an image plane amplification map at the redshift of the source and the weighted amplification is given by:

$$\mu = \frac{\sum_i F_i \mu_i}{\sum_i F_i} \tag{5.1}$$

where i is indexing the pixels of the segmented source and μ_i and F_i are respectively the magnification and flux of the individual pixels.

Sometimes lacking better option, gravitational arc images are kept in the final LAE sample. This happens for example, for the lower exposure cubes where the other images of the same system are too noisy or cannot be extracted/detected, even though they are predicted by Lenstool. An illustration of such a case is displayed in Fig. 5.1. In this situation, the use of the flux weighted magnification ensures that the magnification is consistent with the extraction made and severely

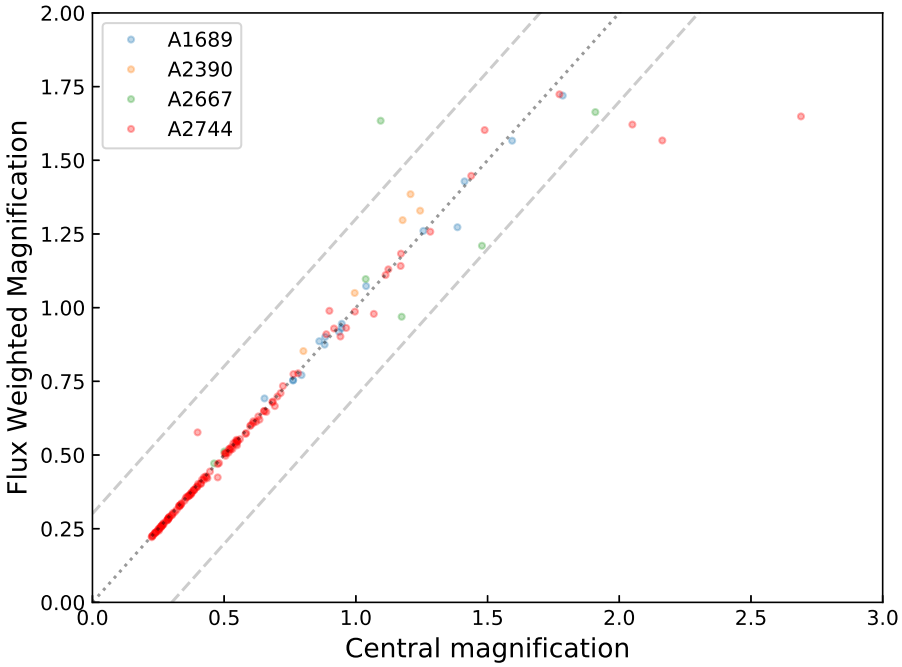

Figure 5.2: Flux weighted amplification versus central magnification. The central dotted line is the 1-1 relation and the two dashed lines correspond to a factor two of difference.

limits the impact of the extremely magnified pixels on the measure of magnification. For extended sources or sources falling close to the critical lines of the clusters, the flux weighted amplification is a more robust estimate compared to the central magnification. For sources with "small" magnification (i.e. $\mu \lesssim 25$), the difference between flux weighted or central magnification is almost negligible, as illustrated in Fig. 5.2. In the rest of the method, the flux weighted magnification is used as the best estimate for all sources.

5.2 Vmax computation summary

Because the volume computation is a complex problem, the complete description and motivations for the implemented method are given in Chapter 4. For the readability and the consistency of this current chapter, a very short summary of the method is nonetheless provided here.

By definition, $V_{\rm max}$ is the volume of the survey where one given source could have been detected. This value has to account for the spectral variation of noise caused by the varying sensitivity of the MUSE instrument, the increased noise caused by the sky emission lines on certain layers (see e.g., Fig. 4.10) and the spatial variations of noise caused by the different exposures in a MUSE mosaic (see e.g., Fig. 4.11 or Fig. 4.13). The computation developed in this work is non parametric and based on individual source features to properly take into account the three points mentioned above.

Because of strong lensing effects, the computation has to be done in the source plane to avoid counting several times areas of the survey that are multiply imaged by the clusters. This is the main difficulty as source plane reconstructions are computationally expensive. Mocking the detection process of individual LAEs in a subsample of wavelength layers of MUSE cubes to produce detectability maps (masks), we are able to obtain 3D masks of the survey in the source plane. One of theses 3D masks is produced for each LAE of the sample, and precisely shows where (spatially

and spectrally) the level of noise would allow the detection of this LAE. On these individual 3D source plane masks, an additional level of refinement is used by combining these masks with a source plane magnification map. This is done to mask the areas of the survey where the magnification would have been too low to allow the detection of a given LAE. This threshold magnification, called limiting magnification (see Eq. 4.6 and 4.7), is computed for each LAE in each cube as the detectability of a given LAE in different cubes depends on both the exposure time and the seeing conditions.

The final volume integration is computed on the unmasked pixels of these 3D source plane masks resulting from the analysis of both noise variations (spatial and spectral) and the magnification fields induced by the clusters, using conventional cosmological volume integration (see Eq. 4.8). To study a possible evolution of the LF with redshift, $V_{\max}$ is computed for four different redshift ranges: $2.9 < z < 6.7$, $2.9 < z < 4$, $4.0 < z < 5.0$ and $5.0 < z < 6.7$ (hereafter $z_{\rm all}$, z_1, z_2 and z_3).

5.3 Completeness determination

The completeness computed in this section is different from what is usually called completeness. The likelihood of detecting a certain source given a certain realization of a noise distribution – called completeness in this work – is separated from the volume computation. The idea behind that, is that all LAEs part of the sample would not have a 100% chance of being detected in their own layer: given a different realization of a same noise distribution, the same source may not have been detected. The completeness described in this section reflects how lucky we were when we detected a specific source, whereas the volume computation reflects the positions in the cubes where this source could have been detected given the observed realization of the noise. The completeness values derived in this section are then used to correct the contribution of each source to the LF (see Sect. 5.4): if a source is detected only one in five times, statistically, four additional and similar LAEs were not seen during the original detection process.

To continue in the non-parametric approach and individual computation developed for the $V_{\max}$ computation, the completeness simulations are done in the image plane, on a source to source basis, using their own profile. The advantage of doing so, is to precisely account for a wide range of source profiles, both spatial and spectral. Given the definition of completeness, the simulations can be restricted to 2D simulations using the detection layer of individual LAEs. The first step to get the completeness of an LAE is to retrieve its detection profile (see Sect. 5.3.1). The second step is to inject this profile in the masked detection layer of the LAE and try to recover all the injected fake sources using the same detection process as the one used to create the input catalog (see Sect. 5.3.2). This second step is repeated many times to derive the variation on the recovered fraction of sources and therefore the uncertainty on the completeness value.

5.3.1 Source profile reconstruction

To extract the detection profiles of LAEs, once again we mock the original detection process. The goal is to obtain a segmentation of the source on which we can apply a flux map.

To produce such a segmentation map, for each LAE, the MUSELET NB image provides the best detection of the source, called hereafter the max-NB image. The layer index of the max-NB image is manually selected from visual inspection of the source in the MUSELET cube. This task is not automated as the redshift is often not precise enough to select the correct MUSELET NB. And for the faintest LAEs, a difference of only one in the index of the layer is enough to miss the a large part of the Lyα signal and would lead to a serious underestimation of the completeness. For consistency with the original detection process, SEXTRACTOR is used with the same configuration as the one used within the MUSELET software. In practice, two steps are performed to recover the

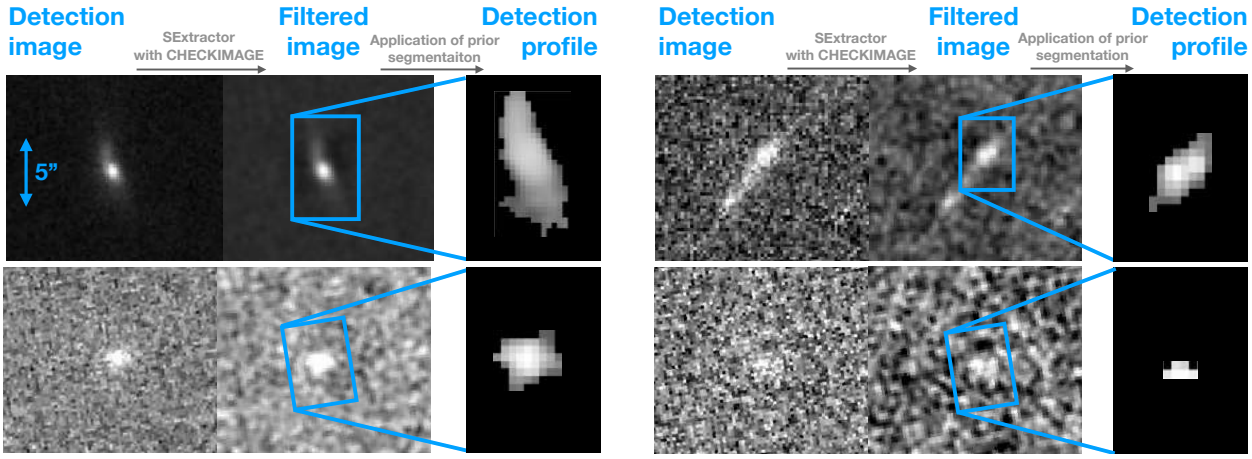

Figure 5.3: Four examples of the process used for retrieve the detection profile of LAEs. For each example, the leftmost image is the max-NB image, the middle one is the filtered image and the right most is the detection profile used for the completeness simulations. The four LAEs used in this figure are A2390-96 (upper left), A2667-30 (upper right), A2744-2956 (lower left) and A2744-12-26 (lower right). These four LAEs have a flag value of 1, meaning that their profile was succesfully extracted using the original detection parameters. The spatial scale for the max-NB images and filtered images are the same across all four examples.

detection profiles:

- From the max-NB image, we force the source extraction using a similar method as the one presented for the flux computation in Sect. 5.1. SExtractor is used on the max-NB image, progressively loosening `DETEC_THRESH` and `MIN_AREA` if the extraction with the original detection parameters (`DETECT_THRESH = 1.3` and `MIN_AREA = 6`) is not successful. The goal of this SExtractor run is to obtain a segmentation of the input LAE on the max-NB image.
- In parallel, we compute the filtered image. This image is produced using `-CHECKIMAGE_TYPE FILTERED` when calling SExtractor. The filtered image is the convolved and background subtracted image that SExtractor uses internally to evaluate whether a certain group of pixel is sufficiently above the background noise to be considered as a detection.

To obtain the detection profile of LAEs, the segmentation obtained in the first step is applied on the filtered map. The point of using the filtered image to retrieve the pixel values is that the background has been removed, and the convolution prevents the inclusion of too much noise in the pixels of the faintest LAEs. Four examples of this process are provided in Fig. 5.3, spanning a wide range of detection conditions, from very bright sources to faint and diffuse LAEs. Even though the method sometimes fails to properly recover a realistic detection profile (see lower right panel of the figure), as long as the few brightest pixels are in the final detection profile, the impact on the completeness computation remains minimal. Indeed only the brightest pixels are needed to ensure the recovery of the injected sources. More details on these technical aspects are given in Sect. 5.3.2.

A flag is associated to each LAE to reflect the quality of its extraction. As mentioned in the previous paragraph, if the extraction fails using the original detection parameters, the detection parameters and the matching radius are progressively loosened using predefined combinations of these three parameters. To each of the predefined combinations, a flag value is associated. A source with a flag 1 is extracted using the original detection parameters and a matching radius of $0.8''$ (i.e., four MUSE pixels). A source with a flag 2 is still quite a good extraction and a source with a flag 3 is untrustworthy because of the higher chance of mismatch and the (too) weak signal

recovered in the extracted pixels. LAEs with a flag 3 are likely to lead to a considerable underestimation of the completeness and are therefore removed from the process at this step of the method.

More than 95% of the LAE sample has a flag value of 1, and all examples displayed in Fig. 5.3 also have a flag value of 1. For the few sources with a flag above 1, several explanations are possible:

- The image used to recover the profiles ($30''$) is smaller than the entire max-NB image. As the SExtractor background estimation depends on the size of the input image, this may slightly affect the detection of some objects. This is most likely the predominant reason for a flag 2 object.
- Small differences in coordinates between the recovered position and the position listed in the input catalog. This may be due to a change in morphology with wavelength or band-width. By increasing the matching radius to recover the profile, a successful extraction is obtained but the flag is also affected and can increase.
- Mis-identification of the max-NB image. In that case the NB used to extract the profile is not the Muselet NB offering the best detection conditions. As the determination of the max-NB image relies on a manual inspection of a Muselet NB subcube centered on the LAE, such an error can happen. The identification of the layer with the best SN is not always easy and may not corresponds with the maximum of the Lyα emission, especially in the wavelength domains heavily affected by the sky emission lines.
- The source is extremely faint and was actually detected with a relaxed set of detection parameters.

We have checked that no LAEs that were expected (forced) to be at a certain position as part of multiple-image system are included in the final sample. This is to say, we have not selected the noisiest images in multiple-image systems.

5.3.2 Source recovery experiments

The detection profiles computed in the previous section are used to make source recovery simulations in the image plane. Using individual profiles retrieved from the detection images allows the properly take into account both the spatial and spectral profiles of the LAEs. Here again the detection process is the same as the original one used to produce the initial source catalog. The only difference, is that instead of using Muselet on the full 3D cubes, we use SExtractor in the same configuration on only one layer of the parent cube for each LAE. This simplification allows a huge gain in computation time.

For each LAE, the input image on which the profile is randomly injected is a masked max-NB image. The mask picked for the max-NB image is picked following the same rule as described in Sect. 4.4.3, that is to say, it is picked based on the S/N of a given LAE in its own detection layer. The point of using such a mask for the simulation is to set a cut in noise level on the input image while still keeping a realistic realization of noise in the rest of the input image. The detection profile is then injected a maximum of 500 times at random positions on the unmasked areas of this input image to produce a mock image. Each time a mock source is injected its position is masked to avoid any overlap with other mock sources. SExtractor is then launched on this mock image with `DETECT_THRESH = 1.3` and `MIN_AREA = 6` to obtain a complete detection catalog. The recovered sources are the sources in the detection catalog that match the input sources based on a spatial match of radius $0.8''$. The completeness is given by the ratio between the number of sources injected and the number of recovered sources. To derive uncertainties on the completeness, the same simulations are performed multiple times and the distribution of recovered fraction gives the uncertainty on the completeness. For the efficiency of the computation, the iterations on the

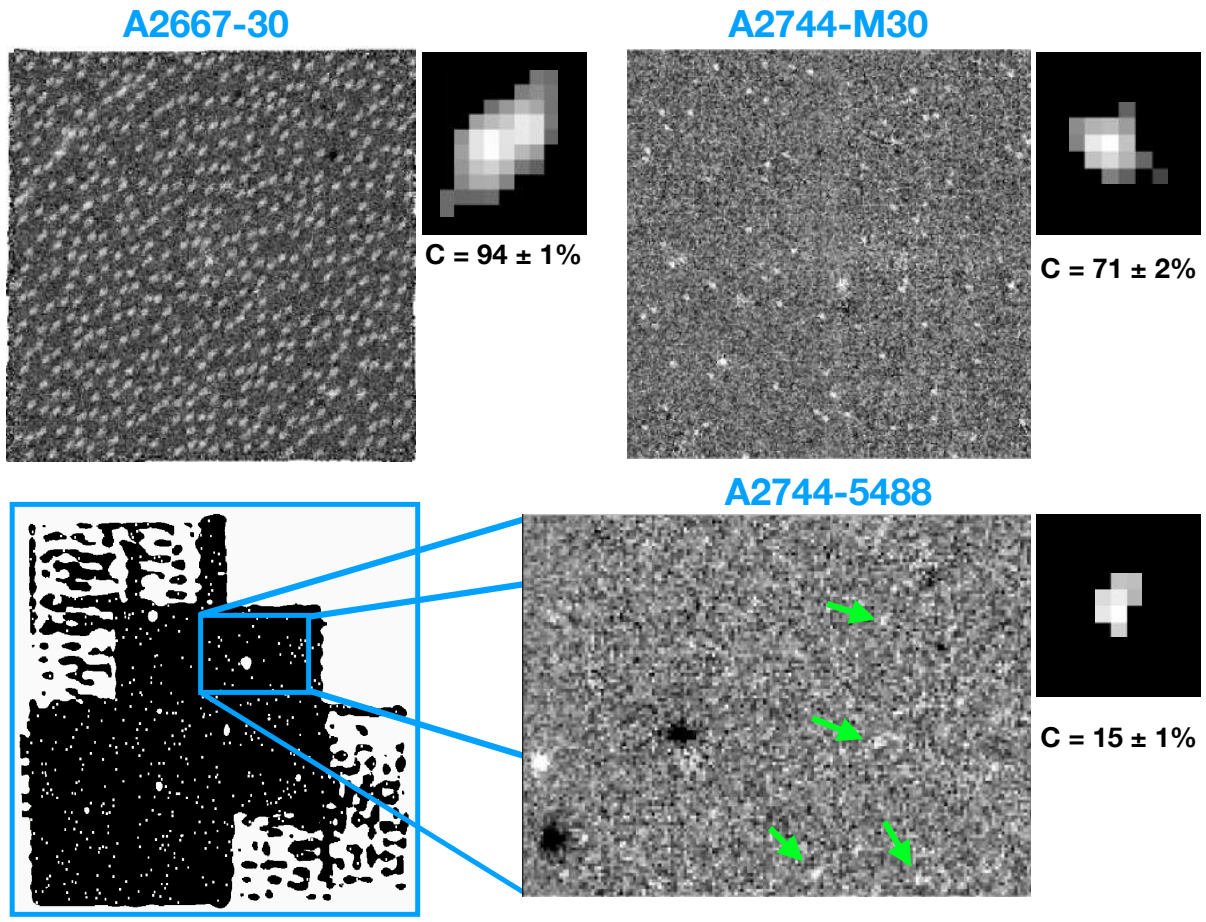

Figure 5.4: Examples of mock images, detection profiles and derived completeness for three LAEs. For A2667-30 the entire mock image is shown, For A2744-M30, the FoV being much larger, only the central and deepest region of the A2744 mosaic is shown. For A2744-5488, because it is so faint and the mock sources hard to see, an even smaller portion of the FoV is displayed. For this LAE, in addition, the mask applied to the A2744-5488 max-NB image is shown and some of the injected mock sources are highlighted with a green arrow. The small white rectangles in the mask correspond to the position of each injected sources masked to avoid any overlap.

source recovery experiments are parallelized.

Examples of mock images and the derived completeness are given in Fig. 5.4 for three LAEs with flag 1 ranging from bright to very faint. For A2667-30, the completeness is almost 100%. This LAE being bright, the mask used to cover the max-NB image has a covering fraction of 0 (i.e., not effectively masked). The original source can be seen in the gravitational arc in the upper left corner of the image. For A2744-M30, no mask is used either, the completeness derived is as high as 70% but the mock sources are already much harder to spot. Finally for A2744-5488, the completeness is around 15%, a large fraction of the max-NB image is masked and the mock sources are barely visible. These examples illustrate three things:

- The higher the signal to noise of the detection, the higher the completeness.
- For sources well detected and easily extracted like A2744-M30, the likelihood of detection is indeed affected by the precise realization of a given noise distribution. Since no mask is used to compute the completeness of this source, it means that everywhere on the mosaic, the (local) average noise level is low enough to allow its detection. Yet the completeness of

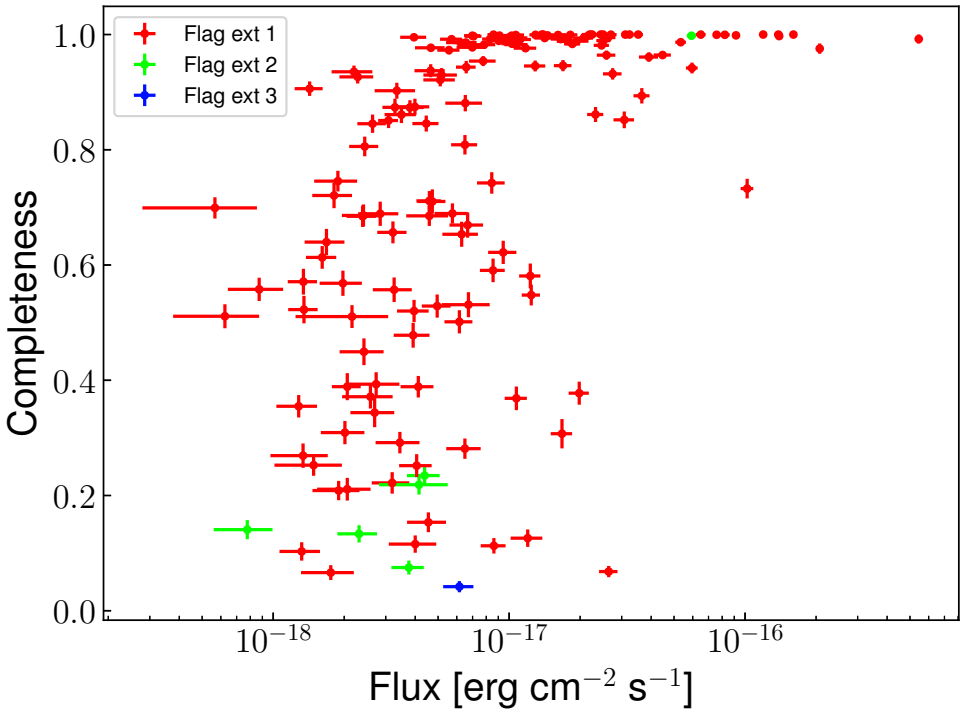

Figure 5.5: Individual completeness for all LAEs of the lensing sample displayed as a function of their detection flux. The value of the extraction flags is encoded in the color.

that source is not 100% showing the effects of the random variation of noise within a certain distribution. In simpler words, this is a good example to show that sometimes, we are just lucky in our detection process.

- For the faintest sources, the volume computation and the masking process is not perfect, otherwise it would be extremely unlikely to have completeness value under 50% since the input image is masked according to the local average noise level on the max-NB image. This aspect is discussed in more details in next section.

5.3.3 Results and discussion

In addition to the LAEs with a flag value of 3, all LAEs with a completeness value below 15% are also removed from the sample used for LF computation. Figure 5.5 summarizes the results of the completeness computation. The results shown in this figure are for the LAEs of the entire lensing sample: unlike the volume computation, the results of the completeness computation are purely source based and completely independent of the rest of the sample. The median and average values are respectively 0.90 and 0.74. Such high completeness value are explained by the fact that the images used as input are masked, leaving only the cleanest parts of the FoVs to perform the simulation with. As seen in this figure, there is no well defined trend between the completeness and the detection flux. This shows the impact of the individual spatial and spectral profile: at a given flux, a more extended source has a lower surface brightness and a lower completeness. And the same goes for the spectral profile: a larger line spreads the Lyα signal on more spectral layers, leaving less flux on the max-NB image with and leading to lower completeness.

Assuming the masking process were perfect, there would be almost no sources with a completeness value under 50%, since the masking process is based on a comparison with the local and

average level of noise. As seen in Fig. 5.5, this is not the case here and only $\sim 20\%$ of the LAEs have their completeness below this limit. On the contrary, having 80% of the sample over the 50% limit, with half of the sample over 90% shows that for most LAEs, the masking process/volume computation is accurate. The goal of this paragraph is to discuss the minority of sources below 50% of completeness.

For these LAEs, the masking process leaves unmasked areas of the survey where the average noise is too high to actually allow the source detection. This means that the $V_{\rm max}$ value is overestimated. In that situation, the meaning of the completeness correction is slightly altered: in addition to its usual definition (probability of detecting a source given a certain noise distribution), it carries an average component that allows for an individual and average $V_{\rm max}$ correction. The max-NB image of such a LAE has a mask with an underestimated covering fraction, leaving uncovered (too) noisy part of the image contribute to a low completeness value. The final completeness value is therefore representative of the error made during the masking process, and in that sense, helps correcting for this error and for the overestimation of $V_{\rm max}$.

A more popular approach to estimate the completeness is to perform heavy Monte Carlo simulations in each cube of the survey to get a parameterized completeness. Such a parameterization allows to compute a volume without needing to dissociate the $V_{\rm max}$ and completeness computation (see Eq. 4.1). The advantages and details of such a method are discussed in the introduction of the previous chapter.

The non parametric method developed in this section is complementary to the volume computation method. Its main strengths is that it is fast and easy to implement while being well suited to account for a wide range of spatial and spectral profiles. This exercise reaches its limits for very low surface brightness LAEs, for which it is almost impossible to determine a proper profile with SExtractor. Such a source was removed from the A2744 sample: A2744-5681. Its completeness value computed were unrealistically low leaving this source with a largely overestimated contribution to the LFs.

5.4 Computing the LF points

In this section, we explain how all the previous steps are combined to build the LF while accounting for all possible sources of uncertainty. In practice, we split the LAE sample in four redshift bins, $2.9 < z < 6.7$, $2.9 < z < 4$, $4.0 < z < 5.0$ and $5.0 < z < 6.7$ (hereafter $z_{\rm all}$, z_1, z_2 and z_3), and apply the process described below to each of them to study a possible evolution of the LF shape with redshift.

The $V_{\rm max}$ method is a binned representation of the LF, and as such the first step is to define luminosity bins. The value of each bin is computed as follows:

$$\Phi(L_i) = \frac{1}{\Delta \log L_i} \sum_j \frac{1}{C_j V_{\rm max,j}} \tag{5.2}$$

The index j refers to the individual LAEs that have a luminosity within the luminosity range centred on L_i, C_j to the individual completeness correction computed in Sect. 5.3, and $V_{\rm max,j}$ to the individual $V_{\rm max}$ value computed in Sect. 5.2 for a given redshift bin. The first term $\Delta \log L_i$ is the width of the luminosity bin in logarithmic space. This normalization is often used in the study of the LF to derive the numerical density expressed per covolume units per luminosity dex. Using this computation, we obtain one single LF. The luminosity binning used is determined in such a way that each bin is properly sampled in both redshift and luminosity. The larger the sample, the smaller the bins can be.

To obtain realistic uncertainties, we use a MC process. From the parent LAE catalog, modified catalogs are generated for each iteration by perturbing the completeness, detection flux and magnification of each LAE. The detection flux and completeness are perturbed within their error bar assuming a Gaussian distribution and for the magnification, a random value is drawn from $P(\mu)$. Combining the random values obtained for the detection flux and the magnification results in a random luminosity, giving the possibility for LAEs with poorly constrained magnification (i.e., highly magnified LAEs) to contribute over several luminosity bins during this iterative process. The perturbed values of completeness value will make the contribution of each LAE vary accordingly. For each iteration a single LF is computed using Eq. 5.2. The distribution of LF values obtained at the end of the MC process is used to compute the average value in linear space and to derive asymmetric errors for each luminosity bin. All the results showed in this thesis are derived using at least 10 000 MC iterations. To obtain the final uncertainties, we combine an estimate of cosmic variance obtained with the cosmic variance calculator from Trenti & Stiavelli (2008)[1] with the Poissonian uncertainty and the error derived from the MC process using for the luminosity bin centred on Li:

$$\Delta\Phi(L_i)^2 = \frac{1}{\Delta \log L_i} \frac{N_{i,c}}{< V_{\rm max} >} \sqrt{\delta_{\rm CV}^2 + \left(\frac{1}{\sqrt{N_i}}\right)^2 + \delta_{\rm MC}^2} \tag{5.3}$$

where $\delta_{\rm MC}$ is the uncertainty derived from the MC iterations, N_i is the observed number of LAE, $\delta_{\rm CV}$ is the estimate of the relative count uncertainty due to cosmic variance, $N_{i,c}$ is the completeness corrected number of LAEs and $< V_{\rm max} >_i$ is the average $V_{\rm max}$ value of the LAEs in that bin. The contribution of Poissonian uncertainty to the final error is given by the $1/\sqrt{N_i}$ term.

An illustration of this process is shown in Fig. 5.6. In this figure, the perturbed LF computed during the MC iterations are shown as cyan transparent lines. The blue points show the LF computed from the non-perturbed original LAE catalog with no error bars. The final points combinning the Poissonian uncertainty, the estimate of cosmic variance and the results of the MC process are shown as red points. The cyan spikes that are seen for $\log L \lesssim 41$, are caused by LAEs with a high contribution to the numerical density and with a very large $P(\mu)$. Such LAEs frequently jump from one luminosity bin to some other during the MC iterations leading to a high dispersion. At lower luminosities, because the magnification is much more constrained and because of the higher number of sources detected, such spikes are less likely to appear. The uncertainty due to cosmic variance on the intrinsic counts of galaxies in a luminosity bin typically range from 15% to 20% for the global LF and from 15% to 30% for the LFs computed in redshift bins because of the reduced volume of the survey. For $\log L \lesssim 41$, the total error budget is dominated by the MC dispersion, which is caused by objects with poorly constrained luminosity jumping from one bin to another during the MC process. The larger the bins the lesser this effect is, as a given source is less likely to jump outside of a larger bin. For $41 \lesssim \log L \lesssim 42$ the Poissonian uncertainty is slightly larger than our estimation of the cosmic variance but does not completely dominate the error budget. Finally for $42 \lesssim log(L)$ the Poissonian uncertainty is the dominant source of error due to the small survey volume and therefore small number of bright sources. The value of the final LF points computed for the four redshift bins are displayed in Table 6.1 in next chapter.

5.4.1 Tests with different luminosity binnings

Because the choice of a specific luminosity binning possibly affect the shape of the LF and the measurements of the Schechter parameters (see Sect. 1.2.3.1), we also compute the LFs using alternative binnings. To create these additional binnings, we restrict the luminosity range to the

[1] available online at `http://casa.colorado.edu/~trenti/CosmicVariance.html`

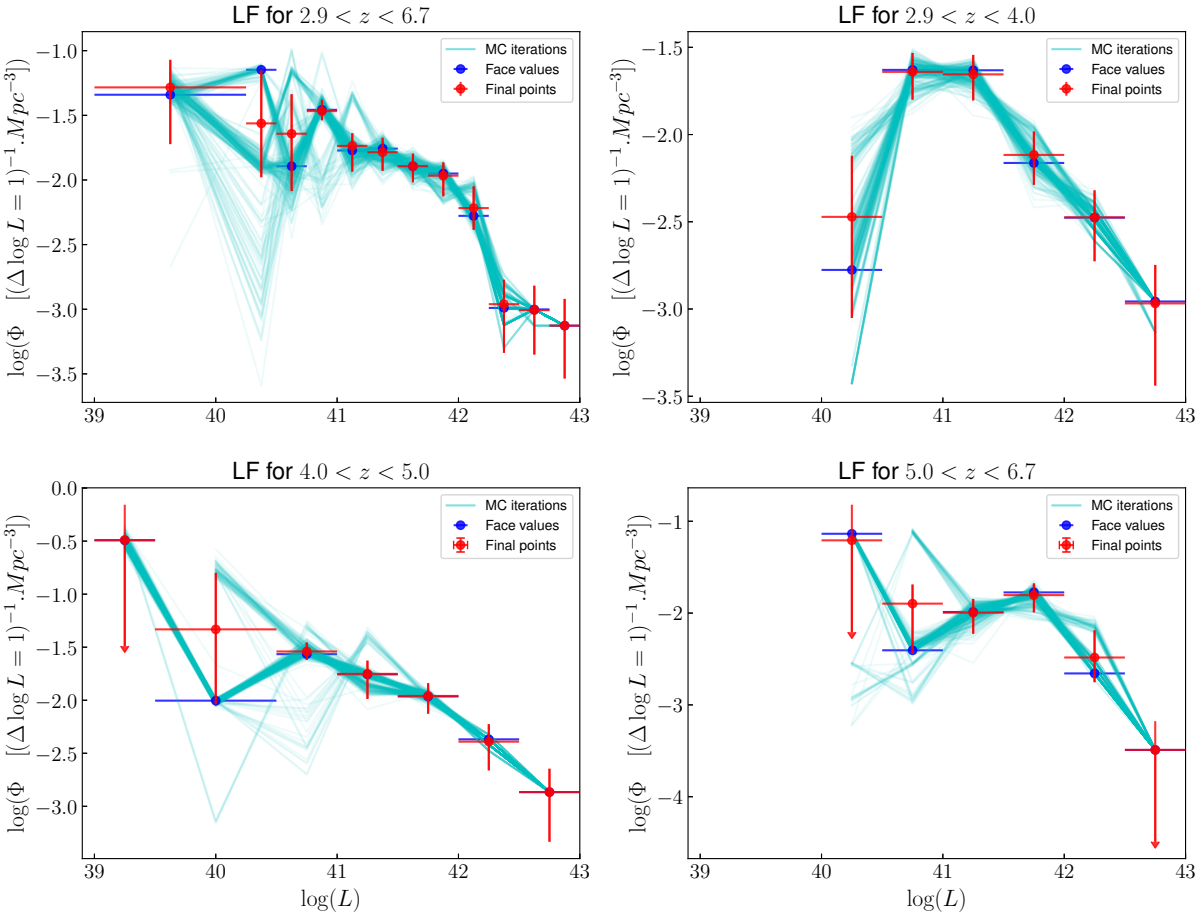

Figure 5.6: Distribution of LF derived during MC iterations are shown a cyan transparent lines, the face value LF built from the non perturbed LAE catalog in shown in blue and the final points with MC uncertainties, Poissonian uncertainties and cosmic variance error count combined are shown in red. For each LF point, the final points is the average in linear space of the distribution resulting from the MC iterations. Because the focus of this plots is the visualization of the MC iterations, all the plots do not have the same y-range

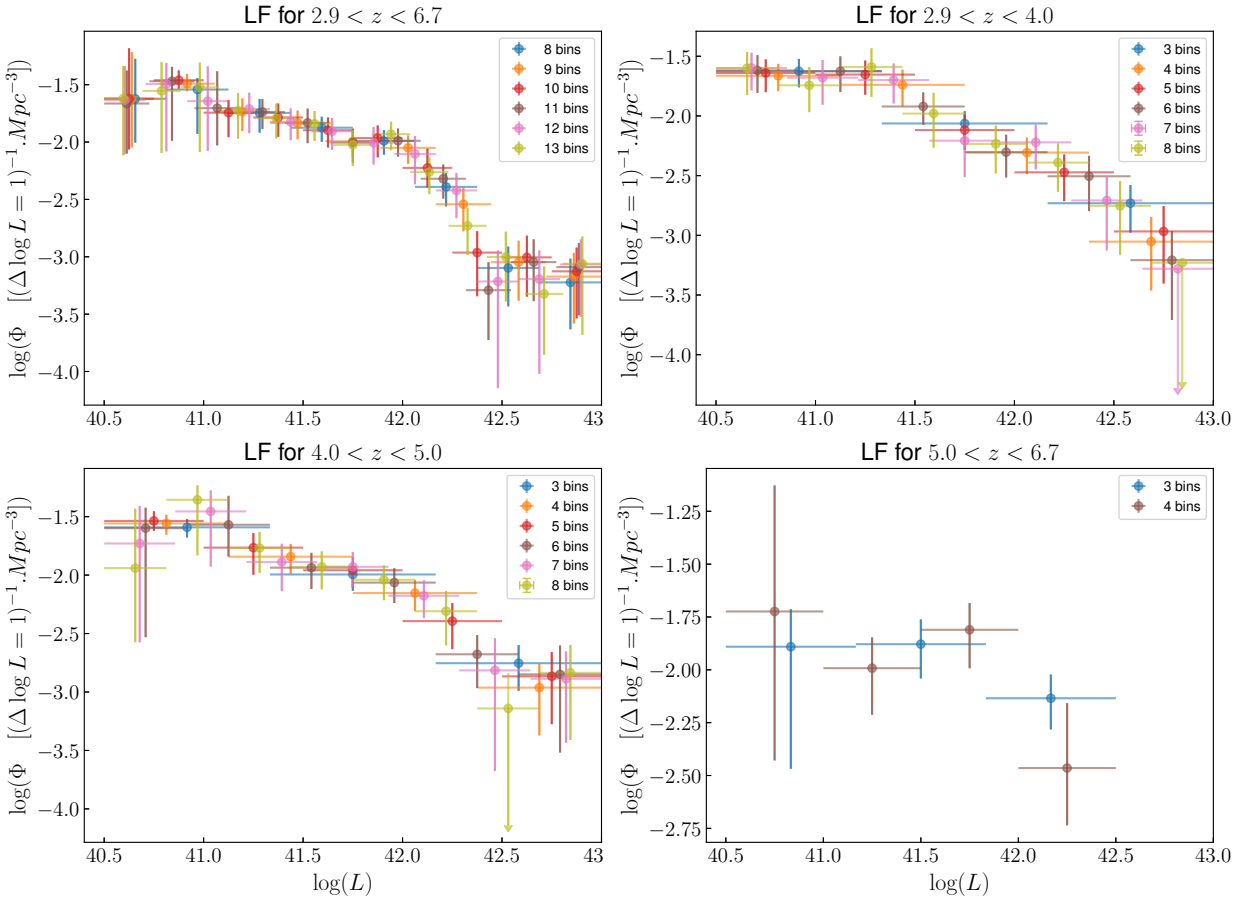

Figure 5.7: LFs derived using the same population but different bin sizes to study the impact of binning on the faint end shape.

range where all the bins are properly sampled and no sign of incompleteness is shown. In this luminosity range, we build the LFs by varying the number of bins. An example of all the LFs computed using different binnings is shown in Fig. 5.7. The first thing to note is that for all four redshift bins, all the tests are consistent with each other. This shows that our LFs are robust and that their shape do not depend significantly on the choice of binning. We can also see that some points transform to upper limits when increasing the number of bins. As the size of the bins decreases, both the Poissonian uncertainty and the dispersion caused by the MC process increase, and if the total combined inferior error is over 100%, the value shifts to an upper limit. For the most populated LFs at lower redshift, we can test many different binnings and still properly sample each bin in both redshift and luminosity. This is obviously not the case at higher redshift where the selected population is less numerous. For z_{all} z_1 and z_2, all the tests show the exact same trend and lead to an almost continuous series of points. For z_2, we notice a small drop at lower luminosity for the tests with the highest number of bins. However, all points remain consistent with the other series due to the larger uncertainties caused by the reduced statistics and the smaller bins. As expected, for z_3 the impact is more important. Because of the much lower number of sources, the reasonable binnings to test are very limited as we can only try with three and four bins. This shows that the results derived for z_3 are less robust and are to be taken with caution.

6 | Results: The LAE LF

Contents

In this chapter we present the results obtained during the LF analysis. The first section (Sect. 6.1) describes the intrinsic properties of the final sample used for the LF computation and makes a comparison with the LAE of the MUSE-HUDF in Drake et al. (2017a) (D17 in this chapter). Section 6.2 presents the different steps of the analysis done on the LF computed in previous chapter. This includes an analysis of the results obtained with the lensing sample only and a Schechter analysis performed with additional data from the literature to complement the bright end of the LFs. Finally, in Sect. 6.3 we discuss the impact of the choice of mass model on our results and the possible implications regarding reionization.

6.1 Presentation of the lensed LAE sample and comparison with the MUSE-HUDF sample

Following the analysis of the multiple systems in Sect. 5.1, the LAE sample consists of 156 lensed LAEs. Four of these are removed during the completeness computation (presented in Sect. 5.3) because it was estimated that their recovered profile was not trustworthy (flag = 3) or because their completeness was below the (arbitrary) 10% threshold. The final sample used for the computation of the LF consists of 152 LAEs: 15 in A1689, 5 in A2390, 7 in A2667 and 125 in A2744. The large difference between the number of sources behind A2744 and the three others is expected for two reasons:

- The A2744 cube has a larger FoV (2×2 MUSE mosaic) and is deeper than the three others with an average of four hours of exposure in each quadrant and an additional 2 hours in the centre (see Fig. 3.4).
- The larger FoV of the A2744 cube allows to reach further away from the critical lines of the cluster, therefore increasing the probed volume as we get close to the edge of the mosaic.

These two combined effects make the volume probed in A2744 much larger than the three other cubes combined and it is therefore not surprising to find most LAEs behind this field. The total volume of the survey is of 16 454 Mpc^3 distributed as follows among the four clusters: 1 492 Mpc^3 for A1689, 720 Mpc^3 for A2390, 881 Mpc^3 for A2667 and 13 361 Mpc^3 A2744. These values are computed using the entire volume of each cube for LAEs in the range $2.9 < z < 6.7$.

Even though this difference in source count is expected, it seems that we are also affected by an over-density of background sources at z = 4 as shown in Fig. 6.1. This overdensity is currently being investigated as a potential primordial group of galaxies by G. Mahler (in preparation). The complete source catalogue is provided in annex in Table D.1 and the Lyman-alpha luminosity distribution corrected for magnification is shown in the right panel of Fig. 6.1. The corrected luminosity $L_{\mathrm{Ly}\alpha}$ is computed from the detection flux $F_{\mathrm{Ly}\alpha}$ with:

$$L_{\mathrm{Ly}\alpha} = \frac{F_{\mathrm{Ly}\alpha}}{\mu} 4\pi D_L^2 \tag{6.1}$$

where μ and D_L are the flux weighted magnification and the luminosity distance of the source. respectively. The uncertainties have been omitted in this plot for clarity. The objects with the highest magnification, which often coincide with the objects with the lower luminosities, tend to have the larger uncertainties as explained in Sect. 3.3.2.

Figure 6.2 shows the completeness computed for each LAE as a function of redshift (or detection wavelength) and detection flux. This figure shows that, apart from the obvious flux - completeness correlation, there is no sign of correlation between the position of sky-emission lines and the completeness. This tends to show that the profile of the sources (and not the flux) is a dominant factor when it comes to estimating the completeness properly. Various values of interest from the final LAE catalog are shown in a correlogram and correlation matrix in Fig. A.1 and Fig. A.2

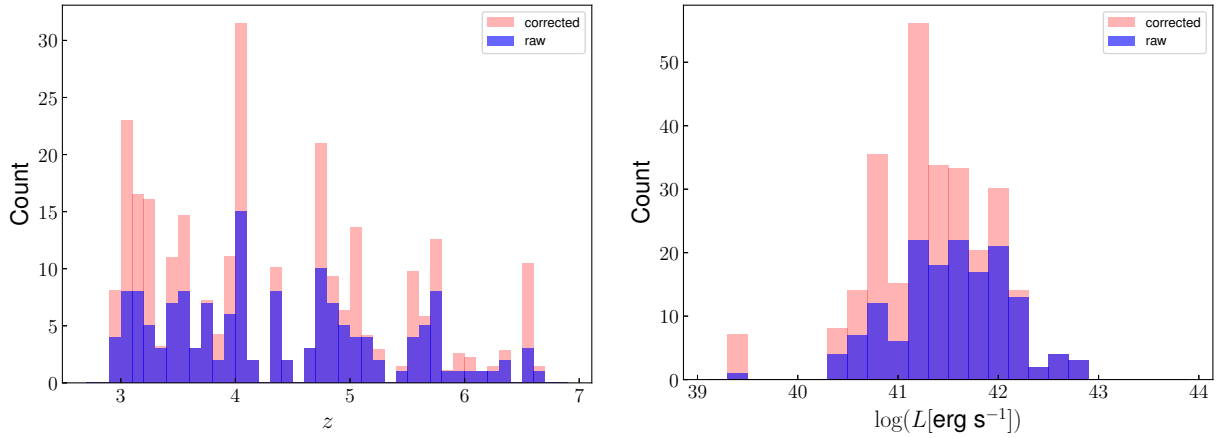

Figure 6.1: Redshift and magnification corrected luminosity distribution of the 152 LAEs used for the LF computation (in blue). The corrected histograms in light red correspond to the histogram of the population weighted by the inverse of the completeness of each source. There is no evidence that the empty bins seen on the redshift histograms are correlated with the presence of sky emission lines.

respectively.

Figure 6.3 compares the final sample with the sample used in the MUSE HUDF LAE LF study D17. The MUSE HUDF (Bacon et al., 2017), with a total of 137 hours of integration, is the deepest MUSE observation to date. It consists of a 3×3 MUSE FoV mosaic, each of the quadrants being a 10 hours exposure, with an additional pointing (udf-10) of 30 hours, overlaid on the mosaic. The population selected in D17 is composed of 481 LAEs found in the mosaic and 123 in the udf-10, for a total of 604 LAEs. On the upper panel of the figure, the plot presents the luminosity of the different samples versus the redshift. Using lensing clusters, the redshift selection tends to be less affected by luminosity bias, especially for higher redshift. On the lower panel, the normalized distribution of the two populations are presented. The strength of the study presented in D17 resides in the large number of sources selected. However, a sharp drop is observed in the distribution at $\log L_{\mathrm{Ly}\alpha} \sim 41.5$. Using the lensing clusters, with ~ 25 hours of exposure time and a much smaller lens-corrected volume of survey, a broader luminosity selection was achieved which makes this present work more suited for the study of the faint end of the LF.

6.2 LF analysis

6.2.1 Lensing sample only

The differential LFs are shown in Fig. 6.4 and the values in Table 6.1 for the four redshift bins. Some points in the LF, shown as empty squares, are considered as unreliable and presented for comparison purpose only. Therefore, they are not used in the subsequent parametric fits. An LF value is considered unreliable when it is dominated by the contribution of a single source, with either a small V_{max} or a low completeness value, due to luminosity and/or redshift sampling. These unreliable points are referred to as "incomplete" hereafter. The rest of the points are fitted with a straight line as a visual guide, the corresponding 68% confidence regions are represented as shaded areas. For z_3, the exercise is limited owing to the large uncertainties and the lack of constraints on the bright end. The measured mean slope for the four LFs are as follows: $\alpha = -1.79^{+0.1}_{-0.09}$ for z_{all},

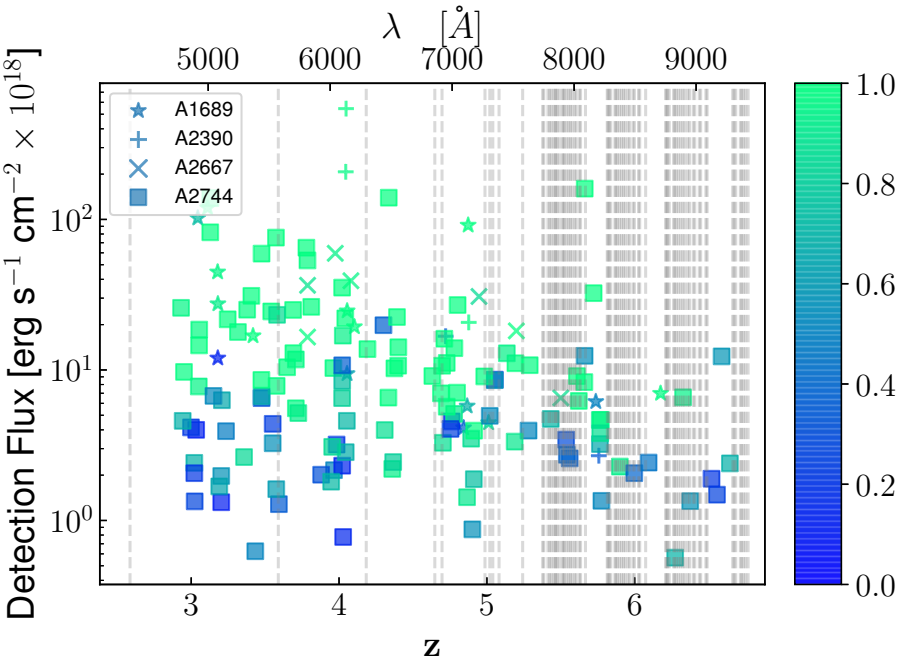

Figure 6.2: Completeness (colour bar) of the sample as a function of redshift and detection flux. Each symbol indicates a different cluster. The light grey vertical lines indicate the position of the main sky lines. There is no obvious correlation in our selection of LAEs between the completeness and the position of the sky lines.

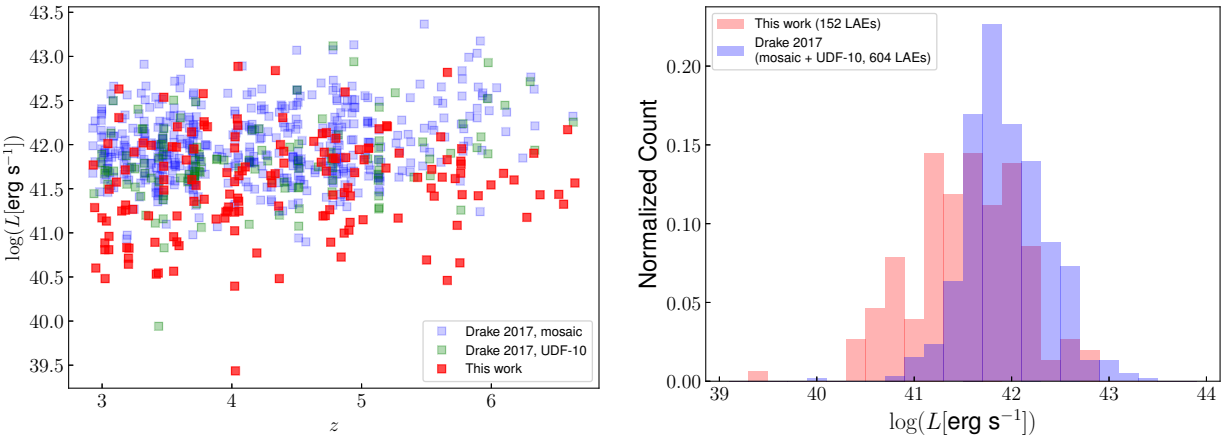

Figure 6.3: Comparison of the 152 LAEs sample used in this work with D17. Left panel: luminosity vs. redshift; error bars have been omitted for clarity. Right panel: luminosity distribution of the two samples, normalized using the total number of sources. The use of lensing clusters allows for a broader selection, both in redshift and luminosity towards the faint end.

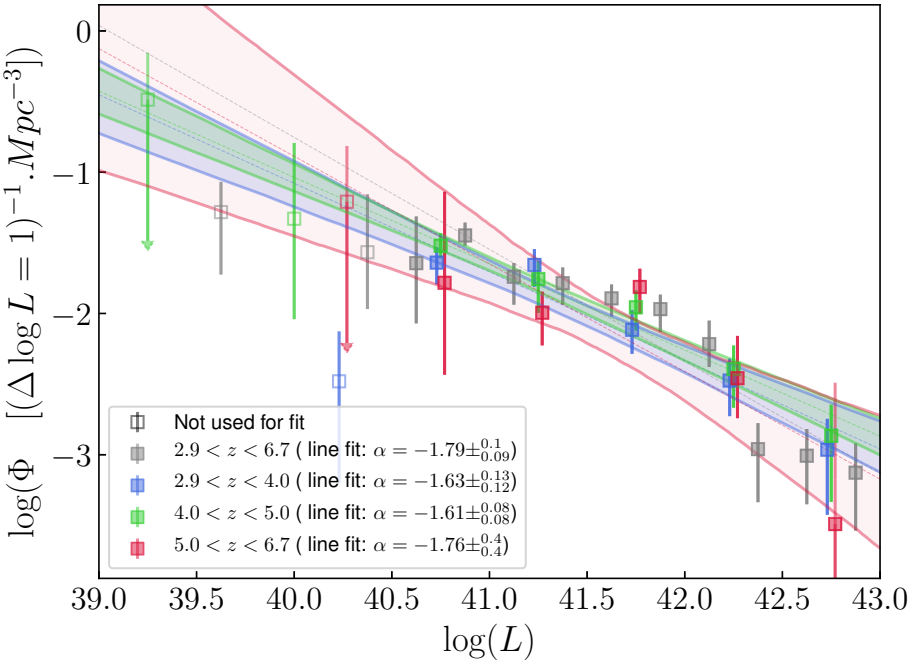

Figure 6.4: Luminosity function points computed for the four redshift bins. Each LF was fitted with a straight dotted line and the shaded areas are the 68% confidence regions derived from these fits. For the clarity of the plot, the confidence area derived for $z_{\rm all}$ is not shown and a slight luminosity offset is applied to the LF points for z_1 and z_3.

$\alpha = -1.63^{+0.13}_{-0.12}$ for z_1, $\alpha = -1.61^{+0.08}_{-0.08}$ for z_2 and $\alpha = -1.76^{+0.4}_{-0.4}$ for z_3. These values are consistent with no evolution of the mean slope with redshift but this conclusion is limited by the low level of constraint on the bright end and the large uncertainties for the highest redshifts.

6.2.2 Schechter fit of the LAE LF

6.2.2.1 Fitting method and results

Since the integrated values of the LFs are of great interest regarding the constraints they can provide on the sources of reionization, each of the LFs is fitted by a Schechter function (see Sect. 1.2.3.1). Because of the use of lensing clusters, the volume of Universe explored is smaller than in blank field surveys. The direct consequence is that we are not very efficient in probing the transition area around L_* and the high luminosity regime of the LF. Instead, the lensing regime is more efficient in selecting faint and low luminosity galaxies and is therefore much more sensitive to the slope parameter. To properly determine the three best parameters, additional data are needed to constrain the global LF. To this aim, previous LFs from the literature are used and combined together into a single average LF with the same luminosity bin size as the LFs derived in this work. This last point is important to ensure that the fits are not dominated by the literature data points that are more numerous with smaller bin sizes and uncertainties. In this way we determine the three Schechter parameters while properly sampling the covariance between them.

All fits are done in the Log space where the Schechter function writes as:

$$\Phi_{\log}(L)d(\log L) = \left(\frac{L}{\log e}\right)\left(\frac{\Phi_*}{L_*}\right)\left(\frac{L}{L_*}\right)^{\alpha}\exp\left(-\frac{L}{L_*}\right)d(\log L), \tag{6.2}$$

using the Python package *Lmfit* (Newville et al., 2014) which is specifically dedicated to nonlinear

Table 6.1: Luminosity bins and LF points used in Fig. 6.5. $< N >$ is the average number of sources in the luminosity bin, and $N_{\rm corr}$ is the average number corrected for completeness. $< V_{\rm max} >$ is the average $V_{\rm max}$ for the sources in the bin. The average values are taken across the multiple MC iterations used to compute the statistical errors on the LF points. The uncertainties on $\log(\Phi)$ are 68% error bars, combining Poissonian error, MC iterations and an estimation of the cosmic variance.

$\log(L)$ erg s^{-1}	$\log(\Phi)$ $(\Delta(\log(L))=1)^{-1}$Mpc^{-3}	$< N >$	$< N_{\rm corr} >$	$< V_{\rm max} >$ Mpc^3
	2.9 < z < 6.7			
$39.00 < \mathbf{39.63} < 40.25$	$-1.28^{+0.21}_{-0.44}$	2.05	8.97	124.68
$40.25 < \mathbf{40.38} < 40.50$	$-1.57^{+0.41}_{-0.40}$	3.52	7.04	4971.62
$40.50 < \mathbf{40.63} < 40.75$	$-1.64^{+0.33}_{-0.43}$	9.43	24.83	10977.19
$40.75 < \mathbf{40.88} < 41.00$	$-1.45^{+0.09}_{-0.07}$	12.77	33.27	12063.96
$41.00 < \mathbf{41.13} < 41.25$	$-1.74^{+0.10}_{-0.20}$	18.68	48.11	12816.23
$41.25 < \mathbf{41.38} < 41.50$	$-1.79^{+0.11}_{-0.15}$	23.28	48.07	12991.31
$41.50 < \mathbf{41.63} < 41.75$	$-1.89^{+0.10}_{-0.13}$	26.81	39.75	13926.47
$41.75 < \mathbf{41.88} < 42.00$	$-1.97^{+0.10}_{-0.16}$	26.15	35.60	14658.58
$42.00 < \mathbf{42.13} < 42.25$	$-2.22^{+0.17}_{-0.16}$	18.08	21.32	15017.49
$42.25 < \mathbf{42.38} < 42.50$	$-2.96^{+0.18}_{-0.38}$	4.22	4.28	15696.11
$42.50 < \mathbf{42.63} < 42.75$	$-3.01^{+0.19}_{-0.34}$	3.94	3.95	16060.71
$42.75 < \mathbf{42.88} < 43.00$	$-3.13^{+0.21}_{-0.41}$	3.00	3.01	16141.73
	2.9 < z < 4.0			
$40.00 < \mathbf{40.25} < 40.50$	$-2.48^{+0.35}_{-0.72}$	1.90	4.73	4430.41
$40.50 < \mathbf{40.75} < 41.00$	$-1.64^{+0.11}_{-0.15}$	14.99	38.65	4145.63
$41.00 < \mathbf{41.25} < 41.50$	$-1.66^{+0.11}_{-0.15}$	18.37	45.65	4468.50
$41.50 < \mathbf{41.75} < 42.00$	$-2.12^{+0.14}_{-0.17}$	14.53	18.14	5178.73
$42.00 < \mathbf{42.25} < 42.50$	$-2.47^{+0.15}_{-0.25}$	8.17	8.69	5216.12
$42.50 < \mathbf{42.75} < 43.00$	$-2.96^{+0.22}_{-0.46}$	2.95	2.95	5437.33
	4.0 < z < 5.0			
$39.00 < \mathbf{39.25} < 39.50$	$-0.49^{+0.33}_{-\infty}$	0.76	5.47	44.11
$39.50 < \mathbf{40.00} < 40.50$	$-1.33^{+0.54}_{-0.71}$	1.79	3.71	939.22
$40.50 < \mathbf{40.75} < 41.00$	$-1.52^{+0.09}_{-0.09}$	4.83	14.76	2818.30
$41.00 < \mathbf{41.25} < 41.50$	$-1.76^{+0.13}_{-0.24}$	13.72	28.05	3706.94
$41.50 < \mathbf{41.75} < 42.00$	$-1.96^{+0.12}_{-0.17}$	19.40	21.96	4113.33
$42.00 < \mathbf{42.25} < 42.50$	$-2.39^{+0.17}_{-0.27}$	8.49	8.58	4254.24
$42.50 < \mathbf{42.75} < 43.00$	$-2.87^{+0.22}_{-0.47}$	3.00	3.02	4430.02
	5.0 < z < 6.7			
$40.00 < \mathbf{40.25} < 40.50$	$-1.21^{+0.39}_{-\infty}$	0.66	1.25	50.28
$40.50 < \mathbf{40.75} < 41.00$	$-1.78^{+0.64}_{-0.65}$	2.43	4.84	2985.57
$41.00 < \mathbf{41.25} < 41.50$	$-1.99^{+0.15}_{-0.23}$	9.88	22.43	4763.46
$41.50 < \mathbf{41.75} < 42.00$	$-1.81^{+0.13}_{-0.19}$	19.06	35.27	5087.77
$42.00 < \mathbf{42.25} < 42.50$	$-2.46^{+0.30}_{-0.28}$	5.61	8.29	5469.76
$42.50 < \mathbf{42.75} < 43.00$	$-3.49^{+0.31}_{-\infty}$	1.00	1.00	6187.25

optimization and that provides robust estimations for confidence intervals. We define an objective function, accounting for the strong asymmetry in the error bars, whose results are then minimized in the least-squares sense, using the default Levenberg-Marquardt method provided by the package. The results of this first minimization are then passed to a MCMC process[1] that uses the same objective function. The uncertainty on the three parameters of the Schechter function (α, Φ_*, L_*) are recovered from the resulting individual posterior distributions. The minimization in the least-square sense is an easy way to fit our data but is not guaranteed to give the most probable parameterization for the LFs. A more robust method would be the maximum-likelihood method. However, because of the non-parametric approach used in this work to build the points of the LF, taking into account the specific complexity of the lensing regime, the implementation of a maximum-likelihood approach such as those developed in D17 or in Herenz et al. (2019) could not be envisaged.

The LF points from the literature used to constrain the bright end are taken from Blanc et al. (2011) and Sobral et al. (2018) for $z_{\rm all}$ and z_1, Dawson et al. (2007), Zheng et al. (2013), and Sobral et al. (2018) for z_2, and finally Ouchi et al. (2010), Santos et al. (2016), Konno et al. (2018), and Sobral et al. (2018) for z_3. The goal is to extend our own data towards the highest luminosities using available high-quality data with enough overlap to check the consistency with the present data set. The best fits and the literature data sets used for the fits are also shown in Fig. 6.5 as full lines and lightly coloured diamonds, respectively. The dark red coloured regions indicate the 68% and 95% confidence areas for the Schechter fit. The best Schechter parameters are listed in Table 6.2. In addition, this Table contains the results obtained when the exact same method of LF computation is applied to the sources of A2744 as an independent data set. This is done to assess the robustness of the method and to see whether or not the addition of low volume and high magnification cubes add significant constraints on the faint end slopes.

The choice of the precise data sets used for the Schechter fits is expected to have a significant impact on the results, including possible systematic effects. To estimate the extent of this effect and its contribution to uncertainties, different series of data sets were used to fit the LF, among those available in a given redshift interval (see Fig. 6.5). The best-fit parameters recovered are found to be always consistent within their own error bars.

6.2.2.2 Impact of luminosity binning

The error bars on the parameters measured during the adjustment of the Schechter function do not account for the uncertainty introduced by the binning of the data. To further test the robustness of the slope measurement different bins were tested for the construction of the LF. The exact same fit process was applied to the resulting LFs. The confidence regions derived from these tests are shown in Fig. 6.6 for all four redshift bins. The bins used to build the LFs shown in Fig. 6.5 are identified in this figure as black lines. We estimate that these bins are amongst the most reliable possibilities and are therefore used as reference. In the following they are referred to as the "optimal" bins. They were determined in such a way that each bin is properly sampled in both redshift and luminosity, and has a reasonable level of completeness.

Figure 6.6 shows that α is very stable for both $z_{\rm all}$ and z_1 and that all the posterior distributions are very similar. Because we are able to probe very low luminosity regimes far below L_* and because of the increased statistics, the effect of binning on the measured slope is almost negligible for these two redshift bins. As redshift increases as a consequence of lower statistics and higher uncertainties, the effects of binning on the measured slope increases. For z_2 the LF is affected by a small over-

[1] *Lmift* uses the emcee algorithm implementation of the emcee Python package (see Foreman-Mackey et al. 2013)

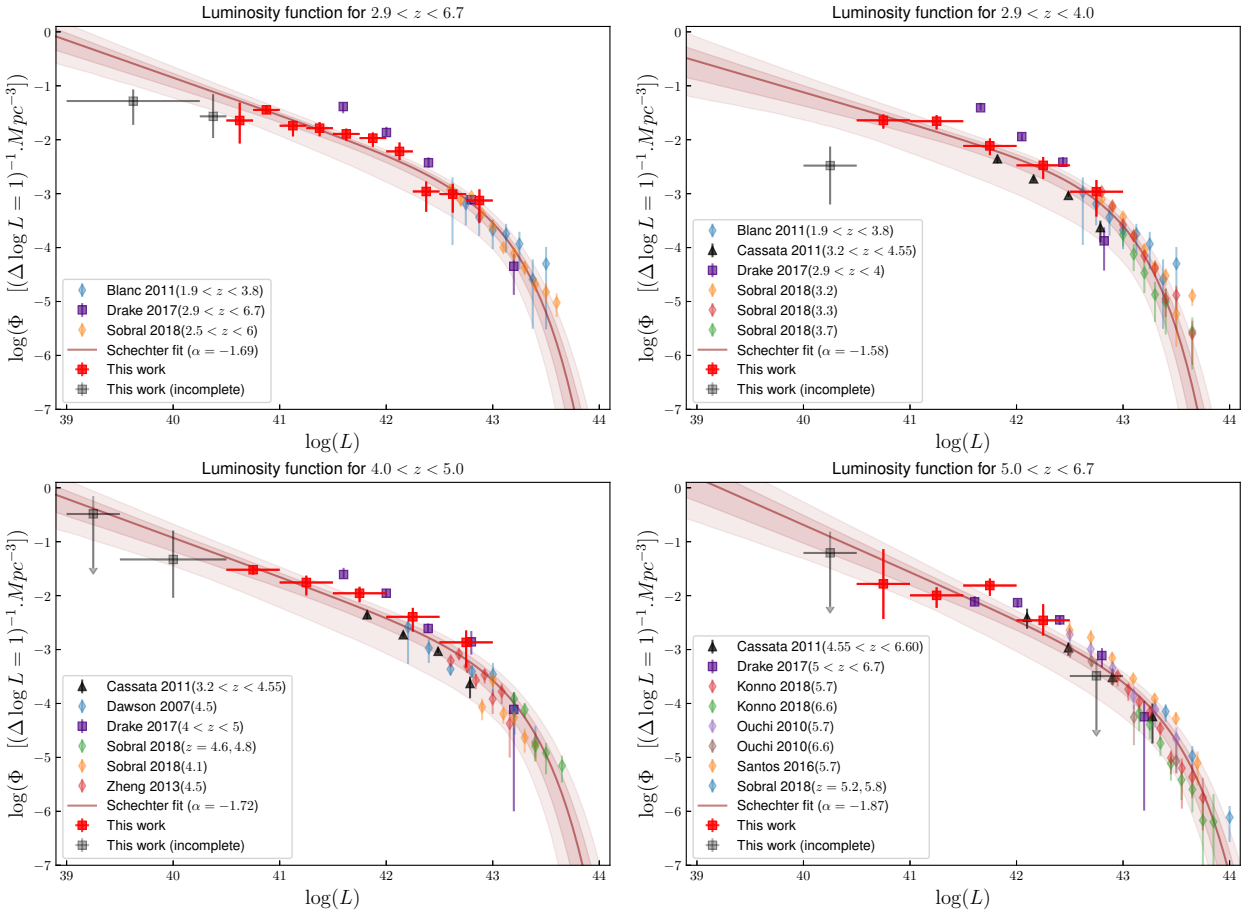

Figure 6.5: Luminosity functions and their respective fits for the four different redshift bins considered in this study. The red and grey squares represent the points derived in this work, where the grey squares are considered incomplete and are not used in the different fits. The literature points used to constrain the bright end of the LFs are shown as lightly coloured diamonds. The black points represent the results obtained by Cassata et al. (2011), which were not used for the fits. The purple squares represent the points derived using the $V_{\rm max}$ method in D17 and are only shown for comparison. The best Schechter fits are shown as a solid line and the 68% and 95% confidence areas as dark red coloured regions, respectively.

density of LAEs at $z \sim 4$ resulting in a higher dispersion on the faint end slope value when testing different binnings. It was ensured that the optimal binning allowed this fit to be consistent with the fit made for $z_{\rm all}$: in both cases the points at $41.5 \lesssim \log L \lesssim 42$, affected by the same sources at $z \sim 4$, are treated as a small overdensity with respect to the Schechter distribution. Finally, for z_3, the lack of statistics seriously limits the possibilities of binnings to test. The only viable options are the two presented on the bottom right panel of Fig. 6.6: in both cases the quality of the fit is poor compared to the other redshift bins, but the measured slopes are consistent within their own error bars.

6.2.2.3 Discussion: Evolution of the LF with redshift

All four fits made using the complete sample are summed up in Fig. 6.7, which shows the evolution of the confidence regions for α, Φ_*, and L_* with redshift. Table 6.2 shows that the results are very similar for z_1 and z_3 when considering A2744 only or the full sample. For $z_{\rm all}$ and z_2 the recovered

Table 6.2: Results of the fit of the Schechter function in the different redshift intervals. The last two columns display the Lyman-alpha flux density and the SFRD as a function of redshift, obtained from the integration of the LFs parameterization obtained in Sect. 6.2.2.1. The errors on the parameters of the Schechter function correspond to 68% confidence interval. ρ_{Ly_α} is computed using a lower integration limit $\log(L) = 40.5$ which is considered to be the completeness limit of this work. For each redshift bin, the Schechter parameters are measured from the the LFs computed from the entire sample and from the LAEs of A2744 only.

		N_{obj}	N_c	Φ_*	$\log L_*$	α	$\log \rho_{Ly\alpha}$	$\log SFRD$
				10^{-4}Mpc^{-3}	erg s^{-1}		erg s^{-1} Mpc^{-3}	$M_\odot$ yr^{-1} Mpc^{-3}
z_{all}	4 clusters	152	278	$6.38^{+3.26}_{-2.46}$	$42.85^{+0.11}_{-0.10}$	$-1.69^{+0.08}_{-0.08}$	$40.08^{+0.04}_{-0.04}$	$-1.94^{+0.04}_{-0.04}$
	A2744	125	235	$3.40^{+2.33}_{-1.59}$	$42.97^{+0.15}_{-0.12}$	$-1.85^{+0.08}_{-0.08}$	$40.14^{+0.04}_{-0.04}$	$-1.88^{+0.04}_{-0.04}$
z_1	4 clusters	61	119	$8.29^{+5.25}_{-3.66}$	$42.77^{+0.12}_{-0.10}$	$-1.58^{+0.11}_{-0.11}$	$39.99^{+0.07}_{-0.07}$	$-2.03^{+0.07}_{-0.07}$
	A2744	40	102	$7.51^{+4.97}_{-3.43}$	$42.78^{+0.13}_{-0.10}$	$-1.58^{+0.12}_{-0.12}$	$39.97^{+0.07}_{-0.07}$	$-2.05^{+0.07}_{-0.07}$
z_2	4 clusters	52	86	$3.67^{+2.51}_{-1.72}$	$42.96^{+0.14}_{-0.11}$	$-1.72^{+0.09}_{-0.09}$	$39.99^{+0.06}_{-0.06}$	$-2.03^{+0.06}_{-0.06}$
	A2744	40	68	$1.52^{+1.45}_{-0.87}$	$43.12^{+0.20}_{-0.15}$	$-1.96^{+0.08}_{-0.09}$	$40.13^{+0.05}_{-0.05}$	$-1.89^{+0.05}_{-0.05}$
z_3	4 clusters	39	73	$1.53^{+0.96}_{-0.68}$	$43.16^{+0.12}_{-0.10}$	$-1.87^{+0.12}_{-0.12}$	$40.03^{+0.11}_{-0.09}$	$-1.99^{+0.11}_{-0.09}$
	A2744	33	64	$1.40^{+0.91}_{-0.64}$	$43.18^{+0.12}_{-0.10}$	$-1.90^{+0.12}_{-0.12}$	$40.05^{+0.12}_{-0.11}$	$-1.97^{+0.12}_{-0.11}$

slopes exhibit a small difference at the $\lesssim 2\sigma$ level. This difference is caused by one single source with $40.5 \lesssim \log L \lesssim 41$, which has a high contribution to the density count. When adding more cubes and sources, the contribution of this LAE is averaged down because of the larger volume and the contribution of other LAEs. This argues in favour of a systematic underestimation of the cosmic variance in this work. Using the results of cosmological simulations to estimate a proper cosmic variance was not possible during this thesis, mainly because of the resolution needed to reach the very small halo scales sampled by strong magnification. This is an importat issue to be addressed in the future.

For the higher redshift bin, even though the same slope is measured when using only the LAEs of A2744, the analysis can only be pushed down to $\log L = 41$ (instead of $\log L = 40.5$ for z_{all}, z_1 and z_2 or when using the full sample). This shows the benefit of increasing the number of lensing fields to avoid a sudden drop in completeness at high redshift. In the following paragraph, only the results obtained with the full sample are discussed.

The values measured for L_* are in good agreement with the literature (e.g. $\log(L_*) = 43.04 \pm 0.14$ in Dawson et al. (2007) for $z \simeq 4.5$, $\log(L_*) = 43.25^{+0.09}_{-0.06}$ in Santos et al. (2016) for $z \simeq 5.7$ and a fixed value of $\alpha = -2.0$, and $\log(L_*) = 43.3^{+0.5}_{-0.9}$ in Hu et al. (2010) for $z \simeq 5.7$ and a fixed value of $\alpha = -2.0$) and these values tend to increase with redshift. This is not a surprise as this parameter is most sensitive to the data points from the literature used to fit the Schechter functions. Given the large degeneracy and therefore large uncertainty affecting the normalization parameter ϕ_*, a direct comparison and discussion with previous studies is difficult and not so relevant. Regarding the α parameter, the Schechter analysis reveals a steepening of the faint end slope with increasing redshift, which in itself means an increase in the observed number of low luminosity LAEs with respect to the bright population with redshift. However, this is a $\sim 1\sigma$ trend that can only be seen in the light of the Schechter analysis, with a solid anchorage of the bright end, and cannot be seen

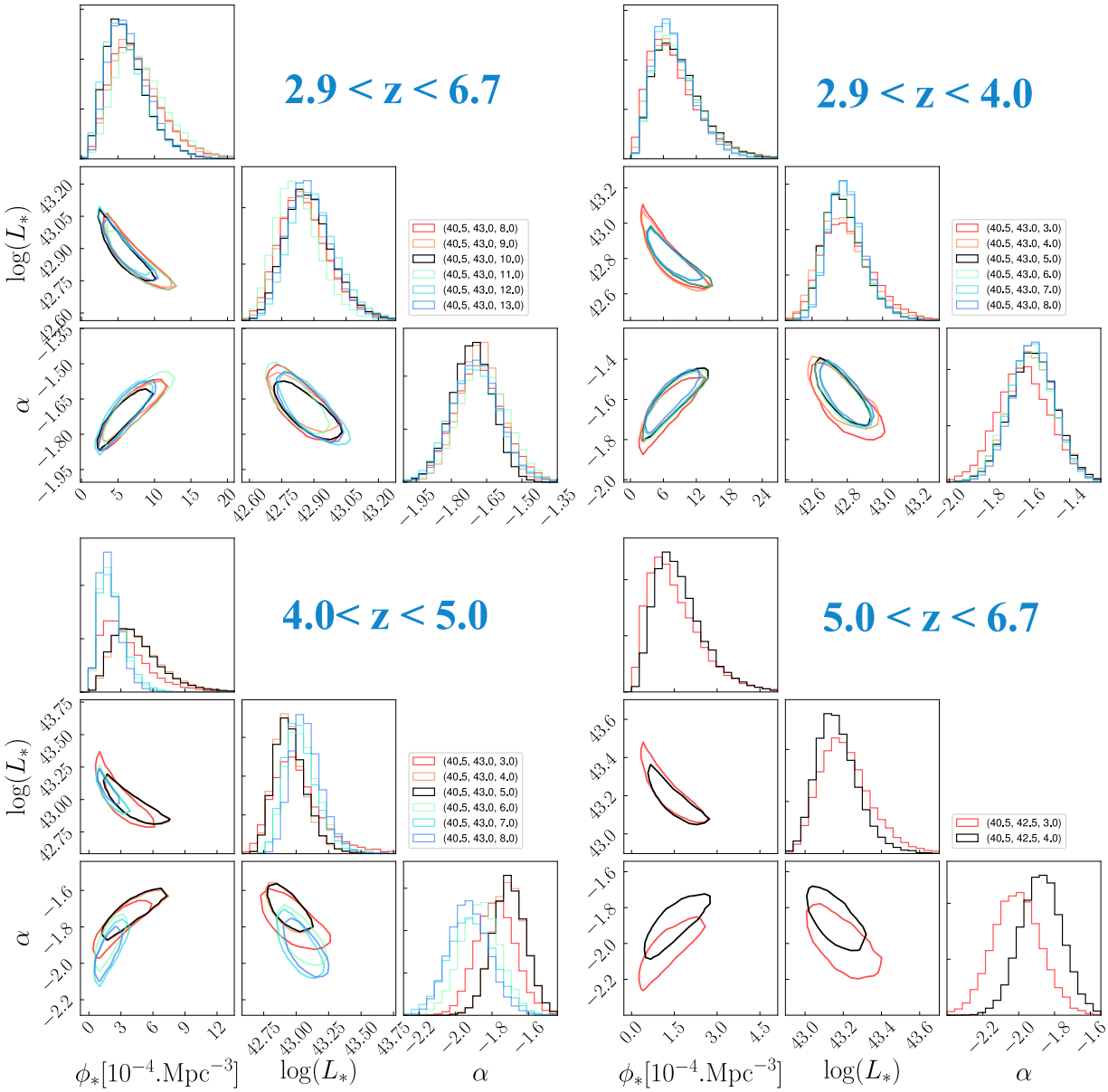

Figure 6.6: Areas of 68% confidence derived on the Schechter parameters when testing different binnings. Left panel shows the results for $2.9 < z < 4.0$ and the right panel those for $5.0 < z < 6.7$. The legends on the plots indicate, from left to right, $\log(L)_{\rm min}$, $\log(L)_{\rm max}$ and the number of bins considered for the fit between these two limits. The black lines show the results obtained from the optimal bins adopted in this work.

using only the points derived in this work (see Fig. 6.4).

Taking advantage from the unprecedented level of constraints on the low luminosity regime, the present analysis confirms a steep faint end slope varying from $\alpha = -1.58^{+0.11}_{-0.11}$ at $2.9 < z < 4$ to $\alpha = -1.87^{+0.12}_{-0.12}$ at $5 < z < 6.7$. The result for the lower redshift bin is not consistent with $\alpha = -2.03^{+1.42}_{-0.07}$ measured using the maximum-likelihood technique in D17. At higher redshift, the slopes measured in D17 are upper limits, which are consistent with all the values in Table 6.2. The points in purple in Fig. 6.5 are the points derived with the $V_{\rm max}$ from this same study. It can be seen that there is a systematic difference, more pronounced at lower luminosity for $z_{\rm all}$, z_1 and

z_2. This difference, taken at face value, could be evidence for a systematic underestimation of the cosmic variance both in this work and in D17. This aspect clearly requires further investigation in the future. Faint end slope values of $\alpha = -2.03^{+0.4}_{-0.3}$ for $z = 5.7$ and $\alpha = -2.6^{+0.6}_{-0.4}$ for $z \sim 5.7$ ($\alpha = -2.5^{+0.5}_{-0.5}$ for $z \sim 6.6$) were found in Santos et al. (2016) and Konno et al. (2018), respectively. These values are reasonably consistent with our own measurement made for z_3. In this case again, the comparison with the literature is quite limited as the faint end slope is often fixed (see e.g. Dawson et al., 2007; Ouchi et al., 2010) or the luminosity range probed is not adequate leading to poor constraints on α.

From Fig. 6.5, we see that the Schechter function provides a relatively good fit for $z_{\rm all}$, z_1, and z_2. The over-density in number count at $z \sim 4$ for $41.5 \lesssim \log L \lesssim 42$ is indeed seen as an over-density with respect to the Schechter distribution. For z_3 however, the fit is not as good with one point well above the 1σ confidence area. At this point it is useful to remember that the final goal of this thesis is not the measurement of the Schechter slope in itself, but is to provide solid constraints on the faint end shape of the LFs. Furthermore it is not certain that such a low luminosity population is expected to follow a Schechter distribution. Some studies have already explored the possibility of a turnover in the LF of UV selected galaxies (e.g. Bouwens et al., 2017; Atek et al., 2018), and the same possibility is not to be excluded for the LAE population. For the specific needs of this work, it remains convenient to adopt a parametric form as it makes the computation of proper integrations with correct error transfer easier (see Sect. 6.3) and facilitates the comparison with previous and future works. When talking about integrated LFs, any reasonable deviations from the Schechter form is of little consequence as long as the fit is representative of the data. In other words, as long as no large extrapolation towards low luminosity is made, our Schechter fits provide a good estimation of the integrated values.

6.3 Discussion: Implication for the reionization

6.3.1 Impact of the mass model

In this section, before going to the integration of the LFs and the constraints and implications for reionization, we discuss the uncertainties introduced by the use of lensing. As part of the HFF programme, several good quality mass models were produced and made publicly available by different teams, using different methodologies. The uncertainties introduced by the use of lensing fields when measuring the faint end of the UV LF are discussed in detail in Bouwens et al. (2017) and Atek et al. (2018) through simulations. A more general discussion on the reason why mass models of the same lensing cluster may differ from one another can be found in Priewe et al. (2017). And finally, a thorough comparison of the mass reconstruction produced by different teams with different methods from simulated lensing clusters and HST images is done in Meneghetti et al. (2017). The uncertainties are of two types:

- The large uncertainties for high magnification values. This aspect is well treated in this work through the use of $P(\mu)$, which allows any source to have a diluted and very asymmetric contribution to the LF over a large luminosity range.
- The possible systematic variation from one mass model to another. This aspect is more complex as it has an impact on both the individual magnification of sources and on the total volume of the survey.

Figure 6.8 illustrates the problem of variation of individual magnification from one mass model to another, using the V4 models produced by the GLAFIC team (Kawamata et al., 2016; Kawamata, 2018), Sharon & Johnson (Johnson et al., 2014), and Keeton that are publicly available on

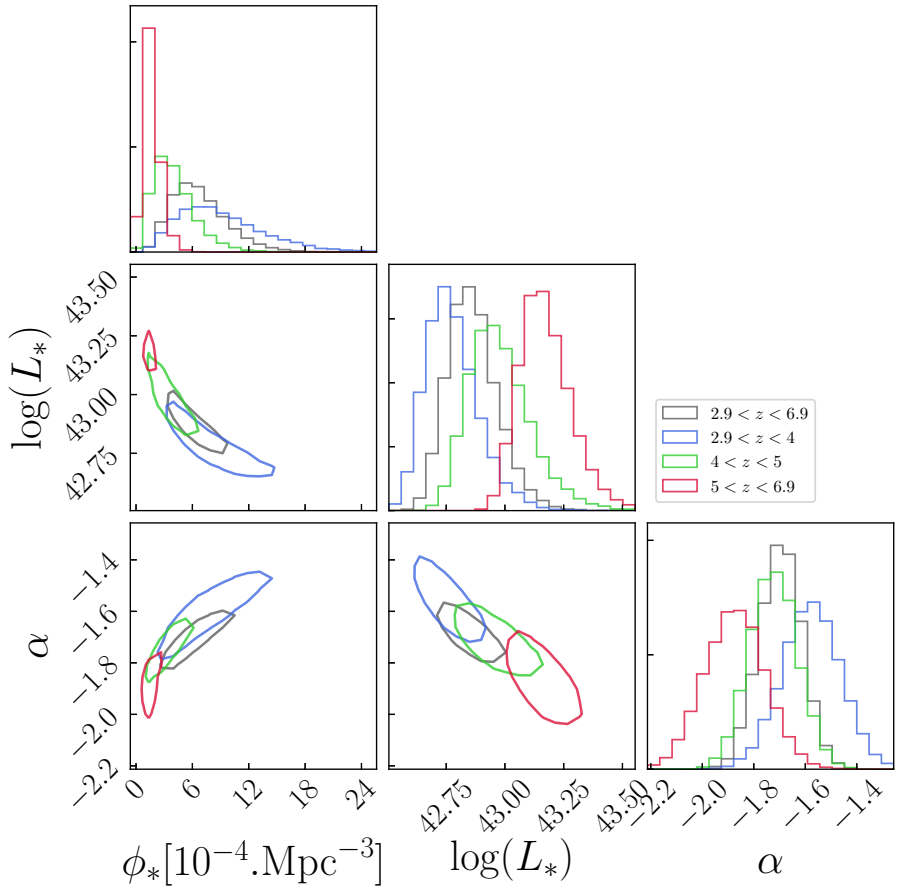

Figure 6.7: Evolution of the Schechter parameters with redshift. The contours plotted correspond to the limits of the 68% confidence areas determined from the results of the fits.

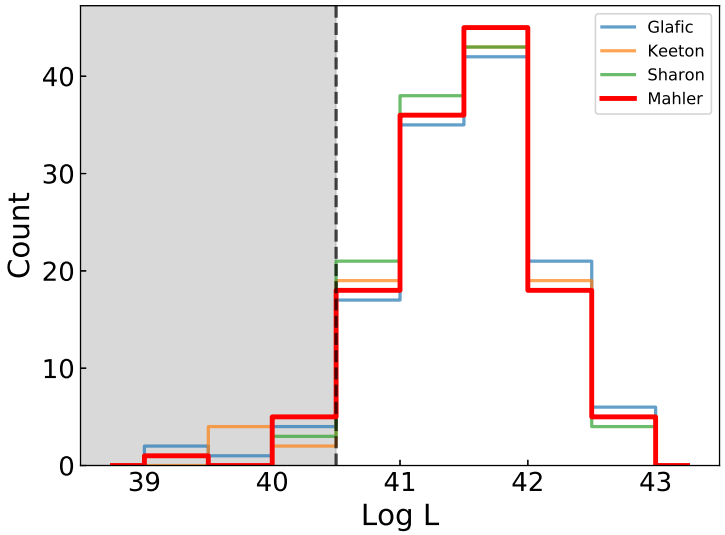

Figure 6.8: Comparative Lyα luminosity histograms obtained using the magnification resulting from different mass models. The grey area represents the completeness limit of this work.

the HFF website [2]. Since we are restricted to the HFF, this comparison can only be done for the LAEs of A2744. The figure shows the Lyman-alpha luminosity histograms when using alternatively the individual magnification provided by these three additional models. The bin size is $\Delta \log L = 0.5$, which is the bin size used in this work for the LFs at z_1, z_2 and z_3. For $\log L > 40.5$ the highest dispersion is of the order of 15%. This shows that even though there is a dispersion when looking at the magnification predicted by the four models, the underlying luminosity population remains roughly the same. Regarding the needs of the LF, this is the most important point.

Figure 10 of Atek et al. (2018) shows an example of the variations of volume probed with rest-frame UV magnitude using different mass models for the lensing cluster MACS1149. This evolution is very similar for the models derived by the Sharon and Keeton teams and, in the worst case scenario, implies a factor of ~ 2 of difference among the models compared in this figure. These important variations are largely caused by the lack of constraints on the mass distribution outside of the multiple image area: a small difference in the outer slope of the mass density affects the overall mass of the cluster and therefore the total volume probed. However, unlike other lensing fields from the HFF programme, A2744 has an unprecedented number of good lensing constraints at various redshifts thanks to the deep MUSE observations. These constraints were shared between the teams and are included in all the V4 models used for comparison in this work. These four resulting mass models are robust and coherent, at the state of the art of what can be achieved with the current facilities. It has also been shown by Meneghetti et al. (2017) based on simulated cluster mass distributions, that the methodology employed by the CATS (the CATS model for A2744 is the model presented in Mahler et al. (2018)) and GLAFIC teams are among the best to recover the intrinsic mass distribution of galaxy clusters. To test the possibility of a systematic error on the survey volume, the surface of the source plane reconstruction of the MUSE FoV is compared at $z = 3.5$ using the same four models as in Fig. 6.8. The source plane reconstruction are shown in Fig. 6.9 and the surfaces are $(1.27')^2$, $(1.13')^2$,$(1.07')^2$, and $(0.99')^2$ using the mass models of Mahler, GLAFIC, Keeton, and Sharon, respectively. The strongest difference is observed between the models of Mahler and Sharon and corresponds to a relatively small difference of only 25%.

[2] `https://archive.stsci.edu/prepds/frontier/lensmodels/`

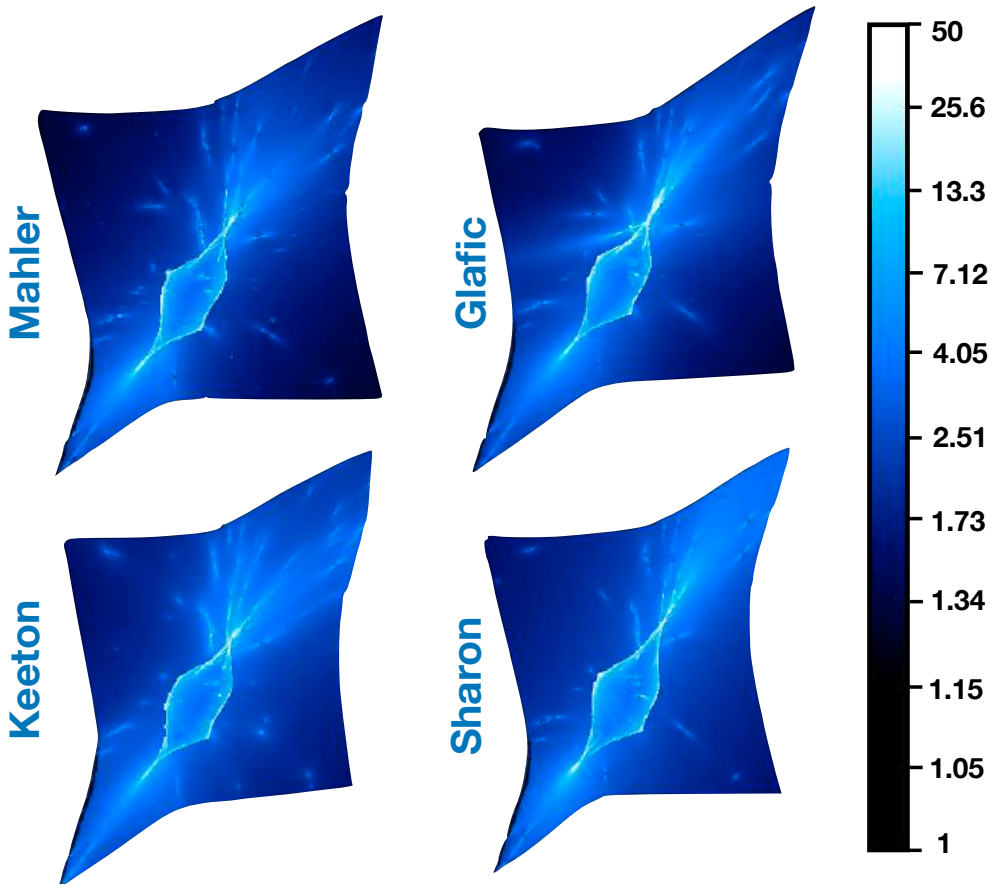

Figure 6.9: Source plane reconstruction of the MUSE A2744 FoV with four mass models at $z = 3.5$.

Given the complex nature of the MUSE data combined with the lensing cluster analysis, precisely assessing the effect of a possible total volume bias is nontrivial and out of the scope of this thesis. From this discussion it seems clear that the use of lensing fields introduces an additional uncertainty on the faint end slope. However the luminosity limit under which this effect becomes dominant remains unknown as all the simulations (Bouwens et al., 2017; Atek et al., 2018) were only done for the UV LF for which the data structure is much simpler.

6.3.2 Ionizing flux density

In order to estimate the contribution of the LAE population to the cosmic reionization, its star formation rate density (SFRD) is computed using the best Schechter parameters derived in the previous section. The integrated luminosity density ρ_{Ly_α} is also determined in the same way. The SFRD produced by the LAE population can be estimated using the following prescription for the (Kennicutt, Jr., 1998) assuming the case B for the recombination (Osterbrock & Ferland, 2006):

$$\mathrm{SFRD}_{\mathrm{Ly}\alpha}[\mathrm{M}_\odot \mathrm{yr}^{-1}\mathrm{Mpc}^{-3}] = L_{Ly\alpha}[\mathrm{erg\ s}^{-1}\ \mathrm{Mpc}^{-3}]/1.05 \times 10^{42}. \tag{6.3}$$

This equation assumes an escape fraction of the Lyman-alpha photons of 1 and is therefore a lower limit for the SFRD. Uncertainties on this integration are estimated with MC iterations, by perturbing the best-fit parameters within their error bars, neglecting the correlations between the parameters. The values obtained for the $\mathrm{SFR}_{\mathrm{Ly}\alpha}$ and $\rho_{\mathrm{Ly}\alpha}$ are presented in Table 6.2 for a lower limit of integration of $\log(L) = 40.5$, which corresponds to the lowest luminosity points used to fit

the LFs (i.e. no extrapolation towards lower luminosities). The value $\log(L) = 44$ is used as upper limit for all integrations. This upper limit has virtually no impact on the final result because the steep drop of the LF at high luminosity.

We show in Fig. 6.10 the results obtained using different lower limits of integration and how they compare to previous studies of both LBG and LAE LFs. The yellow area corresponds to the 1σ and 2σ SFRD needed to fully reionize the Universe, which is estimated from the cosmic ionizing emissivity derived in Bouwens et al. (2015a). The cosmic emissivity was derived using a clumping factor of 3, the conversion to UV luminosity density was done assuming $\log(\xi_{\rm ion} f_{escp})$ = 24.50, where f_{escp} is the escape fraction of UV photons and $\xi_{\rm ion}$ is the Lyman-continuum photon production efficiency. Finally the conversion to SFRD was done with the following relation: $\mathrm{SFRD}[\mathrm{M_\odot yr^{-1}Mpc^{-3}}] = \rho_{\rm UV}[\mathrm{erg\,s^{-1}\,Hz^{-1}\,Mpc^{-3}}]/(8.0 \times 10^{27})$ (see Kennicutt, Jr. 1998; Madau et al. 1998). Because all the slopes of our LFs are over $\alpha = -2$ (for $\alpha < -2$ the integral of the Schechter parameterization diverges), the integrated values increase relatively slowly when decreasing the lower luminosity limit. On the same plot, the SFRD computed from the integration of the LFs derived in Bouwens et al. (2015b) are shown in darker grey for two limiting magnitudes: $M_{\rm UV} = -17$ (which corresponds to the observation limit in this blank field study) and $M_{\rm UV} = -13$, which is thought to be the limit of galaxy formation (e.g. Rees & Ostriker 1977, Mac Low & Ferrara 1999 and Dijkstra et al. 2004).

From this plot, and with $f_{\rm Ly_\alpha} = 1$, we see that the observed LAE population only is not enough to reionize the Universe fully at $z \sim 6$, even with a large extrapolation of 2 dex down to $\log L = 38.5$. However, a straightforward comparison is dangerous: an escape fraction $f_{\rm Ly_\alpha} \gtrsim 0.5$ would be roughly enough to match the cosmic ionizing emissivity needed for reionization at $z \sim 6$. Moreover, in this comparison, we implicitly assumed that the LAE population has the same properties ($\log(f_{\rm esc}\xi_{\rm ion}) = 24.5$) as the LBG population in Bouwens et al. (2015b). A recent study on the typical values of $\xi_{\rm ion}$ and its scatter for typical star-forming galaxies at $z \sim 2$ by Shivaei et al. (2018) has shown that $\xi_{\rm ion}$ is highly uncertain as a consequence of galaxy-to galaxy variations on the stellar population and UV dust attenuation, while most current estimates at high redshift rely on (too) simple prescriptions from stellar population models. The SFRD obtained from LAEs when no evolution in $f_{\rm Ly_\alpha}$ is introduced remains roughly constant as a function of redshift when no extrapolation is introduced and slightly increases with redshift when using $L_{\rm inf} = 38.5$. Figure 6.10 also shows in green/blue, the $\mathrm{SFR_{Ly\alpha}}$ values derived in previous studies of the LAE LF, namely Ouchi et al. (2008), Cassata et al. (2011) (hereafter, O08, C11), and D17. In C11, a basic correction for IGM absorption was performed assuming $f_{\rm Ly_\alpha}$ varying from 15% at $z = 3$ to 50% at $z = 6$ and using a simple radiative transfer prescription from Fan et al. (2006). This correction can easily explain the clear trend of increase of SFRD with redshift and the discrepancy with our points at high redshift. At low redshifts, the IGM correction is lower and the points are in a relatively good agreement. The points in O08 are the result of a full integration of the LFs with a slope fixed at $\alpha = -1.5$ and are in reasonable agreement for all redshift domains. The two higher redshift points derived in D17 are inconsistent with our measurements. This is not a surprise as the slopes derived in D17 are systematically steeper and inconsistent with this work.

The use of an IFU (MUSE) in D17, in Herenz et al. (2019) (H19 in this chapter), and this survey ensures that we better recover the total flux, even though we may still miss the faintest part of the extended Lyman-alpha haloes (see Wisotzki et al. 2016; Leclercq et al. 2017). This is not the case for NB (e.g. O08) or slit-spectroscopy (e.g. Cassata et al., 2011) surveys in which a systematic loss of flux is possible for spatially extended sources or broad emission lines because of the limited aperture of the slits or the limited spectral width of NB filters (see Sect. 2.3). It is noted in H19 that the

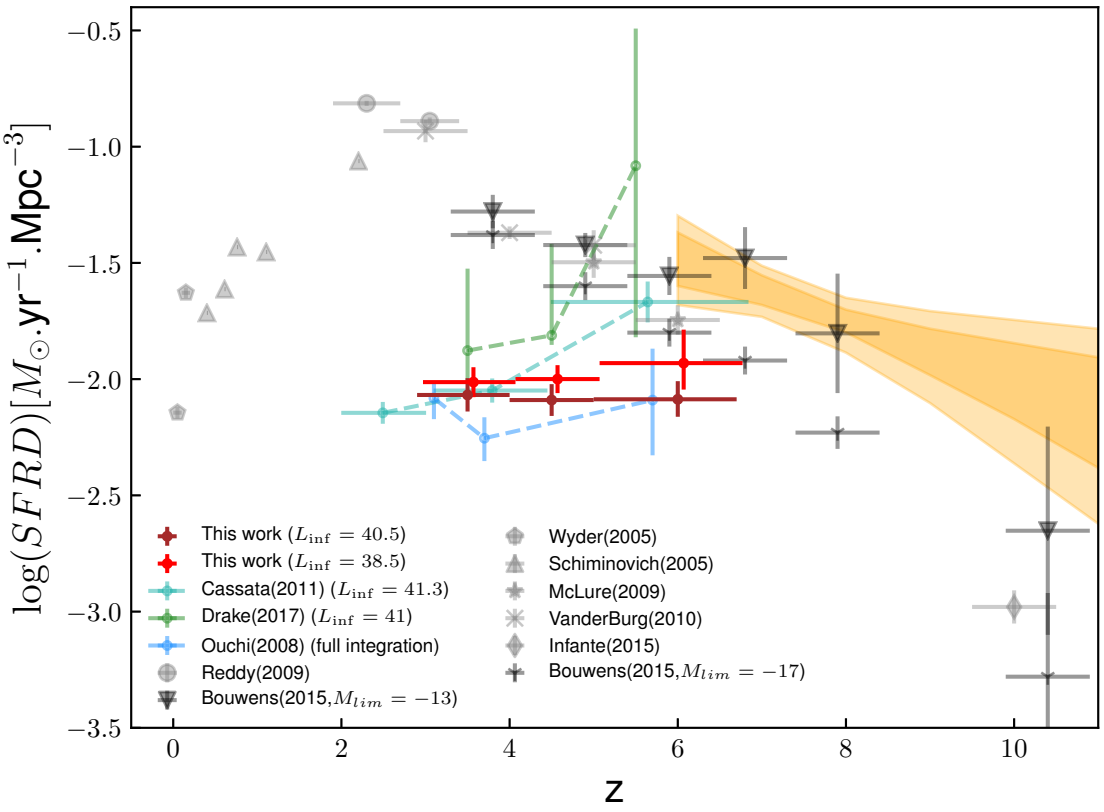

Figure 6.10: Evolution of $\mathrm{SFRD}_{\mathrm{Ly}\alpha}$ with redshift with different lower limits of integration. The limit $\log L = 38.5$ corresponds to a 2 dex extrapolation with respect to the completeness limit in this work. Our results (in red / brown) are compared to SFRD in the literature computed for LBGs (in light grey) and from previous studies of the LAE LF (in green / blue). For the clarity of the plot, a small redshift offset was added to the points with $L_{\mathrm{inf}} = 38.5$. The darker grey points correspond to the SFRD derived from the LFs in Bouwens et al. (2015b) for a magnitude limit of integration of $M_{\mathrm{UV}} = -17$ corresponding to the observation limit, and $M_{\mathrm{UV}} = -13$. The points reported by Cassata et al. (2011) are corrected for IGM absorption. The yellow area corresponds to the 1σ and 2σ estimations of the total SFRD corresponding to the cosmic emissivity derived in Bouwens et al. (2015a).

$3.2 < z < 4.55$ LF estimate of C11 tends to be lower than most literature estimates (including those in H19). One possible explanation would be a systematic loss of flux, which results in a systematic shift of the derived LF towards lower luminosities. Interestingly, when assuming point-like sources to compute the selection function, H19 manages to recover very well the results of C11 for this redshift domain. It is also interesting to see that as luminosity decreases, the LF estimates from C11 become more and more consistent with the points and Schechter parameterization derived in this work. For z_3, the C11 LF is even fully consistent with the Schechter parameterization across the entire luminosity domain (see Fig. 6.5). The following line of thought could explain the concordance of this work with the C11 estimates at lower luminosity and higher redshift: At lower luminosity and higher redshift, a higher fraction of LAEs detected are point-like sources, making the C11 LFs more consistent with our values; and at higher luminosity and lower redshift, more extended LAEs are detected and a more complex correction is needed to get a realistic LF estimate.

The second advantage of using an IFU is linked to the selection of the LAE population. The O08 authors used a NB photometric selection of sources with spectroscopic follow-up to confirm the LAE candidates. This results in an extremely narrow redshift window which is likely to lead to lower completeness of the sample due to the two-step selection process (see again Sect. 2.3). The studies by D17 and H19, adopt the same approach as this work: a blind spectroscopic selection of sources. In addition, as shown in Fig. 6.3 and stated in Sect. 6.2.2.3 when discussing the differences in slope between A2744 alone and the full sample, the use of highly magnified observations allows for a more complete source selection at increasing redshift. The sample used in the present work could arguably have a higher completeness level than other previous studies.

To summarize the above discussion, the observational strategy adopted in this study by combining the use of MUSE and lensing clusters has allowed us to

- reach fainter luminosities, providing better constraints on the faint end slope of the LF, while still taking advantage of the previous studies to constrain the bright end;
- recover a greater fraction of flux for all LAEs;
- cover a large window in redshift and flux;
- reach a higher level of completeness, especially at high redshift.

A steepening of the faint end slope is observed with redshift, which follows what is usually expected. This trend can be explained by a higher proportion of low luminosity LAEs observed at higher redshift owing to higher dust content at lower redshift. On the other hand, the density of neutral hydrogen is expected to increase across the $5 < z < 6.7$ interval, reducing the escape fraction of Lyα photons, a trend affecting LAEs in a different way depending on large-scale structure. While an increase of SFRD with redshift is observed, the evolution of the observed $\mathrm{SFR}_{\mathrm{Ly}\alpha}$ is also affected by f_{Ly_α}. From the point of view of the literature, the expected evolution of f_{Ly_α} is an increase with redshift up to $z \sim 6-7$ and then a sudden drop at higher redshift (see e.g. Clément et al. 2012, Pentericci et al. 2014, or Sect. 1.3.2 for more details). For $z < 6$, the increase of f_{Ly_α} is generally explained by the reduced amount of dust at higher redshift. And for $z \sim 6-7$ and above, we start to probe the reionization era and owing to the increasing amount of neutral hydrogen and the resonant nature of the Lyα, the escape fraction is expected to drop at some point. It has been suggested in Trainor et al. (2015) and Matthee et al. (2016) that the escape fraction would decrease with an increasing SFRD. This would only increase the significance of the trend observed, as it means the points with the higher SFRD would have a larger correction.

Furthermore the derived LFs and the corresponding SFRD values could be affected by bubbles of ionized hydrogen, especially in the last redshift bin. In our current understanding of the phenomenon, reionization is not a homogeneous process (Becker et al., 2015; Bosman et al., 2018). It could be that the expanding areas of ionized hydrogen develop faster in the vicinity of large structures with a high ionising flux, leaving other areas of the Universe practically untouched. There

is increasing observational evidence of this effect (see e.g. Stark et al. 2017 or Sect. 1.3 for more details on the timeline of reionization). It was shown in Matthee et al. (2015), using a simple toy model, that an increased amount of neutral hydrogen in the IGM could produce a flattening of the faint end shape of the LF. This same study also concluded that the clustering of LAEs had a large impact on the individual escape fraction, which makes it difficult to estimate a realistic correction, as the escape fraction should be estimated on a source to source basis.

As previously discussed, it is neither certain nor expected that the LAE population alone is enough to reionize the Universe at $z \sim 6$. However, the LBG and the LAE populations have roughly the same level of contribution to the total SFRD at face value. Depending on the intersection between the two populations, the observed LAEs and LBGs together could produce enough ionizing flux to maintain the ionized state of the Universe at $z \sim 6$.

This question of the intersection is crucial in the study of the sources of reionization. Several authors have addressed the prevalence of LAEs among LBGs, and have shown that the fraction of LAEs increases for low luminosity UV galaxies till $z \sim 6$, whereas the LAE fraction strongly decreases towards $z \sim 7$ (see e.g. Stark et al. 2010, Pentericci et al. 2011 or Sect. 1.3). The important point however is to precisely determine the contribution of the different populations of star-forming galaxies within the same volume, which is a problem that requires the use of 3D/IFU spectroscopy. As a preliminary result, we estimate that $\sim 20\%$ of the sample presented in this study have no detected counterpart on the deep images of the HFFs. This point is precisely addressed in the next chapter.

7 | Intersection of the LAE and LBG populations

Contents

In this chapter we investigate the interrelation between the LAE and LBG selected populations. As part of the HFF, the A2744 field has both extremely deep photometry and a large and deep MUSE coverage, allowing to make a comparison of the two populations within the same volume of Universe. Only the A2744 field is considered in this chapter. For the HFF data, we use the public source catalog released by the Astrodeep collaboration (Merlin et al., 2016; Castellano et al., 2016), which contains photometry in the 7 bands of the HST, the Hawk-I K band and Irac 1 (3.6 µm) and Irac 2 (4.5 µm). For the MUSE data, once again we use the public catalog released in (Mahler et al., 2018)[1].

In Sect. 7.1 we present the method used to select both LAEs and LBGs in this FoV. This selection includes photometric redshift computation and cross matching between the Astrodeep and the MUSE source catalogs. Once a single coherent catalog is built, we study the interrelation between these two populations in Sect. 7.2 with a focus on its evolution with both redshift and luminosity. Finally in Sect. 7.3 we briefly discuss how these results can broaden the conclusions developed in Chpt. 6 regarding the LAEs as potential sources of reionization.

7.1 Source selection

7.1.1 Astrodeep catalog: filtering and cross matching with MUSE detections

The complete method to determine the photometry in the Astrodeep catalog is detailed in Merlin et al. (2016). A brief summary is given in this paragraph. For each of the seven HST filters, both the intra-cluster light (ICL) and brightest-cluster galaxies (BCGs) were modeled and subtracted. The photometry was measured on these processed images with SExtractor. For Hawk-I K band and the two IRAC bands, the photometry was measured with PSF matching techniques using high spatial resolution images as prior for the source segmentation. The complete procedure is detailed in Merlin et al. (2016). The complete catalogue has 3587 entries for the A2744 lensing field, of which 2596 are detected in the F160W image, 976 are detected in a weighted stack of F105W, F125W, F140W and F160W and undetected in F160W only, and 15 are BCGs.

Before comparison with the MUSE sources, the entire Astrodeep catalogue was filtered to remove untrustworthy photometry points and/or sources. Since Hawk-I, IRAC 1 and IRAC 2 have larger PSF than the HST filters, the photometry computed in these three bands is more often contaminated by nearby galaxies. Following the flags given in the catalogue, all photometry entries likely to be contaminated (indicated by flag `COVMAX`, see Merlin et al. (2016)) are shifted to lower magnitude limit. We also remove 220 sources flagged as likely residual of the foreground subtraction (`SEXFLAG > 16` and `VISFLAG > 1`). Finally and because we want to compare LAEs and LBGs within a same volume of Universe, 701 entries of the catalogue that are not within the MUSE FoV are also removed. After these first steps of the selection, 2666 sources are remaining in the Astrodeep catalogue. Note that the Astrodeep catalogue is mostly based on the detection on the HST F160W image and therefore it is mainly an H-band selected sample, also including an additional sample of sources which are undetected on F160W image but appear on stacked infrared image (Y + J + JH + H). This NIR selection is important in the subsequent discussion.

In order to build a single and coherent catalogue, a cross match is done between the remaining 2666 Astrodeep sources and the 171 LAEs of the MUSE catalogue, using a matching radius of $r = 0.8''$ (4 MUSE pixels). In case several entries are pointing toward the same sources of the opposite catalogue, only the closest one is kept. As a result of this match, 113 LAEs are successfully

[1] `http://muse-vlt.eu/science/`

matched to an Astrodeep entry, and 58 are not. The difference in morphology between the UV and Lyα emission as well as the difference in spatial resolution between HST and MUSE data (see Fig. 2.6) are the dominant source of risk for making mismatches. For that reason, all LAEs and their closest Astrodeep counterpart are manually inspected to confirm or not any potential match. In the case of multiple image systems, it is always possible to select the less ambiguous image of the system when assembling the final sample.

At the end of the matching procedure, our merged catalog has 2725 entries of which 113 are seen by both MUSE and HST, and 58 are LAEs with no optical counterparts on HST images.

7.1.2 SED fitting and photometric redshift with HyperZ

For all entries of the merged catalogue, we use NEW−HYPERZ[2], originally developped byBolzonella et al. (2000), to compute photometric redshifts and probability distributions $P(z)$ in the range $z = 0 - 8$. This method is based on the fitting of the photometric Spectral Energy Ditributions (SED) of galaxies. The template library used in this study for these purposes includes 14 templates: 8 evolutionary 1 synthetic SEDs from the Bruzual & Charlot code (Bruzual & Charlot, 2003), with Chabrier IMF (Chabrier, 2003) and solar metallicity, a set of 4 empirical SEDs compiled by (Coleman et al., 1980), and 2 starburst galaxies from the (Kinney et al., 1996) library. Internal extinction is considered as a free parameter following the Calzetti et al. (2000) extinction law, with AV ranging between 0 and 1.0 magnitudes, and no prior in luminosity.

For sources with no spectroscopic redshift, HYPERZ is run two times: the first time to determine the best photometric solution and $P(z)$, and a second time using the results of the first run to constrain the redshift within the uncertainties derived from $P(z)$ and perform Monte Carlo (MC) iterations on the photometry points. The result of this second run is used to measure a distribution of Lyα continuum and UV continuum at 1 500Å from the best SEDs of each source. Finally, the blind photoz are compared to what is obtained using templates of star forming galaxies and young bursts (less than 1 Gyr) extracted from the Starbursts99 library (Leitherer et al., 1999) and forcing the redshift in the $z > 2.9$ range. When comparing the blind photoz obtained during the first pass to the values derived from this final fit, they are found to be in full agreement for the selected LBGs (see Sect. 7.1.3)

For sources with spectroscopic redshift available, a first run is done without constraints to make possible the comparison between the best photometric redshift and the spectroscopic one (see Fig. 7.1). A second run with MC iterations on the photometry points is done, forcing the redshift at the spectroscopic value to measure a distribution of Lyα and UV continuum distributions. To have a comparable magnitude of reference, an absolute UV magnitude (noted M_{1500}) is computed from the UV continuum measured from the best SEDs of each source.

The quality of photometric redshifts is assessed by directly comparing the results for the 113 galaxies with known spectroscopic redshifts in the merged catalog. The results of this comparison are shown in Fig. 7.1. Outliers are defined as sources with $|z_{\rm spec} - z_{\rm phot}| > 0.15(1 + z_{\rm spec})$. The accuracy reached excluding outliers is in average $\Delta z/(1 + z) = -0.011 \pm 0.053$, with median $(\Delta z/(1 + z)) = 0.001$. As seen in Fig. 7.1, a vast majority of galaxies with poor photometric redshifts have an apparent magnitude $m(F125W) \geq 28$ (or a S/N < 5 in this filter). It is also worth noticing that good photometric redshifts are obtained for galaxies with $z \gtrsim 2.9$, which mean that we are fully covering the redshift domain of the Lyα emission in MUSE data.

[2] `http://userpages.irap.omp.eu/~rpello/newhyperz/`

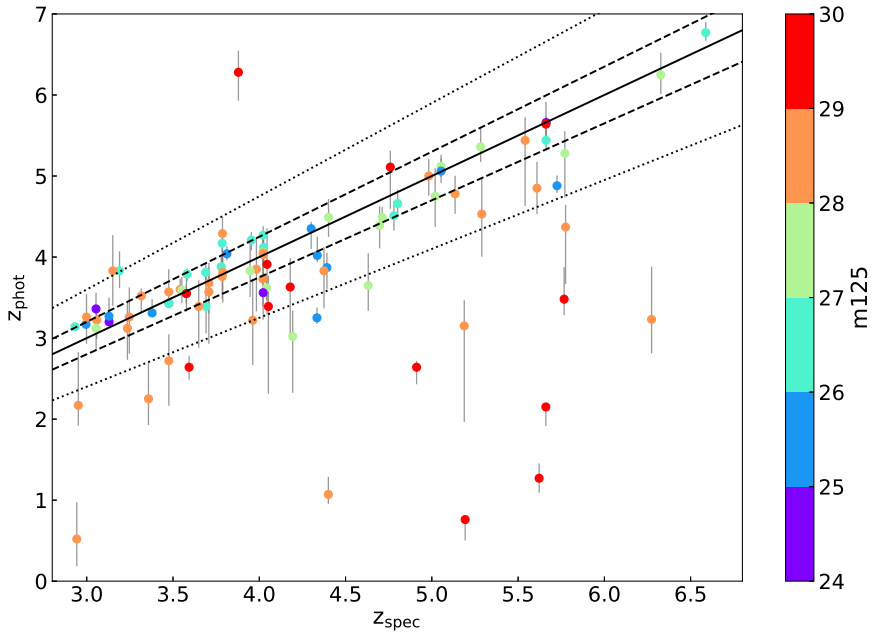

Figure 7.1: Comparison between the spectroscopic and photometric redshift for sources for which both are available. The observed magnitude in the F125W filter is encoded in colour bar. The two series of dashed lines show the relations $z_{\rm phot} = z_{\rm spec} \pm 0.05 \times (1 + z_{\rm spec})$ and $z_{\rm phot} = z_{\rm spec} \pm 0.15 \times (1 + z_{\rm spec})$ respectively. Most of the outliers on this graph are extremely faint sources with low S/N.

7.1.3 selection criteria

The main criterion used for the LBG selection is that a galaxy must have an integrated probability of having a redshift $z > 2.9$ of 60% or more (noted hereafter $P(z > 2.9) \geq 60\%$). Given the accuracy of the photometric redshifts for galaxies with $m \gtrsim 28$ and the trend observed in Fig. 7.1, a S/N> 5 is also required in at least one of the seven HST filters for sources with no spectroscopic redshifts (i.e. pure LBGs). Using this blind photometric redshift approach, 536 are selected as LBGs.

In addition to this blind approach, a colour-colour selection is also applied following the prescriptions in Bouwens et al. (2015b), to select LBGs at $z \sim$3.8, 4.9, 5.9, and 6.8. All 383 sources selected with this additional criterion are within the sample selected via blind SED-fitting, at the exception of ten of them. Manual inspection of these ten objects revealed that they either have unreliable photometric points resulting in poorly constrained or undefined photometric redshift or that they have $z_{\rm phot} \sim 2.9$, causing a large part of their $P(z)$ to be under the $z = 2.9$ and therefore failing the $P(z > 2.9) \geq 60\%$ test.

Finally, the multiple images are removed from the sample. For LAEs, a robust identification of multiple systems is already provided in the MUSE catalogue. In case one image of the system matches an UV counterpart and the other(s) do not, the one with the successful mach is kept. For pure LBGs, the identification of multiple system is done using Lenstool and the mass models of Mahler et al. (2018). The pure LBGs being much more numerous than the LAEs, any misidentification of multiple systems has very low impact on the relative intersection between the LAE and LBG population.

7.2 Results

7.2.1 Overview

Once the original sample is cleaned, limited to the MUSE FoV, cross-matched with MUSE data, SED-fitted and cleaned of multiple images, the remaining sources are divided in three samples:

- sample 1 for galaxies selected as both LAEs and LBGs: **92 sources**
- sample 2 for galaxies selected as LBGs only: **408 sources**
- sample 3 for galaxies selected as LAEs only: **46 sources**

The layout of these 3 samples in the A2744 FoV is shown in Fig. 7.2. One of the concern was that some galaxies would be seen as pure LAEs because their Lyα emission can be detected with MUSE through some bright foreground galaxy whereas their UV continuum cannot (see Sect. 2.3 for a review of emission line and continuum detection with MUSE and HST). Such identification of pure LAEs would be completely artificial as it would not be representative of the intrinsic properties of the source but only of the foreground pollution. By adjusting the selection of the multiple image (when possible), we ensured that this artificial effect is not playing any important role in the final statistics of the three samples described above. In Fig. 7.2, it can be seen that none of the pure LAEs (red circles) falls on top of a bright foreground galaxy that would prevent the detection of an underlying UV continuum.

For the galaxies selected as both LAE and LBG, it is possible to compute their $\mathrm{EW_{Ly\alpha}}$ using their detection flux and the Lyα continuum measured from the best SEDs. For galaxies selected as pure LAE, only a lower limit of $\mathrm{EW_{Ly\alpha}}$ can be determined since by construction of the sample they do not have any UV detection. The $\mathrm{EW_{Ly\alpha}}$ values for sample 1 and 3 are presented in Fig. 7.3. Since the magnification affects both the continuum and the Lyα emission in the same way, no correction is needed.

7.2.2 Evolution with redshift

The three redshift histograms for the three samples considered in this work are shown stacked on top of each other in Fig. 7.4. Table 7.1 display the same information but using the redshift bins used for the LF computation in Chpt. 6. This figure (and Table) shows that the proportion of LAEs (sample 1 and sample 3) increases with redshift. When studying high redshift galaxies and marginalizing over magnitude and Lyα luminosity, a significant part of the galaxy population is missing when looking at only the LBG or LAE population.

Using sample 1 and 2 it is also possible to compute the fraction of LAEs among UV selected galaxies, noted $\mathrm{X_{LAE}}$ (see Sect. 1.3.2 for an introduction to this LAE fraction). This computation is traditionally done for LAEs with $\mathrm{EW_{Ly\alpha}} > 25$Å and divided in two populations: galaxies with $\mathrm{M_{UV}} < -20.25$ and galaxies with $\mathrm{M_{UV}} > -20.25$ (see e.g. Stark et al., 2011; Pentericci et al., 2011; Arrabal Haro et al., 2018). Because of the lensing nature of the sample used for this work, mostly faint galaxies are selected and 98% of the sample falls within the $\mathrm{M_{1500}} > -20.25$ domain (see e.g. Fig. 7.6). The limit $\mathrm{EW_{Ly\alpha}} = 25$Å is shown in Fig. 7.3. The LAE fraction is computed from sample 1 and 3 with the cuts in both $\mathrm{EW_{Ly\alpha}}$ and UV magnitude described above and with no correction for completeness in the LBG or the LAE selection. The results are presented in Fig. 7.5 using the following redshift bins: $2.9 < z < 4.0$, $4.0 < z < 5.0$, $5.0 < z < 6.0$ and $6.0 < \mathrm{z} < 6.7$. This binning was adopted to have enough statistics in each bins and to split the LAE population between the LAEs seen before the end of reionization at $z \gtrsim 6$ and the ones seen after the end of reionization. Our results are compared to the results derived in Stark et al. (2011); Pentericci

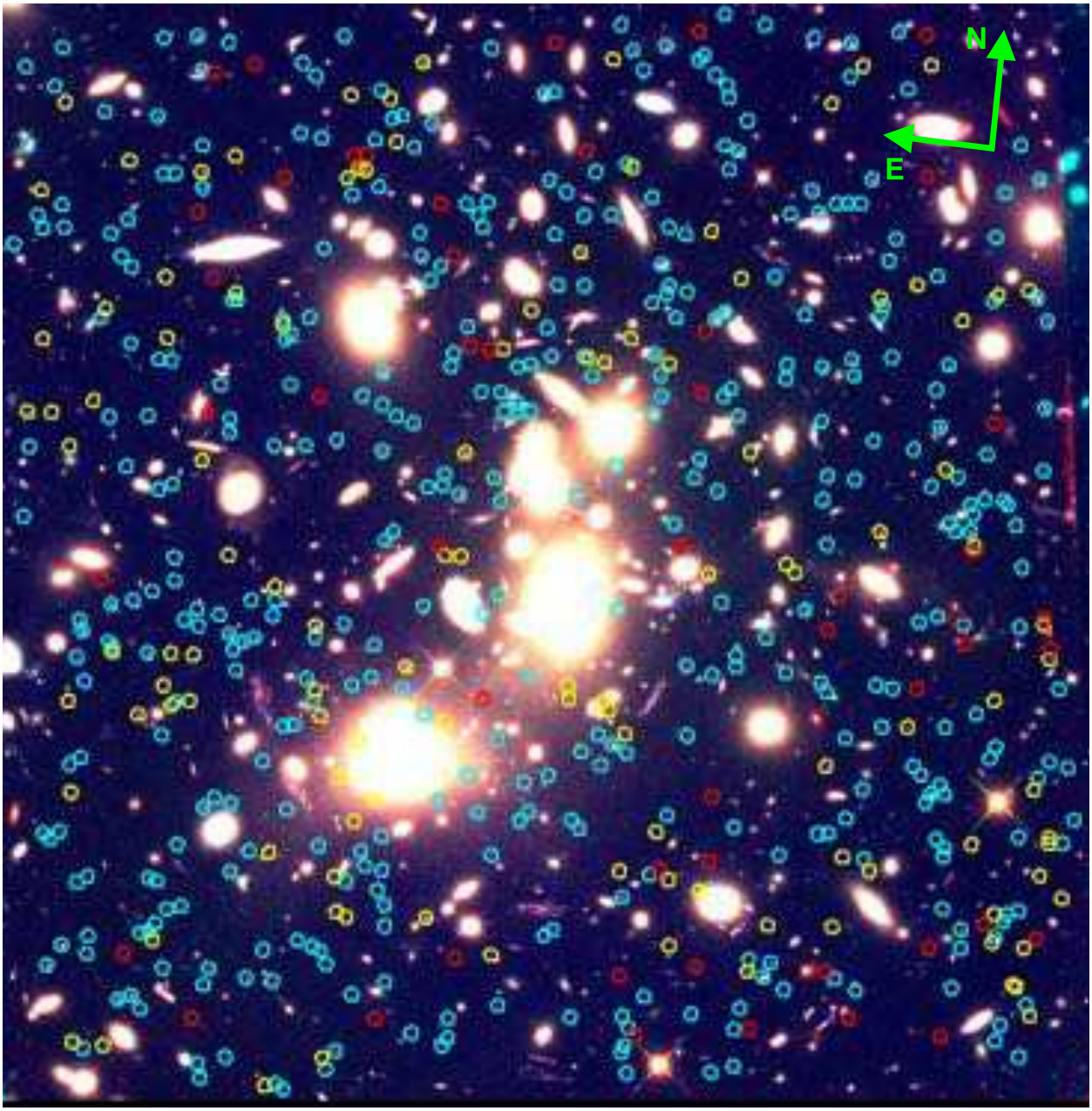

Figure 7.2: Color image of A2744 showing the area covered by the MUSE observations, obtained by combining the following HFF filters: F606W (blue), F814W (green) and F125W (red). The different populations selected in this field are displayed as follows: pure LBG (cyan), LAE with LBG counterpart (yellow) and pure LAE without LBG counterpart (red). Circles are 1.5″in diameter.

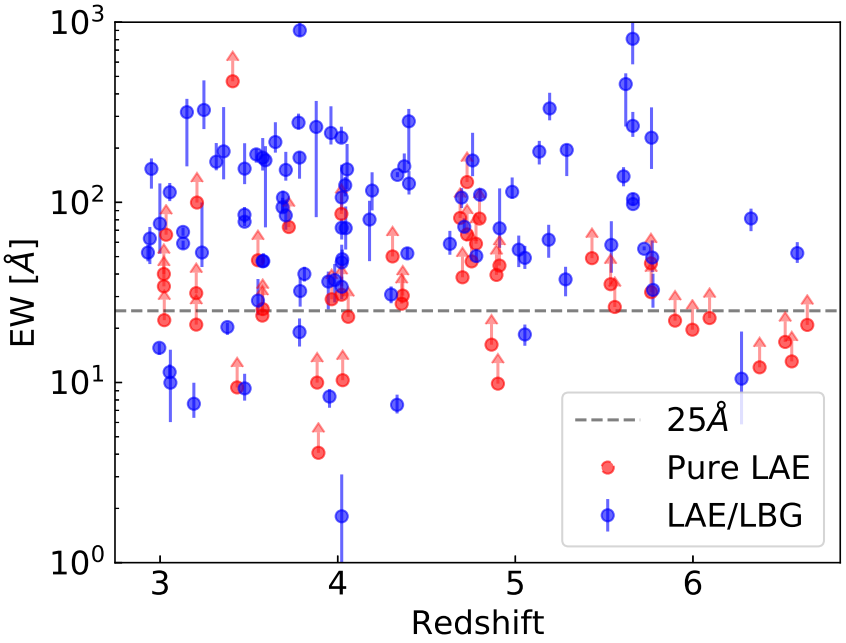

Figure 7.3: Equivalent width of LAEs in the A2744 FoV. The pure LAEs are lower limits since by definition they do not have optical counterparts on HST images. The dashed horizontal line is $EW_{Ly\alpha} = 25$ Å limit.

et al. (2011); Treu et al. (2013); Schenker et al. (2014); Tilvi et al. (2014); De Barros et al. (2017); Arrabal Haro et al. (2018). As expected our value of X_{LAE} drops at $z > 6$, which can be interpreted as an increase in the neutral fraction of hydrogen. Even though all of our points are roughly 1σ consistent with the other values, it appears that they tend to be systematically a bit lower than the previous estimates, at the exception of the points derived in Arrabal Haro et al. (2018). Several explanations are possible and may play a role in this observed trend.

- Because of the lensing nature of our sample, the volume probed is small (only 16 000 Mpc^3 are explored behind A2744 for the redshift range $2.9 < z < 6.7$) and the cosmic variance has a high impact on the observed statistics.
- It is possible that some multiple systems are missed in sample 2. If this is indeed the case, it means that we over estimate the number of LBGs in the fields and therefore underestimate the fraction of LAEs.
- Difference in the selection processes. In this work we use both broad band observations and IFU observations. The combination of these two methods ensures that we are as unbiased as possible in both the LBG and LAE selection in the same volume, range of magnitude and Lyα luminosity explored. For example, Stark et al. (2011) only use multi object spectroscopy to determine the prevalence of LAEs in the LBG population, but these observations are based on drop-out photometric priors (see Stark et al., 2010). On the contrary, Arrabal Haro et al. (2018) only uses NB observations for the selection of the two populations and is therefore more sensitive to the intrinsically bright/high $EW_{Ly\alpha}$ LAEs.

Looking at the evolution of the two populations with redshift only, our understanding of inter-relation of the two populations remains limited. On the next section we investigate the relation between UV magnitude and Lyα luminosity in our three samples of interest.

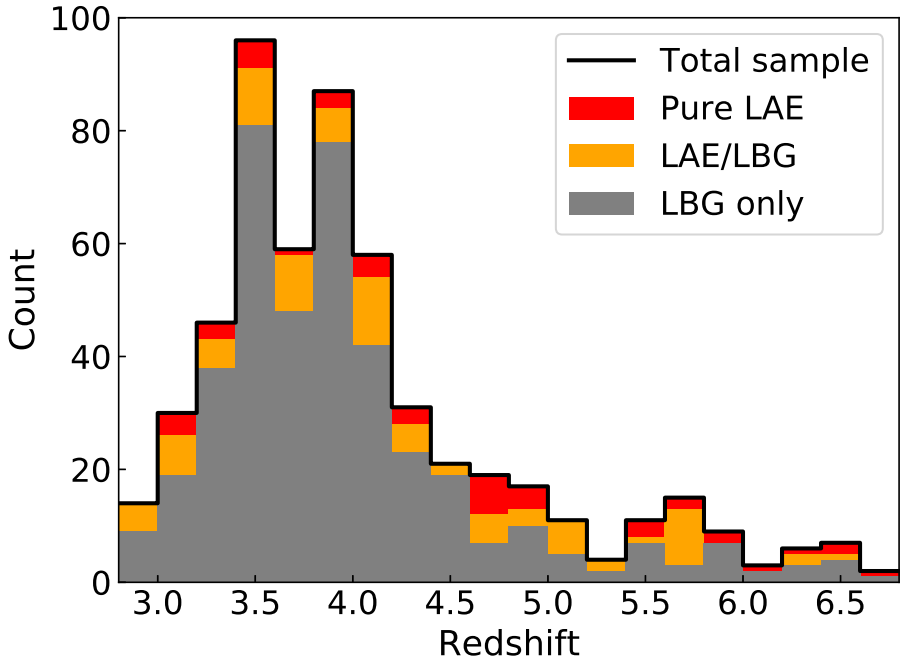

Figure 7.4: Redshift histogram of the three samples stacked on each other. The total sample (black line) is the sum the pure LAEs (red), the pure LBGs (grey) and the intersection of the two (yellow).

Table 7.1: Tables summarizing the interrelation between the LAE and LBG population using the same redshift bins as the ones used for the LAE LF presented in Chpt. 6. Numbers in boldface are absolute number of detection, and the uncertainties corresponds to the Poissonian error count.

	$2.9 \leq z \leq 6.7$	$2.9 \leq z \leq 4.0$	$4.0 \leq z \leq 5.0$	$5.0 \leq z \leq 6.7$
Sample 1: LAE ∩ LBG	**92± 9.6**	**43±6.6**	**27±5.2**	**22±4.7**
	16.9±1.7%	13.2±2.0%	18.0±3.5%	32.8±7.0%
Sample 2: LBG only	**406 ± 20.1**	**286± 16.9**	**105± 10.2**	**33±5.7**
	74.6±3.7%	81.9± 5.2%	70.0±6.8%	49.2±8.5%
Sample 3: LAE only	**46± 6.8**	**16±4.0**	**18±4.2**	**12±3.5**
	8.4± 1.2%	4.9±1.2%	12.0±2.8%	17.9±5.2%
Total	**544± 23.3**	**327±18.1**	**150±12.2**	**67±8.2**

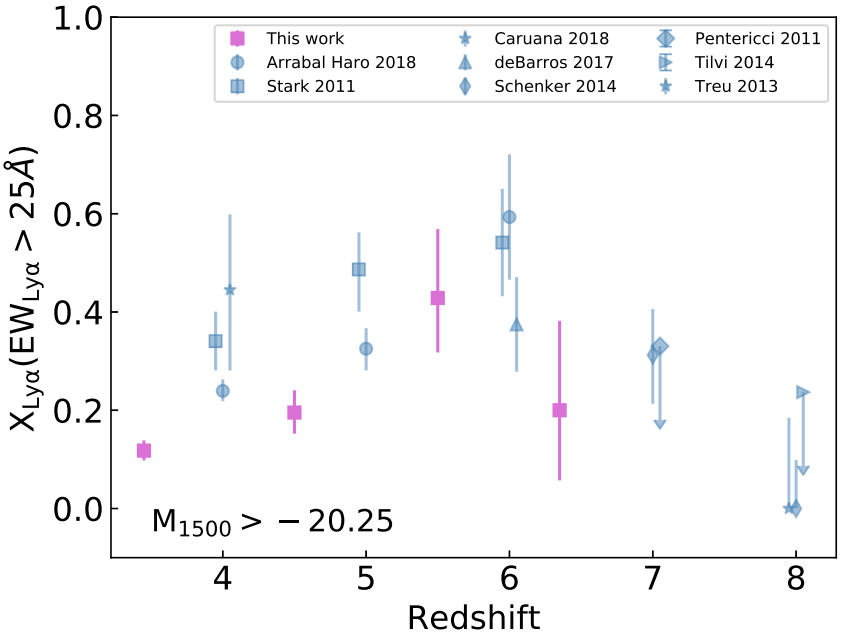

Figure 7.5: Fraction of LAEs with $\mathrm{EW}_{\mathrm{Ly}\alpha} > 25$Å among UV selected galaxies with $\mathrm{M}_{1500} > -20.25$. This fraction is computed from the galaxies in sample 1 and 2. A small redshift offset is applied to some of the points centred on the same redshift value.

7.2.3 Evolution with luminosity and UV magnitude

The main results of this section are summed up in Fig. 7.6 which shows the three samples on a $\log L_{Ly\alpha}$ versus M_{1500} plot where all values are corrected for magnification. In addition, luminosity histogram and absolute UV magnitude histograms are provided on the side.

Only galaxies of sample 1 have both their Lyα luminosity and UV magnitude measured. For the pure LBGs of sample 2, the upper limit of their Lyα emission is determined assuming a constant limit flux of detection $\mathrm{F}_{\mathrm{Ly}\alpha} = 0.3\times10^{-18}$ which is then corrected for magnification and redshift. In a similar way, for the pure LAEs of sample 3, a limit monochromatic flux of $1.510^{-21}\mathrm{erg\,cm^{-2}\,s^{-1}\,Å^{-1}}$ is assumed and is corrected for magnification and redshift to obtain the absolute UV magnitude. For the galaxies of sample 2 and 3, the limits derived are rough but good enough to clearly see some trends on Fig. 7.6.

In addition the equality $\mathrm{SFR}_{\mathrm{Ly}\alpha} = \mathrm{SFR}_{\mathrm{UV}}$ is also represented as a thick blue line. This relation is computed using the standard conversion in Kennicutt, Jr. (1998) between H_α and Lyα and assuming the case B recombination (Osterbrock & Ferland, 2006) for $\mathrm{SFR}_{\mathrm{Ly}\alpha}$, and the common conversion also given in Kennicutt, Jr. (1998) based on a Saltpeter IMF for the UV SFR. (See the paragraph on escape fraction in Sect. 1.3.2 for more details). Using Eq. 1.3, we obtain the relation $\log L_{\mathrm{Ly}\alpha} = 34.80 - 0.4\mathrm{M}_{\mathrm{UV}}$. Since none of the values in Fig. 7.6 are corrected for dust absorption, this equation represents the equality between the two *observed* SFRs. In other words, any galaxy falling on this line has $f_{\mathrm{UV}} = f_{\mathrm{Ly}_\alpha}$. Regarding the assessment of the total ionizing flux density or SFRD, it means that the same ionizing emissivity is deduced when measuring either the UV continuum or the Lyα line flux. The galaxies found above that line therefore have $f_{\mathrm{Ly}_\alpha} > f_{\mathrm{UV}}$ and the ones found below have $f_{\mathrm{Ly}_\alpha} < f_{\mathrm{UV}}$. As already discussed in Sect. 1.3.2, the above equality assumes a stationary and constant regime of star formation which can explain part of the scatter

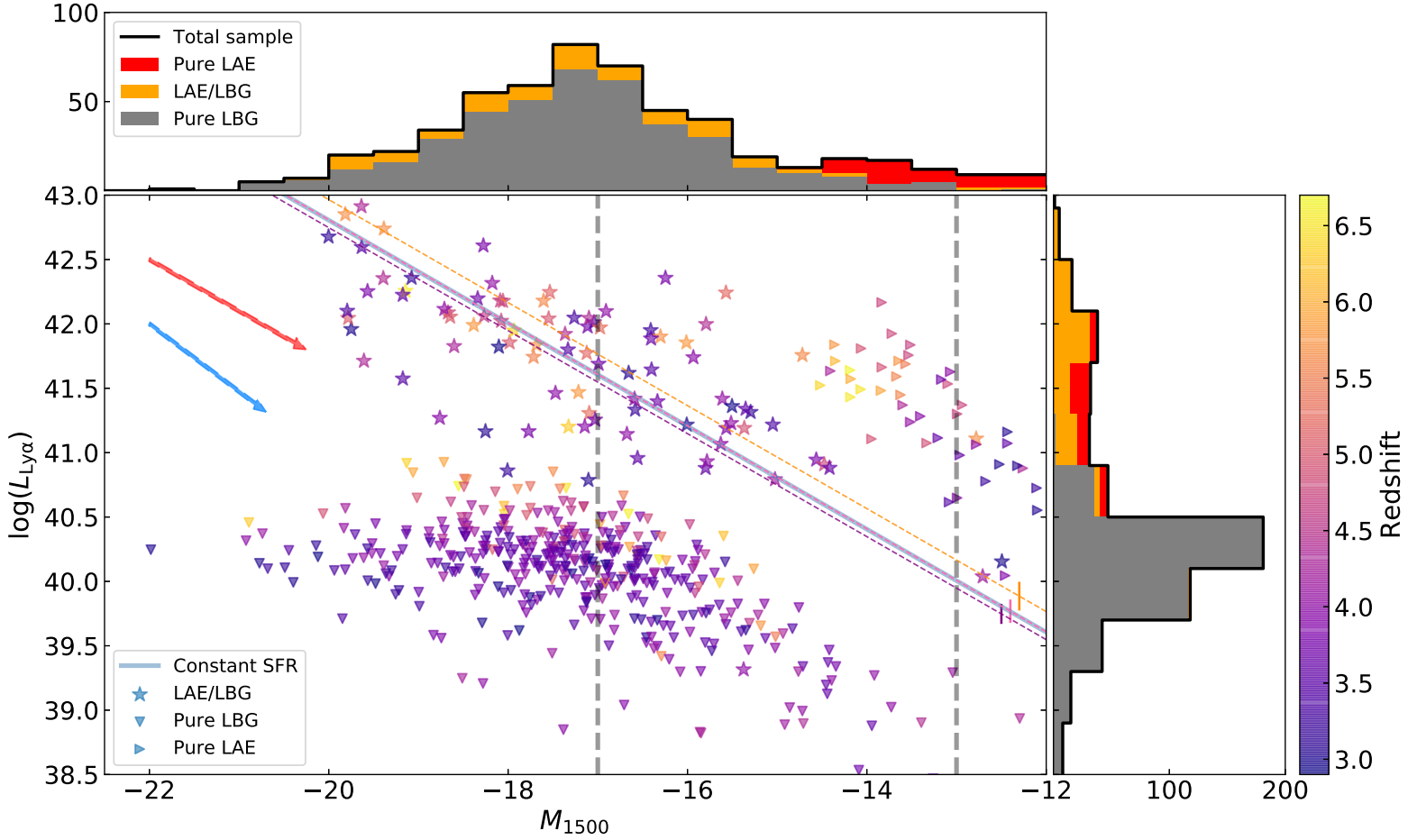

Figure 7.6: Absolute UV magnitude versus Lyα luminosity with redshift encoded in the color bar. On the top (right) are the three UV absolute magnitude (Lyα luminosity) histograms stacked on each other. The sources in sample 2 have upper limit estimation of their Lyα flux and the galaxies of sample 3 have lower limits on their absolute UV magnitude. All values are corrected for magnification. The thick blue line is where $SFR_{Ly\alpha} = SFR_{UV}$. The dashed violet, pink and orange lines correspond to the fit of the of this SFR line with a free offset (i.e. free $f_{Ly_\alpha}/\ f_{uv}$ ratio) when sample 1 is split in the following three redshift bins $2.9 < z < 4.0$, $4.0 < z < 5.0$ and $5.0 < z < 6.7$. The uncertainties on these offsets are shown as vertical lines of the same color. The two vertical grey dashed lines correspond to M_{1500} = -17 and M_{1500} = -13 which are the two limits considered in Bouwens et al. (2015b). The red and blue arrows show respectively the effect of $\mu = 5$ and $A_v = 0.5$.

observed on this figure. This aspect is discussed later in this section.

The three samples appear clearly delimited in this plot. The first thing to notice is that for M_{1500} < - 17 (leftmost grey and vertical dashed line), all SFGs of our sample are selected as LBGs. However and as seen on the top histogram of the figure, when looking at galaxies fainter than M_{1500} = - 17, the proportion of SFGs only seen as LAEs increases. This finding is in agreement with the work of Maseda et al. (2018) which concluded that the LAE selection is better suited to study intrinsically UV faint galaxies. This also suggests that the LAE LF is a better proxy of the SFGs LF when focusing on the faint end. But once again this observed trend depends on the relative depth achieved between MUSE and HST observations: deeper HST observations would increase the number faint LBGs detected. Needless to say that such observations are out of reach for current facilities.

In addition to the $SFR_{Ly\alpha} = SFR_{UV}$ line (thick blue line in Fig. 7.6), the same relation was adjusted with a free offset to the galaxies of sample 1 divided in three redshift bins: $2.9 < z < 4.0$ (43 sources), $4.0 < z < 5.0$ (27 sources) and $5.0 < z < 6.7$ (22 sources). The results are respectively the violet, pink and orange dashed line in Fig. 7.6, and the uncertainties are represented as vertical lines of the same color. Leaving this offset free means leaving the ratio f_{Ly_α}/f_{UV} free, and boils down to measuring its average value over the sample considered. For the two lower redshift bins, the adjusted line is in agreement with $f_{Ly_\alpha} = f_{UV}$ within the 1σ limit and for the third redshift bins we measure $f_{Ly_\alpha} > f_{UV}$ with a significance over the 1σ limit. For all three redshift bins, a large scatter is present which is representative of individual variation of f_{Ly_α}/f_{UV} that can be explained by the dust content, the geometry of the galaxy, the regime of star formation. These aspects are discussed later in Sect. 7.3.

When looking at all the galaxies of sample 1 together, two regimes are appearing. In average, for $M_{1500} \lesssim -17$ the sources tend to be under the $SFR_{Ly\alpha} = SFR_{UV}$ line, and for $M_{1500} \gtrsim -17$ they tend to be over this line. In addition, and following this observed trend, all the galaxies of sample 3 without exception are above that line, showing that with increasing M_{1500} the Lyα escape fraction increases in comparison to the UV photons escape fraction. Once again, such an evolution can be explained by the evolution of the dust content, and the relative distribution of dust and stars in star-forming regions, as discussed in the next section.

7.3 Possible interpretation

We have seen in the previous sections, that IFU observations and LAE selection are more efficient to select intrinsically UV faint galaxies. The increasing relative number of LAEs with redshift is in average coherent with this observation, since following the hierarchical formation of galaxies theory, high redshift galaxies tend to be smaller and fainter. These two observed trends are in agreement with the conclusion and observations developed in Maseda et al. (2018), Arrabal Haro et al. (2018) (see also Fig. 1.15 in Introduction). It is worth noting that the LBG sample used in this thesis is NIR-selected (i.e. selected based on the rest frame continuum between $\sim$ 4 000Å and 2 000Å for $z \sim 3$ to 7 respectively). We expect a systematic trend in the sense that LBG galaxies with extremely blue continuum could have been missed at $z \sim 3-4$ with respect to $z \sim 6-7$. However, this effect can hardly account for the systematic trends presented above.

From Fig. 7.6, we see that when only considering galaxies with M_{1500} < -17, all our LAEs are also selected as LBGs. This value is interesting since it roughly corresponds to observational limit of the deepest HST blank fields (see e.g. Fig. 1.12 which shows the UV LFs derived in Bouwens et al. (2015b)). Regarding the LF and reionization, and neglecting the differences between f_{Ly_α} and f_{UV}, it means that the UV LF does not need further corrections to account for the contribution of

the LAE population.

However for $M_{1500} > -17$, the situation is less clear: as absolute UV magnitude increases, the proportion of LAEs and pure LAEs seems to be increasing. But since the M_{1500} estimates are only lower magnitude limits for the galaxies of samples 3 it is not possible to see whether they probe similar domains of M_{1500} or not. Stacking the galaxies of sample 3 in redshift bins (in a similar way as in Maseda et al. (2018)) would allow us to know more on their average UV continuum, but because of the variations of individual magnification, such a task is not straightforward. In the future, we will need to push the investigation in this direction to get more quantitative results. As for now, the only thing that can be said is that when comparing galaxies of sample 2 and 3 with similar redshifts, it looks like there is little to no overlap in M_{1500} (i.e. lower limits of the yellow points of sample 2 are excluding the M_{1500} range probed by the yellow points of sample 2). In other words, based on the present results it is still difficult to quantify the missing contribution of LAEs to the ionizing flux density with respect to the extrapolation of the UV LF to $M_{1500} \sim -13$, if any.

While this magnitude domain of $M_{1500} > -17$ is mostly out of reach of deep blank fields, it is accessible through observations of strong lensing clusters. The UV LFs computed in Livermore et al. (2017); Bouwens et al. (2017); Atek et al. (2018) using lensing clusters are reasonably well constrained to the level of $M_{1500} \sim -15$ (see Fig. 1.14 in Introduction). For now (and neglecting the differences between $f_{\mathrm{Ly}\alpha}$ and f_{UV}) it seems unlikely that the UV LF are requiring a significant correction to account for contribution of the LAE only population up to $z \sim 7$.

In the previous paragraph we discussed whether the UV LF is efficient to assess the complete numerical density of SFGs in a given volume. From this work it seems plausible that the UV selection is efficient to select all SFGs within the explored range of UV magnitude. Assuming that this is indeed the case does not mean that the UV LF allows to see all the ionizing photons since it remains affected by f_{UV}. And therefore to determine the sources of reionization the crucial point is to know how f_{UV} compares to $f_{\mathrm{Ly}\alpha}$.

The LAEs (sample 1 and sample 3) with $M_{1500} > -17$ on Fig. 7.6 are almost all above the $\mathrm{SFR}_{\mathrm{Ly}\alpha} = \mathrm{SFR}_{\mathrm{UV}}$ line whereas the ones with $M_{1500} < -17$ tend to be under that line, suggesting that $f_{\mathrm{Ly}\alpha} > f_{\mathrm{UV}}$ for faint UV galaxies and $f_{\mathrm{Ly}\alpha} < f_{\mathrm{UV}}$ for UV "bright" galaxies. The ratio $f_{\mathrm{Ly}\alpha}/f_{\mathrm{UV}}$ is also increasing with redshift as shown by the orange dashed adjusting the $f_{\mathrm{Ly}\alpha}/f_{\mathrm{UV}}$ ratio of the galaxies of sample 1 in the redshift range $5.0 < z < 6.7$. This evolutionary trend, taken at face values, suggests that the Lyα emission is better suited for the study of high redshift UV faint ionizing sources, since it appears that we tend to recover more of their ionizing photons.

One possibility suggested by Atek et al. (2014) is that multi-phase ISM with dust can produce an enhancement of the Lyα emission with respect to the non resonant emission at similar wavelength (i.e. Lyman continuum photons, or UV photons in our case). Following this scenario, neutral gas and dust reside in clumps surrounded by an ionized medium. The Lyα photons are scattered when reaching the surface of these clumps while the UV photons can penetrate inside and are more easily absorbed by the dust. Therefore even though $f_{\mathrm{Ly}\alpha}$ decreases with increasing dust content or reddenning (see e.g. Hayes et al., 2011; Atek et al., 2014; Matthee et al., 2016), the ratio $f_{\mathrm{Ly}\alpha}/f_{\mathrm{UV}}$ can increase since f_{UV} decreases faster than $f_{\mathrm{Ly}\alpha}$ in presence of these dusty clumps. In addition, in galaxies observed edge-on, the Lyα photons are able to scatter and go around the dust in the dust barrier while the UV is strongly attenuated when passing directly through it. This can explain part of the scatter and the UV faint LAEs of sample 3 that are far above the blue line.

Finally Atek et al. (2014) observes a decreases fo $\mathrm{SFR}_{\mathrm{Ly}\alpha}$ with increasing $\mathrm{SFR}_{\mathrm{UV}}$, which can be interpreted as a decrease of $f_{\mathrm{Ly}\alpha}$ with increasing UV luminosity. This trend is also predicted by models (see e.g. the model of Garel et al., 2012) and can be explained by the older stellar population in UV bright galaxies. They are more dusty and less clumpy than galaxies with younger stellar population or star bursts. The more uniform dust distribution makes the absorption of Lyα more

likely and can cause $f_{\mathrm{UV}} > f_{\mathrm{Ly}\alpha}$. This is a possible interpretation for the galaxies of sample 1 with $M_{1500} <$ -17 that are observed preferentially under the $\mathrm{SFR_{UV}} = \mathrm{SFR_{Ly}}\alpha$ line in Fig. 7.6.

But all the interpretations described above have to be moderated by the fact that the relation $\mathrm{SFR_{Ly}}\alpha = \mathrm{SFR_{UV}}$ is only valid under the assumption of constant star formation rate as presented in Sect. 1.3.2. When this is not the case, the Lyα emission is no longer representative of the actual SFR owing to the long escape time scale of Lyα radiation. When a recent star burst fades away, the UV emission turns off immediately while the Lyα continues at the same rate since all Lyα photons emitted during the star burst are still going through a lengthy radiative transfer in the galaxy halo. Such process could explain why the galaxies of sample 3 are orders of magnitude over the blue line.

Following the points given in the previous paragraph, the increase of $f_{\mathrm{Ly}\alpha}/f_{\mathrm{UV}}$ with redshift (measured by the evolution of the offset on the purple pink and orange dashed lines) is likely to trace the evolution of the dust distribution. As shown in Hayes et al. (2011), the amount of dust decreases with increasing redshift, as the stellar population become younger. Following this simple evolution and assuming a homogeneous distribution of dust, we would expect a similar increase in both $f_{\mathrm{Ly}\alpha}$ and f_{UV}. This is not what is observed, which leaves an increased clumpiness in the distribution of dust and neutral hydrogen at higher redshift to explain the observed evolution of $f_{\mathrm{Ly}\alpha}/f_{\mathrm{UV}}$.

8 | Conclusion and future prospects

The main remaining questions regarding the sources of cosmic reionization can be summarized as follows:

1- By elimination, star forming galaxies are likely to drive reionization, but this has yet to be confirmed by observations. Can star forming galaxies produce enough ionizing flux density thanks to a large (but still invisible) contribution of extremely faint galaxies, to ensure the reionization of the Universe ?

2 - What is the exact timeline of reionization ? There are evidences of a rapid transition between $6 < z < 7$, but our observational constraints stops at $z \sim 7.5$ for now, leaving the questions of the pace and beginning of reionization open.

3 - What is the shape of the very faint end of the luminosity function of star forming galaxies ? How does it evolve with redshift ? Is there a turn-over in magnitude / luminosity ?

4 - Are we missing a significant portion of star forming galaxies when committing to either the LAE or the LBG selection process ? Is it possible to achieve a better empirical assessment of the star forming galaxies by understanding better the interrelation between the LAE and LBG population ?

5 - Are LAEs and LBGs essentially the same population and we are just unable to see it due to the observational biases inherent to these two selection methods ?

The majority of the work done during this thesis was focused on the determination of the LAE LF behind the strong lensing clusters A1689, A2390, A2667 and A2744 observed with MUSE. The goal of this study was to set constraints on the shape of the faint end of the LAE LF and to constrain the contribution of this population to reionization.

Taking advantage of the great capabilities of the MUSE instrument and using lensing clusters as a tool to reach lower luminosities, we blindly selected a population of 156 spectroscopically identified LAEs behind four lensing clusters that have $2.9 < z < 6.7$ and magnification corrected luminosities $39 \lesssim \log L_{\mathrm{Ly}\alpha} \lesssim 43$. Given the complexity in combining the spectroscopic data cubes of MUSE with gravitational lensing, and taking into account that each source needs an appropriate treatment to properly account for its magnification and representativity, the computation of the LF needed a careful implementation, including some original developments. For these needs, a specific procedure was developed, including the following new methods. First, we created a precise V_{max} computation for the sources found behind lensing clusters based on the creation of 3D masks. This method allows us to precisely map the detectability of a given source in MUSE spectroscopic cubes. These masks are then used to compute the cosmological volume in the source plane. This method could be easily adapted to be used in blank field surveys. Second, we developed a completeness determination based on simulations using the real profile of the sources. Instead of performing a heavy parametric approach based on MC source injection and recovery simulations, which is not ideally suited for lensed galaxies, this method uses the real profile of sources to estimate their individual completeness. The method is faster, more flexible, and accounts in a better way for the specificities of individual sources, both in the spatial and spectral dimensions.

After applying this procedure to the LAE population, the Lyman-alpha LF has been built for different redshift bins using 152 of the 156 detected LAEs. Four LAEs were removed because their contribution was not trustworthy. Because of the observational strategy, this study provides the most reliable constraints on the shape of the faint end of the LFs to date and therefore, a more precise measurement of the integrated SFRD associated with the LAE population. The results and conclusions can be summarized as follows:

- The LAE population found behind the four lensing clusters was split in four redshift bins: $2.9 < z < 6.7$, $2.9 < z < 4.0$, $4.0 < z < 5.9$, and $5.0 < z < 6.7$. Because of the lensing effect, the volume of Universe probed is greatly reduced in comparison to blank field studies. The estimated average volume of Universe probed in the four redshift bins are $\sim 15\,000$ Mpc^3, $\sim 5\,000$ Mpc^3, $\sim 4\,000$ Mpc^3, and $\sim 5\,000$ Mpc^3, respectively.
- The LAE LF was computed for the four redshift bins. By construction of the sample, the derived LFs efficiently probe the low luminosity regime and the data from this survey alone provide solid constraints on the shape of the faint end of the observed LAE LFs. No significant evolution in the shape of the LF with redshift is found using these points only. These results have to be taken with caution given the complex nature of the lensing analysis, on the one hand, and the small effective volume probed by the current sample on the other hand. Our results argue towards a possible systematic underestimation of cosmic variance in the present and other similar studies.
- A Schechter fit of the LAE LF was performed by combining the LAE LF computed in this analysis with data from previous studies to constrain the bright end. As a result of this study, a steep slope was measured for the faint end, varying with redshift between $\alpha = -1.58^{+0.11}_{-0.11}$ at $2.9 < z < 4$ and $\alpha = -1.87^{+0.12}_{-0.12}$ at $5 < z < 6.7$
- The $\mathrm{SFRD}_{\mathrm{Ly}\alpha}$ values were obtained as a function of redshift by the integration of the corresponding Lyman-alpha LF and compared to the levels needed to ionize the Universe as determined in Bouwens et al. (2015a). No assumptions were made regarding the escape fraction of the Lyman-alpha photons and the $\mathrm{SFRD}_{\mathrm{Ly}\alpha}$ derived in this work correspond to the observed values. Because of the well-constrained LFs and a better recovery of the total flux, we estimate that the present results are more reliable than previous studies. Even though the LAE population undoubtedly contributes to a significant fraction of the total SFRD, it remains unclear whether this population alone is enough to ionize the Universe at $z \sim 6$. The results depend on the actual escape fraction of Lyman-alpha photons.
- The LAEs and the LBGs have a similar level of contribution at $z \sim 6$ to the total SFRD level of the Universe. Depending on the intersection between the two populations, the union of both the LAE and LBG populations may be enough to reionize the Universe at $z \sim 6$.

Through this work, we have shown that the capabilities of the MUSE instrument make it an ideal tool to determine the LAE LF. Being an IFU, MUSE allows for a blind survey of LAEs, homogeneous in redshift, with a better recovery of the total flux as compared to classical slit facilities. The selection function is also better understood as compared to NB imaging.

About 20% of the present LAE sample have no identified photometric counterpart, even on the deepest surveys to date, i.e. HFF. This is an important point to keep in mind as this is a first element of response regarding the intersection between the LAE and LBG populations. Also the extension of the method presented here to other lensing fields should make it possible to improve the determination of the Lyman-alpha LF and to make the constraints on the sources of the reionization more robust.

To better understand the interrelation between the LAE and LBG population, we have undertaken a simultaneous search of these two populations within a given volume. The goal of this study

conducted behind the HFF cluster A2744 alone was to see whether it is possible to empirically achieve a better assessment of the SFGs by looking at the intersection of these two populations. The second objective was to further characterize the biases intrinsic to each of these selection methods to investigate whether the segregation between LAEs and LBGs is indeed just an observational bias or the result of intrinsic differences.

The study conducted on A2744 led to the following results:

- For UV faint galaxies ($M_{1500} \geq 20.25$), the fraction of LAE among SFGs increases with redshift up to $z \sim 6$ and decreases for $z \sim 6$, in agreement with previous findings (see e.g. Arrabal Haro et al., 2018).
- The selection of Lyα emitters seems to be more effective than the LBG technique to identify intrisically UV faint galaxies ($M_{1500} >$ - 17) that will be missed in deep blank field surveys. In this respect, our results are in good agreement with Maseda et al. (2018).
- Up to $M_{1500} \sim -17$, the LBG population seems to provide a good representation of the SFGs, in particular when computing the total ionizing flux in the volume explored by current surveys.
- There is no clear evidence, based on the present results, for an intrinsic difference on the properties of the two populations selected as LBG and/or LAE. However, further investigation will be needed to conclude. In particular, some systematic trends appear in the population selected as LBG and LAE, in the sense that the UV-brightest galaxies seem to exhibit a smaller ratio in their $f_{\mathrm{Ly}_\alpha}/f_{\mathrm{UV}}$, increasing towards the faintest luminosities This could be an indication for a different distribution of dust and stars depending on the luminosity. Measuring the UV-slopes of these galaxies could provide additional information in this respect.

To continue and improve on the work done during this thesis, several paths can be followed and are summed up in the paragraphs below. The first and simplest one is to add new cubes as input for the LF computation. Additional cubes would increase the overall volume of Universe explored and in average, would tend to decrease the impact of cosmic variance on the determination of the faint end slope of the LAE LF. New cubes would also add highly magnified ($\mu \gtrsim 30$) sources to the sample. And even though these sources tend to have poorly constrained magnification and luminosity (see Sect. 3.3.2), it may be possible to derive statistically relevant information for $\log L \lesssim 40.5$ (the estimated completeness limit of the LF determined in this thesis) by accumulating enough of them. Finally, if we manage to double the sample in terms of effective volume it would be possible to compute the LFs for two independent and similar data sets and therefore gain further insight on the impact of cosmic variance on the derived results.

Several additional cubes are already available through the GTO collaboration or other external collaborators and are currently being prepared for the LF computation. The results obtained from this new analysis will be the object of a future publication in preparation.

Our current way of accounting for cosmic variances for each point of the LF leaves space for improvement. Using the online calculator of Trenti & Stiavelli (2008), we assume a compact geometry for all four fields and consider the population in each individual luminosity bin of the LFs as independent. None of these two assumptions is correct strictly speaking. The ideal way to improve this aspect of the work would be to draw numerous and random FoVs in results of cosmological simulations, but in practice this is challenging for two reasons. The first one is that the effective area of each of our fields strongly varies depending on the magnification/luminosity considered, and this effect is non trivial to reproduce in simulated FoVs. The second is that the low luminosity of our LAEs implies halo masses that are reaching below the resolution limits of current semi-analytic models (T. Garel, private communication), making them unreliable for our needs.

A last possibility regarding the LAE LF would be to use the exact same method as the one presented in Chapter 5 to compute the LAE LF using the deep MUSE blanks fields surveys (mainly the HUDF) considering them as a limit of the strong lensing case (i.e $\mu = 1$ over the entire FoV). Comparing the results obtained this way to the LF computed using a "normal" parametric selection function (i.e. Drake et al., 2017a; Herenz et al., 2019) would allow to further test our method and possibly improve the way we account for highly magnified objects by tuning, for example, the limit magnification $\mu_{\rm lim}$. In addition, it would allow to have a single determination of the LF over a wider range of luminosity and allow for a more relevant optimization of a Schechter function without the need to use external data sets to constrain the bright end.

Finally, to complete the work done on the intersection between the LAE and LBG population behind the A2744 cluster, the same analysis could be carried out in the background of the A370 cluster which has a deep MUSE coverage with an excellent mass model (Lagattuta et al., 2019) and deep photometry as part of the HFF program. The increased highly magnified volume probed this way would make our conclusions at low Lyα luminosity and/or faint UV magnitudes more relevant.

In the near future, two new telescopes will allow to develop further our understanding of the reionization era and of the first galaxies: the James Webb Space Telescope (JWST) and the Extremely Large Telescope (ELT) which are scheduled for respectively 2021 and 2025.

The JWST is a space based infrared and near infrared observatory with a mirror of effective diameter of 6.5m. It was designed to serve as a successor for the Hubble Space Telescope and has both imaging and spectroscopic capabilities. The combination of the large collecting area with infrared wavelength coverage makes it well suited to study the high redshift Universe. It is expected to detect the first galaxies in the redshift range $7 \lesssim z \lesssim 15$ based on either the detection of the Lyα emission with spectroscopy or the detection of a Gunn-Peterson Trough with deep photometry.

The ELT is an earth based telescope which will be equipped with a 39m main mirror and instruments covering the visible and near infrared. This unprecedented light collecting area will offer new possibilities for high redshift, large area and extremely deep cosmological surveys. It offers a strong synergy with the JWST observations because of its ability to perform large scale spectroscopic follow up observations of galaxies identified with JWST imaging, in a very similar domain of redshift. And in addition, its increased collecting area offers a higher sensitivity for detailed spectroscopic analysis, especially for continuum galaxies or galaxies with absorption lines.

Finally, and to finish this manuscript, it is worth underlying that even in the era of the ELT, the use of strong lensing clusters as gravitational telescopes has a promising future. It has been shown that the efficient IFU technology pioneered with MUSE had greatly improved the quality of the mass model reconstruction and therefore our abilities to use galaxy clusters to see fainter and further. As more instruments of this kind are being developed (e.g. MOSAIC and HARMONI for the ELT) the methodology introduced in this thesis could be looked upon as a pioneering approach to exploit the combination of IFU data and lensing clusters to better understand the process of galaxy formation. Because the depth of the observations evolves roughly as the square root of the exposure time, increasing the depth of observations by a factor of two requires four times more exposure. In this regards, and because telescope time is expensive, observations of strong lensing clusters remain very competitive and efficient as the depth is instantaneously increased at no additional cost other than the complexity of the data processing. The HFF program designed to push the limits of the HST and solely dedicated to observations of strong lensing clusters illustrates perfectly this last point.

Conclusion et perspectives futures

Les principales questions présentées dans l'introduction de ce manuscrit sont les suivantes :

1- Par élimination, les galaxies à formation d'étoiles sont susceptibles d'entraîner la réionisation, mais cela reste encore à confirmer par des observations. Les galaxies à formation d'étoiles peuvent-elles produire suffisamment de densité de flux UV grâce à une contribution importante (mais généralement invisible) de galaxies extrêmement faibles, pour assurer la réionisation de l'Univers ?

2 - Quelle est la chronologie exacte de la réionisation ? Il y a des preuves d'une transition rapide entre $6 < z < 7$, mais nos contraintes observationnelles s'arrêtent à $z \sim 7.5$ pour le moment, laissant la question de l'époque du début de la réionisation ainsi que de la vitesse de transition ouverte.

3 - À quoi ressemble la partie à très faible luminosité de la fonction de luminosité des galaxies à formation d'étoiles ? Est ce que cette partie de lafonction de luminosité évolue avec le redshift ? Existe-t-il une luminosité typique de dessous de la quelle la fonction de luminosité s'effondre ?

4 - Est-ce qu'il nous manque une partie importante des galaxies formant des étoiles lorsque l'on se contente du processus de sélection LAE ou LBG ? Est-il possible d'obtenir une meilleure évaluation empirique des galaxies formant des étoiles en comprenant mieux la relation entre les populations de LAE et de LBG ?

5 - Les LAE et les LBG sont-elles essentiellement la même population sans que nous soyons à même de nous rencontre à cause de biais observationnels ?

La majeure partie du travail effectué au cours de cette thèse a porté sur la détermination de la LAE LF derrière des amas de galaxies à effet de lentille gravitationnelle observés avec MUSE. Le but de cette étude était d'établir des contraintes sur la forme de l'extrémité faible de la LAE LF et de contraindre la contribution de cette population à la réionisation.

Profitant des grandes capacités de l'instrument MUSE et utilisant les amas de galaxies comme outil pour atteindre des LAE de faible luminosité, nous avons sélectionné à l'aveugle une population de 156 LAEs identifiés par spectroscopie derrière quatre amas, dans le domaine de redshift $2.9 < z < 6,7$ et avec une luminosité Lyα corrigée du grossissement $39 \lesssim \log L \lesssim 43$. Étant donné la complexité de combiner les cubes de données spectroscopiques de MUSE avec les observations de lentille gravitationnelle, et tenant compte du fait que chaque source a besoin d'un traitement approprié pour rendre compte correctement son grossissement et de sa représentativité, le calcul de la LF a nécessité une mise en œuvre minutieuse, incluant quelques développements originaux. Pour ces besoins, une procédure spécifique a été développée, incluant les nouvelles méthodes suivantes. Tout d'abord, nous avons créé un calcul précis de $V_{\max}$ pour les sources en arrière plan des amas qui est basé sur la création de masques 3D. Cette méthode nous permet de cartographier avec précision la détectabilité d'une source donnée dans des cubes spectroscopiques MUSE. Ces masques sont ensuite utilisés pour calculer le volume cosmologique dans le plan source de l'amas. Cette méthode pourrait être facilement adaptée pour être utilisée dans des travaux similaires en champs vide. Deuxièmement, nous avons développé un calcul de la completude basé sur des simulations

utilisant le profil réel des sources. Au lieu d'effectuer une approche paramétrique lourde basée sur des simulations d'injection et de re-detection de sources avec de bombreuses iterations. Cette méthode est plus rapide, plus flexible et prend mieux en compte les spécificités des sources individuelles, aussi bien dans la dimension spatiale que spectrale.

Après l'application de cette procédure à la population des LAE, la LAE LF a été construite pour différents bins de redshift en utilisant 152 des 156 LAE détectés. Quatre LAEs ont été supprimés parce que leur contribution n'était pas digne de confiance. En raison de la stratégie d'observation, cette étude fournit les contraintes à plus faible luminosité Lyα obtenues à ce jour, par conséquent, une mesure plus précise de la densité de taux de formation stellaire associée à la population de LAEs. Nos résultats et conclusions peuvent être résumés comme suit :

- La population de LAE trouvée derrière les quatre amas a été divisée en quatre bins de redshift : $2{,}9 < z < 6,7$, $2{,}9 < z < 4,0$, $4{,}0 < z < 5,9$ et $5{,}0 < z < 6,7$. En raison de l'effet de lentille gravitaionnelles, le volume d'Univers sondé est considérablement réduit par rapport aux études en champs vide. Le volume moyen estimé de l'Univers examiné dans ces 4 bins de redshift est de $\sim 15 \sim 15\,000$ Mpc^3, $\sim 5\,000$ Mpc^3, $\sim 4\,000$ Mpc^3, et $\sim 5\,000$ Mpc^3 respectivement.
- La LAE LF a été calculée dans chacun de ces bins. De par la construction de cet échantillon, les LF dérivées sondent efficacement le régime de faible luminosité et la population observée fournit à elle seule des contraintes solides sur la forme de l'extrémité faible des LAE LF. Aucune évolution significative de la forme de la LF avec le redshift n'est trouvée en utilisant uniquement ces premiers points. Ces résultats doivent être pris avec prudence étant donné la nature complexe de l'analyse "lensing", d'une part, et le petit volume effectif examiné par l'échantillon, d'autre part. Nos résultats plaident en faveur d'une possible sous-estimation systématique de la variance cosmique.
- Un ajustement de Schechter de la LAE LF a été effectué en combinant la LAE LF calculée dans cette analyse avec les données d'études antérieures pour contraindre l'extrémité brillante. À la suite de cette étude, on a mesuré une pente prononcée pour l'extrémité faible, variant avec le redshift entre $\alpha = -1,58^{+0,11}_{-0,11}$ à $2,9 < z < 4$ et $\alpha = -1,87^{+0,12}_{-0,12}$ à $5 < z < 6,7$.
- Les valeurs de SFRD$_{\mathrm{Ly}\alpha}$ ont été obtenues en fonction du redshift par l'intégration de nos LFs et comparées aux niveaux nécessaires pour ioniser l'Univers tels que déterminés dans Bouwens et al. (2015a). Aucune hypothèse n'a été faite concernant la fraction d'échappement des photons Lyman-alpha et les valeurs de SFRD$_{\mathrm{Ly}\alpha}$ calculées dans ce travail correspondent aux valeurs observées. En raison des bonnes contraintes obtenues sur la partie faible luminosité de nos LFs et d'une meilleure récupération du flux total, nous estimons que les résultats actuels sont plus fiables que ceux des études précédentes. Même si la population de LAEs contribue sans aucun doute à une fraction importante de la SFRD totale, il n'est pas certain que cette population suffise à elle seule à ioniser l'Univers à $z \sim 6$. Les résultats dépendent de la fraction d'échappement réelle des photons Lyman-alpha.
- Les LAEs et les LBGs ont un niveau de contribution similaire à $z \sim 6$ au niveau total de SFRD de l'Univers. Selon l'intersection entre ces deux populations, l'union des populations LAE et LBG peut suffire à réioniser l'Univers à $z \sim 6$.

Grâce à ce travail, nous avons montré que les capacités de l'instrument MUSE en font un outil idéal pour déterminer la LAE LF. Étant une IFU, MUSE permet une étude aveugle des LAEs, homogène en redshift, avec une meilleure récupération du flux total par rapport au observations spectroscopiques classique avec à l'aide de fente. La fonction de sélection est également mieux comprise que par l'imagerie bande étroite.

Environ 20% de l'échantillon actuel de nos LAEs n'a pas d'équivalent photométrique identifié, même dans les observations les plus profondes à ce jour (i.e le HFF). Il s'agit d'un point important à garder à l'esprit car c'est un premier élément de réponse concernant l'intersection entre les po-

pulations de LAE et de LBG. L'extension de la méthode présentée ici à d'autres champs d'amas devrait également permettre d'améliorer la détermination de la LAE LF et de rendre plus robustes les contraintes sur les sources de la réionisation.

Afin de mieux comprendre l'interrelation entre les populations de LAE et de LBG, nous avons entrepris une recherche simultanée de ces deux populations dans un volume donné. L'objectif de ce second travail était de voir s'il est possible de réaliser empiriquement une meilleure évaluation des galaxies à formation d'étoile en examinant l'intersection de ces deux populations. Le deuxième objectif était de caractériser davantage les biais intrinsèques à chacune de ces méthodes de sélection afin de déterminer si la ségrégation entre les LAE et les LBG n'est effectivement qu'un biais d'observation ou le résultat de différences intrinsèques.

L'étude menée sur A2744 a conduit aux résultats suivants :

- Pour les galaxies à faible continuum UV ($M_{1500} \geq 20.25$), la fraction des LAE parmi les SFGs augmente avec le redshift jusqu'à $z \sim 6$, en accord avec les précédentes études (e.g. Arrabal Haro et al., 2018).
- La sélection des émetteurs Lyα semble être plus efficace que la sélection LBG pour identifier les galaxies a faible continuum UV ($M_{1500} >$ - 17) qui ne seraient pas détectées dans les observation profondes en champs vide. A cet égard, nos résultats sont en bon accord avec Maseda et al. (2018).
- Jusqu'à $M_{1500} \sim -17$, les LBGs semblent fournir une bonne représentation des SFGs, en particulier lors du calcul du flux ionisant total dans les volumes explorés par les relevés actuels.
- Il n'y a pas de preuve claire, basée sur nos résultats actuels, d'une différence intrinsèque entre les populations de LAEs et LBGs. Toutefois, une enquête plus approfondie sera nécessaire pour conclure sur ce point. En particulier, certaines tendances systématiques apparaissent entre ces deux populations, en ce sens que les galaxies les plus brillantes en UV semblent présenter un rapport $f_{\mathrm{Ly}_\alpha}/f_{\mathrm{UV}}$ plus faible et qui augmentant pour les galaxies a fort continuum UV. Ceci pourrait être une indication d'une distribution différente de poussière et d'étoiles en fonction de la luminosité UV. La mesure des pentes UV de ces galaxies pourrait fournir des informations supplémentaires à cet égard.

Afin de poursuivre et d'améliorer le travail effectué au cours de cette thèse, plusieurs pistes peuvent être suivies et sont résumées dans les paragraphes ci-dessous. La première et la plus simple est d'ajouter de nouveaux cubes en entrée pour le calcul de la LF. Des cubes supplémentaires augmenteraient le volume total de l'Univers exploré et, en moyenne, auraient tendance à diminuer l'impact de la variance cosmique sur la détermination de la pente de la LAE LF. De nouveaux cubes ajouteraient également des sources à fort grandissement ($\mu \gtrsim 30$) à l'échantillon. Et même si ces sources ont tendance à avoir un grossissement et une luminosité Lyα mal caractérisés (voir la section 3.3.2), il peut être possible d'obtenir des informations statistiquement pertinentes pour $\log L \lesssim 40.5$ (la limite de complétude estimée de la LF déterminée dans cette thèse) en accumulant suffisamment de ces données. Enfin, si nous parvenons à doubler le volume effectif de l'échantillon, il serait possible de calculer les LFs pour deux ensembles de données indépendants et similaires et d'obtenir ainsi une meilleure compréhension de l'impact de la variance cosmique sur nos résultats.

Plusieurs cubes supplémentaires sont déjà disponibles grâce à la collaboration GTO ou grâce à d'autres collaborateurs externes et sont en cours de préparation pour le calcul de la LF. Les résultats obtenus de cette nouvelle analyse feront l'objet d'une prochaine publication en préparation.

Notre façon actuelle de comptabiliser les variances cosmiques pour chaque point de la LF pourrait être améliorée. En utilisant le calculateur en ligne de Trenti & Stiavelli (2008), nous supposons une géométrie compacte pour les quatre champs et considérons la population dans chaque bin de

luminosité individuelle des LFs comme indépendante. Aucune de ces deux hypothèses n'est correcte à proprement parler. La meilleure façon d'améliorer cet aspect du travail serait de tirer de nombreux champs de vue aléatoires dans les résultats des simulations cosmologiques, mais en pratique, cela reste difficile pour deux raisons. La première est que la surface effective de chacun de nos champs varie fortement en fonction du grossissement/luminosité considéré, et cet effet compliqué à reproduire dans des FoVs simulés. La seconde est que la faible luminosité de nos LAEs implique des masses de halo de matière sombre qui sont inférieures aux limites de résolution des modèles semi-analytiques actuels (T. Garel, communication privée), les rendant peu fiables pour nos besoins.

Une dernière possibilité concernant la LAE LF serait d'utiliser exactement la même méthode que celle présentée dans le chapitre 5 pour calculer la LAE LF en utilisant des observations en champs vides profonds faites par MUSE (principalement le HUDF) en les considérant comme un cas limite des lentilles gravitationnelles (c'est-à-dire $\mu = 1$ sur la FoV totale). Comparer les résultats ainsi obtenus a la LF calculé à l'aide d'une fonction de sélection paramétrique "classique" (i.e. Drake et al., 2017a; Herenz et al., 2019) permettrait de tester davantage notre méthode et éventuellement d'améliorer la façon dont nous tenons compte des objets fortement amplifiés en ajustant, par exemple, les valeurs d'amplification limite $\mu_{\rm lim}$. De plus, cela permettrait d'avoir une détermination unique de la LF sur une plus grande plage de luminosité et permettrait une optimisation plus pertinente d'une fonction de Schechter sans avoir besoin d'utiliser des ensembles de données externes pour en contraindre la partie brillante.

Enfin, pour compléter le travail effectué sur l'intersection entre la population LAE et LBG derrière le cluster A2744, la même analyse pourrait être effectuée en arrière-plan de l'amas A370 qui a une couverture MUSE profonde avec un excellent modèle de masse (Lagattuta et al., 2019) et une photométrie profonde car faisant partie du programme HFF. L'augmentation du volume fortement a fort grandissement ainsi sondé rendrait nos conclusions à faible luminosité Lyα et/ou faible magnitude UV plus pertinentes.

Dans un proche avenir, deux nouveaux télescopes nous permettront de mieux comprendre l'ère de la réionisation et les premières galaxies : le “James Webb Space Telescope (JWST) et le "Extremely Large Telescope" (ELT) qui sont prévus respectivement pour 2021 et 2025.

Le JWST est un observatoire spatial infrarouge et proche infrarouge avec un miroir d'un diamètre effectif de 6,5m. Il a été conçu pour succéder au télescope spatial Hubble et possède des capacités d'imagerie et de spectroscopie. La combinaison de la grande surface collectrice et de la couverture de longueur d'onde infrarouge le rend bien adapté à l'étude de l'Univers à grand redshift. On s'attend à détecter les premières galaxies dans une plage de redshift de $7 \lesssim z \lesssim 15$ grâce soit à la détection de l'émission Lyα par spectroscopie, soit de la détection d'un effet Gunn-Peterson par photométrie profonde.

L'ELT est un télescope terrestre qui sera équipé d'un miroir principal de 39 m et d'instruments couvrant le visible et le proche infrarouge. Cette surface collectrice sans précédent offrira de nouvelles possibilités pour des relevés cosmologiques à grand redshift, de grande surface et extrêmement profonds. Il offre une synergie importante avec les observations du JWST en raison de sa capacité à effectuer des observations de suivi spectroscopiques à grande échelle de galaxies identifiées avec l'imagerie du JWST, et ce dans un domaine de redshift très similaire. De plus, sa grande surface collectrice offre une importante sensibilité pour l'analyse spectroscopique détaillée, en particulier pour les galaxies à continuum ou les galaxies à raies d'absorption.

Enfin, et pour terminer ce manuscrit, il convient de souligner que même à l'époque de l'ELT, l'utilisation d'amas de galaxies comme télescopes gravitationnels a un avenir prometteur. Il a été démontré que la technologie IFU efficace mise au point avec MUSE avait grandement amélioré la

qualité de la reconstruction du modèle de masse et donc notre capacité à utiliser des amas pour voir plus faible et plus loin. Comme d'autres instruments de ce type sont en cours de développement (par exemple MOSAIC et HARMONI pour l'ELT), la méthodologie présentée dans cette thèse pourrait être considérée comme une approche pionnière pour exploiter la combinaison des données IFU et des amas afin de mieux comprendre le processus de formation des galaxies. Comme la profondeur des observations évolue comme la racine carrée du temps d'exposition, l'augmentation de la profondeur des observations par un facteur de deux nécessite quatre fois plus d'exposition. A cet égard, et parce que le temps de télescope est coûteux, les observations d'amas restent très compétitives et efficaces car la profondeur est instantanément augmentée sans coût supplémentaire autre que la complexité du traitement des données. Le programme HFF conçu pour repousser les limites d'observations du HST et dédié exclusivement à l'observation d'amas de galaxies massifs illustre parfaitement ce dernier point.

Bibliography

Adams, J. J., Blanc, G. A., Hill, G. J., et al. 2011, ApJ Supplement Series, 192, 5

Agarwal, B., Dalla Vecchia, C., Johnson, J. L., Khochfar, S., & Paardekooper, J.-P. 2014, MNRAS, 443, 648

Akhlaghi, M. & Ichikawa, T. 2015, ApJ Supplement Series, 220, 1

Arrabal Haro, P., Rodríguez Espinosa, J. M., Muñoz-Tuñón, C., et al. 2018, Monthly Notices of the Royal Astronomical Society, 478, 3740

Atek, H., Kunth, D., Schaerer, D., et al. 2014, Astronomy & Astrophysics, 561, A89

Atek, H., Richard, J., Kneib, J.-p., & Schaerer, D. 2018, MNRAS, 479, 5184

Bacon, R., Brinchmann, J., Richard, J., et al. 2015, A&A, 575, A75

Bacon, R., Conseil, S., Mary, D., et al. 2017, A&A, 608, A1

Bacon, R., Vernet, J., Borisova, E., et al. 2014, The Messenger, 157, 13

Bañados, E., Venemans, B. P., Mazzucchelli, C., et al. 2018, Nature, 553, 473

Barkana, R., Haiman, Z., & Ostriker, J. P. 2001, The Astrophysical Journal, 558, 482

Baron, D. & Poznanski, D. 2017, MNRAS, 465, 4530

Becker, G. D., Bolton, J. S., Madau, P., et al. 2015, MNRAS, 447, 3402

Becker, R. H., Fan, X., White, R. L., et al. 2001, The Astronomical Journal, 122, 2850

Bertin, E. & Arnouts, S. 1996, A&A Supplement Series, 117, 393

Bina, D., Pelló, R., Richard, J., et al. 2016, A&A, 14

Blanc, G. a., Adams, J. J., Gebhardt, K., et al. 2011, ApJ, 736, 31

Bolzonella, M., Miralles, J. M., & Pelló, R. 2000, A&A, 363, 476

Bosman, S. E. I., Fan, X., Jiang, L., et al. 2018, MNRAS, 479, 1055

Bouché, N., Finley, H., Schroetter, I., et al. 2016, ApJ, 820, 121

Bouwens, R., Illingworth, G., Franx, M., & Ford, H. 2007, ApJ, 670, 928

Bouwens, R. J., Illingworth, G. D., Oesch, P. A., et al. 2015a, ApJ, 811, 140

Bouwens, R. J., Illingworth, G. D., Oesch, P. A., et al. 2015b, ApJ, 803, 34

Bouwens, R. J., Oesch, P. A., Illingworth, G. D., Ellis, R. S., & Stefanon, M. 2017, ApJ, 843, 129

Broadhurst, T., Benitez, N., Coe, D., et al. 2005, ApJ, 621, 53

Bruzual, G. & Charlot, S. 2003, MNRAS, 344, 1000

Calzetti, D., Armus, L., Bohlin, R. C., et al. 2000, The Astrophysical Journal, 533, 682

Caminha, G., Karman, W., Rosati, P., et al. 2016, A&A, 595, A100

Cantalupo, S., Pezzulli, G., Lilly, S. J., et al. 2019, MNRAS, 483, 5188

Caruana, J., Bunker, A. J., Wilkins, S. M., et al. 2014, MNRAS, 443, 2831

Caruana, J., Wisotzki, L., Herenz, E. C., et al. 2018, MNRAS, 473, 30

Cassata, P., Le Fèvre, O., Garilli, B., et al. 2011, A&A, 525, A143

Cassata, P., Tasca, L. A. M., Fevre, O. L., et al. 2015, Astronomy & Astrophysics, 573, A24

Castellano, M., Amorín, R., Merlin, E., et al. 2016, Astronomy & Astrophysics, 590, A31

Chabrier, G. 2003, Publications of the Astronomical Society of the Pacific, 115, 763

Charlot, S. & Fall, S. M. 1993, ApJ, 415, 580

Clément, B., Cuby, J. G., Courbin, F., et al. 2012, A&A, 538, A66

Clowe, D., Bradač, M., Gonzalez, A. H., et al. 2006, The Astrophysical Journal, 648, L109
Coleman, G. D., Wu, C.-C., & Weedman, D. W. 1980, The Astrophysical Journal Supplement Series, 43, 393
Contini, T., Epinat, B., Bouché, N., et al. 2016, A&A, 591, A49
Covone, G., Kneib, J.-P., Soucail, G., et al. 2006, A&A, 456, 409
Cowie, L. L. & Hu, E. M. 1998, AJ, 115, 1319
Dawson, S., Rhoads, J. E., Malhotra, S., et al. 2007, ApJ, 671, 1227
De Barros, S., Pentericci, L., Vanzella, E., et al. 2017, Astronomy & Astrophysics, 608, A123
de Bennassuti, M., Salvadori, S., Schneider, R., Valiante, R., & Omukai, K. 2017, MNRAS, 465, 926
de La Vieuville, G., Bina, D., Pello, R., et al. 2019, arXiv e-prints, arXiv:1905.13696
De Lucia, G., Kauffmann, G., Springel, V., et al. 2004, MNRAS, 348, 333
Dijkstra, M., Haiman, Z., Rees, M. J., & Weinberg, D. H. 2004, ApJ, 601, 666
Dijkstra, M., Lidz, A., & Wyithe, J. S. B. 2007, MNRAS, 377, 1175
Drake, A., Garel, T., & Wisotzki, L. 2017a, A&A, 608
Drake, A. B., Guiderdoni, B., Blaizot, J., et al. 2017b, MNRAS, 278, 267
Dressler, A., Henry, A., Martin, C. L., et al. 2015, ApJ, 806, 19
Elíasdóttir, Á., Limousin, M., Richard, J., et al. 2007, arXiv e-prints, arXiv:0710.5636
Faber, S. M. & Jackson, R. E. 1976, ApJ, 204, 668
Fan, X., Narayanan, V. K., Lupton, R. H., et al. 2001, The Astronomical Journal, 122, 2833
Fan, X., Strauss, M. A., Becker, R. H., et al. 2006, AJ, 132, 117
Fan, X., White, R. L., Davis, M., et al. 2000, The Astronomical Journal, 120, 1167
Felten, J. E. 1976, ApJ, 207, 700
Finkelstein, S. L., Ryan Russell E., J., Papovich, C., et al. 2015, ApJ, 810, 71
Foreman-Mackey, D., Hogg, D. W., Lang, D., & Goodman, J. 2013, PASP, 125, 306
Frebel, A., Chiti, A., Ji, A. P., Jacobson, H. R., & Placco, V. M. 2015, ApJ, 810, L27
Gallego, S. G., Cantalupo, S., Lilly, S., et al. 2018, MNRAS, 475, 3854
Garel, T., Blaizot, J., Guiderdoni, B., et al. 2012, MNRAS, 422, 310
Greig, B., Mesinger, A., & Bañados, E. 2019, MNRAS, 484, 5094
Greig, B., Mesinger, A., Haiman, Z., & Simcoe, R. A. 2017, MNRAS, 466, 4239
Guaita, L., Talia, M., Pentericci, L., et al. 2017, A&A, 606, A19
Guérou, A., Emsellem, E., Krajnović, D., et al. 2016, A&A, 591, A143
Guérou, A., Krajnović, D., Epinat, B., et al. 2017, A&A, 608, A5
Gunn, J. E. & Peterson, B. A. 1965, ApJ, 142, 1633
Guth, A. H. 1981, PRD, 23, 347
Harikane, Y., Ouchi, M., Shibuya, T., et al. 2018, ApJ, 859, 84
Hashimoto, T., Garel, T., Guiderdoni, B., et al. 2017, Astronomy & Astrophysics, 608, A10
Hayes, M., Schaerer, D., Stlin, G., et al. 2011, ApJ, 730, 8
Herenz, E. C., Urrutia, T., Wisotzki, L., et al. 2017, A&A, 606, A12
Herenz, E. C. & Wisotzki, L. 2017, A&A, 602, A111
Herenz, E. C., Wisotzki, L., Saust, R., et al. 2019, A&A, 621, A107
Hu, E., Cowie, L., Songaila, A., et al. 2016, ApJ, 825, L7
Hu, E. M., Cowie, L. L., Barger, A. J., et al. 2010, ApJ, 725, 394
Hu, E. M., Cowie, L. L., Capak, P., et al. 2004, The Astronomical Journal, 127, 563
Husband, K., Bremer, M., Stanway, E., et al. 2013, MNRAS, 432, 2869
Husser, T.-O., Kamann, S., Dreizler, S., et al. 2016, A&A, 588, A148
Inami, H., Bacon, R., Brinchmann, J., et al. 2017, Astronomy & Astrophysics, 608, A2
Japelj, J., Vanzella, E., Fontanot, F., et al. 2017, MNRAS, 468, 389
Jiang, L., McGreer, I. D., Fan, X., et al. 2016, ApJ, 833, 222

Johnson, T. L., Sharon, K., Bayliss, M. B., et al. 2014, ApJ, 797, 48
Jullo, E. & Kneib, J. P. 2009, MNRAS, 395, 1319
Jullo, E., Kneib, J. P., Limousin, M., et al. 2007, New Journal of Physics, 9, 447
Kamann, S., Bastian, N., Husser, T. O., et al. 2018a, MNRAS, 480, 1689
Kamann, S., Husser, T. O., Brinchmann, J., et al. 2016, A&A, 588, A149
Kamann, S., Husser, T. O., Dreizler, S., et al. 2018b, MNRAS, 473, 5591
Karman, W., Grillo, C., Balestra, I., et al. 2016, A&A, 585, A27
Kashikawa, N., Shimasaku, K., Malkan, M. A., et al. 2006, ApJ, 648, 7
Kawamata, R. 2018, ApJ, 855, 4
Kawamata, R., Oguri, M., Ishigaki, M., Shimasaku, K., & Ouchi, M. 2016, ApJ, 819, 0
Kennicutt, Jr., R. C. 1998, ApJ, 498, 541
Kinney, A. L., Calzetti, D., Bohlin, R. C., et al. 1996, The Astrophysical Journal, 467, 38
Kneib, J.-P., Ellis, R. S., Smail, I., Couch, W. J., & Sharples, R. M. 1996, ApJ, 471, 643
Kneib, J.-P. & Natarajan, P. 2011, The Astronomy and Astrophysics Review, 19, 47
Konno, A., Ouchi, M., Shibuya, T., et al. 2018, PASJ, 70, S16
Lagattuta, D. J., Richard, J., Bauer, F. E., et al. 2019, MNRAS, 485, 3738
Lagattuta, D. J., Richard, J., Clément, B., et al. 2017, MNRAS, 469, 3946
Laursen, P., Sommer-Larsen, J., & Razoumov, A. O. 2011, ApJ, 728, 52
Leclercq, F., Bacon, R., Wisotzki, L., et al. 2017, A&A, 608, A8
Leitherer, C., Schaerer, D., Goldader, J. D., et al. 1999, the Astrophysical Journal Supplement Series, 123, 3
Limousin, M., Richard, J., Jullo, E., et al. 2007, ApJ, 668, 643
Livermore, R. C., Finkelstein, S. L., & Lotz, J. M. 2017, ApJ, 835, 113
Lotz, J. M., Koekemoer, A., Coe, D., et al. 2017, ApJ, 97
Lynds, R. 1971, ApJ, 164, L73
Mac Low, M. & Ferrara, A. 1999, ApJ, 513, 142
Madau, P. 1995, ApJ, 441, 18
Madau, P., Pozzetti, L., & Dickinson, M. 1998, ApJ, 498, 106
Mahler, G., Richard, J., Clément, B., et al. 2018, MNRAS, 692, 663
Malhotra, S. & Rhoads, J. E. 2002, ApJ, 565, L71
Markevitch, M. 2006, in ESA Special Publication, Vol. 604, The X-ray Universe 2005, ed. A. Wilson, 723
Martin, C. L. & Sawicki, M. 2004, ApJ, 603, 414
Maseda, M. V., Bacon, R., Franx, M., et al. 2018, ApJ Letters, 865, L1
Maselli, A., Gallerani, S., Ferrara, A., & Choudhury, T. 2007, MNRAS, 376, L34
Mason, C. A., Fontana, A., Treu, T., et al. 2019, MNRAS, 485, 3947
Mason, C. A., Treu, T., Dijkstra, M., et al. 2018, ApJ, 856, 2
Mason, C. A., Treu, T., Schmidt, K. B., et al. 2015, ApJ, 805, 79
Matthee, J., Sobral, D., Gronke, M., et al. 2018, A&A, 619, A136
Matthee, J., Sobral, D., Oteo, I., et al. 2016, MNRAS, 458, 449
Matthee, J., Sobral, D., Santos, S., et al. 2015, MNRAS, 451, 400
McGreer, I. D., Jiang, L., Fan, X., et al. 2013, ApJ, 768, 105
McGreer, I. D., Mesinger, A., & D'Odorico, V. 2015, MNRAS, 447, 499
McQuinn, M. 2012, MNRAS, 426, 1349
Meneghetti, M., Natarajan, P., Coe, D., et al. 2017, MNRAS, 3216, 3177
Merlin, E., Amorín, R., Castellano, M., et al. 2016, Astronomy & Astrophysics, 590, A30
Merten, J., Meneghetti, M., Postman, M., et al. 2015, ApJ, 806, 4
Miralda-Escudé, J., Cen, R., Ostriker, J. P., & Rauch, M. 1996, ApJ, 471, 582
Miralda-Escude, J. 1998, The Astrophysical Journal, 501, 15

Monreal-Ibero, A., Weilbacher, P., & Wendt, M. 2018, A&A, 615, A33
Mortlock, D. J., Warren, S. J., Venemans, B. P., et al. 2011, Nature, 474, 616
Newville, M., Stensitzki, T., Allen, D. B., & Ingargiola, A. 2014, Zenodo
Ocvirk, P., Gillet, N., Shapiro, P. R., et al. 2016, MNRAS, 463, 1462
Oesch, P., Bouwens, R., Illingworth, G., et al. 2014, ApJ, 786, 108
Okamoto, T., Gao, L., & Theuns, T. 2008, MNRAS, 390, 920
Oke, J. B. & Gunn, J. E. 1983, ApJ, 266, 713
Olmstead, A., Rigby, J. R., Swinbank, M., & Veilleux, S. 2014, AJ, 148
Ono, Y., Ouchi, M., Shimasaku, K., et al. 2010, ApJ, 724, 1524
Orieux, F., Giovannelli, J.-f., & Rodet, T. 2010, OSA, 27, 1593
Orsi, A., Lacey, C. G., Baugh, C. M., & Infante, L. 2008, Monthly Notices of the Royal Astronomical Society, 391, 1589
Osterbrock, D. E. & Ferland, G. J. 2006, Mercury, 35, 40
Ouchi, M., Harikane, Y., Shibuya, T., et al. 2018, PASJ, 70, S13
Ouchi, M., Shimasaku, K., Akiyama, M., Simpson, C., & Saito, T. 2008, ApJ Supplement Series, 301
Ouchi, M., Shimasaku, K., Furusawa, H., et al. 2003, ApJ, 582, 60
Ouchi, M., Shimasaku, K., Furusawa, H., et al. 2010, ApJ, 723, 869
Ouchi, M., Shimasaku, K., Okamura, S., et al. 2004, ApJ, 611, 660
Paardekooper, J. P., Khochfar, S., & Dalla, C. 2013, MNRAS, 429, L94
Parsa, S., Dunlop, J. S., & McLure, R. J. 2018, MNRAS, 474, 2904
Partridge, R. B. & Peebles, P. J. E. 1967, Astrophysical Journal, 147, 868
Patricio, V., Richard, J., Carton, D., et al. 2018, MNRAS, 28, 1
Pelló, R., Hudelot, P., Laporte, N., et al. 2018, A&A, 620, A51
Pelló, R., Kneib, J., & Bruzual, G. 1998, Astrophysics and Space Science, 263, 55
Pello, R., Le Borgne, J.-F., Soucail, G., Mellier, Y., & Sanahuja, B. 1991, ApJ, 366, 405
Pentericci, L., Fontana, A., Vanzella, E., et al. 2011, ApJ, 743, 132
Pentericci, L., Vanzella, E., Fontana, A., et al. 2014, ApJ, 793, 113
Penzias, A. & Wilson, R. 1965, ApJ, 142, 419
Pérez-González, P. G., Cava, A., Barro, G., et al. 2013, ApJ, 762, 46
Piqueras, L., Conseil, S., Shepherd, M., et al. 2017, ArXiv e-prints, arXiv:1710.03554
Planck Collaboration, Adam, R., Ade, P. A. R., et al. 2016a, Astronomy & Astrophysics, 594, A1
Planck Collaboration, Ade, P., Aghanim, N., et al. 2016b, A&A, 594, A20
Planck Collaboration, Ade, P., Aghanim, N., et al. 2016c, A&A, 594, A13
Planck Collaboration, Ade, P. A. R., Aghanim, N., et al. 2016d, Astronomy & Astrophysics, 594, A24
Press, W. H. & Schechter, P. 1974, ApJ, 187, 425
Priewe, J., Williams, L. L. R., Liesenborgs, J., Coe, D., & Rodney, S. A. 2017, MNRAS, 465, 1030
Raiter, A., Schaerer, D., & Fosbury, R. A. E. 2010, Astronomy & Astrophysics, 523, A64
Rauch, M., Haehnelt, M., Bunker, A., et al. 2008, ApJ, 681, 856
Rees, M. J. & Ostriker, J. P. 1977, MNRAS, 179, 541
Rhoads, J. E., Malhotra, S., Dey, A., et al. 2000, ApJ, 545, L85
Richard, J., Jauzac, M., Limousin, M., et al. 2014, MNRAS, 444, 268
Richard, J., Patricio, V., Martinez, J., et al. 2015, MNRAS: Letters, 446, L16
Richard, J., Pelló, R., Schaerer, D., Le Borgne, J. F., & Kneib, J. P. 2006, A&A, 456, 861
Richard, J., Smith, G. P., Kneib, J. P., et al. 2010, MNRAS, 404, 325
Richard, J., Stark, D. P., Ellis, R. S., et al. 2008, ApJ, 685, 705
Ricotti, M. & Ostriker, J. 2004a, MNRAS, 350, 539
Ricotti, M. & Ostriker, J. P. 2004b, MNRAS, 352, 547

Roth, M. M., Sandin, C., Kamann, S., et al. 2018, A&A, 618, A3
Santos, S., Sobral, D., & Matthee, J. 2016, MNRAS, 14, 1
Schaerer, D. 2003, Astronomy & Astrophysics, 397, 527
Schaye, J., Crain, R. A., Bower, R. G., et al. 2015, MNRAS, 446, 521
Schechter, P. L. 1976, APJ, 297 - 306, 610
Schenker, M. A., Ellis, R. S., Konidaris, N. P., & Stark, D. P. 2014, The Astrophysical Journal, 795, 20
Schmidt, M. 1968, ApJ, 151, 393
Schneider, P., Ehlers, J., & Falco, E. E. 1992, Gravitational Lenses, Astronomy and Astrophysics Library (Berlin, Heidelberg: Springer Berlin Heidelberg), 112
Schroetter, I., Bouché, N., Wendt, M., et al. 2016, ApJ, 833, 39
Shankar, F., Crocce, M., Miralda-Escudé, J., Fosalba, P., & Weinberg, D. H. 2010, ApJ, 718, 231
Shibuya, T., Ouchi, M., Harikane, Y., et al. 2018a, PASJ, 70, S15
Shibuya, T., Ouchi, M., Konno, A., et al. 2018b, PASJ, 70, S14
Shivaei, I., Reddy, N. A., Siana, B., et al. 2018, ApJ, 855, 42
Sobacchi, E. & Mesinger, A. 2015, Monthly Notices of the Royal Astronomical Society, 453, 1843
Sobral, D. & Matthee, J. 2019, A&A, 623, A157
Sobral, D., Matthee, J., Best, P., et al. 2017, MNRAS, 466, 1242
Sobral, D., Santos, S., Matthee, J., et al. 2018, MNRAS, 476, 4725
Somerville, R. S. & Primack, J. R. 1999, MNRAS, 310, 1087
Soto, K. T., Lilly, S. J., Bacon, R., Richard, J., & Conseil, S. 2016, MNRAS, 458, 3210
Soucail, G., Mellier, Y., Fort, B., Mathez, G., & Cailloux, M. 1988, A&A, 191, L19
Sousbie, T., Pichon, C., & Kawahara, H. 2011, MNRAS, 414, 384
Springel, V., White, S. D., Jenkins, A., et al. 2005, Nature, 435, 629
Stark, D. P., Ellis, R. S., Bunker, A., et al. 2009, ApJ, 697, 1493
Stark, D. P., Ellis, R. S., Charlot, S., et al. 2017, MNRAS, 464, 469
Stark, D. P., Ellis, R. S., Chiu, K., Ouchi, M., & Bunker, A. 2010, MNRAS, 408, 1628
Stark, D. P., Ellis, R. S., & Ouchi, M. 2011, The Astrophysical Journal, 728, L2
Steidel, C. C., Adelberger, K. L., Giavalisco, M., Dickinson, M., & Pettini, M. 1999, ApJ, 519, 1
Steidel, C. C., Giavalisco, M., Pettini, M., Dickinson, M., & Adelberger, K. L. 1996, ApJ, 462, L17
Swinbank, A., Vernet, J., Smail, I., et al. 2015, MNRAS, 449, 1298
Tempel, E., Stoica, R., Mart\'\inez, V., et al. 2014, MNRAS, 438, 3465
Tilvi, V., Papovich, C., Finkelstein, S., et al. 2014, ApJ, 794, 5
Tornatore, L., Ferrara, A., & Schneider, R. 2007, MNRAS, 382, 945
Trainor, R. F., Steidel, C. C., Strom, A. L., & Rudie, G. C. 2015, ApJ, 809, 89
Trenti, M. & Stiavelli, M. 2008, The Astrophysical Journal, 676, 767
Treu, T., Schmidt, K. B., Trenti, M., Bradley, L. D., & Stiavelli, M. 2013, The Astrophysical Journal, 775, L29
Utsumi, Y., Goto, T., Kashikawa, N., et al. 2010, ApJ, 721, 1680
van Breukelen, C., Jarvis, M. J., & Venemans, B. P. 2005, MNRAS, 359, 895
van der Walt, S., Schönberger, J. L., Nunez-Iglesias, J., et al. 2014, PeerJ, 2, e453
Venemans, B., Findlay, J., Sutherland, W., et al. 2013, ApJ, 779, 24
Ventou, E., Contini, T., Bouché, N., et al. 2017, A&A, 608, A9
Verhamme, A., Orlitová, I., Schaerer, D., et al. 2017, Astronomy & Astrophysics, 597, A13
Verhamme, A., Schaerer, D., & Maselli, A. 2006, A&A, 460, 397
Vogelsberger, M., Genel, S., Springel, V., et al. 2014, MNRAS, 444, 1518
Volonteri, M. 2010, The Astronomy and Astrophysics Review, 18, 279
Volonteri, M., Habouzit, M., Pacucci, F., & Tremmel, M. 2016, in IAU Symposium, Vol. 319, Galaxies at High Redshift and Their Evolution Over Cosmic Time, ed. S. Kaviraj, 72–79

Weilbacher, P. M., Monreal-Ibero, A., Verhamme, A., et al. 2018, A&A, 611, A95
Weilbacher, P. M., Streicher, O., Urrutia, T., et al. 2012, in Software and Cyberinfrastructure for Astronomy II, Vol. 8451, 84510B
Weilbacher, P. M., Streicher, O., Urrutia, T., et al. 2014, 485, 451
Westra, E., Heath Jones, D., Lidman, C. E., et al. 2006, Astronomy & Astrophysics, 455, 61
White, S. & Rees, M. 1978, MNRAS, 183, 341
Willott, C. J., Delorme, P., Reylé, C., et al. 2010, ApJ, 139, 906
Wise, J. H., Turk, M. J., Norman, M. L., & Abel, T. 2012, ApJ, 745, 50
Wisotzki, L., Bacon, R., Blaizot, J., et al. 2016, A&A, 587, A98
Wisotzki, L., Bacon, R., Brinchmann, J., et al. 2018, Nature, 562, 229
Zabl, J., Bouché, N. F., Schroetter, I., et al. 2019, MNRAS, 485, 1961
Zaroubi, S. 2013, in Astrophysics and Space Science Library, Vol. 396, The First Galaxies, ed. T. Wiklind, B. Mobasher, & V. Bromm, 45
Zheng, Z. Y., Finkelstein, S. L., Finkelstein, K., et al. 2013, MNRAS, 431, 3589

List of Figures

List of Tables

A | Various plots

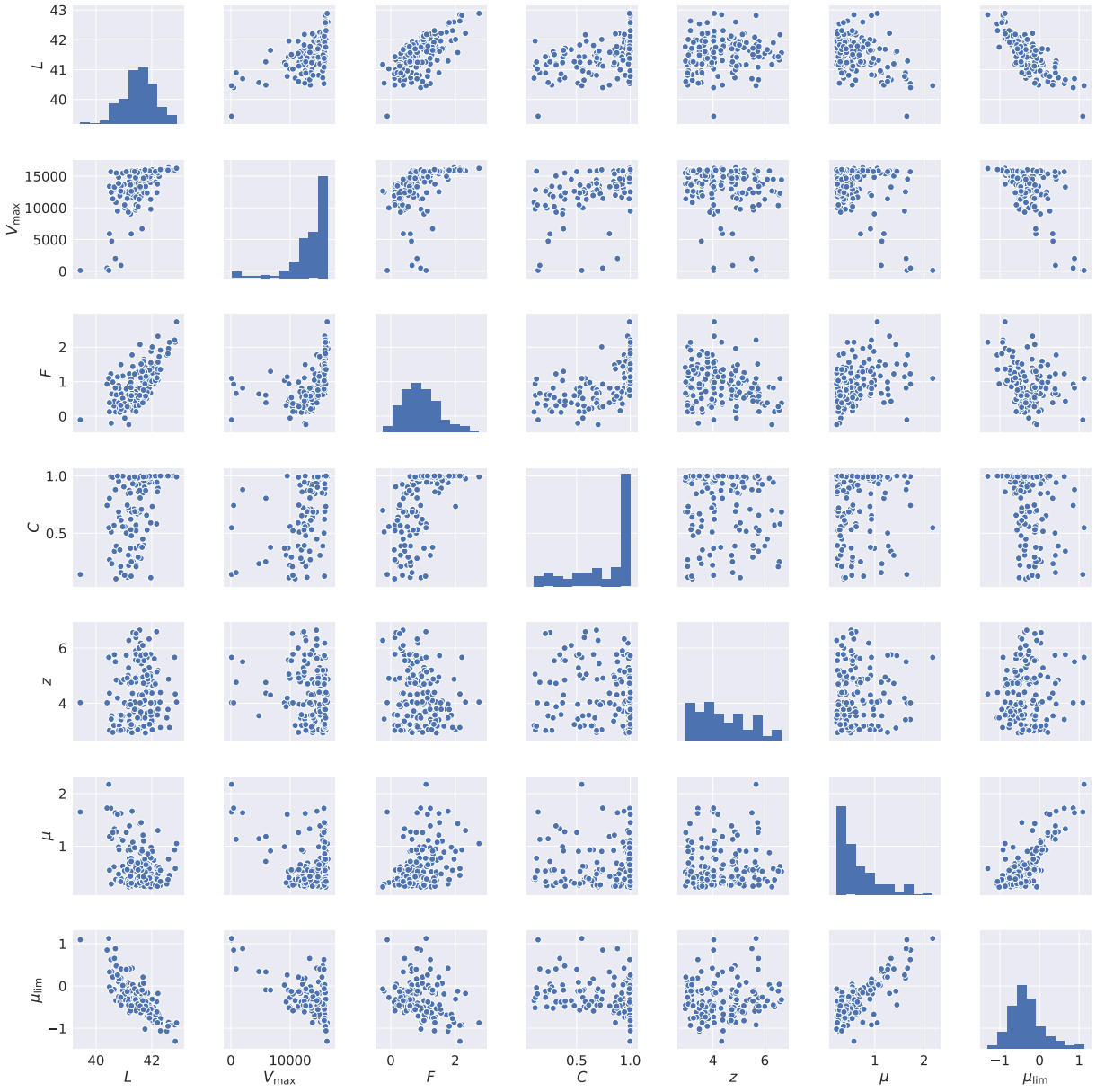

Figure A.1: Correlogram of some values of interest in the final catalog used to compute the LF. For representation purposes, the entries of this array are normalized or transformed as follows: L is $\log L_{\mathrm{Ly}\alpha}$, F is the Lyα detection flux transformed as $F = \log(10^{18} \times F_{\mathrm{Ly}\alpha}[\mathrm{erg\,s^{-1}\,cm^{-2}}])$ and both μ and μ_{lim} are shown in Log. No transformation is applied to V_{max} (in Mpc^3), the completeness noted C and the redshift z.

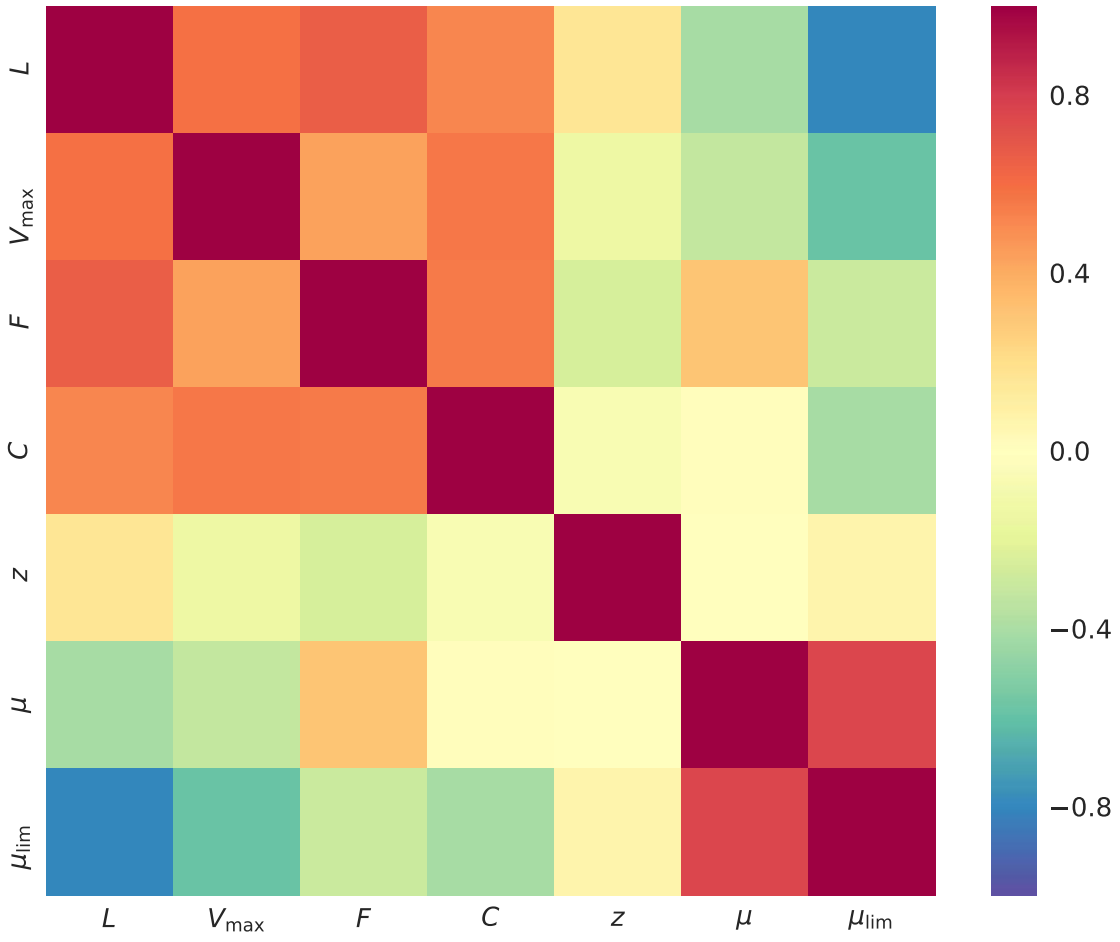

Figure A.2: Correlation matrix. The same entries and normalizations as for Fig. A.1 are used.

B | A&A publication: de La Vieuville et al. 2019a

A&A 628, A3 (2019)
https://doi.org/10.1051/0004-6361/201834471

Astronomy & Astrophysics

Faint end of the $z \sim 3$–7 luminosity function of Lyman-alpha emitters behind lensing clusters observed with MUSE⋆

G. de La Vieuville[1], D. Bina[1], R. Pello[1], G. Mahler[2], J. Richard[2], A. B. Drake[3], E. C. Herenz[4], F. E. Bauer[5,6,7], B. Clément[2], D. Lagattuta[2], N. Laporte[1,8], J. Martinez[2], V. Patrício[2,9], L. Wisotzki[10], J. Zabl[1], R. J. Bouwens[11], T. Contini[1], T. Garel[2,12], B. Guiderdoni[2], R. A. Marino[13], M. V. Maseda[11], J. Matthee[13], J. Schaye[11], G. Soucail[1]

[1] Institut de Recherche en Astrophysique et Planétologie (IRAP), Université de Toulouse, CNRS, UPS, CNES, 14 avenue Edouard Belin, 31400 Toulouse, France
e-mail: gdelavieuvil@irap.omp.eu
[2] Univ. Lyon, Univ. Lyon1, ENS de Lyon, CNRS, Centre de Recherche Astrophysique de Lyon UMR5574, 69230 Saint-Genis-Laval, France
[3] Max Planck Institute für Astronomie, Königstuhl 17, 69117 Heidelberg, Germany
[4] Department of Astronomy, Stockholm University, AlbaNova University Centre, 106 91 Stockholm, Sweden
[5] Instituto de Astrofísica, Facultad de Física, Pontificia Universidad Católica de Chile, Casilla 306, Santiago 22, Chile
[6] Space Science Institute, 4750 Walnut Street, Suite 205, Boulder, CO 80301, USA
[7] Millenium Institute of Astrophysics, Santiago, Chile
[8] Department of Physics and Astronomy, University College London, Gower Street, London WC1E 6BT, UK
[9] Dark Cosmology Centre, Niels Bohr Institute, University of Copenhagen, Juliane Maries Vej 30, 2100 Copenhagen, Denmark
[10] Leibniz-Institut für Astrophysik Potsdam (AIP), An der Sternwarte 16, 14482 Potsdam, Germany
[11] Leiden Observatory, Leiden University, PO Box 9513, 2300 RA Leiden, The Netherlands
[12] Observatoire de Genève, Université de Genève, 51 Ch. des Maillettes, 1290 Versoix, Switzerland
[13] Department of Physics, ETH Zurich, Wolfgang–Pauli–Strasse 27, 8093 Zurich, Switzerland

Received 19 October 2018 / Accepted 29 May 2019

ABSTRACT

Contact. This paper presents the results obtained with the Multi-Unit Spectroscopic Explorer (MUSE) at the ESO Very Large Telescope on the faint end of the Lyman-alpha luminosity function (LF) based on deep observations of four lensing clusters. The goal of our project is to set strong constraints on the relative contribution of the Lyman-alpha emitter (LAE) population to cosmic reionization.
Aims. The precise aim of the present study is to further constrain the abundance of LAEs by taking advantage of the magnification provided by lensing clusters to build a blindly selected sample of galaxies which is less biased than current blank field samples in redshift and luminosity. By construction, this sample of LAEs is complementary to those built from deep blank fields, whether observed by MUSE or by other facilities, and makes it possible to determine the shape of the LF at fainter levels, as well as its evolution with redshift.
Methods. We selected a sample of 156 LAEs with redshifts between $2.9 \leq z \leq 6.7$ and magnification-corrected luminosities in the range $39 \lesssim \log L_{\mathrm{Ly}_\alpha}\,[\mathrm{erg\,s^{-1}}] \lesssim 43$. To properly take into account the individual differences in detection conditions between the LAEs when computing the LF, including lensing configurations, and spatial and spectral morphologies, the non-parametric $1/V_{\mathrm{max}}$ method was adopted. The price to pay to benefit from magnification is a reduction of the effective volume of the survey, together with a more complex analysis procedure to properly determine the effective volume V_{max} for each galaxy. In this paper we present a complete procedure for the determination of the LF based on IFU detections in lensing clusters. This procedure, including some new methods for masking, effective volume integration and (individual) completeness determinations, has been fully automated when possible, and it can be easily generalized to the analysis of IFU observations in blank fields.
Results. As a result of this analysis, the Lyman-alpha LF has been obtained in four different redshift bins: $2.9 < z < 6.7$, $2.9 < z < 4.0$, $4.0 < z < 5.0$, and $5.0 < z < 6.7$ with constraints down to $\log L_{\mathrm{Ly}_\alpha} = 40.5$. From our data only, no significant evolution of LF mean slope can be found. When performing a Schechter analysis also including data from the literature to complete the present sample towards the brightest luminosities, a steep faint end slope was measured varying from $\alpha = -1.69^{+0.08}_{-0.08}$ to $\alpha = -1.87^{+0.12}_{-0.12}$ between the lowest and the highest redshift bins.
Conclusions. The contribution of the LAE population to the star formation rate density at $z \sim 6$ is $\lesssim$50% depending on the luminosity limit considered, which is of the same order as the Lyman-break galaxy (LBG) contribution. The evolution of the LAE contribution with redshift depends on the assumed escape fraction of Lyman-alpha photons, and appears to slightly increase with increasing redshift when this fraction is conservatively set to one. Depending on the intersection between the LAE/LBG populations, the contribution of the observed galaxies to the ionizing flux may suffice to keep the universe ionized at $z \sim 6$.

Key words. gravitational lensing: strong – galaxies: high-redshift – dark ages, reionization, first stars – galaxies: clusters: general – galaxies: luminosity function, mass function

⋆ Table E.1 and the four MUSE cubes used in this work are only available at the CDS via anonymous ftp to cdsarc.u-strasbg.fr (130.79.128.5) or via http://cdsarc.u-strasbg.fr/viz-bin/qcat?J/A+A/628/A3, or at http://muse-vlt.eu/science/

1. Introduction

Reionization is an important change of state of the universe after recombination, and many resources have been devoted in recent years to understand this process. The formation of the first structures, stars, and galaxies marked the end of the dark ages. Following the formation of the first structures, the density of ionizing photons was high enough to allow the ionization of the entire neutral hydrogen content of the intergalactic medium (IGM). It has been established that this state transition was mostly completed by $z \sim 6$ (Fan et al. 2006; Becker et al. 2015). However the identification of the sources responsible for this major transition and their relative contribution to the process is still a matter of substantial debate.

Although quasars were initially considered as important candidates owing to their ionising continuum, star-forming galaxies presently appear as the main contributors to the reionization (see e.g. Robertson et al. 2013, 2015; Bouwens et al. 2015a; Ricci et al. 2017). However a large uncertainty still remains on the actual contribution of quasars, as the faint population of quasars at high redshift remains poorly constrained (see e.g. Willott et al. 2010; Fontanot et al. 2012; McGreer et al. 2013). There are two main signatures currently used for the identification of star-forming galaxies around and beyond the reionization epoch. The first signature is the Lyman "drop-out" in the continuum bluewards with respect to Lyman-alpha from the combined effect of interstellar and intergalactic scattering by neutral hydrogen. Different redshift intervals can be defined to select Lyman break galaxies (LBGs) using the appropriate colour–colour diagrams or photometric redshifts. Extensive literature is available on this topic since the pioneering work by Steidel et al. (1996) (see e.g. Ouchi et al. 2004; Stark et al. 2009; McLure et al. 2009; Bouwens et al. 2015b, and the references therein). The second method is the detection of the Lyman-alpha line to target Lyman-alpha emitters (hereafter LAEs). The "classical" approach is based on wide-field narrow-band (NB) surveys, targeting a precise redshift bin (e.g. Rhoads et al. 2000; Kashikawa et al. 2006; Konno et al. 2014). More recent methods made efficient use of 3D/IFU spectroscopy in pencil beam mode with the Multi-Unit Spectroscopic Explorer (MUSE) at the Very Large Telecope (VLT; Bacon et al. 2015), which is a technique presently limited to $z \sim 7$ in the optical domain.

Based on LBG studies, the UV luminosity function (LF) evolves strongly at $z \geq 4$, with a depletion of bright galaxies with increasing redshift on one hand, and the slope of the faint end becoming steeper on the other hand (Bouwens et al. 2015b). This evolution is consistent with the expected evolution of the halo mass function during the galaxy assembly process. Studies of LAEs have found a deficit of strongly emitting ("bright") Lyman-alpha galaxies at $z \geq 6.5$, whereas no significant evolution is observed below $z \sim 6$ (Kashikawa et al. 2006; Pentericci et al. 2014; Tilvi et al. 2014); this trend is attributed to either an increase in the fraction of neutral hydrogen in the IGM or an evolution of the parent population, or both. The LBGs and LAEs constitute two different observational approaches to selecting star-forming galaxies, which are partly overlapping. The prevalence of Lyman-alpha emission in well-controlled samples of star-forming galaxies is also a test for the reionization history. However, a complete and "as unbiased as possible" census of ionizing sources can only be enabled through 3D/IFU spectroscopy without any photometric preselection.

As pointed out by different authors (see e.g. Maizy et al. 2010), lensing clusters are more efficient than blank fields for detailed (spectroscopic) studies at high redshift and also to explore the faint end of the LF. In this respect, they are complementary to observations in wide blank fields, which are needed to set reliable constraints on the bright end of both the UV and LAE LF. Several recent results in the Hubble Frontier Fields (HFF; Lotz et al. 2017) fully confirm the benefit expected from gravitational magnification (see e.g. Laporte et al. 2014, 2016; Atek et al. 2014; Infante et al. 2015; Ishigaki et al. 2015; Livermore et al. 2017).

This paper presents the results obtained with MUSE (Bacon et al. 2010) at the ESO VLT on the faint end of the LAE LF based on deep observations of four lensing clusters. The data were obtained as part of the MUSE consortium Guaranteed Time Observations (GTO) programme and first commissioning run. The final goal of our project in lensing clusters is to set strong constraints on the relative contribution of the LAE population to cosmic reionization. As shown in Richard et al. (2015) for SMACSJ2031.8-4036, Bina et al. (2016) for A1689, Lagattuta et al. (2017) for A370, Caminha et al. (2016) for AS1063, Karman et al. (2016) for MACS1149 and Mahler et al. (2018) for A2744, MUSE is ideally designed for the study of lensed background sources, in particular for LAEs at $2.9 \leq z \leq 6.7$. The MUSE instrument provides a blind survey of the background population, irrespective of the detection or not of the associated continuum. This instrument is also a unique facility capable of deriving the 2D properties of "normal" strongly lensed galaxies, as recently shown by Patricio et al. (2018). In this project, an important point is that MUSE allows us to reliably recover a greater fraction of the Lyman-alpha flux for LAE emitters, as compared to usual long-slit surveys or even NB imaging.

The precise aim of the present study is to further constrain the abundance of LAEs by taking advantage of the magnification provided by lensing clusters to build a blindly selected sample of galaxies which is less biased than current blank field samples in redshift and luminosity. By construction, this sample of LAEs is complementary to those built in deep blank fields, whether observed by MUSE or by other facilities, and makes it possible to determine in a more reliable way the shape of the LF towards the faintest levels and its evolution with redshift. We focus on four well-known lensing clusters from the GTO sample, namely Abell 1689, Abell 2390, Abell 2667, and Abell 2744. In this study we present the method and we establish the feasibility of the project before extending this approach to all available lensing clusters observed by MUSE in a future work.

In this paper we present the deepest study of the LAE LF to date, combining deep MUSE observations with the magnification provided by four lensing clusters. In Sect. 2, we present the MUSE data together with the ancillary *Hubble* Space Telescope (HST) data used for this project as well as the observational strategy adopted. The method used to extract LAE sources in the MUSE cubes is presented in Sect. 3. The main characteristics and the references for the four lensing models used in this article are presented in Sect. 4, knowing that the present MUSE data were also used to identify new multiply-imaged systems in these clusters, and therefore to further improve the mass models. The selection of the LAE sample used in this study is presented in Sect. 5. Section 6 is devoted to the computation of the LF. In this Section we present the complete procedure developed for the determination of the LF based on IFU detections in lensing clusters; some additional technical points and examples are given in Appendices A–D. This procedure includes novel methods for masking, effective volume integration and (individual) completeness determination, using as far as possible the true spatial and spectral morphology of LAEs instead of a parametric

Table 1. Main characteristics of MUSE observations.

	FoV	Seeing	Integration(h)	RA (J2000)	Dec (J2000)	ESO programme
A1689	$1' \times 1'$	$0.9''$–$1.1''$	1.8	197°52′39″	−1°20′42″	60.A-9100(A)
A2390	$1' \times 1'$	$0.75''$	2	328°23′53″	17°41′48″	094.A-0115(B)
A2667	$1' \times 1'$	$0.62''$	2	357°54′50″	−26°05′03″	094.A-0115(A)
A2744 (a)	$2' \times 2'$	$0.58''$	16.5	3°35′14″	−30°23′54″	094.A-0115(B)
A2744 (b)	$1' \times 1'$	$0.58''$	2	3°35′14″	−30°23′54″	094.A-0115(B)

Notes. The A2744 field was splitted in two (part a and part b) because of the additional pointing covering the centre of the 2×2 MUSE mosaic. For A1689 and A2390, the seeing was measured on the white light image obtained from the final datacube. For A2667 and A2744, the seeing was obtained by fitting a MUSE reconstructed F814W image with a seeing convolved HST F814W image (see Patricio et al. 2018 for A2667 and Mahler et al. 2018 for A2744).

approach. The parametric fit of the LF by a Schechter function, including data from the literature to complete the present sample, is presented in Sect. 7. The impact of mass model on the faint end and the contribution of the LAE population to the star formation rate density (SFRD) are discussed in Sect. 8. Conclusions and perspectives are given in Sect. 9.

Throughout this paper we adopt the following cosmology: $\Omega_\Lambda = 0.7$, $\Omega_m = 0.3$ and $H_0 = 70\,\mathrm{km\,s^{-1}\,Mpc^{-1}}$. Magnitudes are given in the AB system (Oke & Gunn 1983). All redshifts quoted are based on vacuum rest-frame wavelengths.

2. Data

2.1. MUSE observations

The sample used in this study consists of four different MUSE cubes of different sizes and exposure times, covering the central regions of well-characterized lensing clusters: Abell 1689, Abell 2390, Abell 2667, and Abell 2744 (resp. A1689, A2390, A2667 and A2744 hereafter). These four clusters already had well constrained mass models before the MUSE observations, as they benefited from previous spectroscopic observations. The reference mass models can be found in Richard et al. (2010; LoCuSS) for A2390 and A2667, in Limousin et al. (2007) for A1689, and in Richard et al. (2014) for the Frontier Fields cluster A2744.

The MUSE instrument has a $1' \times 1'$ field of view (FoV) and a spatial pixel size of $0.2''$, the covered wavelength range from 4750 Å to 9350 Å with a 1.25 Å sampling, effectively making the detection of LAEs possible between redshifts of $z = 2.9$ and 6.7. The data were obtained as part of the MUSE GTO programme and first commissioning run (for A1689 only). All the observations were conducted in the nominal WFM-NOAO-N mode of MUSE. The main characteristics of the four fields are listed in Table 1. The geometry and limits of the four FoVs are shown on the available HST images, in Fig. 1.

A1689. Observations were already presented in Bina et al. (2016) from the first MUSE commissioning run in 2014. The total exposure was divided into six individual exposures of 1100 s. A small linear dither pattern of $0.2''$ was applied between each exposure to minimize the impact of the structure of the instrument on the final data. No rotation was applied between individual exposures.

A2390, A2667, and A2744. The same observational strategy was used for all three cubes: the individual pointings were divided into exposures of 1800 s. In addition to a small dither pattern of $1''$, the position angle was incremented by 90° between each individual exposure to minimize the striping patterns caused by the slicers of the instrument. A2744 is the only mosaic included in the present sample. The strategy was to completely cover the multiple-image area. For this cluster, the exposures of the four different FoVs are as follows: 3.5, 4, 4, 5 hours of exposure plus an additional 2 hours at the centre of the cluster (see Fig. 1 in Mahler et al. 2018 for the details of the exposure map). For A2390 and A2667, the centre of the FoV was positioned on the central region of the cluster as shown in Table 1 and Fig. 1.

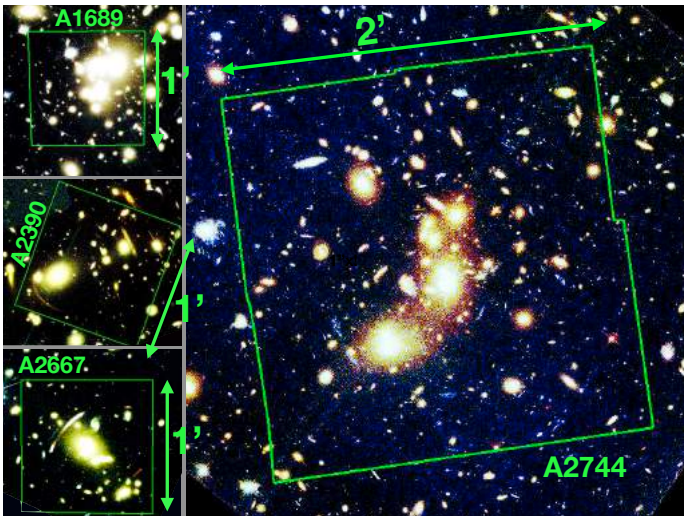

Fig. 1. MUSE footprints overlaid on HST deep colour images. North is up and east is to the left. The images are obtained from the F775W, F625W, F475W filters for A1689, from F850LP, F814W, F555W for A2390, from F814W, F606W, F450W for A2667, and from F814W, F606W, F435W for A2744.

2.2. MUSE data reduction

All the MUSE data were reduced using the MUSE ESO reduction pipeline (Weilbacher et al. 2012, 2014). This pipeline includes bias subtraction, flat fielding, wavelength and flux calibrations, basic sky subtraction, and astrometry. The individual exposures were then assembled to form a final data cube or a mosaic. An additional sky line subtraction was performed with the Zurich Atmosphere Purge software (ZAP; Soto et al. 2016). This software uses principal component analysis to characterize the residuals of the first sky line subtraction to further remove them from the cubes. Even though the line subtraction is improved by this process, the variance in the wavelength layers affected by the presence of sky lines remains higher, making the source detection more difficult on these layers. For simplicity,

Table 2. Ancillary HST observations.

–	Instrument	Filter	Exp (ks)	PID	Date
A1689	ACS	F475W	9.5	9289	2002
	ACS	F625W	9.5	9289	2002
	ACS	F775W	11.8	9289	2002
	ACS	F850LP	16.6	9289	2002
A2390	WFPC2	F555W	8.4	5352	1994
	WFPC2	F814W	10.5	5352	1994
	ACS	F850LP	6.4	1054	2006
A2667	WFPC2	F450W	12	8882	2001
	WFPC2	F606W	4	8882	2001
	WFPC2	F814W	4	8882	2001
	NICMOS	F110W	18.56	10504	2006
	NICMOS	F160W	13.43	10504	2006
A2744	ACS	F435W	45	13495	2013-14
	ACS	F606W	25	13495	2013–14
	ACS	F814W	105	13495	2013–14
	WFC3	F105W	60	13495	2013–14
	WFC3	F125W	30	13495	2013–14
	WFC3	F140W	25	13495	2013–14
	WFC3	F160W	60	13495	2013–14

Notes. From left to right: HST instrument used, filter, exposure time, programme ID (PID), and observation epoch.

hereafter we simply use the term layer to refer to the monochromatic images in MUSE cubes.

2.3. Complementary data (HST)

For all MUSE fields analysed in this paper, complementary deep data from HST are available. They were used to help the source detection process in the cubes but also for modelling the mass distribution of the clusters (see Sect. 4). A brief list of the ancillary HST data used for this project is presented in Table 2. For A1689 the data are presented in Broadhurst et al. (2005). For A2390 and A2667, a very thorough summary of all the HST observations available are presented in Richard et al. (2008) and more recently in Olmstead et al. (2014) for A2390. A2744 is part of the HFF programme, which comprises the deepest observations performed by HST on lensing clusters. All the raw data and individual exposures are available from the Mikulski Archive for Space Telescopes (MAST), and the details of the reduction are addressed in the articles cited above.

3. Detection of the LAE population

3.1. Source detection

The MUSE instrument is very efficient at detecting emission lines (see for example Bacon et al. 2017; Herenz et al. 2017). On the contrary, deep photometry is well suited to detect faint objects with weak continua, with or without emission lines. To build a complete catalogue of the sources in a MUSE cube, we combined a continuum-guided detection strategy based on deep HST images (see Table 2 for the available photometric data) with a blind detection in the MUSE cubes. Many of the sources end up being detected by both approaches and the catalogues are merged at the end of the process to make a single master catalogue. The detailed method used for the extraction of sources in A1689 and A2744 can be found in Bina et al. (2016) and Mahler et al. (2018)[1], respectively. The general method used for A2744, which contains the vast majority of sources in the present sample, is summarized below.

The presence of diffuse intra-cluster light (ICL) makes the detection of faint sources difficult in the cluster core, in particular for multiple images located in this area. A running median filter computed in a window of 1.3″ was applied to the HST images to remove most of the ICL. The ICL-subtracted images were then weighted by their inverse variance map and combined to make a single deep image. The final photometric detection was performed by `SExtractor` (Bertin & Arnouts 1996) on the weighted and combined deep images.

For the blind detection on the MUSE cubes, the `Muselet` software was used (MUSE Line Emission Tracker, written by J. Richard[2]). This tool is based on `SExtractor` to detect emission-line objects from MUSE cubes. It produces spectrally weighted, continuum-subtracted NB images (NB) for each layer of the cube. The NB images are the weighted average of five wavelength layers, corresponding to a spectral width of 6.25 Å. These images form a NB cube, in which only the emission-line objects remain. This `Sextractor` tool is then applied to each of the NB images. At the end of the process, the individual detection catalogues are merged together and sources with several detected emission lines are assembled as one single source.

After building the master catalogue, all spectra were extracted and the redshifts of galaxies were measured. For A1689, A2390, and A2667, 1D spectra were extracted using a fixed 1.5″ aperture. For A2744, the extraction area is based on the `SExtractor` segmentation maps obtained from the deblended photometric detections described above. At this stage, the extracted spectra are only used for the redshift determination. The precise measurement of the total line fluxes requires a specific procedure, which is described in Sect. 3.2. Extracted spectra were manually inspected to identify the different emission lines and accurately measure the redshift.

A system of confidence levels was adopted to reflect the uncertainty in the measured redshifts, following Mahler et al. (2018), which has some examples that illustrate the different cases. All the LAEs used in the present paper belong to the confidence categories 2 and 3, meaning that they all have fairly robust redshift measurements. For LAEs with a single line and no continuum detected, the wide wavelength coverage of MUSE, the absence of any other line, and the asymmetry of the line were used to validate the identification of the Lyman-alpha emission. For A1689, A2390, and A2667 most of the background galaxies are part of multiple-image systems, and are therefore confirmed high redshift galaxies based on lensing considerations.

In total 247 LAEs were identified in the four fields: 17 in A1689, 18 in A2390, 15 in A2667, and 197 in A2744. The important difference between the number of sources found in the different fields results from a well-understood combination of field size, magnification regime, and exposure time, as explained in Sect. 5.

3.2. Flux measurements

The flux measurement is part of the main procedure developed and presented in Sect. 6 to compute the LF of LAEs in lensing

[1] The complete catalogue of MUSE sources detected by G. Mahler in A2744 is publicly available at `http://muse-vlt.eu/science/a2744/`.

[2] Publicly available as part of the python MPDAF package (Piqueras et al. 2017): `http://mpdaf.readthedocs.io/en/latest/muselet.html`.

clusters observed with MUSE. We discuss this in this section to understand the selection of the final sample of galaxies used to build the LF.

For each LAE, the flux measurement in the Lyman-alpha line was done on a continuum subtracted NB image that contains the whole Lyman-alpha emission. For each source, we built a sub-cube centred on the Lyman-alpha emission, plus adjacent blue and red sub-cubes used to estimate the spectral continuum. The central cube is a square of size 10″ and the spectral range depends on the spectral width of the line. To determine this width and the precise position of the Lyman-alpha emission, all sources were manually inspected. The blue and red sub-cubes are centred on the same spatial position, with the same spatial extent, and are 20 Å wide in the wavelength direction. A continuum image was estimated from the average of the blue and red sub-cubes and this image was subtracted pixel-to-pixel from the central NB image. For sources with large full width at half maximum (FWHM), the NB used for flux measurement can regroup more than 20 wavelength layers (or equivalently 25 Å).

Because `SExtractor` with `FLUX_AUTO` is known to provide a good estimate of the total flux of the sources to the 5% level (see e.g. the `SExtractor` Manual, Sect. 10.4, Fig. 8.), it was used to measure the flux and the corresponding uncertainties on the continuum-subtracted images. The `FLUX_AUTO` routine is based on Kron first moment algorithm, and is well suited to account for the extended Lyman-alpha haloes that can be found around many LAEs (see Wisotzki et al. 2016 for the extended nature of the Lyman-alpha emission). In addition, the automated aperture is useful to account properly for the distorted images that are often found in lensing fields. As our sample contains faint, low surface brightness sources, and given that the NB images are not designed to maximize the signal-to-noise ratio (S/N), it is sometimes challenging to extract sources with faint or low-surface brightness Lyman-alpha emission. In order to measure their flux we force the extraction at the position of the source. To do so, the `SExtractor` detection parameters were progressively loosened until a successful extraction was achieved. An extraction was considered successful when the source was recovered at less than a certain matching radius ($r_m \sim 1''$) from the original position given by `Muselet`. Such an offset is sometimes observed between the peak of the UV continuum and the Lyman-alpha emission in case of high magnification. A careful inspection was needed to make sure that no errors or mismatches were introduced in the process.

Other automated alternatives to `SExtractor` exist to measure the line flux (see e.g. `LSDCat` in Herenz et al. 2017 or `NoiseChisel` in Akhlaghi & Ichikawa 2015 or a curve of growth approach as developed in Drake et al. 2017). A comparison between these different methods is encouraged in the future but beyond the scope of the present analysis.

4. Lensing clusters and mass models

In this work, we used detailed mass models to compute the magnification of each LAE, and the source plane projections of the MUSE FoVs at various redshifts. These projections were needed when performing the volume computation (see Sect. 6.1). The mass models were constructed with `Lenstool`, using the parametric approach described in Kneib et al. (1996), Jullo et al. (2007), and Jullo & Kneib (2009). This parametric approach relies on the use of analytical dark-matter (DM) halo profiles to describe the projected 2D mass distribution of the cluster. Two main contributions are considered by `Lenstool`: one for each large-scale structure of the cluster and one for each massive cluster galaxy. The parameters of the individual profiles are optimized through a Monte Carlo Markov chain (MCMC) minimization. The `Lenstool` software aims at reducing the cumulative distance in the parameter space between the predicted position of multiple images obtained from the model, and the observed images. The presence of several robust multiple systems greatly improves the accuracy of the resulting mass model. The use of MUSE is therefore a great advantage as it allowed us to confirm multiple systems through spectroscopic redshifts and also to discover new systems (e.g. Richard et al. 2015; Bina et al. 2016; Lagattuta et al. 2017; Mahler et al. 2018). Some of the models used in this study are based on the new constraints provided by MUSE. An example of source plane projection of the MUSE FoVs is provided in Fig. 2.

Because of the large number of cluster members, the optimization of each individual galaxy-scale clump cannot be achieved in practice. Instead, a relation combining the constant mass-luminosity scaling relation described in Faber & Jackson (1976) and the fundamental plane of elliptical galaxies is used by `Lenstool`. This assumption allows us to reduce the parameter space explored during the minimization process, leading to more constrained mass models, whereas individual parameterization of clumps would lead to an extremely degenerate final result and therefore, a poorly constrained mass model. The analytical profiles used were double pseudo-isothermal elliptical potentials (dPIEs) as described in Elíasdóttir et al. (2007). The ellipticity and position angle of these elliptical profiles were measured for the galaxy-scale clumps with `SExtractor` taking advantage of the high spatial resolution of the HST images.

Because the brightest cluster galaxies (BCGs) lie at the centre of clusters, they are subjected to numerous merging processes and are not expected to follow the same light-mass scaling relation. They are modelled separately in order to not bias the final result. In a similar way, galaxies that are close to the multiple images or critical lines are sometimes manually optimized because of the significant impact they can have on the local magnification and geometry of the critical lines.

The present MUSE survey has allowed us to improve the reference models available in previous works. Table 3 summarizes their main characteristics. For A1689, the model used is an improvement made on the model of Limousin et al. (2007), previously presented in Bina et al. (2016). For A2390, the reference model is presented in Pello et al. (1991), Richard et al. (2010), and the recent improvements in Pello et al. (in prep.) For A2667, the original model was obtained by Covone et al. (2006) and was updated in Richard et al. (2010). For A2744, the gold model presented in Mahler et al. (2018) was used, including as novelty the presence of NorthGal and SouthGal, which are two background galaxies included in the mass model because they could have a local influence on the position and magnification of multiple images.

5. Selection of the final LAE sample

To obtain the final LAE sample used to build the LF, only one source per multiple-image system was retained. The ideal strategy would be to keep the image with the highest S/N, which often coincides with the image with highest magnification. However, it is more secure for the needs of the LF determination to keep the sources with the most reliable flux measurement and magnification determination. In practice, it means that we often chose the less distorted and most isolated image. The flux and extraction of all sources among multiple systems were manually reviewed to select the best one to be included in the final sample.

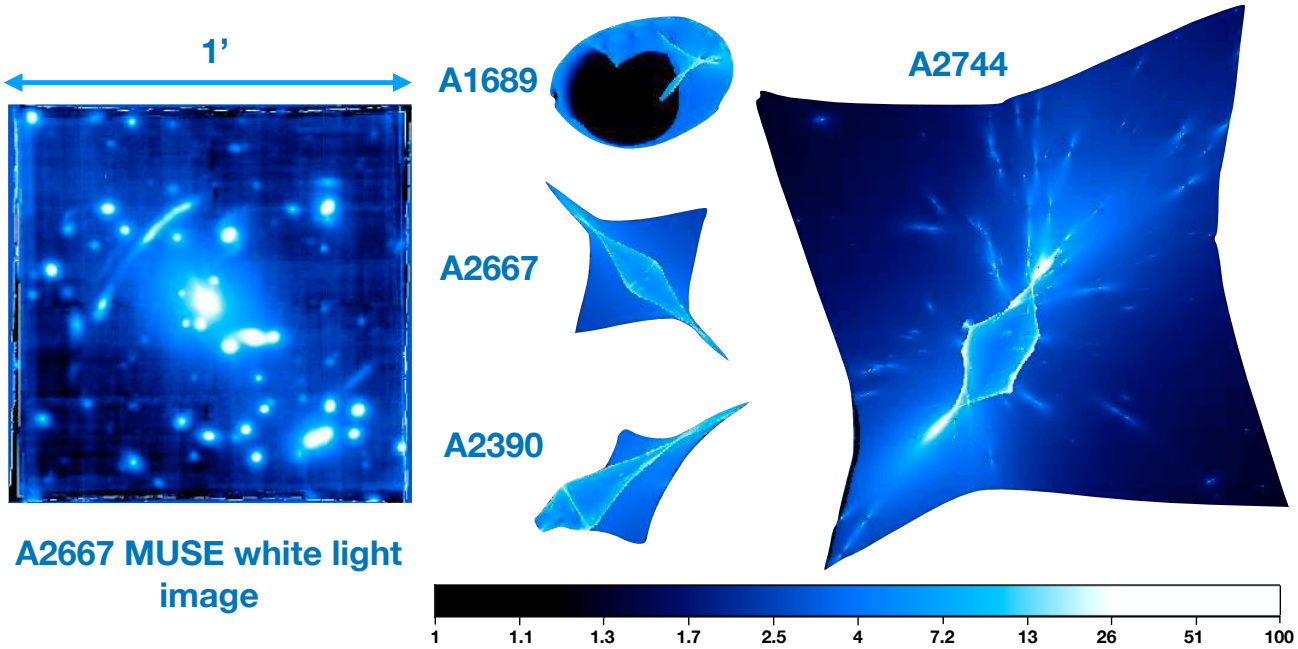

Fig. 2. *Left panel*: MUSE white light image of the A2667 field represented with a logarithmic colour scale. *Right panel*: projection of the four MUSE FoVs in the source plane at $z = 3.5$, combined with the magnification map encoded in the colour. All images on this figure are at the same spatial scale. In the case of multiply imaged area, the source plane magnification values shown correspond to the magnification of the brightest image.

Table 3. Summary of the main mass components for the lensing models used for this work.

Cluster	Clump	$\Delta\alpha$ ($''$)	$\Delta\delta$ ($''$)	e	θ	$r_{\rm core}$ (kpc)	$r_{\rm cut}$ (kpc)	σ_0 (km s^{-1})	Ref.
A1689	DM1	$0.6^{+0.2}_{-0.2}$	$-8.9^{+0.4}_{-0.4}$	$0.22^{+0.01}_{-0.01}$	$91.8^{+1.4}_{-0.8}$	$100.5^{+4.6}_{-4.0}$	[1515.7]	$1437.3^{+20.0}_{-11.1}$	(1)
rms = 2.87″	DM2	$-70.0^{+1.4}_{-1.5}$	$47.9^{+2.3}_{-4.1}$	$0.80^{+0.04}_{-0.05}$	$80.5^{+2.7}_{-2.5}$	$70.0^{+8.0}_{-5.3}$	[500.9]	$643.2^{+0.5}_{-4.5}$	
$n_{\rm const}$ = 128	BCG	$-1.3^{+0.2}_{-0.3}$	$0.1^{+0.4}_{-0.5}$	$0.50^{+0.03}_{-0.05}$	$61.6^{+9.6}_{-4.0}$	$6.3^{+1.2}_{-1.2}$	$132.2^{+42.0}_{-31.5}$	$451.6^{+11.6}_{-12.1}$	
$n_{\rm free}$ = 33	Gal1	[49.1]	[31.5]	$0.60^{+0.07}_{-0.16}$	$119.3^{+6.2}_{-10.0}$	$26.6^{+3.4}_{-4.1}$	$179.6^{+2.5}_{-27.8}$	$272.8^{+4.5}_{-21.5}$	
	Gal2	$45.1^{+0.2}_{-0.9}$	$32.1^{+0.6}_{-1.1}$	$0.79^{+0.05}_{-0.03}$	$42.6^{+2.3}_{-1.9}$	$18.1^{+0.3}_{-3.4}$	$184.8^{+1.2}_{-11.1}$	$432.7^{+16.6}_{-33.4}$	
	L^* Gal					[0.15]	$18.1^{+0.7}_{-2.2}$	$151.9^{+7.0}_{-0.3}$	
A2390	DM1	$31.6^{+1.8}_{-1.3}$	$15.4^{+0.4}_{-1.0}$	$0.66^{+0.03}_{-0.02}$	$214.7^{+0.5}_{-0.3}$	$261.5^{+8.5}_{-5.2}$	[2000.0]	$1381.9^{+23.0}_{-17.6}$	(2)
rms = 0.33″	DM2	[−0.9]	[−1.3]	$0.35^{+0.05}_{-0.03}$	$33.3^{+1.2}_{-1.6}$	$25.0^{+1.8}_{-1.1}$	$750.4^{+100.2}_{-65.5}$	$585.1^{+20.0}_{-9.7}$	(3)
$n_{\rm const}$ = 45	BCG1	[46.8]	[12.8]	$0.11^{+0.10}_{-0.01}$	$114.8^{+26.8}_{-31.5}$	[0.05]	$23.1^{+3.0}_{-1.6}$	$151.9^{+5.9}_{-7.5}$	(4)
$n_{\rm free}$ = 18	L^* Gal					[0.15]	[45.0]	$185.7^{+5.3}_{-3.3}$	
A2667	DM1	$0.2^{+0.5}_{-0.4}$	$1.3^{+0.5}_{-0.4}$	$0.46^{+0.02}_{-0.02}$	$-44.4^{+0.2}_{-0.3}$	$79.33^{+1.1}_{-1.1}$	[1298.7]	$1095.0^{+5.0}_{-3.7}$	(5)
rms = 0.47″	L^* Gal					[0.15]	[45.0]	$91.3^{+4.5}_{-4.5}$	(3)
$n_{\rm const}$ = 47									
$n_{\rm free}$ = 9									
A2744	DM1	$-2.1^{+0.3}_{-0.3}$	$1.4^{+0.0}_{-0.4}$	$0.83^{+0.01}_{-0.02}$	$90.5^{+1.0}_{-1.1}$	$85.4^{+5.4}_{-4.5}$	[1000.0]	$607.1^{+7.6}_{-0.2}$	(6)
rms = 0.67″	DM2	$-17.1^{+0.2}_{-0.3}$	$-15.7^{+0.4}_{-0.3}$	$0.51^{+0.02}_{-0.02}$	$45.2^{+1.3}_{-0.8}$	$48.3^{+5.1}_{-2.2}$	[1000.0]	$742.8^{+20.1}_{-14.2}$	
$n_{\rm const}$ = 134	BCG1	[0.0]	[0.0]	[0.21]	[−76.0]	[0.3]	[28.5]	$355.2^{+11.3}_{-10.2}$	
$n_{\rm const}$ = 30	BCG2	[−17.9]	[−20.0]	[0.38]	[14.8]	[0.3]	[29.5]	$321.7^{+15.3}_{-7.3}$	
	NGal	[−3.6]	[24.7]	[0.72]	[−33.0]	[0.1]	[13.2]	$175.6^{+8.7}_{-13.8}$	
	SGal	[−12.7]	[−0.8]	[0.30]	[−46.6]	[0.1]	$6.8^{+93.3}_{-3.2}$	$10.6^{+43.2}_{-3.6}$	
	L^* Gal					[0.15]	$13.7^{+1.0}_{-0.6}$	$155.5^{+4.2}_{-5.9}$	

Notes. The values of RMS indicated are computed from the position of multiply imaged galaxies in the image plane, $n_{\rm const}$ and $n_{\rm free}$ correspond to the number of constraints passed to `Lenstool` and the number of free parameters to be optimized, respectively. The coordinates $\Delta\alpha$ and $\Delta\delta$ are in arcsec with respect to the following reference points: A1689: $\alpha = 197°52'23''$, $\delta = -1°20'28''$, A2390: $\alpha = 328°24'12''$, $\delta = 17°41'45''$, A2667: $\alpha = 357°54'51''$, $\delta = -26°05'03''$ A2744: $\alpha = 3°35'11''$, $\delta = -30°24'01''$. The ellipticity e, is defined as $(a^2 - b^2)/(a^2 + b^2)$, where a and b are the semi-major and the semi-minor axes of the ellipse. The position angle, θ, provides the orientation of the semi-major axis of the ellipse measured counterclockwise with respect to the horizontal axis. Finally, $r_{\rm core}$, $r_{\rm cut}$, and σ_0 are the core radii, cut radii, and central velocity dispersion, respectively.

References. (1) Limousin et al. (2007), (2) Pello et al. (1991), (3) Richard et al. (2010), (4) Pello et al. (in prep.), (5) Covone et al. (2006), and (6) the gold model from Mahler et al. (2018).

All the sources for which the flux measurement failed or that were too close to the edge of the FoV were removed from the final sample. One extremely diffuse and low surface brightness source (Id : A2744, 5681) was also removed as it was impossible to properly determine its profile for the completeness estimation in Sect. 6.2.1.

The final sample consists of 156 lensed LAEs: 16 in A1689, 5 in A2390, 7 in A2667, and 128 in A2744. Out of these 156 sources, four are removed at a later stage of the analysis for completeness reasons (see Sect. 6.2.2) leaving 152 to compute the LFs. The large difference between the clusters on the number of sources detected is expected for two reasons:

– The A2744 cube is a 2×2 MUSE FoV mosaic and is deeper than the three other fields: on average four hours exposure time for each quadrant, whereas all the others have two hours or less of integration time (see Table 1).
– The larger FoV allows us to reach further away from the critical lines of the cluster, therefore increasing the probed volume as we get close to the edges of the mosaic.

This makes the effective volume of universe explored in the A2744 cube much larger (see end of Sect. 6.1.2) than in the three other fields combined. It is therefore not surprising to find most of the sources in this field. This volume dilution effect is most visible when looking at the projection of the MUSE FoVs in the source plane (see Fig. 2). Even though this difference is expected, it seems that we are also affected by an over-density of background sources at $z = 4$ as shown in Fig. 3. This over-density is currently being investigated as a potential primordial group of galaxies (Mahler et al., in prep.). The complete source catalogue is provided in Table E.1 and the Lyman-alpha luminosity distribution corrected for magnification can be found on the lower panel of Fig. 3. The corrected luminosity L_{Ly_α} was computed from the detection flux F_{Ly_α} with

$$L_{\mathrm{Ly}_\alpha} = \frac{F_{\mathrm{Ly}_\alpha}}{\mu} 4\pi D_{\mathrm{L}}^2, \tag{1}$$

where μ and D_{L} are the magnification and luminosity distance of the source, respectively. In this section and in the rest of this work, a flux weighted magnification is used to better account for extended sources and for sources detected close to the critical lines of the clusters where the magnification gradient is very strong. This magnification is computed by sending a segmentation of each LAE in the source plane with `Lenstool`, measuring a magnification for each of its pixels and making a flux weighted average of it. A full probability density of magnification $P(\mu)$ is also computed for each LAE and used in combination with its uncertainties on F_{Ly_α} to obtain a realistic luminosity distribution when computing the LFs (see Sect. 6.3). Objects with the highest magnification are affected by the strongest uncertainties and tend to have very asymmetric $P(\mu)$ with a long tail towards high magnifications. Because of this effect, LAEs with $\log L < 40$ should be considered with great caution.

Figure 4 compares our final sample with the sample used in the MUSE HUDF LAE LF study (Drake et al. 2017, hereafter D17). The MUSE HUDF (Bacon et al. 2017), with a total of 137 hours of integration, is the deepest MUSE observation to date. It consists of a 3×3 MUSE FoV *mosaic*, each of the quadrants being a 10 hours exposure, with an additional pointing (*udf-10*) of 30 h, overlaid on the mosaic. The population selected in D17 is composed of 481 LAEs found in the *mosaic* and 123 in the *udf-10*, for a total of 604 LAEs. On the upper panel of the figure, the plot presents the luminosity of the different samples versus the redshift. Using lensing clusters, the redshift selection tends to be less affected by luminosity bias, especially for higher redshift. On the lower panel, the normalized distribution of the two populations is presented. The strength of the study presented in D17 resides in the large number of sources selected. However, a sharp drop is observed in the distribution at $\log L \sim 41.5$. Using the lensing clusters, with ∼25 h of exposure time and a much smaller lens-corrected volume of survey, a broader luminosity selection was achieved. As discussed in the following sections, despite a smaller number of LAEs compared to D17, the sample presented in this paper is more sensitive to the faint end of the LF by construction.

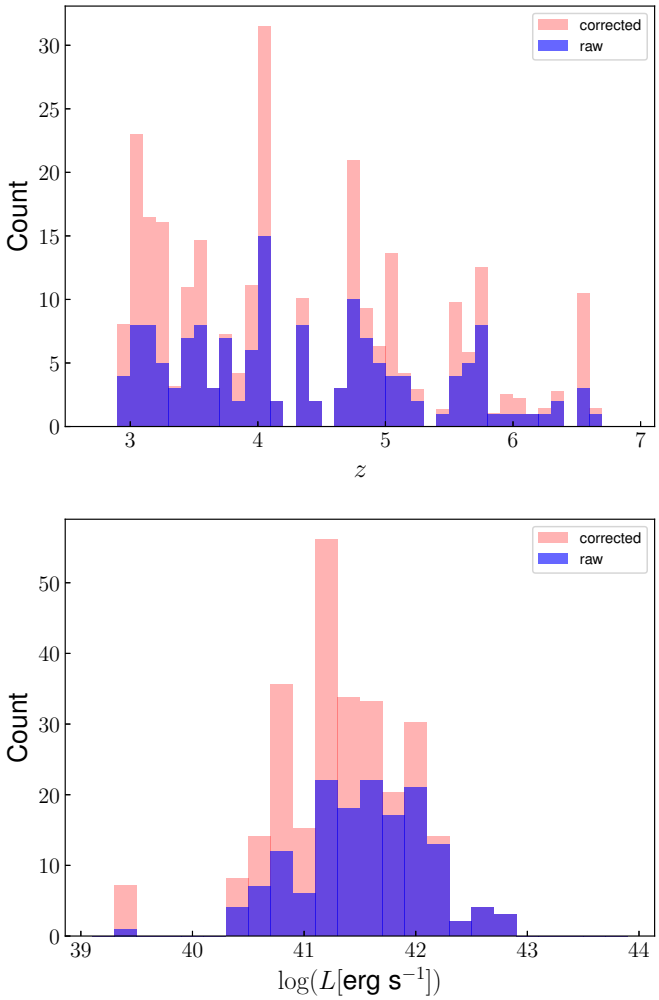

Fig. 3. Redshift and magnification corrected luminosity distribution of the 152 LAEs used for the LF computation (in blue). The corrected histograms in light red correspond to the histogram of the population weighted by the inverse of the completeness of each source (see Sect. 6.2). The empty bins seen on the redshift histograms are not correlated with the presence of sky emission lines.

6. Computation of the luminosity function

Because of the combined use of lensing clusters and spectroscopic data cubes, it is extremely challenging to adopt a parametric approach to determine a selection function. By construction, the sample of LAEs used in this paper includes sources coming from very different detection conditions, from intrinsically bright emitters with moderate magnification to highly magnified galaxies that could not have been detected far from the critical lines.

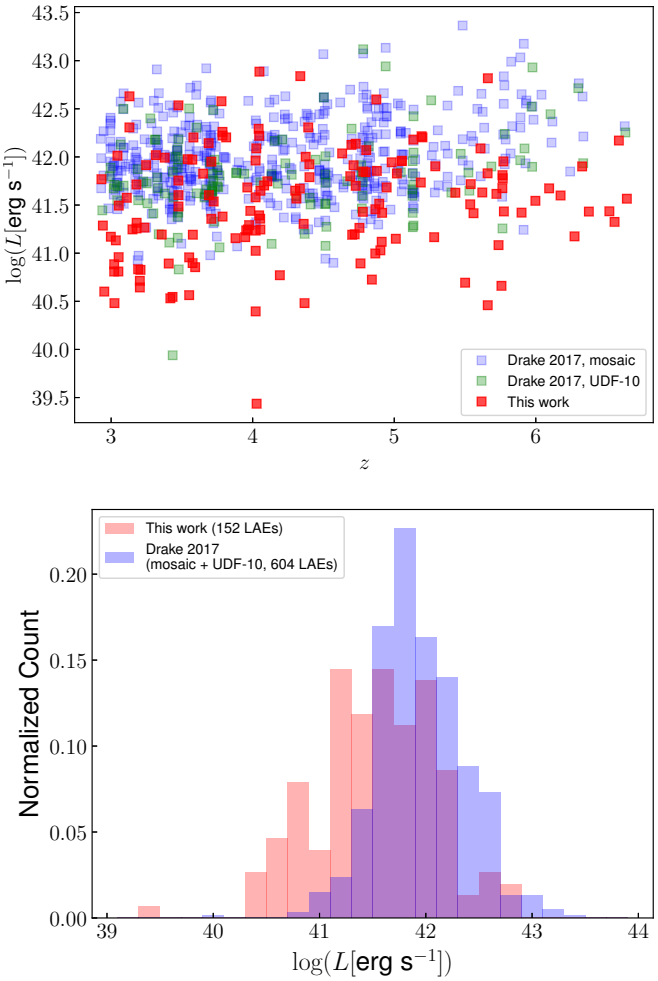

Fig. 4. Comparison of the 152 LAEs sample used in this work with D17. *Upper panel*: luminosity vs. redshift; error bars have been omitted for clarity. *Lower panel*: luminosity distribution of the two samples, normalized using the total number of sources. The use of lensing clusters allows for a broader selection, both in redshift and luminosity towards the faint end.

To properly take into account these differences when computing the LF, we adopted a non-parametric approach allowing us to treat the sources individually: i.e. the $1/V_{\rm max}$ method (Schmidt 1968; Felten 1976). We present in this section the four steps developed to compute the LFs:

(i) The flux computation, performed for all the *detected* sources. This step was already described in Sect. 3.2 as the selection of the final sample relies partly on the results of the flux measurements.
(ii) The volume computation for each of the sources included in the final sample, presented in Sect. 6.1.
(iii) The completeness estimation using the real source profiles (both spatial and spectral), presented in Sect. 6.2.
(iv) The computation of the points of the differential LF, using the results of the volume computation and the completeness estimations, presented in Sect. 6.3.

6.1. Volume computation in spectroscopic cubes in lensing clusters

The $V_{\rm max}$ value is defined as the volume of the survey where an individual source could have been detected. The inverse value, $1/V_{\rm max}$, is used to determine the contribution of one source

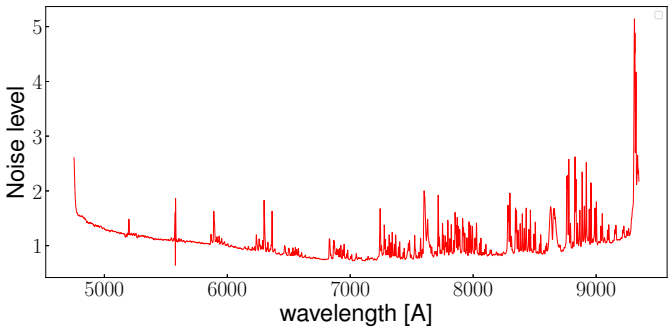

Fig. 5. Evolution of the noise level with wavelength inside the A1689 MUSE cube. We define the noise level of a given wavelength layer of a cube as the spatial median of the RMS layer over a normalization factor. The noise spikes that are more prominent in the red part of the cube are caused by sky lines.

to a numerical density of galaxies. Because this survey consists of several FoV, the $V_{\rm max}$ value for a given source must be determined from all the fields that are part of the survey, including the fields in which the source is not actually present. The volumes were computed in the source plane to avoid multiple counting of parts of the survey that are multiply imaged. For that, we used `Lenstool` to get the projection of the MUSE fields in the source plane and then used these projections to compute the volume (see Fig. 2 for an example of source plane projection). In this analysis, the volume computation was performed independently from the completeness estimation, focussing on the spectral noise variations of the cubes only.

The detectability of each LAEs needs to be evaluated on the entire survey to compute $V_{\rm max}$. This task is not straightforward, as the detectability depends on many different factors:

– The flux of the source: The brighter the source, the higher the chances to be detected. For a given spatial profile, brighter sources have higher $V_{\rm max}$ values.
– The surface brightness and line profile of the source: For a given flux, a compact source would have a higher surface brightness value than an extended one, and therefore would be easier to detect. This aspect is especially important as most LAEs have an extended halo (see Wisotzki et al. 2016).
– The local noise level: At first approximation, it depends on the exposure time. This point is especially important for mosaics in which noise levels are not the same on different parts of the mosaic as the noisier parts contribute less to the $V_{\rm max}$ values.
– The redshift of the source: The Lyman-alpha line profile of a source may be affected by the presence of strong sky lines in the close neighbourhood. The cubes themselves have strong variations of noise level caused by the presence of those sky emission lines (see e.g. Fig. 5).
– The magnification induced by the cluster.: Where the magnification is too small, the faintest sources could not have been detected.
– The seeing variation from one cube to another.

This shows that to properly compute $V_{\rm max}$, each source has to be individually considered. The easiest method to evaluate the detectability of sources is to simply mask the brightest objects of the survey, assuming that no objects could be detected behind them. This can be achieved from a white light image, using a mask generated from a `SExtractor` segmentation map. The volume computation can then be done on the unmasked pixels and only where the magnification is high enough to allow the detection of the source. However, as shown in Appendix C,

this technique has some limitations to account for the 3D morphologies of real LAEs. For this reason, a method to determine precisely the detectability map (referred to as detection mask or simply masks hereafter) of individual sources has been developed. As the detection process in this work is based on 2D collapsed images, we adopted the same scheme to build the 2D detection masks, and from these, built the 3D masks in the source plane adapted to each LAE of the sample. Using these individual source plane 3D masks, and as previously mentioned, the volume integration was performed on the unmasked pixels only where the magnification is high enough. In the paragraphs below, we quickly summarize the method adopted to produce masks for 2D images and explain the reasons that lead to the complex method detailed in Sects. 6.1.1 and 6.1.2.

The basic idea of our method for producing masks for 2D images is to mimic the `SExtractor` source detection process. For each pixel in the detection image, we determine whether the source could have been detected, had it been centred on this pixel. For this pseudo-detection, we fetch the values of the brightest pixels of the source (hereafter Bp) and compare them pixel-to-pixel to the background root mean square maps (RMS maps) produced by `SExtractor` from the detection image. The pixels where this pseudo-detection is successful are left unmasked, and where it failed, the pixels are masked. Technical details of the method for 2D images can be found in Appendix A. The detection masks produced in this way are binary masks and show where the source could have been detected. We use the term "covering fraction" to refer to the fraction of a single FoV covered by a mask. A covering fraction of 1 means that the source could not be detected anywhere on the image, whereas a covering fraction of 0 means that the source could be detected on the entire image.

This method of producing the detection masks from 2D images is precise and simple to implement when the survey consists of 2D photometric images. However, when dealing with 3D spectroscopic cubes, its application becomes much more complicated owing to the strong variations of noise level with wavelength in the cubes. Because of these variations, the detectability of a single source through the cubes cannot be represented by a single mask, duplicated on the spectral axis to form a 3D mask. An example of the spectral variations of noise level in a MUSE cube is provided in Fig. 5. These spectral variations are very similar for the four cubes. "Noise level" is used to refer to the average level of noise on a single layer. It is determined from the RMS cubes, which are created by `SExtractor` from the detection cube (i.e. the `Muselet` cube of NB images). For a layer i of the RMS cube, the noise level corresponds to the spatial median of the RMS layer over a normalization factor as follows:

$$\text{Noise level}(\text{RMS}_\text{i}) = \frac{\langle \text{RMS}_\text{i} \rangle_{x,y}}{\langle \text{RMS}_\text{median} \rangle_{x,y}}. \quad (2)$$

In this equation $\langle .. \rangle_{x,y}$ is the spatial median operator. The 2D median RMS map, RMS_median, is obtained from a median along the wavelength axis for each spatial pixel of the RMS cube. The normalization is the spatial median value of the median RMS map. The main factor responsible for the high frequency spectral variations of noise level is the presence of sky lines affecting the variance of the cubes.

To properly account for the noise variations, the detectability of each source has to be evaluated throughout the spectral direction of the cubes by creating a series of detection masks from individual layers. These masks are then projected into the source plane for the volume computation. This step is the severely limiting factor, as it would take an excessive amount of computation time. For a sample of 160 galaxies in four cubes, sampling different noise levels in cubes at only ten different wavelengths, we would need to do 6400 `Lenstool` projections. This represents more than 20 days of computation on a 60 CPU computer, and it is still not representative of the actual variations of noise level versus wavelength. To circumvent this difficulty, we developed a new approach that allows for a fine sampling of the noise level variations while drastically limiting the number of source plane reconstructions. A flow chart of the method described in the next sections is provided in Fig. 6.

6.1.1. Masking 3D cubes

The general idea of the method is to use a S/N proxy of individual sources instead of comparing their flux to the actual noise. In other words, the explicit computation of the detection mask for every source, wavelength layer, and cube is replaced by a set of pre-computed masks for every cube, covering a wide range of S/N values, in such a way that a given source can be assigned the mask corresponding to its S/N in a given layer. Two independent steps were performed before assembling the final 3D masks: First, the evolution of S/N values is computed through the spectral dimension of the cubes for each LAE. Second, for each cube, a series of 2D detection masks were created for an independent set of S/N values. This is referred to as the S/N curves hereafter. These two steps are detailed below. The final 3D detection masks were then assembled by successively picking the 2D mask that corresponds to the S/N value of the source at a given wavelength in a given cube. This process was done for all sources individually.

For the first step, the S/N value of a given source was defined as follows, from the bright pixels profile of the source and a RMS map, by comparing the maximum flux of the brightest pixels profile ($\max(Bp)$) to the noise level of that RMS map.

For each layer of the RMS cube, we computed the S/N value the source would have had at that spectral position in the cube. We point out that this is not a proper S/N value (hence the use of the term "proxy") as the normalization used to define the noise levels in Eq. (2) depends on the cube. For a layer i of the RMS cube, the corresponding S/N_i value is given by

$$S/N_\text{i} = \frac{\max(Bp)}{\text{Noise level}(\text{RMS}_\text{i})}. \quad (3)$$

An example of a S/N curve defined this way is provided in Fig. 7. For a given source, this computation was done on every layer of every cube part of the survey. When computing the S/N of a given source in a cube different from the parent cube, the seeing difference (see Table 1) is accounted for by introducing convolution or deconvolution procedure to set the detection image of the LAE to the resolution of the cube considered. As a result for each LAE, three additional images are produced. The four images (original detection image plus the three simulated ones) are then used to measure the value of the brightest pixels in all four seeing conditions. For the deconvolution a python implementation of a Wiener filter part of the Scikit-image package (van der Walt et al. 2014) was used. The deconvolution algorithm itself is presented in Orieux et al. (2010) and for all these computations, the PSF of the seeing is assumed to be Gaussian.

For the second step, 2D masks are created from a set of S/N values that encompass all the possible values for our sample. To produce a single 2D mask, the two following inputs are needed: the list of bright pixels of the source Bp and the RMS maps produced from the detection image (in our case, the NB images produced by `Muselet`). To limit the number of masks produced, two

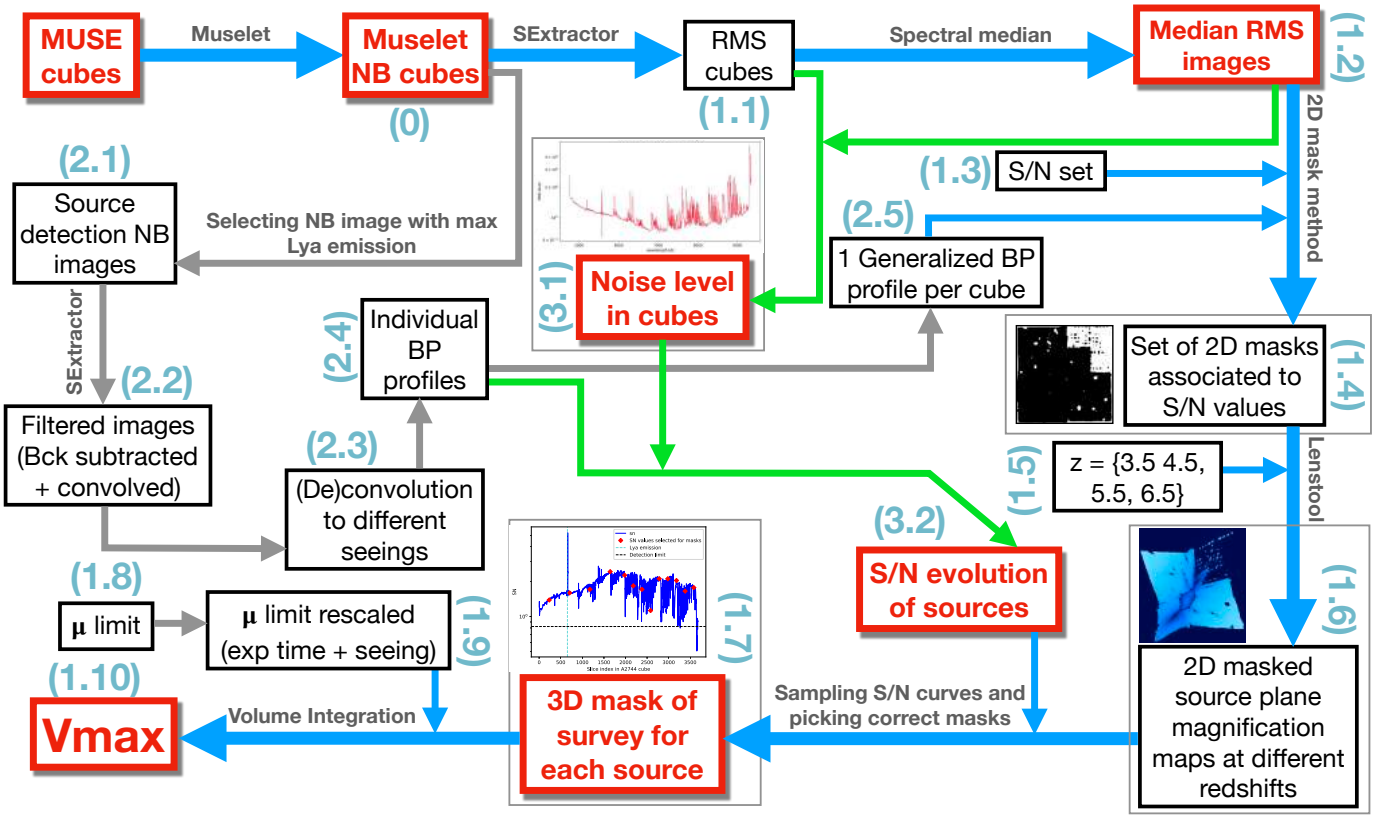

Fig. 6. Flow chart of the method used to produce the 3D masks and to compute V_{max}. The key points are shown in red and the main path followed by the method is indicated in blue. All the steps related to the determination of the bright pixels are shown in grey. The steps related to the computation of the S/N of each source are indicated in green. The numbered labels in light blue refer to the bullet points in Appendix D that briefly sum up all the differnt steps of this figure.

simplifications were introduced, the main one being that all RMS maps of a same cube present roughly the same pattern down to a certain normalization factor. This is equivalent to saying that all individual layers of the RMS cube can be approximately modelled and reproduced by a properly rescaled version of the same median RMS map. The second simplification is the use of four generalized bright-pixel profiles (hereafter Bp_g). To be consistent with the seeing variations, one profile is computed for each cluster, taking the median of all the individual LAE profiles computed from the detection images simulated in each seeing condition (see Fig. A.1 for an example of generalized bright pixel profile, also including the effect of seeing). These profiles are normalized in such a way that $\max(Bp_g) = 1$. For each value of the S/N set defined, a mask is created for each cluster from its median RMS map and the corresponding Bp_g, meaning that the 2D detection masks are no longer associated with a specific source, but with a specific S/N value.

Using the definition of S/N adopted in Eq. (3), the four Bp_g are rescaled to fit any S/N_j value of the S/N set and to obtain profiles that are directly comparable to the median RMS maps:

$$S/N_j = \frac{\max(c_j \times Bp_g)}{\text{Noise level}(\text{RMS}_{\text{median}})} \quad (4)$$

where c_j is the scaling factor. According to Eq. (2), the noise level of the median RMS maps is just 1, and as mentioned above $\max(Bp_g) = 1$. We can see that the scaling factor is simply $c_j = S/N_j$. Therefore the four sets of bright-pixels profiles $S/N_j \times Bp_g$ and the corresponding median RMS maps are used as input to produce the set of 2D detection masks.

After the completion of these two steps, the final 3D detection masks were assembled for every source individually. For this purpose, a subset of wavelength values (or equivalently, a subset of layer index) drawn from the wavelength axis of a MUSE cube was used to resample the S/N curves of individual sources. For each source and each entry of this wavelength subset, the procedure fetches the value in the S/N set that is the closest to the measured value, and returns the associated 2D detection mask, effectively assembling a 3D mask. An example of this 2D sampling is provided in Fig. 7. To each of the red points resampling the S/N curve, a pre-computed 2D detection mask is associated, and the higher the density of the wavelength sampling, the higher the precision on the final reconstructed 3D mask. The important point is that to increase the sampling density, we do not need to create more masks and therefore it is not necessary to increase the number of source plane reconstructions.

6.1.2. Volume integration

In the previous section we presented the construction of 3D masks in the image plane for all sources with a limited number of 2D masks. For the actual volume computation, the same was achieved in the source plane by computing the source plane projection of all the 2D masks, and combining these masks with the magnification maps. Thanks to the method developed in the previous subsection, the number of source plane reconstructions only depends on the length of the S/N set initially defined and the number of MUSE cubes used in the survey. It depends neither on the number of sources in the sample nor the accuracy of

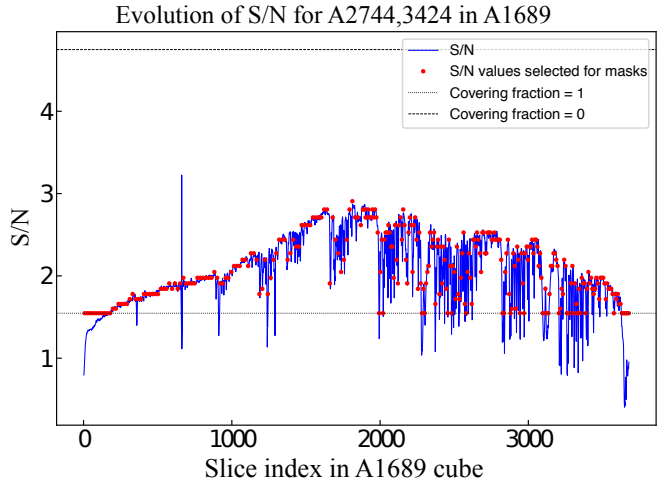

Fig. 7. Example of the 3D masking process. The blue solid line represents the variations of the S/N across the wavelength dimension for the source A2744-3424 in the A1689 cube. The red points over-plotted represent the 2D resampling made on the S/N curve with ~300 points. To each of these red points, a mask with the closest S/N value is associated. The short and long dashed black lines represent the S/N level for which a covering fraction of 1 (detected nowhere) and 0 (detected everywhere) are achieved, respectively. For all the points between these two lines, the associated masks have a covering fraction ranging from 1 to 0, meaning that the source is always detectable on some regions of the field.

the sampling of the S/N variations. For the projections, we used `PyLenstool`[3], which allows for an automated use of `Lenstool`. Reconstruction of the source plane was performed for different redshift values to sample the variation of both the shape of the projected area and the magnification. In practice, the variations are very small with redshift and we reduce the redshift sampling to $z = 3.5, 4.5, 5.5$, and 6.5.

In a very similar way to what is described at the end of the previous section, 3D masks were assembled and combined with magnification maps, in the source plane. In addition to the closest S/N value, the procedure also looks for the closest redshift bin in such a way that, for a given point $(\lambda_k, S/N_k)$ of the resampled S/N curve, the redshift of the projection is the closest to $z_k = \frac{\lambda_k}{\lambda_{Ly_\alpha}} - 1$.

The last important aspect to take into account when computing V_{max} is to limit the survey to the regions where the magnification is such that the source could have been detected. The condition is given by

$$\frac{\mu_{lim}}{\mu} \frac{F_d}{\delta F_d} = 1, \tag{5}$$

where μ is the flux weighted magnification of the source, F_d the detection flux, and δF_d the uncertainty on the detection which reflects the local noise properties. This condition simply states that μ_{lim} is the magnification that would allow for a S/N of 1 under which the detection of the source would be impossible. It is complex to find a S/N criterion to use that would be coherent with the way `Muselet` works on the detection images, since the images used for the flux computation are different and of variable spectral width compared to the `Muslet` NBs. Therefore, this criterion for the computation of μ_{lim} is intentionally conservative to avoid overestimating the steepness of the faint end slope.

[3] Python module written by G. Mahler, publicly available at `http://pylenstool.readthedocs.io/en/latest/index.html`.

To be consistent with the difference in seeing values and in exposure time from cube to cube, μ_{lim} is computed for each LAE and for each MUSE cube (i.e. four values for a given LAE). A source only detected because of very high magnification in a shallow and bad seeing cube (e.g. A1689) would need a much smaller magnification to be detected in a deeper and better seeing cube (e.g. A2744). For the exposure time difference, the ratio of the median RMS value of the entire cube is used, and for the seeing the ratio of the squared seeing value is used. In other words, the limiting magnification in A2744 for a source detected in A1689 is given by

$$\mu_{lim,A2744} = \frac{\langle RMS_{A274} \rangle_{x,y,\lambda}}{\langle RMS_{A1689} \rangle_{x,y,\lambda}} \frac{s^2_{A2744}}{s^2_{A1689}} \times \mu_{lim,A1689}, \tag{6}$$

where $\langle .. \rangle_{x,y,\lambda}$ is the median operator over the three axis of the RMS cubes and s is the seeing. The exact same formula can be applied to compute the limit magnification of any source in any cube. This simple approximation is sufficient for now as only the volume of the rare LAEs with very high magnification are dominated by the effects of the limiting magnification.

The volume integration is performed from one layer of the source plane projected (and masked) cubes to the next, counting only pixels with $\mu > \mu_{lim}$. For this integration, the following cosmological volume formula was used:

$$V = \omega \frac{c}{H_0} \int_{z_{min}}^{z_{max}} \frac{D_L^2(z')}{(1+z')^2 E(z')} dz', \tag{7}$$

where ω is the angular size of a pixel, D_L is the luminosity distance, and $E(z)$ is given by

$$E(z) = \sqrt{\Omega_m (1+z)^3 + (1 - \Omega_m - \Omega_\Lambda)(1+z)^2 + \Omega_\Lambda}. \tag{8}$$

In practice, and for a given source, when using more than 300 points to resample the S/N curve along the spectral dimension, a stable value is reached for the volume (i.e. less than 5% of variation with respect to a sampling of 1000 points). A comparison is provided in Appendix C between the results obtained with this method and the equivalent findings when a simple mask based on `SExtractor` segmentation maps is adopted instead. The maximum co-volume explored between $2.9 < z < 6.7$, accounting for magnification, is about 16 000 Mpc^3, distributed as follows among the four clusters: ~900 Mpc^3 for A1689, ~800 Mpc^3 for A2390, ~600 Mpc^3 for A2667, and ~13 000 Mpc^3 for A2744.

6.2. Completeness determination using real source profiles

Completeness corrections account for the sources missed during the selection process. Applying the correction is crucial for the study of the LF. The procedure used in this article separates, on one hand, the contribution to incompleteness due to S/N effects across the detection area, and the contribution due to masking across the spectral dimension on the other hand (see V_{max} in Sect. 6.1).

The 3D masking method presented in the previous section aims to map precisely the volume where a source could be detected. However, an additional completeness correction was needed to account for the fact that a source does not have a 100% chance of being detected on its own wavelength layer. In the continuity of the non-parametric approach developed for the volume computation, the completeness was determined for individual sources. To better account for the properties of sources,

namely their spatial and spectral profiles, simulations were performed using their real profiles instead of parameterized realizations. Because the detection of sources was done in the image plane, the simulations were also performed in the image plane on the actual masked detection layer of a given source (i.e. the layer of the NB image cube containing the peak of the Lyman-alpha emission of the source). The mask used on the detection layer was picked using the same method as described in Sect. 6.1.1, leaving only the cleanest part of the layer available for the simulations.

6.2.1. Estimating the source profile

To get an estimate of the real source profile, we used the `Muselet` NB image that captures the peak of the Lyman-alpha emission (called the max-NB image hereafter). Using a similar method to that presented in Sect. 3.2, the extraction of sources on the max-NB images were forced by progressively loosening the detection criterion. The vast majority of our sources were successfully detected on the first try using the original parameters used by `Muselet` for the initial detection of the sample: `DETECT_THRES` = `1.3` and `MIN_AREA` = `6`.

To recover the estimated profile of a source, the pixels belonging to the source were extracted on the filtered image according to the segmentation map. The filtered image is the convolved and background-subtracted image that `SExtractor` uses for the detection. The use of filtered images allowed us to retrieve a background-subtracted and smooth profile for each LAE. Figure 8 presents examples of source profile recovery for three representative LAEs.

A flag was assigned to each extracted profile to reflect the quality of the extraction, based on a predefined set of parameters (detection threshold, minimum number of pixels, and matching radius) used for the successful extraction of the source. A source with flag 1 is extremely trustworthy, and was recovered with the original set of parameters used for initial automated detection of the sample. A source with flag 2 is still a robust extraction and a source with flag 3 is doubtful and is not used for the LF computation. Of the LAEs, 95% were properly recovered with a flag value of 1. The summary of flag values is shown in Table 5. The three examples presented in Fig. 8 have a flag value of 1 and were recovered using `DETECT_THRESH` = `1.3`, `MIN_AREA` = `6` and a matching radius of 0.8″. Objects with flag >1 are less than 5% of the total sample. For the few sources with an extraction flag above 1, several possible explanations are found, listed by order of importance as follows:

- The image used to recover the profiles (30″) is smaller than the entire max-NB image. As the `SExtractor` background estimation depends on the size of the input image, this may slightly affect the detection of some objects. This is most likely the predominant reason for a flag value of two.
- There is a small difference in the coordinates between the recovered position and listed position. This may be due to a change in morphology with wavelength or bandwidth. By increasing the matching radius to recover the profile, we obtained a successful extraction but we also increased the value of the extraction flag.
- The NB used does not actually correspond to the NB that leads the source to be detected. By picking the NB image that catches the maximum of the Lyman-alpha emission we do not necessarily pick the layer with the cleanest detection. For example the peak could fall in a very noisy layer of the cube, whereas the neighbouring layers would provide a much cleaner detection.
- The source is extremely faint and was actually detected with relaxed detection parameters or manually detected.

We checked that we did not include LAEs that were expected to be at a certain position as part of multiple-image system. This is to say, we did not select the noisiest images in multiple-image systems.

Table 5. Summary of the extraction flag values for sources in the different lensing fields (see text for details).

Flag	A1689	A2390	A2667	A2744	All Sample
1	16	5	7	121	149
2	0	0	0	6	6
3	0	0	0	1	1
Total	16	5	7	128	156

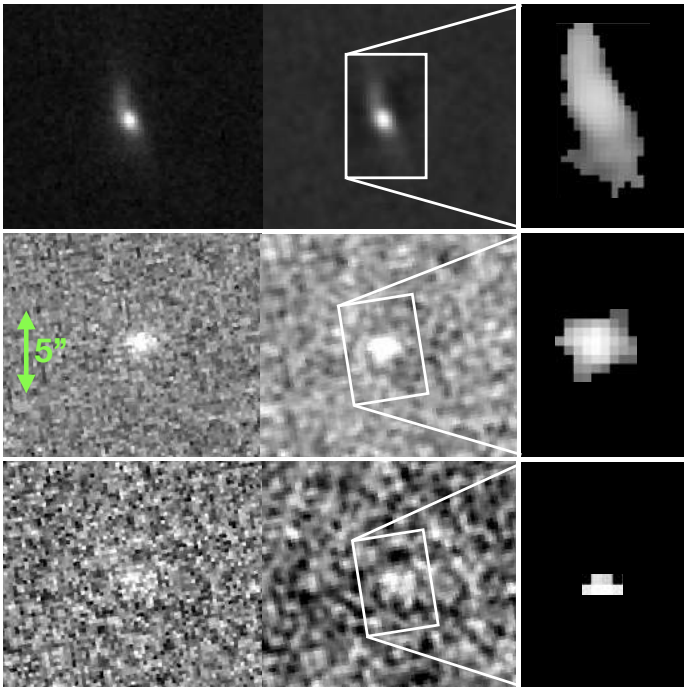

Fig. 8. Example of source profile recovery for three representative LAEs. *Left column*: detection image of the source in the `Muselet` NB cube (i.e. the max-NB image). *Middle column*: filtered image (convolved and background-subtracted) produced by `SExtractor` from the image in the *left column*. *Right column*: recovered profile of the source obtained by applying the segmentation map on the filtered image. The spatial scale is not the same as for the two leftmost columns. All the sources presented in this figure have a flag value of 1.

6.2.2. Recovering mock sources

Once a realistic profile for all LAEs was obtained, source recovery simulations were conducted. For this step, the detection process was exactly the same as that initially used for the sample detection. However, since we limited the simulations to the max-NB (see Sect. 6.2.1) images and not the entire cubes, we did not need to use the full `Muselet` software. To gain computation time, we only used `SExtractor` on the max-NB images, using the same configuration files that `Muselet` uses, to reproduce the initial detection parameters. In this section, the set of parameters were also `DETECT_THRESH` = `1.3` and `MIN_AREA` = `6`.

To create the mock images, we used the masked max-NB images. Each source profile was randomly injected many times on the corresponding detection max-NB image, avoiding overlapping. After running the detection process on the mocks, the recovered sources were matched to the injected sources based on their position. The completeness values were derived by comparing the number of successful matches to the number of injected sources. The process was repeated 40 times to derive the associated uncertainties.

The results of the completeness obtained for each source of the sample are shown in Fig. 9. The average completeness value over the entire sample is 0.74 and the median value is 0.90. The values are this high because we used masked NB images, effectively making source recovery simulations on the cleanest part of the detection layer only. As seen on this figure, there is no well-defined trend between completeness and detection flux. At a given flux, a compact source detected on a clean layer of the cube has a higher completeness than a diffuse source with the same flux detected on a layer affected by a sky line. Four LAEs with a flag value of 3 or with a completeness value less than 10% are not used for the computation of the LFs in Sect. 6.3.

A more popular approach to estimate the completeness would be to perform heavy Monte Carlo (MC) simulations for each of the cubes in the survey to get a parameterized completeness (see Drake et al. 2017 for an example). The classical approach consists in injecting sources with parameterized spatial and spectral morphologies and retrieving the completeness as a function of redshift and flux. This method is extremely time consuming, in particular for IFUs where the extraction process is lengthy and tedious. The main advantage of computing the completeness based on the real source profile is that it allows us to accurately account for the different shapes and surface brightnesses of individual sources. And because the simulations are done on the detection image of the source in the cubes, we are also more sensitive to the noise increase caused by sky lines. As seen in Fig. 10, except from the obvious flux–completeness correlation, it is difficult to identify correlations between completeness and redshift or sky lines. This tends to show that the profile of the sources is a dominant factor when it comes to estimating the completeness properly. The same conclusion was reached in D17 and in Herenz et al. (2019). A non-parametric approach of completeness is therefore better suited in the case of lensing clusters, where a proper parametric approach is almost impossible to implement because of the large number of parameters to take into account (e.g. spatial and spectral morphologies including distortion effects, lensing configuration, and cluster galaxies).

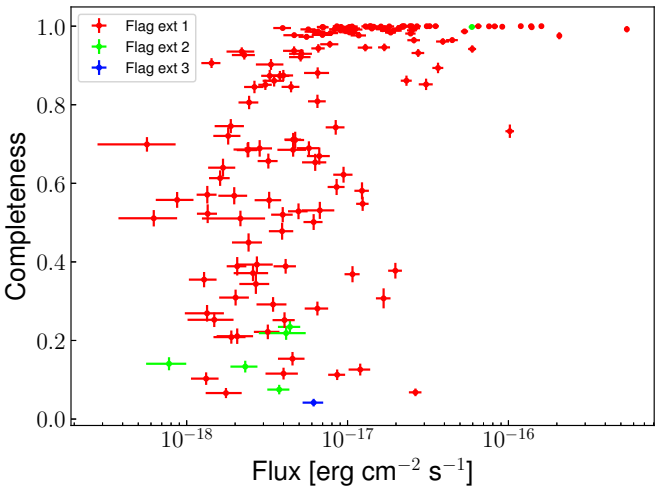

Fig. 9. Completeness value for LAEs vs. their detection flux. Colours indicate the detection flags. We note that only the incompleteness owing to S/N on the unmasked regions of the detection layer is plotted in this graph (see Sect. 6.2).

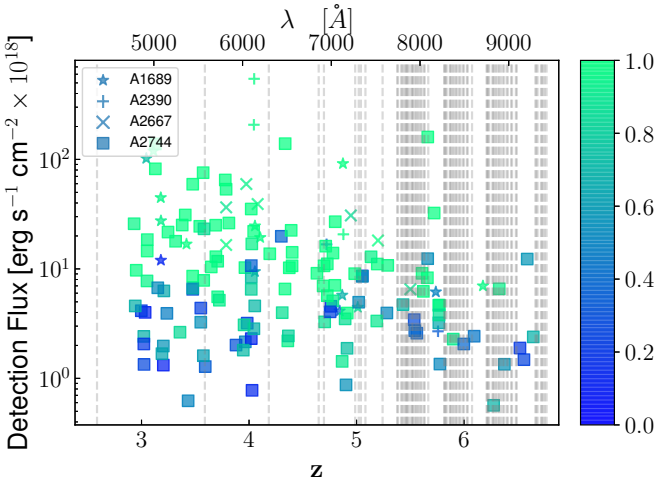

Fig. 10. Completeness (colour bar) of the sample as a function of redshift and detection flux. Each symbol indicates a different cluster. The light grey vertical lines are indicated by the main sky lines. There is no obvious correlation in our selection of LAEs between the completeness and the position of the sky lines.

6.3. Determination of the luminosity function

To study the possible evolution of the LF with redshift, the 152 LAE population has been subdivided into several redshift bins: $z1 : 2.9 < z < 4.0$, $z2 : 4.0 < z < 5.0$, and $z3 : 5.0 < z < 6.7$. In addition to these three LFs, the global LF for the entire sample $z_{\rm all} : 2.9 < z < 6.7$ was also determined. For a given redshift and luminosity bin, the following expression to build the points of the differential LFs was used:

$$\Phi(L_{\rm i}) = \frac{1}{\Delta \log L_{\rm i}} \sum_{\rm j} \frac{1}{C_{\rm j} V_{\rm max,j}}, \quad (9)$$

where $\Delta \log L_{\rm i}$ corresponds to the width of the luminosity bin in logarithmic space, j is the index corresponding to the sources falling in the bin indexed by i, and $C_{\rm j}$ stands for the completeness correction of the source j.

To account for the uncertainties affecting each LAE properly, MC iterations are performed to build 10 000 catalogues from the original catalogue. For each LAE in the parent catalogue, a random magnification is drawn from its $P(\mu)$, and a random flux and completeness values are also drawn assuming a Gaussian distribution of width fixed by their respective uncertainties. A single value of the LF was obtained at each iteration following Eq. (9). The distribution of LF values obtained at the end of the process was used to derive the average in linear space and to compute asymmetric error bars. The MC iterations are well suited to account for LAEs with poorly constrained luminosities. This happens for sources close, or even on, the critical lines of the clusters. Drawing random values from their probability density and uncertainties for magnification and flux results in a luminosity distribution (see Eq. (1)), which allows these sources to have a diluted contribution across several luminosity bins.

For the estimation of the cosmic variance, we used the cosmic variance calculator presented in Trenti & Stiavelli (2007). Lacking other options, a single compact geometry made of the

union of the effective areas of the four FoVs is assumed and used as input for the calculator. The blank field equivalent of our survey is an angular area of about $1.2' \times 1.2'$. Given that a MUSE FoV is a square of size $1'$, the observed area of the present survey is roughly $7' \times 7'$ square. Our survey is therefore roughly equivalent to a bit more than only one MUSE FoV in a blank field. The computation is done for all the bins as the value depends on the average volume explored in each bin as well as on the intrinsic number of sources. The uncertainty due to cosmic variance on the intrinsic counts of galaxies in a luminosity bin typically range from 15% to 20% for the global LF and from 15% to 30% for the LFs computed in redshift bins. For $\log(L) \lesssim 41$, the total error budget is dominated by the MC dispersion, which is mainly caused by objects with poorly constrained luminosity jumping from one bin to another during the MC process. The larger the bins the lesser this effect because a given source is less likely to jump outside of a larger bin. For $41 \lesssim \log(L) \lesssim 42$ the Poissonian uncertainty is slightly larger than the cosmic variance but does not completely dominate the error budget. Finally for $42 \lesssim \log(L)$, the Poissonian uncertainty is the dominant source of error due to the small volume and therefore the small number of bright sources in the survey.

The data points of the derived LFs and the corresponding error bars are listed in Table 6. These LF points provide solid constraints on the shape of the faint end of the LAE distribution. In the following sections, we elaborate on these results and discuss the evolution of the faint end slope as well as the implications for cosmic reionization.

7. Parametric fit of the luminosity function

The differential LFs are presented in Fig. 11 for the four redshift bins. Some points in the LF, shown as empty squares, are considered as unreliable and presented for comparison purpose only. Therefore, they are not used in the subsequent parametric fits. An LF value is considered unreliable when it is dominated by the contribution of a single source, with either a small $V_{\rm max}$ or a low completeness value, due to luminosity and/or redshift sampling. These unreliable points are referred to as "incomplete" hereafter. The rest of the points are fitted with a straight line as a visual guide, the corresponding 68% confidence regions are represented as shaded areas. For z_3, the exercise is limited owing to the large uncertainties and the lack of constraints on the bright end. The measured mean slope for the four LFs are as follows: $\alpha = -1.79^{+0.1}_{-0.09}$ for $z_{\rm all}$, $\alpha = -1.63^{+0.13}_{-0.12}$ for z_1, $\alpha = -1.61^{+0.08}_{-0.08}$ for z_2 and $\alpha = -1.76^{+0.4}_{-0.4}$ for z_3. These values are consistent with no evolution of the mean slope with redshift.

In addition, and because the integrated value of each LF is of great interest regarding the constraints they can provide on the sources of reionization, the different LFs were fitted with the standard Schechter function (Schechter 1976) using the formalism described in Dawson et al. (2007). The Schechter function is defined as

$$\Phi(L)\mathrm{d}L = \frac{\Phi_*}{L_*}\left(\frac{L}{L_*}\right)^{\alpha} \exp\left(-\frac{L}{L_*}\right)\mathrm{d}L, \quad (10)$$

where Φ_* is a normalization parameter, L_* a characteristic luminosity that defines the position of the transition from the power law to the exponential law at high luminosity, and α is the slope of the power law at low luminosity. In logarithmic scale the Schechter function is written as

$$\Phi_{\log}(L)\mathrm{d}(\log L) = \left(\frac{L}{\log e}\right)\left(\frac{\Phi_*}{L_*}\right)\left(\frac{L}{L_*}\right)^{\alpha} \exp\left(-\frac{L}{L_*}\right)\mathrm{d}(\log L). \quad (11)$$

This function represents the numerical density per logarithmic luminosity interval. The fits were done using the Python package *Lmfit* (Newville et al. 2014), which is specifically dedicated to nonlinear optimization and provides robust estimations for confidence intervals. We define an objective function, accounting for the strong asymmetry in the error bars, whose results are then minimized in the least-squares sense, using the default Levenberg–Marquardt method provided by the package. The results of this first minimization are then passed to a MCMC process[4] that uses the same objective function. The uncertainty on the three parameters of the Schechter function (α, L_*, Φ_*) are recovered from the resulting individual posterior distributions. The minimization in the least-square sense is an easy way to fit our data but is not guaranteed to give the most probable parameterization for the LFs. A more robust method would be the maximum-likelihood method. However, because of the nonparametric approach used in this work to build the points of the LF, taking into account the specific complexity of the lensing regime, the implementation of a maximum-likelihood approach such as those developed in D17 or in Herenz et al. (2019) could not be envisaged.

Because of the use of lensing clusters, the volume of Universe explored is smaller than in blank field surveys. The direct consequence is that we are not very efficient in probing the transition area around L_* and the high luminosity regime of the LF. Instead, the lensing regime is more efficient in selecting faint and low luminosity galaxies and is therefore much more sensitive to the slope parameter. To properly determine the three best parameters, additional data are needed to constrain the bright end of the LFs. To this aim, previous LFs from the literature are used and combined together into a single average LF with the same luminosity bin size as the LFs derived in this work. This last point is important to ensure that the fits are not dominated by the literature data points that are more numerous with smaller bin sizes and uncertainties. In this way we determine the three Schechter parameters while properly sampling the covariance between them.

The choice of the precise data sets used for the Schechter fits is expected to have a significant impact on the results, including possible systematic effects. To estimate the extent of this effect and its contribution to uncertainties, different series of data sets were used to fit the LF, among those available in a given redshift interval (see Fig. 13). The best-fit parameters recovered are found to be always consistent within their own error bars.

In addition, the error bars do not account for the error introduced by the binning of the data. To further test the robustness of the slope measurement and to recover more realistic error bars, different bins were tested for the construction of the LF. The exact same fit process was applied to the resulting LFs. The confidence regions derived from these tests are shown in Fig. 12 for z_1 and z_3. The bins used hereafter to build the LFs are identified in this figure as black lines. We estimate that these bins are amongst the most reliable possibilities, and in the following they are referred to as the "optimal" bins. They were determined in such a way that each bin is properly sampled in both redshift and luminosity, and has a reasonable level of completeness. Figure 12 shows that α is very stable for z_1 and that all the posterior distributions are very similar. Because we are able to probe very low luminosity regimes far below L_*, the effect of binning on the measured slope is negligible for $z_{\rm all}$ because of the increased statistics. As redshift increases as a consequence

[4] *Lmfit* uses the emcee algorithm implementation of the emcee Python package (see Foreman-Mackey et al. 2013)

Table 6. Luminosity bins and LF points used in Fig. 13.

$\log(L)$ erg s^{-1}	$\log(\Phi)$ $(\Delta(\log(L)) = 1)^{-1}$ Mpc^{-3}	$\langle N \rangle$	$\langle N_{\rm corr} \rangle$	$\langle V_{\rm max} \rangle$ Mpc^3
	$2.9 < z < 6.7$			
$39.00 < 39.63 < 40.25$	$-1.28^{+0.21}_{-0.44}$	2.05	8.97	124.68
$40.25 < 40.38 < 40.50$	$-1.57^{+0.41}_{-0.40}$	3.52	7.04	4971.62
$40.50 < 40.63 < 40.75$	$-1.64^{+0.33}_{-0.43}$	9.43	24.83	10977.19
$40.75 < 40.88 < 41.00$	$-1.45^{+0.09}_{-0.07}$	12.77	33.27	12063.96
$41.00 < 41.13 < 41.25$	$-1.74^{+0.10}_{-0.20}$	18.68	48.11	12816.23
$41.25 < 41.38 < 41.50$	$-1.79^{+0.11}_{-0.15}$	23.28	48.07	12991.31
$41.50 < 41.63 < 41.75$	$-1.89^{+0.10}_{-0.13}$	26.81	39.75	13926.47
$41.75 < 41.88 < 42.00$	$-1.97^{+0.10}_{-0.16}$	26.15	35.60	14658.58
$42.00 < 42.13 < 42.25$	$-2.22^{+0.17}_{-0.16}$	18.08	21.32	15017.49
$42.25 < 42.38 < 42.50$	$-2.96^{+0.18}_{-0.38}$	4.22	4.28	15696.11
$42.50 < 42.63 < 42.75$	$-3.01^{+0.19}_{-0.34}$	3.94	3.95	16060.71
$42.75 < 42.88 < 43.00$	$-3.13^{+0.21}_{-0.41}$	3.00	3.01	16141.73
	$2.9 < z < 4.0$			
$40.00 < 40.25 < 40.50$	$-2.48^{+0.35}_{-0.72}$	1.90	4.73	4430.41
$40.50 < 40.75 < 41.00$	$-1.64^{+0.11}_{-0.15}$	14.99	38.65	4145.63
$41.00 < 41.25 < 41.50$	$-1.66^{+0.11}_{-0.15}$	18.37	45.65	4468.50
$41.50 < 41.75 < 42.00$	$-2.12^{+0.14}_{-0.17}$	14.53	18.14	5178.73
$42.00 < 42.25 < 42.50$	$-2.47^{+0.15}_{-0.25}$	8.17	8.69	5216.12
$42.50 < 42.75 < 43.00$	$-2.96^{+0.22}_{-0.46}$	2.95	2.95	5437.33
	$4.0 < z < 5.0$			
$39.00 < 39.25 < 39.50$	$-0.49^{+0.33}_{-\infty}$	0.76	5.47	44.11
$39.50 < 40.00 < 40.50$	$-1.33^{+0.54}_{-0.71}$	1.79	3.71	939.22
$40.50 < 40.75 < 41.00$	$-1.52^{+0.09}_{-0.09}$	4.83	14.76	2818.30
$41.00 < 41.25 < 41.50$	$-1.76^{+0.13}_{-0.24}$	13.72	28.05	3706.94
$41.50 < 41.75 < 42.00$	$-1.96^{+0.12}_{-0.17}$	19.40	21.96	4113.33
$42.00 < 42.25 < 42.50$	$-2.39^{+0.17}_{-0.27}$	8.49	8.58	4254.24
$42.50 < 42.75 < 43.00$	$-2.87^{+0.22}_{-0.47}$	3.00	3.02	4430.02
	$5.0 < z < 6.7$			
$40.00 < 40.25 < 40.50$	$-1.21^{+0.39}_{-\infty}$	0.66	1.25	50.28
$40.50 < 40.75 < 41.00$	$-1.78^{+0.64}_{-0.65}$	2.43	4.84	2985.57
$41.00 < 41.25 < 41.50$	$-1.99^{+0.15}_{-0.23}$	9.88	22.43	4763.46
$41.50 < 41.75 < 42.00$	$-1.81^{+0.13}_{-0.19}$	19.06	35.27	5087.77
$42.00 < 42.25 < 42.50$	$-2.46^{+0.30}_{-0.28}$	5.61	8.29	5469.76
$42.50 < 42.75 < 43.00$	$-3.49^{+0.31}_{-\infty}$	1.00	1.00	6187.25

Notes. The value $\langle N \rangle$ is the average number of sources in the luminosity bin and $N_{\rm corr}$ is the average number corrected for completeness. The value $\langle V_{\rm max} \rangle$ is the average $V_{\rm max}$ for the sources in the bin. The average values are taken across the multiple MC iterations used to compute the statistical errors on the LF points. The uncertainties on $\log(\Phi)$ are 68% error bars, combining Poissonian error, MC iterations, and an estimation of the cosmic variance.

of lower statistics and higher uncertainties, the effects of binning on the measured slope increases. For z_2 the LF is affected by a small overdensity of LAEs at $z \sim 4$ resulting in a higher dispersion on the faint end slope value when testing different binnings. It was ensured that the optimal binning allowed this fit to be consistent with the fit made for $z_{\rm all}$: in both cases the points at $41.5 \lesssim \log L \lesssim 42$, affected by the same sources at $z \sim 4$, are treated as a small overdensity with respect to the Schechter distribution. Finally, for z_3, the lack of statistics seriously limits the possibilities of binnings to test. The only viable options are the two presented on the right panel of Fig. 12: in both cases the quality of the fit is poor compared to the other redshift bins, but the measured slopes are consistent within their own error bars.

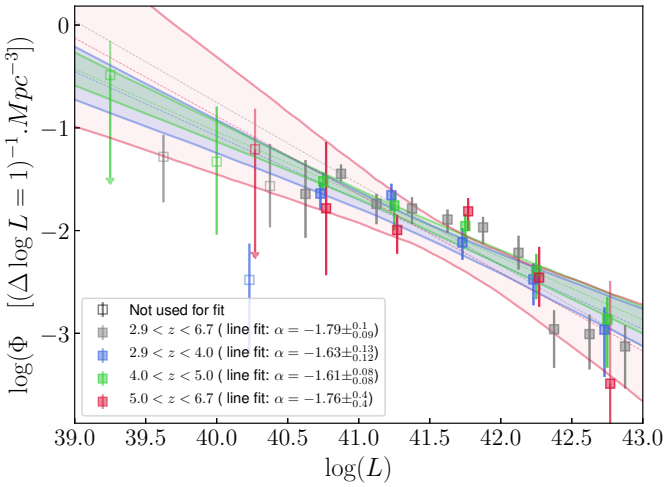

Fig. 11. Luminosity function points computed for the four redshift bins. Each LF was fitted with a straight dotted line and the shaded areas are the 68% confidence regions derived from these fits. For the clarity of the plot, the confidence area derived for $z_{\rm all}$ is not shown and a slight luminosity offset is applied to the LF points for z_1 and z_3.

The LF points from the literature used to constrain the bright end are taken from Blanc et al. (2011) and Sobral et al. (2018) for $z_{\rm all}$ and z_1, Dawson et al. (2007), Zheng et al. (2013), and Sobral et al. (2018) for z_2, and finally Ouchi et al. (2010), Santos et al. (2016), Konno et al. (2018), and Sobral et al. (2018) for z_3. The goal is to extend our own data towards the highest luminosities using available high-quality data with enough overlap to check the consistency with the present data set. The best fits and the literature data sets used for the fits are also shown in Fig. 13 as full lines and lightly coloured diamonds, respectively. The dark red coloured regions indicate the 68% and 95% confidence areas for the Schechter fit. The best Schechter parameters are listed in Table 7. In addition, this table contains the results obtained when the exact same method of LF computation is applied to the sources of A2744 as an independent data set. This is done to assess the robustness of the method and to see whether or not the addition of low volume and high magnification cubes add significant constraints on the faint end slopes. All four fits made using the complete sample are summed up in Fig. 14, which shows the evolution of the confidence regions for α, Φ_*, and L_* with redshift.

Table 7 shows that the results are very similar for $z1$ and $z3$ when considering A2744 only or the full sample. For $z_{\rm all}$ and z_2 the recovered slopes exhibit a small difference at the $\lesssim 2\sigma$ level. This difference is caused by one single source with $40.5 \lesssim \log L \lesssim 41$, which has a high contribution to the density count. When adding more cubes and sources, the contribution of this LAE is averaged down because of the larger volume and the contribution of other LAEs. This argues in favour of a systematic underestimation of the cosmic variance in this work. Using the results of cosmological simulations to estimate a proper cosmic variance is out of the scope of this paper. For the higher redshift bin, even though the same slope is measured when using only the LAEs of A2744, the analysis can only be pushed down to $\log L = 41$ (instead of $\log L = 40.5$ for the other redshift bins or when using the full sample). This shows the benefit of increasing the number of lensing fields to avoid a sudden drop in completeness at high redshift. The effect of increasing the number of lensing fields will be addressed in a future article in preparation. In the following, only the results obtained with the full sample are discussed

The values measured for L_* are in good agreement with the literature (e.g. $\log(L_*) = 43.04 \pm 0.14$ in Dawson et al. (2007) for $z \simeq 4.5$, $\log(L_*) = 43.25^{+0.09}_{-0.06}$ in Santos et al. (2016) for $z \simeq 5.7$ and a fixed value of $\alpha = -2.0$, and $\log(L_*) = 43.3^{+0.5}_{-0.9}$ in Hu et al. (2010) for $z \simeq 5.7$ and a fixed value of $\alpha = -2.0$) and these values tend to increase with redshift. This is not a surprise as this parameter is most sensitive to the data points from the literature used to fit the Schechter functions. Given the large degeneracy and therefore large uncertainty affecting the normalization parameter ϕ_*, a direct comparison and discussion with previous studies is difficult and not so relevant. Regarding the α parameter, the Schechter analysis reveals a steepening of the faint end slope with increasing redshift, which in itself means an increase in the observed number of low luminosity LAEs with respect to the bright population with redshift. However, this is a $\sim 1\sigma$ trend that can only be seen in the light of the Schechter analysis, with a solid anchorage of the bright end, and cannot be seen using only the points derived in this work (see e.g. Fig. 11).

Taking advantage of the unprecedented level of constraints on the low luminosity regime, the present analysis has confirmed a steep faint end slope varying from $\alpha = -1.58^{+0.11}_{-0.11}$ at $2.9 < z < 4$ to $\alpha = -1.87^{+0.12}_{-0.12}$ at $5 < z < 6.7$. The result for the lower redshift bin is not consistent with $\alpha = -2.03^{+1.42}_{-0.07}$ measured using the maximum-likelihood technique in D17. At higher redshift, the slopes measured in D17 are upper limits, which are consistent with all the values in Table 7. The points in purple in Fig. 13 are the points derived with the $V_{\rm max}$ from this same study. It can be seen that there is a systematic difference, increasing at lower luminosity for $z_{\rm all}$, z_1 and z_2. This difference, taken at face value, could be evidence for a systematic underestimation of the cosmic variance both in this work and in D17. This aspect clearly requires further investigation in the future. Faint end slope values of $\alpha = -2.03^{+0.4}_{-0.3}$ for $z = 5.7$ and $\alpha = -2.6^{+0.6}_{-0.4}$ for $z \sim 5.7$ ($\alpha = -2.5^{+0.5}_{-0.5}$ for $z \sim 6.6$) were found in Santos et al. (2016) and Konno et al. (2018), respectively. These values are reasonably consistent with our measurement made for z_3. In this case again, the comparison with the literature is quite limited as the faint end slope is often fixed (see e.g. Dawson et al. 2007; Ouchi et al. 2010) or the luminosity range probed is not adequate leading to poor constraints on α.

From Fig. 13, we see that the Schechter function provides a relatively good fit for $z_{\rm all}$, z_1, and z_2. The over-density in number count at $z \sim 4$ for $41.5 \lesssim \log L \lesssim 42$ is indeed seen as an over-density with respect to the Schechter distribution. For z_3 however, the fit is not as good with one point well above the 1σ confidence area. The final goal of this work is not the measurement of the Schechter slope in itself, but to provide a solid constraint on the shape of the faint end of the LF. Furthermore it is not certain that such a low luminosity population is expected to follow a Schechter distribution. Some studies have already explored the possibility of a turnover in the LF of UV selected galaxies (e.g. Bouwens et al. 2017; Atek et al. 2018), and the same possibility is not to be excluded for the LAE population. For the specific needs of this work, it remains convenient to adopt a parametric form as it makes the computation of proper integrations with correct error transfer easier (see Sect. 8) and facilitates the comparison with previous and future works. When talking about integrated LFs, any reasonable deviations from the Schechter form is of little consequence as long as the fit is representative of the data. In other words, as long as no large extrapolation towards low luminosity is made, our Schechter fits provide a good estimation of the integrated values.

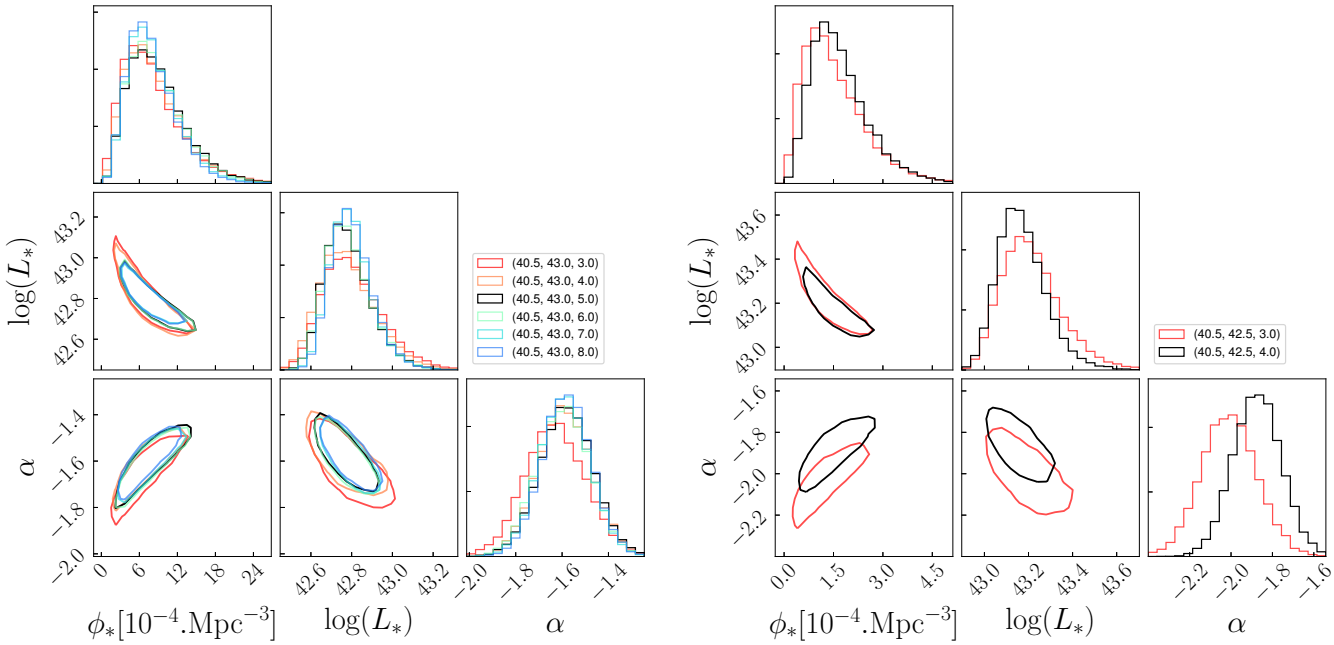

Fig. 12. Areas of 68% confidence derived on the Schechter parameters when testing different binnings. *Left panel*: results for $2.9 < z < 4.0$ and the *right panel* those for $5.0 < z < 6.7$. The legends on the plots indicate, *from left to right*, $\log(L)_{\rm min}$, $\log(L)_{\rm max}$ and the number of bins considered for the fit between these two limits. The black lines show the results obtained from the optimal bins adopted in this work.

8. Discussion and contribution of LAEs to reionization

In this section, before going to the integration of the LFs and the constraints and implications for reionization, we discuss the uncertainties introduced by the use of lensing. As part of the HFF programme, several good quality mass models were produced and made publicly available by different teams, using different methodologies. The uncertainties introduced by the use of lensing fields when measuring the faint end of the UV LF are discussed in detail in Bouwens et al. (2017) and Atek et al. (2018) through simulations. A more general discussion on the reason why mass models of the same lensing cluster may differ from one another can be found in Priewe et al. (2017). And finally, a thorough comparison of the mass reconstruction produced by different teams with different methods from simulated lensing clusters and HST images is done in Meneghetti et al. (2017). The uncertainties are of two types:

– The large uncertainties for high magnification values. This aspect is well treated in this work through the use of $P(\mu)$, which allows any source to have a diluted and very asymmetric contribution to the LF over a large luminosity range. This aspect was already addressed in Sect. 5.
– The possible systematic variation from one mass model to another. This aspect is more complex as it has an impact on both the individual magnification of sources and on the total volume of the survey.

Figure 15 illustrates the problem of variation of individual magnification from one mass model to another, using the V4 models produced by the GLAFIC team (Kawamata et al. 2016; Kawamata 2018), Sharon & Johnson (Johnson et al. 2014), and Keeton that are publicly available on the HFF website[5]. Since we are restricted to the HFF, this comparison can only be done for the LAEs of A2744. The figure shows the Lyman-alpha luminosity histograms when using alternatively the individual magnification provided by these three additional models. The bin size is $\Delta \log L = 0.5$, which is the bin size used in this work for the LFs at z_1,z_2 and z_3. For $\log L > 40.5$ the highest dispersion is of the order of 15%. This shows that even though there is a dispersion when looking at the magnification predicted by the four models, the underlying luminosity population remains roughly the same. Regarding the needs of the LF, this is the most important point.

Figure 10 of Atek et al. (2018) shows an example of the variations of volume probed with rest-frame UV magnitude using different mass models for the lensing cluster MACS1149. This evolution is very similar for the models derived by the Sharon and Keeton teams and, in the worst case scenario, implies a factor of ∼2 of difference among the models compared in this figure. These important variations are largely caused by the lack of constraints on the mass distribution outside of the multiple image area: a small difference in the outer slope of the mass density affects the overall mass of the cluster and therefore the total volume probed. However, unlike other lensing fields from the HFF programme, A2744 has an unprecedented number of good lensing constraints at various redshifts thanks to the deep MUSE observations. These constraints were shared between the teams and are included in all the V4 models used for comparison in this work. These four resulting mass models are robust and coherent, at the state of the art of what can be achieved with the current facilities. It has also been shown by Meneghetti et al. (2017) based on simulated cluster mass distributions, that the methodology employed by the CATS (the CATS model for A2744 is the model presented in Mahler et al. 2018) and GLAFIC teams are among the best to recover the intrinsic mass distribution of galaxy clusters. To test the possibility of a systematic error on the survey volume, the surface of the source plane reconstruction of the MUSE FoV is compared at $z = 4.5$ using the same four models as in Fig. 15. The surfaces are $(1.23')^2$, $(1.08')^2$,$(1.03')^2$, and $(0.94')^2$ using the mass models of Mahler, GLAFIC, Keeton, and Sharon, respectively. The strongest difference is observed between the models of Mahler and Sharon and corresponds to a relatively small difference of only 25%.

[5] https://archive.stsci.edu/prepds/frontier/lensmodels/

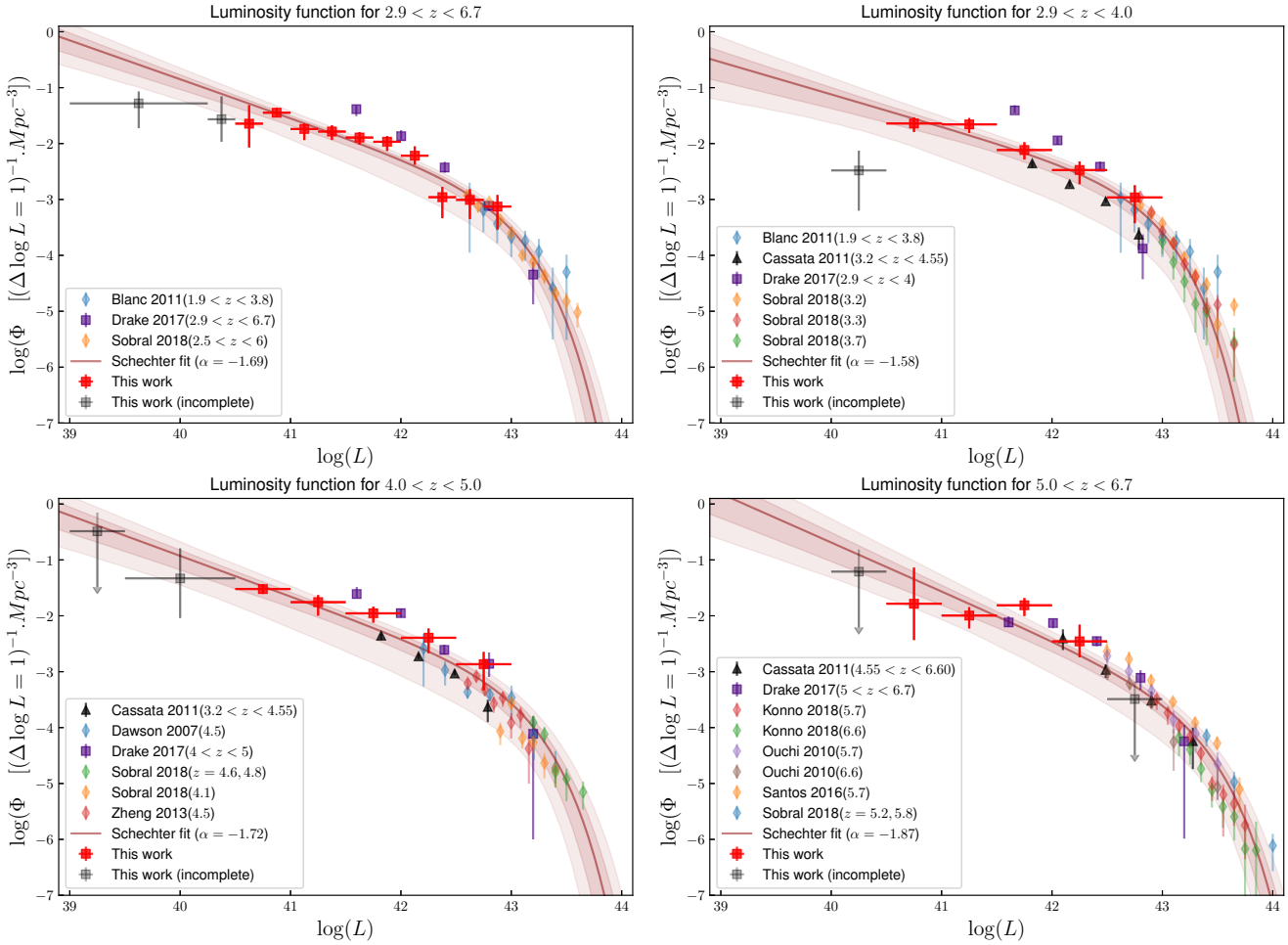

Fig. 13. Luminosity functions and their respective fits for the 4 different redshift bins considered in this study. The red and grey squares represent the points derived in this work, where the grey squares are considered incomplete and are not used in the different fits. The literature points used to constrain the bright end of the LFs are shown as lightly coloured diamonds. The black points represent the results obtained by Cassata et al. (2011), which were not used for the fits. The purple squares represent the points derived using the $V_{\rm max}$ method in D17 and are only shown for comparison. The best Schechter fits are shown as a solid line and the 68% and 95% confidence areas as dark red coloured regions, respectively.

Given the complex nature of the MUSE data combined with the lensing cluster analysis, precisely assessing the effect of a possible total volume bias is nontrivial and out of the scope of this paper. From this discussion it seems clear that the use of lensing fields introduces an additional uncertainty on the faint end slope. However the luminosity limit under which this effect becomes dominant remains unknown as all the simulations (Bouwens et al. 2017; Atek et al. 2018) were only done for the UV LF for which the data structure is much simpler.

In order to estimate the contribution of the LAE population to the cosmic reionization, its SFRD was computed. From the best parameters derived in the previous section, the integrated luminosity density $\rho_{\rm Ly_\alpha}$ was estimated. The SFRD produced by the LAE population can be estimated using the following prescription for the (Kennicutt 1998) assuming the case B for the recombination (Osterbrock & Ferland 2006):

$$\mathrm{SFRD}_{\rm Ly_\alpha}\,[M_\odot\,\mathrm{yr}^{-1}\,\mathrm{Mpc}^{-3}] = L_{\rm Ly_\alpha}\,[\mathrm{erg\,s}^{-1}\,\mathrm{Mpc}^{-3}]/1.05\times10^{42}. \quad (12)$$

This equation assumes an escape fraction of the Lyman-alpha photons ($f_{\rm Ly_\alpha}$) of 1 and is therefore a lower limit for the SFRD. Uncertainties on this integration were estimated with MC iterations, by perturbing the best-fit parameters within their rescaled error bars, neglecting the correlations between the parameters. The values obtained for the $\mathrm{SFRD}_{\rm Ly_\alpha}$ and $\rho_{\rm Ly_\alpha}$ are presented in Table 7 for a lower limit of integration of $\log(L) = 40.5$, which corresponds to the lowest luminosity points used to fit the LFs (i.e. no extrapolation towards lower luminosities). The equation $\log(L) = 44$ is used as upper limit for all integrations. The upper limit has virtually no impact on the final result because the LF drops so steeply at higher luminosity.

We show in Fig. 16 the results obtained using different lower limits of integration and how they compare to previous studies of both LBG and LAE LFs. The yellow area corresponds to the 1σ and 2σ SFRD needed to reionize the universe fully, which is estimated from the cosmic ionizing emissivity derived in Bouwens et al. (2015a). The cosmic emissivity was derived using a clumping factor of 3, the conversion to UV luminosity density was done assuming $\log(\xi_{\rm ion} f_{\rm escp}) = 24.50$, where $f_{\rm escp}$ is the escape fraction of UV photons and $\xi_{\rm ion}$ is the Lyman-continuum photon production efficiency. Finally the conversion to SFRD was done with the following relation: $\mathrm{SFRD}\,[M_\odot\,\mathrm{yr}^{-1}] = \rho_{\rm UV}/(8.0\times10^{27})$ (see Kennicutt 1998; Madau et al. 1998). Because all the slopes are over $\alpha = -2$ (for $\alpha < -2$ the integral of the Schechter parameterization diverges), the integrated values increase relatively slowly when decreasing the lower luminosity limit. On the same plot, the SFRD computed from the integration of the LFs derived in Bouwens et al. (2015b) are shown in darker grey for two limiting magnitudes: $M_{\rm UV} = -17$ (which is the observation

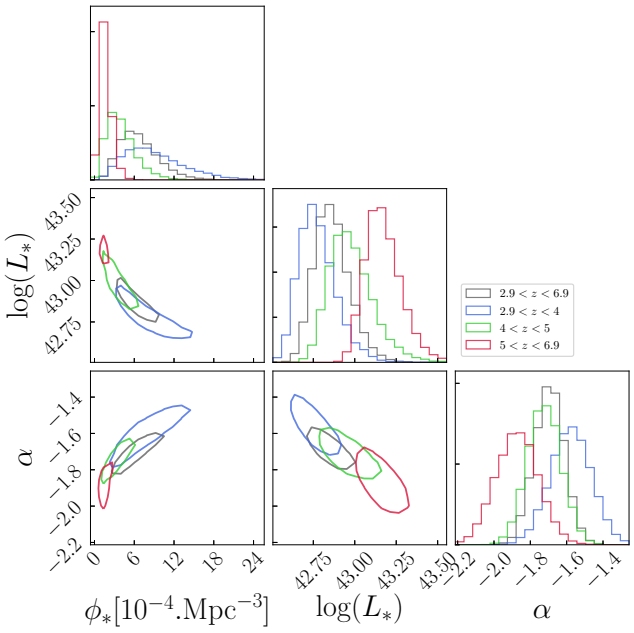

Fig. 14. Evolution of the Schechter parameters with redshift. The contours plotted correspond to the limits of the 68% confidence areas determined from the results of the fits.

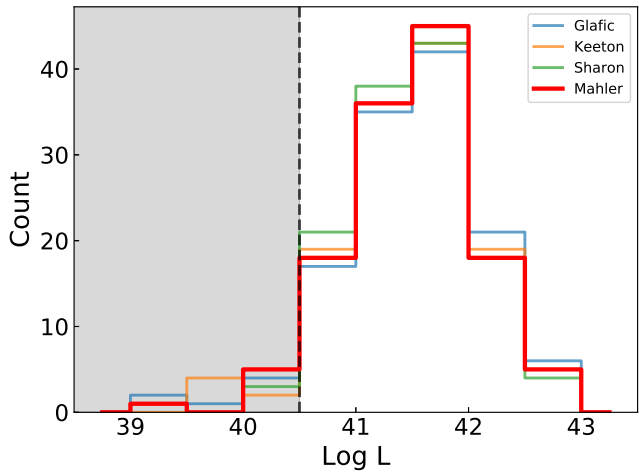

Fig. 15. Comparative Lyman-alpha luminosity histograms obtained using the magnification resulting from different mass models. The grey area represents the completeness limit of this work.

limit) and $M_{\mathrm{UV}} = -13$, which is thought to be the limit of galaxy formation (e.g. Rees & Ostriker 1977; Mac Low & Ferrara 1999; Dijkstra et al. 2004).

From this plot, and with $f_{\mathrm{Ly}_\alpha} = 1$, we see that the observed LAE population only is not enough to reionize the universe fully at $z \sim 6$, even with a large extrapolation of 2 dex down to $\log L = 38.5$. However, a straightforward comparison is dangerous: an escape fraction $f_{\mathrm{Ly}_\alpha} \gtrsim 0.5$ would be roughly enough to match the cosmic ionizing emissivity needed for reionization at $z \sim 6$. Moreover, in this comparison, we implicitly assumed that the LAE population has the same properties ($\log(f_{\mathrm{esc}}\xi_{\mathrm{ion}}) = 24.5$) as the LBG population in Bouwens et al. (2015b). A recent study on the typical values of ξ_{ion} and its scatter for typical star-forming galaxies at $z \sim 2$ by Shivaei et al. (2018) has shown that ξ_{ion} is highly uncertain as a consequence of galaxy-to galaxy variations on the stellar population and UV dust attenuation, while most current estimates at high-z rely on (too) simple prescriptions from stellar population models. The SFRD obtained from LAEs when no evolution in f_{Ly_α} is introduced remains roughly constant as a function of redshift when no extrapolation is introduced and slightly increases with redshift when using $L_{\mathrm{inf}} = 38.5$. Figure 16 shows in green/blue, the $\mathrm{SFRD}_{\mathrm{Ly}_\alpha}$ values derived in previous studies of the LAE LF, namely Ouchi et al. (2008; hereafter O08), Cassata et al. (2011; hereafter C11), and D17. In C11, a basic correction for IGM absorption was performed assuming f_{Ly_α} varying from 15% at $z = 3$ to 50% at $z = 6$ and using a simple radiative transfer prescription from Fan et al. (2006). This correction can easily explain the clear trend of increase of SFRD with redshift and the discrepancy with our points at higher redshift. At lower redshifts, the IGM correction is lower and the points are in a relatively good agreement. The points in O08 are the result of a full integration of the LFs with a slope fixed at $\alpha = -1.5$ and are in reasonable agreement for all redshift domains. The two higher redshift points derived in D17 are inconsistent with our measurements. This is not a surprise as the slopes derived in D17 are systematically steeper and inconsistent with this work.

The use of an IFU (MUSE) in D17, in Herenz et al. (2019; hereafter H19), and this survey ensures that we better recover the total flux, even though we may still miss the faintest part of the extended Lyman-alpha haloes (see Wisotzki et al. 2016). This is not the case for NB (e.g. O08) or slit-spectroscopy (e.g. Cassata et al. 2011) surveys in which a systematic loss of flux is possible for spatially extended sources or broad emission lines because of the limited aperture of the slits or the limited spectral width of NB filters. It is noted in H19 that the $3.2 < z < 4.55$ LF estimates in C11 tend to be lower than most literature estimates (including those in H19). One possible explanation would be a systematic loss of flux, which results in a systematic shift of the derived LF towards lower luminosities. Interestingly, when assuming point-like sources to compute the selection function, H19 manages to recover very well the results of C11 for this redshift domain. It is also interesting to see that as luminosity decreases, the LF estimates from C11 become more and more consistent with the points and Schechter parameterization derived in this work. For z_3, the C11 LF is even fully consistent with the Schechter parameterization across the entire luminosity domain (see Fig. 13). The following line of thought could explain the concordance of this work with the C11 estimates at lower luminosity and higher redshift: At lower luminosity and higher redshift, a higher fraction of LAEs detected are point-like sources, making the C11 LFs more consistent with our values; and at higher luminosity and lower redshift, more extended LAEs are detected and a more complex correction is needed to get a realistic LF estimate.

The second advantage of using an IFU is linked to the selection of the LAE population. The O08 authors used a NB photometric selection of sources with spectroscopic follow-up to confirm the LAE candidates. This results in an extremely narrow redshift window which is likely to lead to lower completeness of the sample due to the two-step selection process. The studies by D17 and H19, adopt the same approach as this work: a blind spectroscopic selection of sources. In addition, as shown in Fig. 4 and stated in Sect. 7 when discussing the differences in slope between A2744 alone and the full sample, the use of highly magnified observations allows for a more complete source selection at increasing redshift. The sample used in the present work could arguably have a higher completeness level than other previous studies.

To summarize the above discussion, the observational strategy adopted in this study by combining the use of MUSE and lensing clusters has allowed us to

Table 7. Results of the fit of the Schechter function in the different redshift intervals.

		N_{obj}	$N_{corrected}$	Φ_* 10^{-4} Mpc^{-3}	$\log L_*$ erg s^{-1}	α	$\log \rho_{Ly\alpha}$ erg s^{-1} Mpc^{-3}	$\log$ SFRD $M_\odot$ yr^{-1} Mpc^{-3}
$2.9 < z < 6.7$	All clusters	152	278	$6.38^{+3.26}_{-2.46}$	$42.85^{+0.11}_{-0.10}$	$-1.69^{+0.08}_{-0.08}$	$40.08^{+0.04}_{-0.04}$	$-1.94^{+0.04}_{-0.04}$
	A2744 only	125	235	$3.40^{+2.33}_{-1.59}$	$42.97^{+0.15}_{-0.12}$	$-1.85^{+0.08}_{-0.08}$	$40.14^{+0.04}_{-0.04}$	$-1.88^{+0.04}_{-0.04}$
$2.9 < z < 4.0$	All clusters	61	119	$8.29^{+5.25}_{-3.66}$	$42.77^{+0.12}_{-0.10}$	$-1.58^{+0.11}_{-0.11}$	$39.99^{+0.07}_{-0.07}$	$-2.03^{+0.07}_{-0.07}$
	A2744 only	40	102	$7.51^{+4.97}_{-3.43}$	$42.78^{+0.13}_{-0.10}$	$-1.58^{+0.12}_{-0.12}$	$39.97^{+0.07}_{-0.07}$	$-2.05^{+0.07}_{-0.07}$
$4.0 < z < 5.0$	All clusters	52	86	$3.67^{+2.51}_{-1.72}$	$42.96^{+0.14}_{-0.11}$	$-1.72^{+0.09}_{-0.09}$	$39.99^{+0.06}_{-0.06}$	$-2.03^{+0.06}_{-0.06}$
	A2744 only	40	68	$1.52^{+1.45}_{-0.87}$	$43.12^{+0.20}_{-0.15}$	$-1.96^{+0.08}_{-0.09}$	$40.13^{+0.05}_{-0.05}$	$-1.89^{+0.05}_{-0.05}$
$5.0 < z < 6.7$	All clusters	39	73	$1.53^{+0.96}_{-0.68}$	$43.16^{+0.12}_{-0.10}$	$-1.87^{+0.12}_{-0.12}$	$40.03^{+0.11}_{-0.09}$	$-1.99^{+0.11}_{-0.09}$
	A2744 only	33	64	$1.40^{+0.91}_{-0.64}$	$43.18^{+0.12}_{-0.10}$	$-1.90^{+0.12}_{-0.12}$	$40.05^{+0.12}_{-0.11}$	$-1.97^{+0.12}_{-0.11}$

Notes. The last two columns list the Lyman-alpha flux density and the SFRD as a function of redshift, obtained from the integration of the LFs derived in Sect. 7. The errors on the parameters of the Schechter function correspond to 68% confidence interval. The values ρ_{Ly_α} are computed using a lower integration limit $\log(L) = 40.5$, which is considered to be the completeness limit of this work. For each redshift bin, the Schechter parameters are measured from the LFs computed from the entire sample and from the LAEs of A2744 only.

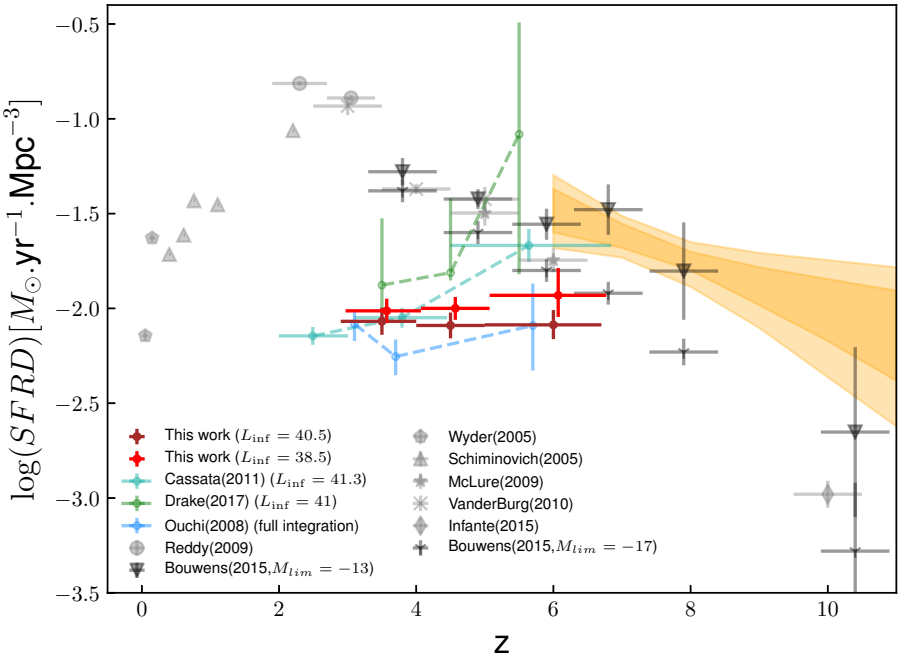

Fig. 16. Evolution of the SFRD with redshift with different lower limits of integration. The limit $\log L = 38.5$ corresponds to a 2 dex extrapolation with respect to the completeness limit in this work. Our results (in red/brown) are compared to SFRD in the literature computed for LBGs (in light grey) and from previous studies of the LAE LF (in green/blue). For the clarity of the plot, a small redshift offset was added to the points with $L_{inf} = 38.5$. The darker grey points correspond to the SFRD derived from the LFs in Bouwens et al. (2015b) for a magnitude limit of integration of $M_{UV} = -17$ corresponding to the observation limit, and $M_{UV} = -13$. The points reported by Cassata et al. (2011) are corrected for IGM absorption. The yellow area corresponds to the 1σ and 2σ estimations of the total SFRD corresponding to the cosmic emissivity derived in Bouwens et al. (2015a).

– Reach fainter luminosities, providing better constraints on the faint end slope of the LF, while still taking advantage of the previous studies to constrain the bright end;
– Recover a greater fraction of flux for all LAEs;
– Cover a large window in redshift and flux;
– Reach a higher level of completeness, especially at high redshift.

A steepening of the faint end slope is observed with redshift, which follows what is usually expected. This trend can be explained by a higher proportion of low luminosity LAEs observed at higher redshift owing to higher dust content at lower redshift. On the other hand, the density of neutral hydrogen is expected to increase across the $5 < z < 6.7$ interval, reducing the escape fraction of Lyman-alpha photons, a trend affecting LAEs in a different way depending on large-scale structure. While an increase of SFRD with redshift is observed, the evolution of the observed SFRD$_{Ly_\alpha}$ is also affected by f_{Ly_α}. From the point of view of the literature, the expected evolution of f_{Ly_α} is an increase with redshift up to $z \sim 6$–7 and then a sudden drop at higher redshift (see e.g. Clément et al. 2012; Pentericci et al. 2014). For $z < 6$, the increase of f_{Ly_α} is generally explained by the reduced amount of dust at higher redshift. And for $z \sim 6$–7 and above, we start to probe the reionization era and owing to the increasing amount of neutral hydrogen and the resonant nature of the Ly$_\alpha$, the escape fraction is expected to drop at some point. It has been suggested in Trainor et al. (2015) and Matthee et al. (2016) that the escape fraction would decrease with an increasing SFRD. This would only increase the significance of the trend observed, as it means the points with the higher SFRD would have a larger correction.

Furthermore the derived LFs and the corresponding SFRD values could be affected by bubbles of ionized hydrogen, especially in the last redshift bin. In our current understanding of the phenomenon, reionization is not a homogeneous process (Becker et al. 2015; Bosman et al. 2018). It could be that the expanding areas of ionized hydrogen develop faster in the vicinity of large structures with a high ionising flux, leaving other areas of the universe practically untouched. There is increasing observational evidence of this effect (see e.g. Stark et al. 2017).

It was shown in Matthee et al. (2015), using a simple toy model, that an increased amount of neutral hydrgen in the IGM could produce a flattening of the faint end shape of the LF. This same study also concluded that the clustering of LAEs had a large impact on the individual escape fraction, which makes it difficult to estimate a realistic correction, as the escape fraction should be estimated on a source to source basis.

As previously discussed, it is neither certain nor expected that the LAE population alone is enough to reionize the universe at $z \sim 6$. However, the LBG and the LAE population have roughly the same level of contribution to the total SFRD at face value. Depending on the intersection between the two populations, the observed LAEs and LBGs together could produce enough ionizing flux to maintain the ionized state of the universe at $z \sim 6$.

This question of the intersection is crucial in the study of the sources of reionization. Several authors have addressed the prevalence of LAE among LBG galaxies, and have shown that the fraction of LAE increases for low luminosity UV galaxies till $z \sim 6$, whereas the LAE fraction strongly decreases towards $z \sim 7$ (see e.g. Stark et al. 2010, Pentericci et al. 2011). The important point however is to precisely determine the contribution of the different populations of star-forming galaxies within the same volume, which is a problem that requires the use of 3D/IFU spectroscopy. As a preliminary result, we estimate that ∼20% of the sample presented in this study have no detected counterpart on the deep images of the HFFs. A similar analysis is being conducted on the deepest observations of MUSE on the Hubble Ultra Deep Field (Maseda et al. 2018).

9. Conclusions

The goal of this study was to set constraints on the sources of cosmic reionization by studying the LAE LF. Taking advantage of the great capabilities of the MUSE instrument and using lensing clusters as a tool to reach lower luminosities, we blindly selected behind four lensing clusters a population of 156 spectroscopically identified LAEs that have $2.9 < z < 6.7$ and magnification corrected luminosities $39 \lesssim \log L \lesssim 43$.

Given the complexity in combining the spectroscopic data cubes of MUSE with gravitational lensing, and taking into account that each source needs an appropriate treatment to properly account for its magnification and representativity, the computation of the LF needed a careful implementation, including some original developments. For these needs, a specific procedure was developed, including the following new methods: First, we created a precise $V_{\rm max}$ computation for the sources found behind lensing clusters is based on the creation of 3D masks. This method allows us to precisely map the detectability of a given source in MUSE spectroscopic cubes. These masks are then used to compute the cosmological volume in the source plane. This method could be easily adapted to be used in blank field surveys. Second, we developed a completeness determination based on simulations using the real profile of the sources. Instead of performing a heavy parametric approach based on MC source injection and recovery simulations, which is not ideally suited for lensed galaxies, this method uses the real profile of sources to estimate their individual completeness. The method is faster, more flexible, and accounts in a better way for the specificities of individual sources, both in the spatial and spectral dimensions.

After applying this procedure to the LAE population, the Lyman-alpha LF has been built for different redshift bins using 152 of the 156 detected LAEs. Four LAEs were removed because their contribution was not trustworthy. Because of the observational strategy, this study provides the most reliable constraints on the shape of the faint end of the LFs to date and therefore, a more precise measurement of the integrated SFRD associated with the LAE population. The results and conclusions can be summarized as follows:

- The LAE population found behind the four lensing clusters was split in four redshift bins: $2.9 < z < 6.7$, $2.9 < z < 4.0$, $4.0 < z < 5.9$, and $5.0 < z < 6.7$. Because of the lensing effect, the volume of universe probed is greatly reduced in comparison to blank field studies. The estimated average volume of universe probed in the four redshift bins are ∼15 000 Mpc^3, ∼5000 Mpc^3, ∼4000 Mpc^3, and ∼5000 Mpc^3, respectively.
- The LAE LF was computed for the four redshift bins. By construction of the sample, the derived LFs efficiently probe the low luminosity regime and the data from this survey alone provide solid constraints on the shape of the faint end of the observed LAE LFs. No significant evolution in the shape of the LF with redshift is found using these points only. These results have to be taken with caution given the complex nature of the lensing analysis, on the one hand, and the small effective volume probed by the current sample on the other hand. Our results argue towards a possible systematic underestimation of cosmic variance in the present and other similar works.
- A Schechter fit of the LAE LF was performed by combining the LAE LF computed in this analysis with data from previous studies to constrain the bright end. As a result of this study, a steep slope was measured for the faint end, varying with redshift between $\alpha = -1.58^{+0.11}_{-0.11}$ at $2.9 < z < 4$ and $\alpha = -1.87^{+0.12}_{-0.12}$ at $5 < z < 6.7$
- The $\mathrm{SFRD}_{\mathrm{Ly}_\alpha}$ values were obtained as a function of redshift by the integration of the corresponding Lyman-alpha LF and compared to the levels needed to ionize the universe as determined in Bouwens et al. (2015a). No assumptions were made regarding the escape fraction of the Lyman-alpha photons and the $\mathrm{SFRD}_{\mathrm{Ly}_\alpha}$ derived in this work correspond to the observed values. Because of the well-constrained LFs and a better recovery of the total flux, we estimate that the present results are more reliable than previous studies. Even though the LAE population undoubtedly contributes to a significant fraction of the total SFRD, it remains unclear whether this population alone is enough to ionize the universe at $z \sim 6$. The results depend on the actual escape fraction of Lyman-alpha photons.
- The LAEs and the LBGs have a similar level of contribution at $z \sim 6$ to the total SFRD level of the universe. Depending on the intersection between the two populations, the union of both the LAE and LBG populations may be enough to reionize the universe at $z \sim 6$.

Through this work, we have shown that the capabilities of the MUSE instrument make it an ideal tool to determine the LAE LF. Being an IFU, MUSE allows for a blind survey of LAEs, homogeneous in redshift, with a better recovery of the total flux as compared to classical slit facilities. The selection function is also better understood as compared to NB imaging.

About 20% of the present LAE sample have no identified photometric counterpart, even on the deepest surveys to date, i.e. HFF. This is an important point to keep in mind as this is a first element of response regarding the intersection between the LAE and LBG populations. Further investigation is needed to better quantify this intersection. Also the extension of the method presented in this paper to other lensing fields should make it possible to improve the determination of the Lyman-alpha LF and to make the constraints on the sources of the reionization more robust.

Acknowledgements. We thank the anonymous referee for their critical review and useful suggestions. This work has been carried out thanks to the support of the OCEVU Labex (ANR-11-LABX-0060) and the A*MIDEX project (ANR-11-IDEX-0001-02) funded by the "Investissements d'Avenir" French government programme managed by the ANR. Partially funded by the ERC starting grant CALENDS (JR, VP, BC, JM), the Agence Nationale de la recherche bearing the reference ANR-13-BS05-0010-02 (FOGHAR), and the "Programme National de Cosmologie and Galaxies" (PNCG) of CNRS/INSU, France. GdV, RP, JR, GM, JM, BC, and VP also acknowledge support by the Programa de Cooperacion Cientifica – ECOS SUD Program C16U02. NL acknowledges funding from the European Research Council (ERC) under the European Union's Horizon 2020 research and innovation programme (grant agreement No 669253), ABD acknowledges support from the ERC advanced grant "Cosmic Gas". LW acknowledges support by the Competitive Fund of the Leibniz Association through grant SAW-2015-AIP-2, and TG acknowledges support from the European Research Council under grant agreement ERC-stg-757258 (TRIPLE).. Based on observations made with ESO Telescopes at the La Silla Paranal Observatory under programme IDs 060.A-9345, 094.A-0115, 095.A-0181, 096.A-0710, 097.A0269, 100.A-0249, and 294.A-5032. Also based on observations obtained with the NASA/ESA *Hubble* Space Telescope, retrieved from the Mikulski Archive for Space Telescopes (MAST) at the Space Telescope Science Institute (STScI). STScI is operated by the Association of Universities for Research in Astronomy, Inc. under NASA contract NAS 5-26555. This research made use of Astropy, a community-developed core Python package for Astronomy (Astropy Collaboration 2013). All plots in this paper were created using Matplotlib (Hunter 2007).

References

Akhlaghi, M., & Ichikawa, T. 2015, ApJS, 220, 1
Astropy Collaboration (Robitaille, T. P., et al.) 2013, A&A, 558, A33
Atek, H., Richard, J., Kneib, J.-P., et al. 2014, ApJ, 786, 60
Atek, H., Richard, J., Kneib, J.-P., & Schaerer, D. 2018, MNRAS, 479, 5184
Bacon, R., Accardo, M., Adjali, L., et al. 2010, Proc. SPIE, 7735, 773508
Bacon, R., Brinchmann, J., Richard, J., et al. 2015, A&A, 575, A75
Bacon, R., Conseil, S., Mary, D., et al. 2017, A&A, 608, A1
Becker, G. D., Bolton, J. S., Madau, P., et al. 2015, MNRAS, 447, 3402
Bertin, E., & Arnouts, S. 1996, A&AS, 117, 393
Bina, D., Pelló, R., Richard, J., et al. 2016, A&A, 590, A14
Blanc, G. A., Adams, J. J., Gebhardt, K., et al. 2011, ApJ, 736, 31
Bosman, S. E. I., Fan, X., Jiang, L., et al. 2018, MNRAS, 479, 1055
Bouwens, R. J., Illingworth, G. D., Oesch, P. A., et al. 2015a, ApJ, 811, 140
Bouwens, R. J., Illingworth, G. D., Oesch, P. A., et al. 2015b, ApJ, 803, 34
Bouwens, R. J., Oesch, P. A., Illingworth, G. D., Ellis, R. S., & Stefanon, M. 2017, ApJ, 843, 129
Broadhurst, T., Benitez, N., Coe, D., et al. 2005, ApJ, 621, 53
Caminha, G., Karman, W., Rosati, P., et al. 2016, A&A, 595, A100
Cassata, P., Le Fèvre, O., Garilli, B., et al. 2011, A&A, 525, A143
Clément, B., Cuby, J. G., Courbin, F., et al. 2012, A&A, 538, A66
Covone, G., Kneib, J.-P., Soucail, G., et al. 2006, A&A, 456, 409
Dawson, S., Rhoads, J. E., Malhotra, S., et al. 2007, ApJ, 671, 1227
Dijkstra, M., Haiman, Z., Rees, M. J., & Weinberg, D. H. 2004, ApJ, 601, 666
Drake, A., Garel, T., & Wisotzki, L. 2017, A&A, 608, A1
Elíasdóttir, Á., Limousin, M., Richard, J., et al. 2007, ArXiv e-prints [arXiv:0710.5636]
Faber, S. M., & Jackson, R. E. 1976, ApJ, 204, 668
Fan, X., Strauss, M. A., Becker, R. H., et al. 2006, AJ, 132, 117
Felten, J. E. 1976, ApJ, 207, 700
Fontanot, F., Cristiani, S., & Vanzella, E. 2012, MNRAS, 425, 1413
Foreman-Mackey, D., Hogg, D. W., Lang, D., & Goodman, J. 2013, PASP, 125, 306
Herenz, E. C., Urrutia, T., Wisotzki, L., et al. 2017, A&A, 606, A12
Herenz, E. C., Wisotzki, L., Saust, R., et al. 2019, A&A, 621, A107
Hu, E. M., Cowie, L. L., Barger, A. J., et al. 2010, ApJ, 725, 394
Hunter, J. D. 2007, Comput. Sci. Eng., 9, 90
Infante, L., Zheng, W., Laporte, N., et al. 2015, ApJ, 815, 18
Ishigaki, M., Kawamata, R., Ouchi, M., et al. 2015, ApJ, 799, 12
Johnson, T. L., Sharon, K., Bayliss, M. B., et al. 2014, ApJ, 797, 48
Jullo, E., & Kneib, J. P. 2009, MNRAS, 395, 1319
Jullo, E., Kneib, J. P., Limousin, M., et al. 2007, New J. Phys., 9, 447
Karman, W., Grillo, C., Balestra, I., et al. 2016, A&A, 585, A27
Kashikawa, N., Shimasaku, K., Malkan, M. A., et al. 2006, ApJ, 648, 7
Kawamata, R. 2018, ApJ, 855, 4
Kawamata, R., Oguri, M., Ishigaki, M., Shimasaku, K., & Ouchi, M. 2016, ApJ, 819
Kennicutt, Jr., R. C. 1998, ApJ, 498, 541
Kneib, J.-P., Ellis, R. S., Smail, I., Couch, W. J., & Sharples, R. M. 1996, ApJ, 471, 643
Konno, A., Ouchi, M., Ono, Y., et al. 2014, ApJ, 797, 16
Konno, A., Ouchi, M., Shibuya, T., et al. 2018, PASJ, 70, S16
Lagattuta, D. J., Richard, J., Clément, B., et al. 2017, MNRAS, 469, 3946
Laporte, N., Streblyanska, A., Clement, B., et al. 2014, A&A, 562, L8
Laporte, N., Infante, L., Troncoso Iribarren, P., et al. 2016, ApJ, 820, 98
Limousin, M., Richard, J., Jullo, E., et al. 2007, ApJ, 668, 643
Livermore, R. C., Finkelstein, S. L., & Lotz, J. M. 2017, ApJ, 835, 113
Lotz, J. M., Koekemoer, A., Coe, D., et al. 2017, ApJ, 837, 97
Mac Low, M., & Ferrara, A. 1999, ApJ, 513, 142
Madau, P., Pozzetti, L., & Dickinson, M. 1998, ApJ, 498, 106
Mahler, G., Richard, J., Clément, B., et al. 2018, MNRAS, 692, 663
Maizy, A., Richard, J., de Leo, M., Pelló, R., & Kneib, J. 2010, A&A, 509, A105
Maseda, M. V., Bacon, R., Franx, M., et al. 2018, ApJ, 865, L1
Matthee, J., Sobral, D., Santos, S., et al. 2015, MNRAS, 451, 400
Matthee, J., Sobral, D., Oteo, I., et al. 2016, MNRAS, 458, 449
McGreer, I. D., Jiang, L., Fan, X., et al. 2013, ApJ, 768, 105
McLure, R., Cirasuolo, M., Dunlop, J., Foucaud, S., & Almaini, O. 2009, MNRAS, 395, 2196
Meneghetti, M., Natarajan, P., Coe, D., et al. 2017, MNRAS, 3216, 3177
Newville, M., Stensitzki, T., Allen, D. B., & Ingargiola, A. 2014, Astrophysics Source Code Library [record ascl:1606.014]
Oke, J. B., & Gunn, J. E. 1983, ApJ, 266, 713
Olmstead, A., Rigby, J. R., Swinbank, M., & Veilleux, S. 2014, AJ, 148, 15
Orieux, F., Giovannelli, J.-F., & Rodet, T. 2010, OSA, 27, 1593
Osterbrock, D. E., & Ferland, G. J. 2006, Mercury, 35, 40
Ouchi, M., Shimasaku, K., Okamura, S., et al. 2004, ApJ, 611, 660
Ouchi, M., Shimasaku, K., Akiyama, M., Simpson, C., & Saito, T. 2008, ApJS, 176, 301
Ouchi, M., Shimasaku, K., Furusawa, H., et al. 2010, ApJ, 723, 869
Patricio, V., Richard, J., Carton, D., et al. 2018, MNRAS, 28, 1
Pello, R., Le Borgne, J.-F., Soucail, G., Mellier, Y., & Sanahuja, B. 1991, ApJ, 366, 405
Pentericci, L., Fontana, A., Vanzella, E., et al. 2011, ApJ, 743, 132
Pentericci, L., Vanzella, E., Fontana, A., et al. 2014, ApJ, 793, 113
Piqueras, L., Conseil, S., Shepherd, M., et al. 2017, ArXiv e-prints [arXiv:1710.03554]
Priewe, J., Williams, L. L. R., Liesenborgs, J., Coe, D., & Rodney, S. A. 2017, MNRAS, 465, 1030
Rees, M. J., & Ostriker, J. P. 1977, MNRAS, 179, 541
Rhoads, J. E., Malhotra, S., Dey, A., et al. 2000, ApJ, 545, L85
Ricci, F., Marchesi, S., Shankar, F., La Franca, F., & Civano, F. 2017, MNRAS, 465, 1915
Richard, J., Stark, D. P., Ellis, R. S., et al. 2008, ApJ, 685, 705
Richard, J., Smith, G. P., Kneib, J. P., et al. 2010, MNRAS, 404, 325
Richard, J., Jauzac, M., Limousin, M., et al. 2014, MNRAS, 444, 268
Richard, J., Patricio, V., Martinez, J., et al. 2015, MNRAS, 446, L16
Robertson, B. E., Furlanetto, S. R., Schneider, E., et al. 2013, ApJ, 768, 71
Robertson, B. E., Ellis, R. S., Furlanetto, S. R., & Dunlop, J. S. 2015, ApJ, 802, L19
Santos, S., Sobral, D., & Matthee, J. 2016, MNRAS, 14, 1
Schechter, P. L. 1976, ApJ, 203, 297
Schiminovich, D., Ilbert, O., Arnouts, S., et al. 2005, ApJ, 619, L47
Schmidt, M. 1968, ApJ, 151, 393
Shivaei, I., Reddy, N. A., Siana, B., et al. 2018, ApJ, 855, 42
Sobral, D., Santos, S., Matthee, J., et al. 2018, MNRAS, 476, 4725
Soto, K. T., Lilly, S. J., Bacon, R., Richard, J., & Conseil, S. 2016, MNRAS, 458, 3210
Stark, D. P., Ellis, R. S., Bunker, A., et al. 2009, ApJ, 697, 1493
Stark, D. P., Ellis, R. S., Chiu, K., Ouchi, M., & Bunker, A. 2010, MNRAS, 408, 1628
Stark, D. P., Ellis, R. S., Charlot, S., et al. 2017, MNRAS, 464, 469
Steidel, C. C., Giavalisco, M., Pettini, M., Dickinson, M., & Adelberger, K. L. 1996, ApJ, 462, L17
Tilvi, V., Papovich, C., Finkelstein, S., et al. 2014, ApJ, 794, 5
Trainor, R. F., Steidel, C. C., Strom, A. L., & Rudie, G. C. 2015, ApJ, 809, 89
Trenti, M., & Stiavelli, M. 2007, ApJ, 676, 767
van der Burg, R., Hildebrandt, H., & Erben, T. 2010, A&A, 523, A74
van der Walt, S., Schönberger, J. L., Nunez-Iglesias, J., et al. 2014, PeerJ, 2, e453
Weilbacher, P. M., Streicher, O., Urrutia, T., et al. 2012, Proc. SPIE, 8451, 84510B
Weilbacher, P. M., Streicher, O., Urrutia, T., et al. 2014, ASP conf. ser., 485, 451
Willott, C. J., Delorme, P., Reylé, C., et al. 2010, ApJ, 139, 906
Wisotzki, L., Bacon, R., Blaizot, J., et al. 2016, A&A, 587, A98
Zheng, Z. Y., Finkelstein, S. L., Finkelstein, K., et al. 2013, MNRAS, 431, 3589

Appendix A: Method to create a mask for a 2D image

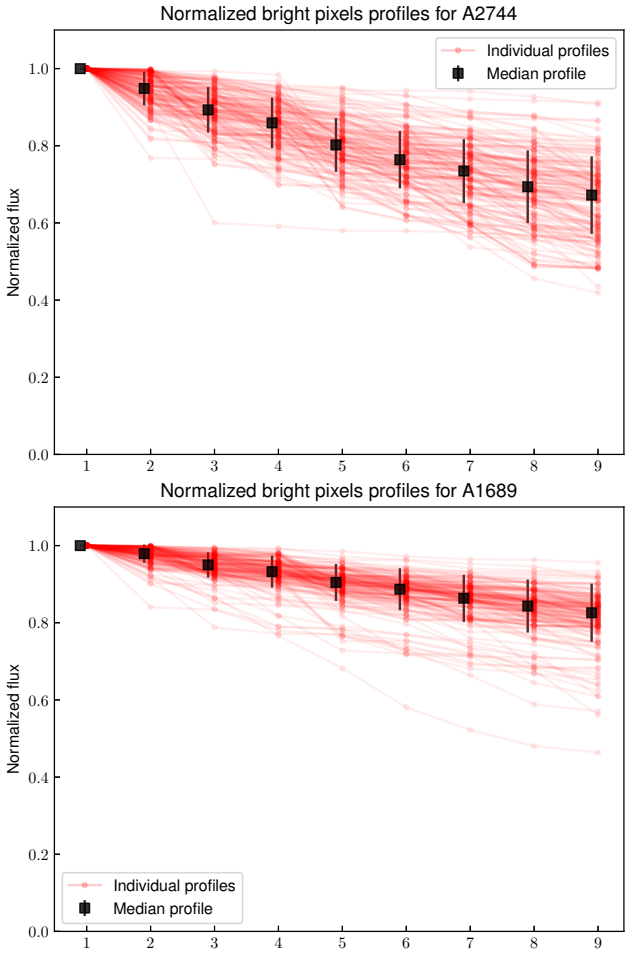

Fig. A.1. Individual bright pixel profiles of all LAEs computed in the seeing condition of A2744 (*top*) and A1689 (*bottom*). We note that these are not spatial profiles as two consecutive pixels may not be adjacent on the image. Only the `MIN_AREA`-th first pixels are necessary to compute a mask (`MIN_ARE` = 6 was used in this work).

In this section we describe the generic method used to create a mask from the detection image of one given source. The goal is to produce a binary mask or detection mask that indicate where the source could have been detected. The details on how this generic method can be adapted to produce masks for spectroscopic cubes can be found in Sect. 6.1. The method relies on the detection process itself. For each pixel of the detection image, this approach checks whether the object would have been detected had it been centred on that pixel. This is done by comparing the local noise to the signal of the brightest pixels of the source used as input.

The method is based on `SExtractor`. To perform the source detection, `SExtractor` uses a set of parameters, the most important of which are the `DETECT_THRESH` and `MIN_AREA`. The first parameter corresponds to a detection threshold and the second to a minimal number of neighbouring pixels. `SExtractor` works on a convolved and background subtracted image called the filtered image. A source is only detected if at least `MIN_AREA` neighbouring pixels are `DETECT_THRESH` times above the background RMS map (shortened to only RMS map) produced from the detection image. This RMS map is the noise map of the background image also computed by `SExtractor`. The comparison between the filtered image and the RMS map is done pixel to pixel meaning that `filtered[x,y]` is compared to `RMS[x,y]`

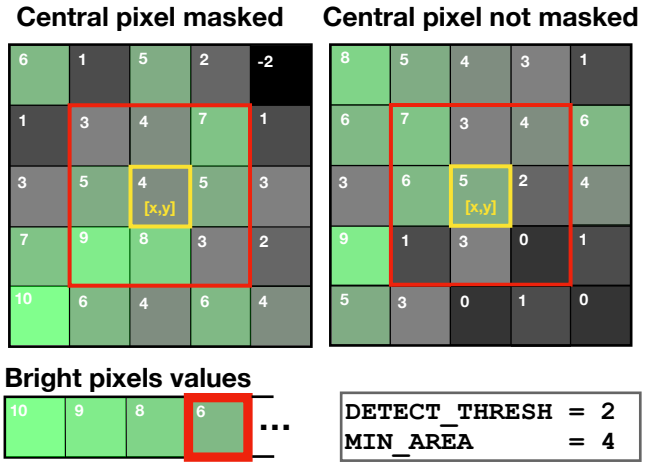

Fig. A.2. Illustration of the criterion used to create the mask. The grid represents part of an RMS map. To determine whether the central pixel [x,y] is masked or not, the bright pixels values shown on the bottom left are used; in this example, only the `MIN_AREA`-th pixel value = 6 is used to compare with the local noise. Considering the central pixel $[x, y]$, the comparison to the local noise is only done for the 9 pixels adjacent pixels (i.e. red square). The values used for the detection threshold and the minimal area in this example are 2 and 4, respectively. On the *left*, none of the pixels in the red area have values that are strictly less than `min(Bp)/DETECT_THRESH` = 3, which results in the central pixel being masked. On the *right panel*, three pixels fulfil the condition and the central pixel is not masked.

The detection mask computation method is based on the same two parameters: `DETECTION_THRESH` and `MIN_AREA`. From the filtered image, the procedure selects only the `MIN_AREA` brightest pixels of the source, (we call this list of values `Bp`) and compares these to the RMS map. The bright pixels profiles of our LAE sample are shown on Fig. A.1 for illustration purpose. This list contains all the information related to the spatial features of the input source needed by the method. The adopted criterion is close to that applied by `SExtractor` for the detection even though it is not, strictly speaking, the same:

- For each pixel `[x,y]` of the RMS map, a list of nine RMS pixels is created; the list contains the central RMS pixel and the eight connected neighbouring RMS pixel values. We call this list `local_noise[x,y]`.
- From the `Bp` list that contains the brightest pixel of the input source, `min(Bp)` is determined and only this value used for the comparison to `local_noise`. For the comparison, the following criterion is used: if any value in `local_noise[x,y]` fulfils the condition `min(Bp)/DETECT_THRESH` < `local_noise[x,y]`, then the pixel `[x,y]` is masked. In all of the other cases, the central pixel remains unmasked. This criterion is a bit looser than that used by SExtractor as the comparison is only done for `min(Bp)` and not for all the pixels. However assuming that the noise in a certain small area is not too drastically different, the `SExtractor` criterion and the criterion we use are still very close. If `min(Bp)` fulfils the criterion, is it very likely that the other bright pixels, who all have higher signal values, also fulfils the same criterion at some point on the nine pixel area.
- The operation is performed for each pixel of the RMS map.

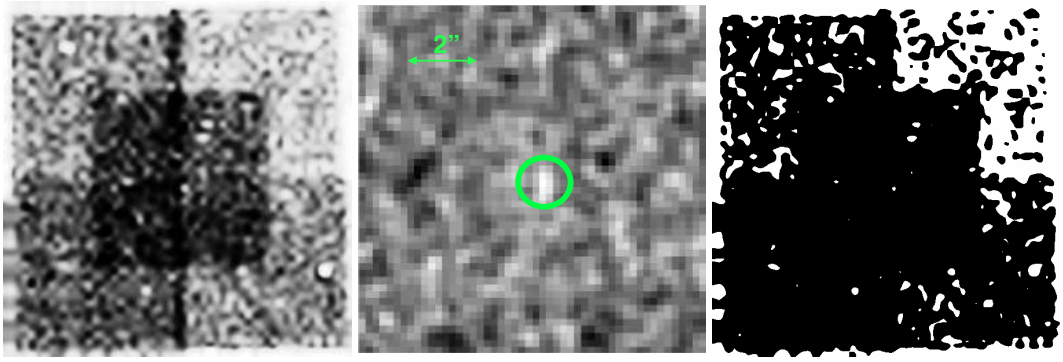

Fig. A.3. *Left panel*: example of RMS maps produced from one slice of the A2744 cube. The large-scale patterns are due to the different exposure times for the different parts of the mosaic. In the deepest part of this field, the noise is reduced because of a longer integration time. *Middle panel*: filtered image centred on one of the faint LAE in the A2744 field. The brightest pixels `Bp` were defined from this image. The size of the field is ∼10″. *Right panel*: mask produced by this method for the source shown in the middle panel, the masked pixels are shown in white. We can see on this image that the mask patterns closely follow the RMS map.

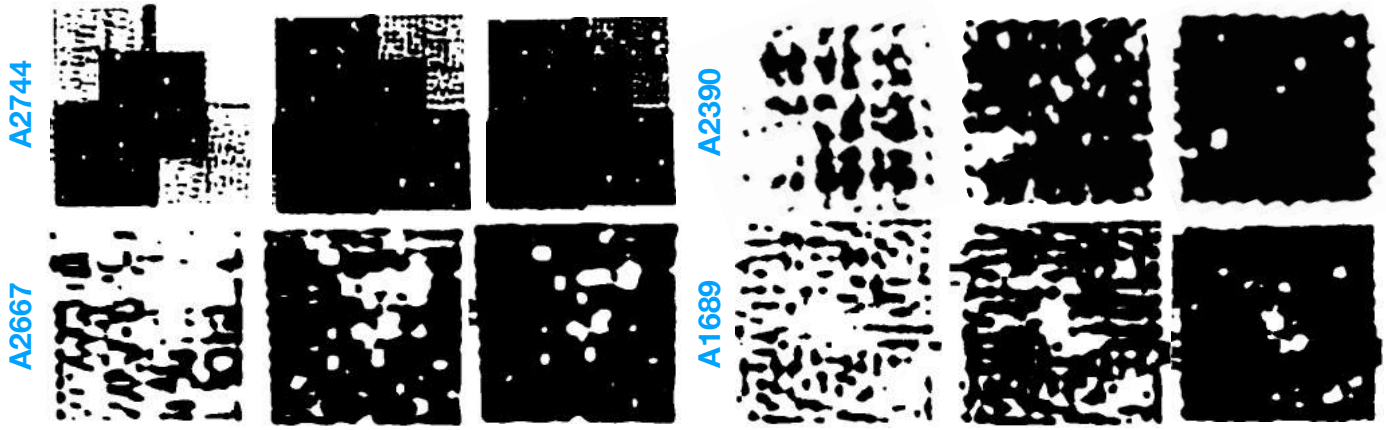

Fig. B.1. Representative examples of masks obtained in the different fields for different S/N values. The masked pixels are shown in white. For each field, the S/N values used to build the mask increase *from left to right*.

An example of application is given in Fig. A.2. In both cases, the lowest values of the bright pixel list are compared to the nine pixels in the area set by the red square. The lowest value of the `Bp` list is set to 6. Using `DETECT_THRESH` = 2, for the central pixel to be masked, none of the values in the red area must be strictly less than `min(Bp) / DETECT_THRESH` = 3. However, for the central pixel to remain unmasked, only one pixel in the red area has to be strictly less than 3, which is true for three pixels on the example on the right.

An example of RMS maps, filtered image, and mask produced for a given source is provided on Fig. A.3. The RMS and filtered maps are directly produced by `SExtractor`. The bright pixels determined on the filtered image are compared to the RMS map to produce the mask according to the method presented above.

This exercise can be used to simulate the detectability of a given source in an image completely independent of the input source. This is useful, for example, in the case of a survey that consists of different and independent FoVs. In that situation, the differences in seeing condition have to be accounted for when measuring the bright pixel profile of the source. This can be achieved through convolution or deconvolution of the original image of the source. An example of how the seeing affects the determination of the bright pixel profiles is shown on Fig. A.1.

Appendix B: Mask examples using median RMS maps

In this section we illustrate the results found when applying the method presented in Appendix A to the different cubes, for LAEs detected with different S/N values. A sample of representative masks is presented on Fig. B.1. These masks were used for masking the 3D cubes during the volume computation. They were created with the method described in Sect. 6.1.1, including a median RMS map for each data cube and a median bright pixel profile to be rescaled in agreement with the actual S/N of the source. The S/N values used to build the masks increase from left to right. We note that, in this case, this is not a real S/N but a proxy (see Sect. 6.1.1 for details).

We see that at lower S/N values, the masks are efficient to retrieve the instrumental patterns. At higher S/N values, these patterns disappear, and only the bright galaxies and the edge of the FoVs remain masked. For A2744, we see that the masks are very efficient to account for the difference in exposure time in the mosaic. The central quadrant of the mosaic, being the deepest, is mostly not masked, whereas the upper right quadrant, being the shallowest, is only unmasked for the highest S/N values.

Appendix C: Comparison of the different volume computation methods

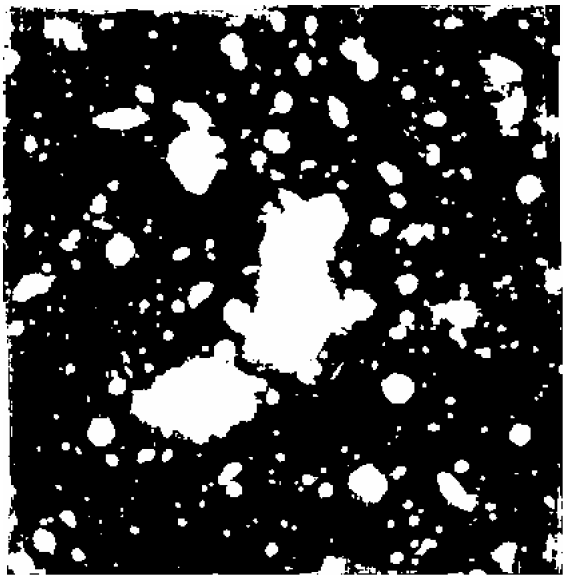

Fig. C.1. Mask of the A2744 FoV, created from a MUSE white light image of the cluster using a `SExtractor` segmentation map. The masked pixels are shown in white. This type of mask is mostly efficient to mask the brightest sources and haloes.

In this section we compare the results obtained when computing the $V_{\rm max}$ using the method adopted in this study to the classical integration based on a unique mask. We present in Fig. C.2 the comparison between the $V_{\rm max}$ values obtained from these two different methods. The first (on the y-axis) is used in this project, based on 3D masks, following the noise variation through the MUSE cubes. The second (on the x-axis) uses a mask generated from a unique `SExtractor` segmentation map, which is replicated across the spectral dimension. An example of such a mask is provided in Fig. C.1. It is mostly efficient to mask the brightest sources and haloes on the image. Comparing this mask to the masks presented in Fig. B.1, we see that they are completely different. Whereas the 3D masks adopted in this paper are able to follow the differences in exposure time while encoding the instrumental noise patterns, the simple masks provide a unique pattern for all sources, irrespective of their S/N values. This results in the following effects as seen in Fig. C.2: First, a unique mask translates into a unique $V_{\rm max}$ value for a large number of sources, as only the lensing effects play a role in the determination of $V_{\rm max}$. This corresponds to the vertical pattern on the right-hand side of Fig. C.2. Second, using the adaptive mask method, systematically lower $V_{\rm max}$ values are obtained. And more interestingly, for sources in A1689, A2390, and A2667, we see that the differences are less pronounced (or even not significant for some sources) than for the sources in the A2744 mosaic.

To explain the first point, it is important to understand that when using a single mask, the only factor that could influence the $V_{\rm max}$ value is the limit magnification $\mu_{\rm lim}$ (see Sect. 6.1.2). A source with a higher $\mu_{\rm lim}$ value would end up with a smaller $V_{\rm max}$ as the area of the survey with large magnification is smaller. For the bright sources of the sample, it could be that the computed $\mu_{\rm lim}$ would be under the lower magnification reached on the survey. For those sources, the volume was integrated on the entire survey area. Using the 3D mask method, $\mu_{\rm lim}$ still plays a role but it is no longer the only factor affecting the final volume value and the local noise level is properly taken into account.

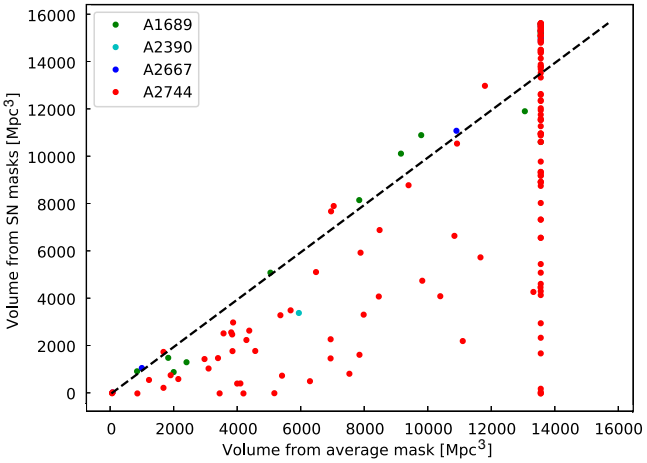

Fig. C.2. Comparison of the results of $V_{\rm max}$ computation using the average mask obtained from a unique `SExtractor` segmentation map (x-axis) and the 3D masks adopted in this paper, following the evolution of noise through the MUSE cubes (y-axis). See text for details.

To explain the second point and to illustrate the systematical difference between the two methods, we can consider a faint source detected in one of the deepest parts of the A2744 mosaic. When comparing the source to the noise level in the rest of the mosaic, the quadrants with the lower integration time end up being completely masked. As for the three other cubes, their contribution is zero as they have even less integration time. In that case, only a small portion of the mosaic has a significant contribution to the $V_{\rm max}$ value and it results in a low $V_{\rm max}$. However, all sources detected in A1689, A2390, or A2667 could have been detected anywhere in the A2744 mosaic. Because the A2744 FoV accounts for 80% of the total volume, only $\mu_{\rm lim}$ affects the final contribution of A2744, and the contribution of the smaller fields is not that significant. This explains the correlation between the two methods for the sources detected in the three shallower fields.

Appendix D: Detailed procedure for volume computation in lensed MUSE cubes

In this appendix, we provide an overview and a quick description of all the steps needed to compute $V_{\rm max}$. The details are explained in the main text. The goal of this section is to provide a synthetic view to explain the method. The numbers on the notes below refer to the steps listed in Fig. 6 as follows:

- (0) The NB cubes consist of all the NB images produced by `Muselet`. All LAEs were detected on those NB images. Details on those NB images are provided in Sect. 3.1
- (1.1) Background RMS maps produced separately by `SExtractor` and assembled into a RMS cube. The RMS cube are cubes of noise that are used to track the spectral evolution of noise levels in cubes.
- (1.2) Median of the RMS cubes along the spectral axis. One median RMS image is obtained per cube. They are used to mock the 2D `SExtractor` detection process.
- (1.3) Set of S/N values designed to encompass all possible values in the LAE sample. The definition used for S/N is provided in Eq. (3).

– (1.4) Using a generalized bright-pixels profile (see Fig. A.1) and the median RMS maps, a 2D detection mask is built for each value of the S/N set and for each cube; the method is described in Appendix A.
– (1.5) Redshift values used to sample the evolution of the source plan projections and magnification maps.
– (1.6) Source plan projection of the set of 2D masks combined with magnification maps for different redshift.
– (1.7) For each LAE, the final 3D survey masks are assembled from the set of source plane projections. The procedure browse the S/N curves (see Fig. 7, and picks the precomputed 2D source plane projection computed from the correct S/N value and the appropriate redshift value. Details on this can be found in Sects. 6.1.1 and 6.1.2).
– (1.8) Minimal magnification to allow the detection of a given LAE in its parent cube. This first value is computed from the error on the flux detection, which is indicative of the local noise level. See definition in Eq. (5).
– (1.9) A rescaled limit magnification (see definition in Eq. (6)) is computed for each LAE and for the three additional cubes. This is done to account for the differences in both seeing and exposure time. All the details about limiting magnification are explained in Sect. 6.1.2. For each LAE, the four $\mu_{\rm lim}$ values are used to restrict the volume computation to the areas of the source plan projection with a magnification high enough to allow the detection of this LAE.
– (1.10) Volume of the survey where a given source could have been detected. For one LAE, this volume is computed from the source plane projected 3D masks, on the pixels with a high enough magnification.
– (2.1) For each LAE, the NB containing the max of its Lyman-alpha emission is selected. The cleanest detection was obtained on this slice of the NB cube.
– (2.2) Filtered map produced with `SExtractor`. See Appendix A for details.
– (2.3) From the original filtered map produced for each LAE in the parent cube, three additional images are produced to the resolution of the additional cubes the LAE does not belong to using convolution or deconvolution.
– (2.4) Individual bright-pixel profiles are retrieved for the four different seeing conditions from the filtered images and the three additional images produced in the previous step. The bright-pixel profiles contain the information related to the spatial profile of the LAEs.
– (2.5) The four generalized bright-pixel profiles are the median of the individual bright-pixel profiles computed for each seeing condition (see Fig. A.1). These generalized profiles are used to limit the number of mask computed and simplify the production of 3D masks.
– (3.1) The noise level in cubes is an average measure of noise in a given slice of a cube. It is defined in Eq. (3) and an example is provided in Fig. 5.
– (3.2) Combining the definition of noise levels and the individual bright-pixels profiles, the evolution of S/N for individual sources is computed through the cubes with Eq. (4) (see Sect. 6.1.1 and Fig. 7).

Appendix E: Additional table

Table E.1. Main characteristics of the 152 LAEs used to build the LFs.

Id	z	F_{Ly_α} erg s^{-1} cm^2	μ	log(Ly$_\alpha$) erg s^{-1}	Comp	$V_{\max}$ Mpc^3	Ra °	Dec °
A1689, 619	3.0446	102.06 ± 6.27	$7.95^{+0.60}_{-0.25}$	42.01	73.3 ± 1.7	16015.9	197.874204	−1.351669
A1689, 1028	3.1109	119.36 ± 3.36	$26.83^{+2.80}_{-0.90}$	41.58	100.0 ± 0.0	15913.4	197.881592	−1.344253
A1689, LN9	3.1789	44.72 ± 3.75	$7.69^{+0.55}_{-0.52}$	41.71	96.4 ± 0.7	15946.6	197.875790	−1.349321
A1689, 1404	3.1800	11.99 ± 1.84	$5.90^{+0.22}_{-0.38}$	41.26	12.6 ± 1.5	15791.5	197.879760	−1.336681
A1689, 835	3.1806	27.48 ± 2.48	$11.84^{+0.66}_{-1.23}$	41.31	93.2 ± 1.0	15835.8	197.878000	−1.348089
A1689, LN10	3.4182	16.84 ± 1.36	$52.42^{+44.51}_{-10.64}$	40.53	99.4 ± 0.3	15698.1	197.870362	−1.347675
A1689, LN26	4.0541	9.44 ± 1.29	$8.51^{+0.54}_{-0.40}$	41.25	62.2 ± 2.0	15805.0	197.870413	−1.352380
A1689, LN13	4.0548	24.66 ± 1.82	$8.82^{+0.69}_{-0.66}$	41.65	98.1 ± 0.6	15943.8	197.871113	−1.349303
A1689, LN14	4.1038	19.34 ± 2.37	$5.66^{+0.35}_{-0.21}$	41.75	98.9 ± 0.5	15930.8	197.879200	−1.337292
A1689, LN25	4.8426	4.12 ± 0.66	$18.74^{+2.84}_{-1.65}$	40.73	38.9 ± 1.9	15509.8	197.869410	−1.348497
A1689, LN15	4.8668	5.75 ± 0.92	$4.92^{+0.38}_{-0.32}$	41.46	68.9 ± 1.8	15851.1	197.876460	−1.352164
A1689, 1379	4.8734	91.53 ± 2.22	$5.68^{+0.38}_{-0.18}$	42.60	99.9 ± 0.2	16352.6	197.877970	−1.336814
A1689, LN17	5.0117	4.46 ± 0.56	$8.28^{+0.46}_{-0.45}$	41.15	84.5 ± 1.4	15818.2	197.870830	−1.352020
A1689, LN18	5.7369	6.16 ± 0.83	$18.22^{+1.44}_{-1.22}$	41.08	50.1 ± 2.0	15711.5	197.880900	−1.345920
A1689, LN19	6.1752	6.98 ± 1.00	$7.49^{+0.24}_{-0.56}$	41.60	97.8 ± 0.7	15835.2	197.876070	−1.350196
A2390, L1	4.0454	207.18 ± 6.97	$19.81^{+1.22}_{-0.53}$	42.22	97.6 ± 0.9	15832.3	328.390790	17.701650
A2390, 96	4.0475	544.64 ± 6.51	$11.22^{+0.55}_{-0.33}$	42.89	99.2 ± 0.8	16246.7	328.396350	17.692954
A2390, 134	4.7210	16.75 ± 1.74	$24.27^{+3.28}_{-0.32}$	41.20	30.7 ± 2.5	15010.8	328.391020	17.697558
A2390, 71	4.8773	20.70 ± 1.97	$7.12^{+0.25}_{-0.24}$	41.85	99.4 ± 0.3	15810.7	328.400050	17.689222
A2390, 243	5.7574	2.69 ± 0.57	$21.33^{+1.26}_{-0.74}$	40.66	34.4 ± 2.5	13282.3	328.405510	17.698954
A2667, 24	3.7872	16.54 ± 1.52	$9.32^{+1.16}_{-0.34}$	41.38	99.2 ± 0.4	15732.7	357.917309	−26.082718
A2667, 25	3.7872	36.51 ± 2.85	$2.96^{+0.08}_{-0.06}$	42.22	89.4 ± 1.3	15869.4	357.906046	−26.078152
A2667, 30	3.9743	59.56 ± 3.40	$46.08^{+24.71}_{-6.34}$	41.29	94.2 ± 0.9	14522.8	357.920596	−26.079189
A2667, 33	4.0803	39.13 ± 3.63	$12.50^{+0.88}_{-0.49}$	41.70	96.1 ± 0.8	15696.9	357.910908	−26.080737
A2667, 38	4.9467	30.77 ± 3.07	$16.22^{+2.42}_{-1.04}$	41.68	85.2 ± 1.5	15368.8	357.919470	−26.082619
A2667, 41	5.1993	18.18 ± 1.30	$3.25^{+0.10}_{-0.07}$	42.20	99.9 ± 0.1	15939.4	357.906303	−26.078569
A2667, 62	5.5003	6.52 ± 1.16	$43.08^{+10.58}_{-4.85}$	40.69	88.1 ± 1.4	2002.1	357.906020	−26.091870
A2744, 8683	2.9315	25.86 ± 2.33	$3.22^{+0.12}_{-0.08}$	41.77	96.4 ± 0.8	15527.9	3.572765	−30.394612
A2744, 11626	2.9422	4.59 ± 0.93	$1.75^{+0.06}_{-0.03}$	41.29	68.5 ± 1.7	13744.9	3.606868	−30.385573
A2744, 5005	2.9513	9.71 ± 0.87	$18.10^{+1.63}_{-0.82}$	40.60	98.9 ± 0.5	11423.4	3.595135	−30.404478
A2744, 4010	2.9986	4.15 ± 1.34	$2.17^{+0.04}_{-0.04}$	41.17	21.9 ± 1.7	12801.1	3.575187	−30.407353
A2744, 10544	3.0211	2.41 ± 0.46	$2.95^{+0.10}_{-0.06}$	40.81	68.6 ± 1.9	13832.2	3.592539	−30.387649
A2744, M10	3.0213	2.06 ± 0.53	$2.11^{+0.04}_{-0.05}$	40.88	21.1 ± 2.0	12606.1	3.568189	−30.400041
A2744, M11	3.0234	1.34 ± 0.36	$3.48^{+0.07}_{-0.12}$	40.48	26.9 ± 2.1	13373.2	3.581978	−30.408336
A2744, M12	3.0337	4.00 ± 0.91	$2.34^{+0.05}_{-0.04}$	41.13	11.6 ± 1.5	12826.9	3.573038	−30.401722
A2744, 3424	3.0511	7.76 ± 1.00	$9.70^{+0.41}_{-0.55}$	40.81	95.4 ± 0.9	14816.9	3.593917	−30.409719
A2744, M24	3.0532	14.55 ± 1.16	$12.90^{+0.92}_{-0.73}$	40.96	99.8 ± 0.2	15480.4	3.590349	−30.410597
A2744, 11701	3.0543	18.54 ± 1.44	$4.80^{+0.12}_{-0.12}$	41.49	98.4 ± 0.5	15555.7	3.585514	−30.385878
A2744, 7858	3.1291	82.08 ± 4.02	$3.47^{+0.11}_{-0.08}$	42.31	100.0 ± 0.1	15869.5	3.574989	−30.396797
A2744, 7721	3.1295	138.50 ± 5.81	$2.78^{+0.10}_{-0.05}$	42.63	100.0 ± 0.0	15962.4	3.571429	−30.396950
A2744, 11196	3.1508	6.72 ± 1.55	$3.31^{+0.12}_{-0.09}$	41.25	53.1 ± 2.2	13573.4	3.578329	−30.383213

Notes. The value F_{Ly_α} is the detection flux of the LAE, expressed in 10^{-18} units, μ is the flux weighted magnification of the source, and the error bars correspond to the 68% asymmetric errors computed from $P\mu$,log Ly$_\alpha$ is the Lyman-alpha luminosity corrected for magnification. No error bars are associated with the luminosity value, as this uncertainty is accounted for during the MC iterations needed to build the LFs. "Comp" is the completeness expressed in percentage. The $V_{\max}$ value given in this table are computed for $2.9 < z < 6.9$.

C | A&A publication: de La Vieuville et al. 2019b

Astronomy & Astrophysics manuscript no. article_temp
September 30, 2019

MUSE observations towards the lensing cluster A2744: Intersection between the LBG and LAE populations at z∼3-7

G. de La Vieuville[1], R. Pelló[1], J. Richard[2], G. Mahler[3], L. Lévêque[1], F. E. Bauer[456], D. J. Lagattuta[2], J. Blaizot[2], T. Contini[1], T. Garel[7], H. Kusakabe[7], N. Laporte[3,1], J. Martinez[2], M. V. Maseda[9], D. Schaerer[7], K. B. Schmidt[8], and A. Verhamme[7]

[1] Institut de Recherche en Astrophysique et Planétologie (IRAP), Université de Toulouse, CNRS, UPS, CNES, 14 Av. Edouard Belin, F-31400 Toulouse, Francee-mail: gdelavieuvil@irap.omp.eu,rpello@irap.omp.eu
[2] Univ Lyon, Univ Lyon1, Ens de Lyon, CNRS, Centre de Recherche Astrophysique de Lyon (CRAL) UMR5574, F-69230, Saint-Genis-Laval, France
[3] Department of Astronomy, University of Michigan, 1085 S. University Ave., Ann Arbor, MI 48109, USA Department of Physics and Astronomy, University College London, Gower Street, London WC1E 6BT, UK
[4] Instituto de Astrofísica and Centro de Astroingeniería, Facultad de Física, Pontificia Universidad Católica de Chile, Casilla 306, Santiago 22, Chile
[5] Space Science Institute, 4750 Walnut Street, Suite 205, Boulder, Colorado 80301, USA
[6] Millenium Institute of Astrophysics (MAS), Nuncio Monseñor Sótero Sanz 100, Providencia, Santiago, Chile
[7] Observatoire de Genéve, Université de Genève, 51 Ch. des Maillettes, 1290 Versoix, Switzerland
[8] Leibniz-Institut für Astrophysik Potsdam (AIP), An der Sternwarte 16, D-14482 Potsdam, Germany
[9] Leiden Observatory, Leiden University, P.O. Box 9513, 2300 RA, Leiden, The Netherlands

Received ; accepted

ABSTRACT

We present a study of the intersection between the populations of star forming galaxies (SFGs) selected as either Lyman break galaxies (LBGs) or Lyman-alpha emitters (LAEs) in the redshift range $2.9-6.7$, within the same volume of universe sampled by the Multi-Unit Spectroscopic Explorer (MUSE) behind the Hubble Frontier Fields lensing cluster A2744. We define three samples of star-forming galaxies: LBG galaxies with an LAE counterpart (92 galaxies), LBG galaxies without LAE counterpart (408 galaxies) and LAE galaxies without an LBG counterpart (46 galaxies). These galaxies are intrinsically faint due to the lensing nature of the sample ($M_{1500} \geq$-20.5). The fraction of LAEs among all selected star-forming galaxies increases with redshift up to $z \sim 6$ and decreases for higher redshifts, in agreement with previous findings. The evolution of these two populations with UV magnitude and Lyα luminosity shows that the the LAE selection is able to identify intrinsically UV faint galaxies with $M_{1500} \geq$-15 that are typically missed in the deepest lensing photometric surveys but that the LBG population seems to fairly represent the total population of star-forming galaxies down to $M_{1500} \sim -15$. Galaxies with $M_{1500} < -17$ tend to have $SFR_{Ly\alpha} < SFR_{uv}$, whereas the opposite trend is observed for faint galaxies with $M_{1500} > -17$, including galaxies only detected by their Lyα emission. The same trend is observed for galaxies with redshifts below and above $z \sim$5, suggesting an evolution in the relative escape fraction $f_{Ly\alpha}/f_{UV}$. There is no clear evidence, based on the present results, for an intrinsic difference on the properties of the two populations selected as LBG and/or LAE. The observed trends could be explained by a combination of several facts, like the existence of different star-formation regimes, the dust content, the relative distribution and morphology of dust and stars, or the stellar populations.

Key words. galaxies: high-redshift – cosmology: dark ages, reionization, first stars

1. Introduction

Intrinsically faint star-forming galaxies (hereafter SFGs) are presently considered as the main sources responsible for cosmic reionization. Ultra-deep photometry obtained by the *Hubble Space Telescope* (*HST*) on blank fields combined with ground-based photometry and spectroscopy has fundamentally improved our knowledge of the galaxy UV Luminosity Function (LF) up to $z \sim 10$ (see e.g. Bouwens et al. 2004; McLure et al. 2013; Bouwens et al. 2015b; Finkelstein et al. 2015, and the references therein). The integration of the UV LF is used to derive the evolution of the cosmic star-formation density, and the density of ionizing radiation (usually assuming a constant star-formation rate), while the two key parameters being the slope of the faint-end of the LF and the faint-end integration limit (see e.g. Bouwens et al. 2015a). Up to $z \sim$7, current observations reach as deep as $M_{1500} \sim -17$ in blank fields, that is about three magnitudes brighter than the faint-end UV luminosity limit which is needed to reionize the universe at $z \sim$ 6-7. Using lensing clusters as gravitational telescopes makes it possible to reach $M_{1500} \sim -15$ at $z \sim$7 therefore improving our constraints on the contribution of SFGs to reionization (See for example the work done in Atek et al. (2015) and Livermore et al. (2017) using data from the *Hubble Frontier Fields* (HFF) project (Lotz et al. 2017)).

However, the ability of SFG to reionize the universe depends not only on the faint-end slope of the UV LF (and its actual shape) and the faint-end integration limit, but also on the escape fraction of ionizing radiation. In addition, most samples used for this exercise, either in blank fields or in lensing fields, are photometrically selected and have few if any spectroscopic redshifts available. The interrelation between the different SFG

populations, selected as Lyman-Break Galaxies (LBGs) or Lyman Alpha Emitters (LAEs), has not been studied extensively in the same volume of the universe due to observational limitations. The same holds for the relative escape fractions of Lyα and UV photons (i.e., the ability of observed quantities such as Lyα and rest-frame UV fluxes to trace the ionizing radiation and noted hereafter $f_{\mathrm{Ly}\alpha}$ and f_{uv}). Recent pioneering studies have started to address this issue in blank fields, such as Arrabal Haro et al. (2018) using the SHARDS Survey of the GOODS-N field, based on deep imaging survey using 25 medium band filters or Inami et al. (2017) and Maseda et al. (2018), both based on ultra-deep IFU data on the *Hubble Ultra Deep Field* (HUDF) from MUSE (the Multi-Unit Spectroscopic Explorer Bacon et al. 2010, 2017).

In this paper, we investigate the intersection between the populations of SFGs selected as LBGs and LAEs in the range $2.9 < z < 6.7$, within the same volume of universe sampled by MUSE behind the HFF lensing cluster Abell 2744 (hereafter A2744). For the first time, such a combined survey is performed behind a lensing cluster, using the deepest images available from the HFF. Taking advantage of the magnification provided by the lensing cluster, the survey reaches an average depth of $M_{1500} \sim -15$ and probes galaxies as faint as $M_{1500} \sim -12$ in some areas, and Lyα luminosities in the range $40 \lesssim \log(L_{Ly\alpha}) \lesssim 43$. We investigate the prevalence of Lyα emission among the faintest LBG population ($M_{1500} > -20.25$), as well as the relationship between Lyα and UV luminosity. In Sect. 2 we briefly describe the relevant MUSE and HFF data available for this study. Sect. 3 presents the selection of LBG and LAE samples at $z \sim$ 3-7 behind A2744. The results on the intersection of LBG and LAE populations are presented and discussed in Sect. 4. Conclusions are given in Sect. 5.

The cosmology adopted throughout this paper is $\Omega_\Lambda = 0.7$, $\Omega_m = 0.3$ and $H_0 = 70$ km s^{-1} Mpc^{-1} All magnitudes are given in the AB system (Oke & Gunn 1983).

2. MUSE and HFF data of A2744

MUSE integral-field observations of A2744 were carried out as part of the MUSE Guaranteed Time Observing (GTO) program on lensing clusters (GTO Program 094.A-0115; PI: Richard) (see Mahler et al. 2018; de La Vieuville et al. 2019, for additional information.) The field observed was a 2×2 MUSE mosaic covering the entire multiple-image area, with exposure times ranging between 3.5 and 5 hours per pointing, plus a central pointing with 2 additional hours of exposure centered at α=00:14:20.95 δ=-30:23:53.9 (J2000). All details regarding MUSE data reduction, source detection process and mass model construction can be found in Mahler et al. (2018). Throughout this study we use the gold mass model presented in Table 4 of Mahler et al. (2018) which has an average RMS of multiple images in the image plane of 0.67″. The MUSE catalogue includes 171 LAEs [1] before multiple image removal, with redshift in the range $2.9 < z < 6.7$. All LAEs were detected with MUSELET[2], a detection software for emission lines in MUSE cubes. Table 1 summarizes the effective lens-corrected volume surveyed by the MUSE observations behind A2744. The detection flux of the LAEs are measured with SExtractor (Bertin & Arnouts 1996) using `MAG_AUTO`, on continuum subtracted NB images manually adjusted to the spectral width of each LAE. The entire method and its motivations are explained in Sect. 3.2 of de La Vieuville et al. (2019).

[1] publicly available at `http://muse-vlt.eu/science/a2744/`

[2] MUSELET is part of the python MPDAF package (Piqueras et al. 2017)

The selection of LBGs in this field is based on the HFF observations of A2744 (ID: 13495, P.I: J. Lotz). Seven filters are available for Hubble Space Telescope data, three from the Advanced Camera for Surveys (ACS: F435W, F606W, F814W), and four from the Wide Field Camera 3 (WFC3: F105W, F125W, F140W, and F160W). In this study we use self-calibrated data provided by STScI (version v1.0 for WFC3 and v1.0-epoch2 for ACS), with a pixel size of 60 mas. The full MUSE mosaic is contained within all these seven HFF bands. We used the photometric catalog released by Astrodeep (Merlin et al. 2016; Castellano et al. 2016), which also includes imaging from VLT/Hawk-I K-band and the first two *Spitzer*/IRAC bands. For each of the seven *HST* filters, both the intra-cluster light (ICL) and bright-cluster galaxies (BCGs) were modeled and subtracted. The photometry was measured on these processed images with SExtractor (Bertin & Arnouts 1996), with PSF matching techniques using high spatial resolution images as priors for the source segmentation. The complete procedure is detailed in Merlin et al. (2016). The complete catalogue has 3587 entries for the entire A2744 lensing field, of which 2596 are detected in the F160W image, a further 976 are detected in a weighted stack of F105W, F125W, F140W and F160W and undetected in F160W alone, and 15 are BCGs. Note that the Astrodeep catalog is NIR-selected by construction, and this fact could have some implications on the subsequent results.

Before any comparison with the MUSE source catalogue, the entire Astrodeep catalogue was filtered to remove untrustworthy photometry points and/or sources. Since VLT/Hawk-I, IRAC 1 and IRAC 2 have larger PSFs than the *HST* filters, the photometry computed in these three bands is more often contaminated by nearby galaxies. Following the flags given in the catalogue, all photometric entries likely to be affected by this effect (indicated by flag COVMAX; see Merlin et al. (2016)) were given an upper detection limit in these filters when computing photometric redshifts. We also removed 220 sources flagged as likely residuals of the foreground subtraction (SEXFLAG > 16 and VISFLAG > 1). Finally, the catalogue was cut to the exact MUSE FoV, leading to a final selection of 2666 sources detected in the Astrodeep catalogue within the MUSE mosaic.

In order to build a single coherent catalogue, a cross match was performed between the remaining 2666 Astrodeep sources and the 171 LAEs of the MUSE catalogue, using a matching radius of $r = 0.8''$ (4 MUSE pixels). In case several entries are pointing towards the same source, only the closest match is kept. The difference in morphology between the UV and Lyα emission (see e.g. Leclercq et al. 2017; Wisotzki et al. 2018) and the distortions induced by lensing are likely to be the dominant causes of mismatch. For this reason, all LAEs and their closest Astrodeep counterpart were manually inspected to confirm or reject the match. In the case of multiple-image systems, it is always possible to select the less ambiguous image of the system when assembling the final sample (see below). At the end of the matching process, the merged catalogue contains 2724 galaxies of which 113 are seen in both the MUSE and Astrodeep catalogue, and 58 are LAEs with no detected UV counterpart in the Astrodeep catalogue.

3. Selection of LBG and LAE galaxies at z∼2.9-6.7

Two different methods were used to select LBG galaxies in this field among the sources detected by Astrodeep in the MUSE field of view: the usual three-band dropout technique applied to HFF data, and a method based on pure photometric redshifts and probability distributions. For the dropout, we adopted the

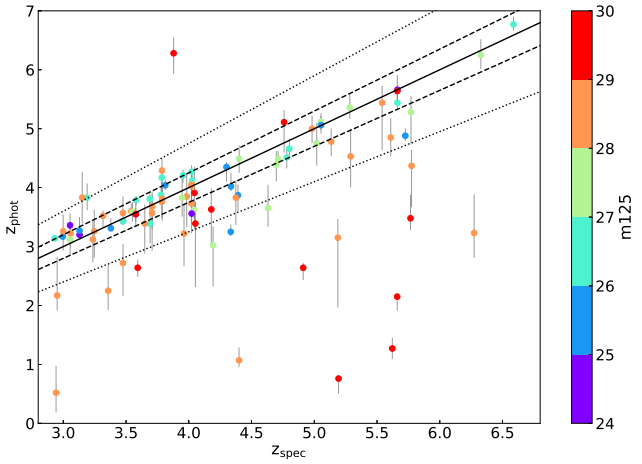

Fig. 1. Comparison between photometric and spectroscopic redshifts for galaxies spectroscopically confirmed at z ~3-7. Long-dashed and dashed lines display the locus of $z_{\rm phot} = z_{\rm spec} \pm 0.05(1+z)$ and $\pm 0.15(1+z)$ respectively, and solid black line is the one-to-one relation. Colors encode the observed magnitudes in the F125W filter, showing that a vast majority of galaxies with poor photometric redshifts have m(F125W) $\geq$ 28.

same criteria as proposed by Bouwens et al. (2015b) for the selection of galaxies at z ~3.8, 4.9, 5.9, and 6.8. For the latter, galaxies with photometric redshifts higher than $z \geq$2.9 and integrated probability distributions $P(z > 2.9) > 0.6$ were selected as LBGs. In all cases, a S/N higher than 3σ was required at this stage in at least one of the filters encompassing the rest-frame UV.

For all Astrodeep entries in the final catalog presented in Sect. 2, and even though photometric redshift are already published by the Astrodeep collaboration, we used SED fitting technique to compute their photometric redshift and their redshift probability distribution (noted $P(z)$). This is done in the range z =[0,8] with the code *New−Hyperz*[3], originally developed by Bolzonella et al. (2000). This method is based on the fitting of the photometric Spectral Energy Distributions (SED) of galaxies. The template library used in this study includes 14 templates: eight evolutionary synthetic SEDs from the Bruzual & Charlot code (Bruzual & Charlot 2003), with Chabrier IMF (Chabrier 2003) and solar metallicity; a set of four empirical SEDs compiled by Coleman et al. (1980); and two starburst galaxies from the Kinney et al. (1996) library. Internal extinction is considered as a free parameter following the Calzetti et al. (2000) extinction law, with A_V ranging between 0 and 1.0 magnitudes, and no prior in luminosity. The quality of photometric redshifts is assessed by directly comparing the results for the galaxies with known spectroscopic redshifts in the LBG sample. Outliers are defined as sources with $|z_{\rm spec} - z_{\rm phot}| > 0.15(1 + z_{\rm spec})$. The average accuracy reached excluding outliers is $\Delta z/(1+z) = -0.011 \pm 0.053$, with a median at $\Delta z/(1+z) = 0.001$. As seen in Fig. 1, the vast majority of galaxies with poor photometric redshifts have m(F125W) $\geq$ 28 (or a S/N <5 in this filter). It is also worth noticing that good photometric redshifts could be obtained for galaxies with $z \gtrsim 2.9$, that is fully covering the redshift domain where the Lyα line can be detected by MUSE.

Given the trends found for the quality of photometric redshifts computed with *New−Hyperz*, a S/N higher than 5 was requested in at least one of the seven *HST* filters for sources with no spectroscopic redshifts. For galaxies with spectroscopic confirmation, no S/N criterion was imposed. Using this blind photometric redshift procedure, 536 galaxies are selected as LBGs.

For comparison, the three-band dropout technique selects 383 objects, all of them included within the sample obtained with blind photometric redshifts, with only ten exceptions. Inspection of these ten objects revealed that they have either unreliable photometric points, resulting in poorly constrained or undefined photometric redshift, or that they have $z_{\rm phot} \sim 2.9$ with a large part of their $P(z)$ under the $z = 2.9$ threshold, therefore failing the $P(z > 2.9) \geq 60\%$ criterion.

Because we want to be as inclusive as possible in our selection, only the galaxies selected from their UV continuum and photometric redshift are considered in the rest of this work. For the sake of simplicity, we will continue using the term "LBG" to refer to this photo-z sample. And even though the presence of a break is not strictly required in our selection, it remains the main feature picked up by *New−Hyperz* to compute the photometric redshift for most of our galaxies.

Finally, all images were inspected to identify multiple systems. For LAEs, a robust identification of multiple systems is already provided in the MUSE catalogue. For LBGs with no LAE counterparts, the identification of multiple system is done using Lenstool (Kneib et al. 1996; Jullo et al. 2007; Jullo & Kneib 2009) and the predictions of the mass models presented in Mahler et al. (2018). Therefore, for all identified multiple image systems for both LAEs and LBGs we only keep one object counterpart, to avoid including objects twice in our analysis. In case one LAE image of a system matches with an UV counterpart and the other(s) do not, the one with the UV counterpart is kept.

4. The intersection between LBG and LAE populations

The following samples are defined in the MUSE field behind A2744 after the selection process and multiple image removal presented in Sect. 3:

- Sample 1: LBG galaxies with Lyα emission (hereafter LBG + LAE). 92 galaxies are included in this sample.
- Sample 2: LBG galaxies without Lyα emission, including 408 galaxies with only photometric redshift.
- Sample 3: LAE galaxies without an LBG counterpart. This sample includes 46 galaxies.

Fig. 2 displays the different populations selected in this field overlaid on a false color image of A2744. In practice, the matching between the centroids of LBG and LAE galaxies is usually better than 0.1″(average value in the LBG + LAE sample). In the selection above, one concern is that some galaxies would be seen as pure LAEs because their Lyα emission can be detected by MUSE overlaid on some bright foreground galaxy, whereas their UV continuum cannot be detected. Such identification of pure LAEs would be completely artificial as it would not be representative of the intrinsic properties of the source but only of the foreground contamination. The risk has been limited by the selection of the most representative image in multiple-imaged systems (when possible), as explained in Sect. 3. Indeed, as displayed in Fig. 2, none of the pure LAEs (red circles) falls on top of a bright foreground galaxy that would prevent the detection of an underlying UV continuum.

In order to determine the values of the UV continuum, in particular the Lyα continuum and the absolute magnitudes

[3] http://userpages.irap.omp.eu/~rpello/newhyperz/

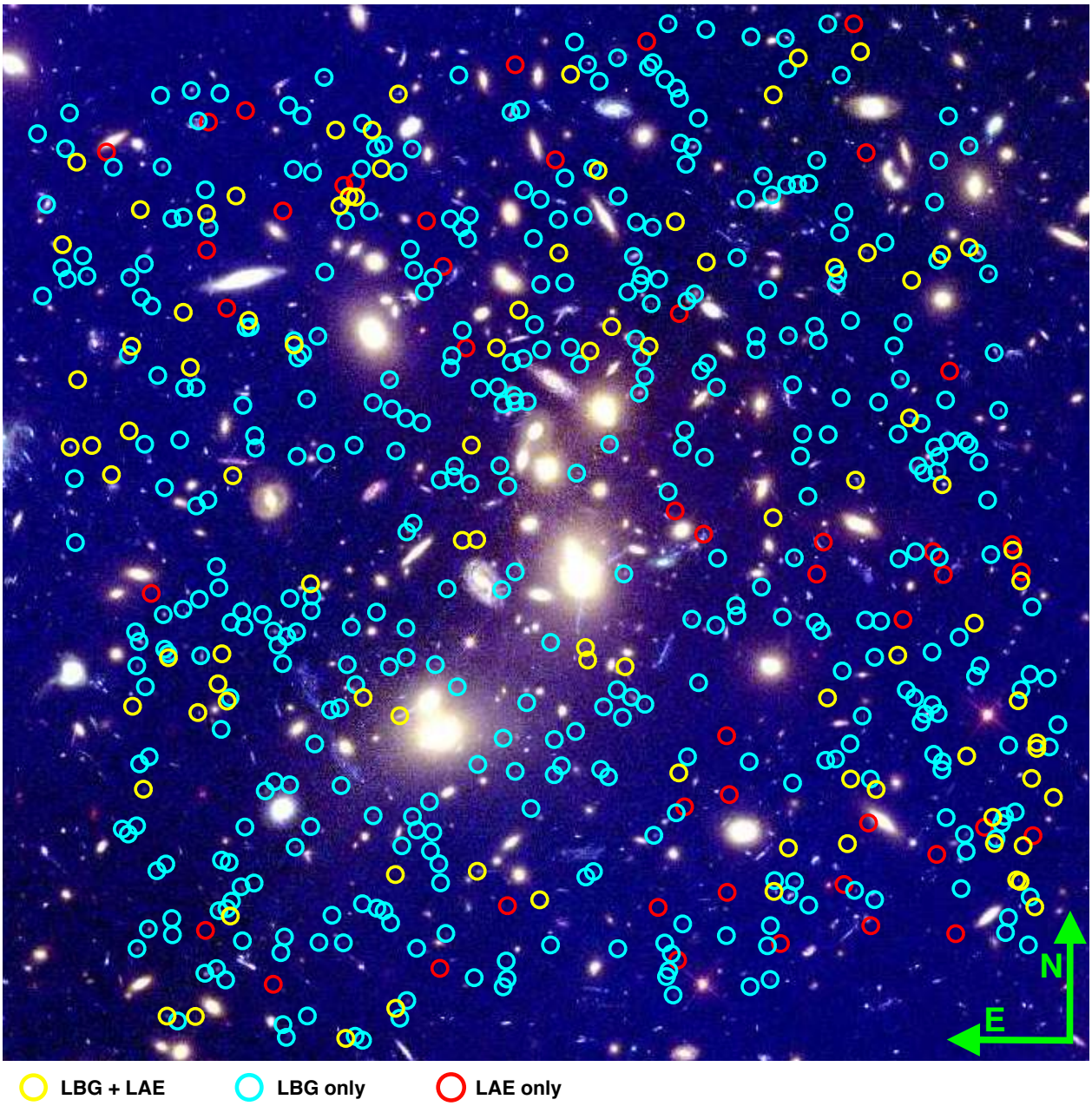

Fig. 2. False-color image of A2744 showing the area covered by the MUSE observations, obtained by combining the following HFF filters: F435W (blue), F606W (green) and F814W (red). The different populations selected in this field at $2.9 < z < 6.7$ are displayed as follows: LBG without LAE counterpart in cyan (408), LBG with LAE counterpart in yellow (92) and LAE without LBG counterpart in red (58). Cricles are 1.5″in diameter.

M_{1500}, a SED-fitting process was adopted using star-forming and young star-bursts templates (age <1Gyr) extracted form the Starbursts99 library (Leitherer et al. 1999). To estimate the uncertainty on both the Lyα continuum and M_{1500}, we performed Monte Carlo (MC) iterations by drawing the photometry points within their error bars and iteration of the SED-fitting process. In practice, for sources without spectroscopic redshifts, *New−Hyperz* was run two times: the first time to determine the best photometric solution and $P(z)$ as described in Sect. 3, and a second time using the results of the first run to fix the best-fit redshift and perform the MC iterations. When comparing the blind photo-z obtained during the first pass to the one derived with the Starbursts99 library of templates (leaving the full redshift range free), they are found to be in full agreement for all galaxies selected as LBGs. For sources with spectroscopic redshifts, the redshift was fixed to the spectroscopic value during MC iterations.

For the galaxies selected as both LAE and LBG, it is possible to compute their $EW_{Ly\alpha}$ using their detection flux and the Lyα continuum measured from the best-fit SEDs. For galaxies selected as pure LAEs and pure LBGs, only lower and upper limits of the $EW_{Ly\alpha}$ can be determined respectively. The evolution of the rest frame $EW_{Ly\alpha}$ with redshift for the three samples is presented in Fig. 3. Since the magnification affects both the continuum and the Lyα emission in the same way, no additional correction is needed. For the LBG with no LAE counterpart of Sample 2, the upper limit of their Lyα emission is determined assuming a constant limiting flux of $F(Ly\alpha) = 1{\times}10^{-18}$ erg cm^{-2} s^{-1}. This conservative estimate corresponds to the flux

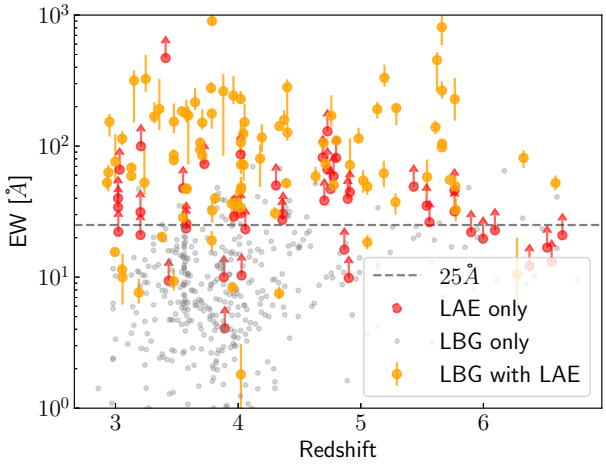

Fig. 3. Redshift distribution of the rest-frame EW for Lyα emission in the three samples. For the LBG without LAE counterpart in grey, the values are upper limit and the error bars have been omitted for clarity. The dashed horizontal line corresponds to $EW_{Ly\alpha}$ =25 Å.

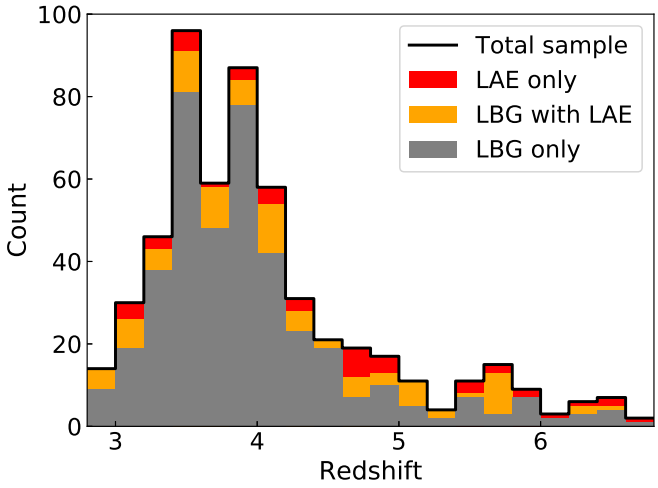

Fig. 4. Redshift distribution of the three samples defined in this study.

limit above which more than 90% of the LAEs detected behind A2744 are found.

4.1. Evolution with redshift

Redshift histograms for the three samples considered in this study are shown stacked on top of each other in Fig. 4. Table 1 displays the same information but with the redshift bins used in de La Vieuville et al. (2019) for the computation of the LAE LF. As seen in the Table and figure, the proportion of LAEs (i.e. LBG + LAE and LAE only) among SFGs increases with redshift.

Using Sample 1 and 2 (LAE + LBG and LBG only) it is also possible to compute the fraction of LAEs with $EW_{Ly\alpha}$ > 25Å among our UV-selected sample, noted X_{LAE}. This fraction, used to express the prevalence of LAEs among the LBG population, is often divided into two populations: galaxies with M_{1500} < −20.25 and galaxies with M_{1500} >-20.25 (see e.g. Stark et al. 2011; Pentericci et al. 2011; Arrabal Haro et al. 2018). Because of the lensing nature of the present sample, it is mostly dominated by faint galaxies and 98% of the sample falls within the M_{1500} > −20.25 domain. The limit $EW_{Ly\alpha}$ =25 Å is shown in Fig. 3 and again most of our LAE sample falls above that limit. The LAE fraction is computed from Sample 1 and 2 with the cuts in both $EW_{Ly\alpha}$ and UV magnitude described above. The results are presented with and without completeness correction for the LAE selection in Fig. 5 using the following redshift bins: $2.9 < z < 4.0$, $4.0 < z < 5.0$, $5.0 < z < 6.0$ and $6.0 < z < 6.7$. This binning was adopted to reach enough statistics in each bin and to easily compare with previous results, in particular around the z ~6 epoch.

The completeness of the LAE election is done using the method presented in de La Vieuville et al. (2019). The individual maximum covolume of detection of each LAE is determined in the A2744 cube and is noted $V_{max,i}$. This computation is done in the source plane, simulating the detectability of individual LAEs across numerous spectral layers (or monochromatic layers) and restricting the computation to the spatial areas where the magnification field is high enough to allow the detection of the LAE. An additional correction noted C_i is considered to account for the fact that the LAE does not have a 100% chance of being detected on its own spectral layer, due to the random variation of noise across the spatial dimension of the layer. This C_i takes values in the range 0 - 1 and is computed on the detection layer of individual LAEs by injecting their own detection profile multiple times across the FoV and trying to recover it. All the technical details related to the computation of $V_{max,i}$ and C_i can be found in de La Vieuville et al. (2019).

The factor $1/C_i V_{max,i}$ gives a numerical density for one LAE. To compute a correction from this numerical density, two additional quantities are introduced: the limit magnification noted μlim, i and $V(> \mu)$. The limit magnification is the magnification value under which the S/N of a given LAE drops under one and represents the minimum value of magnification for a specific LAE to be detected. The second one is the volume of observation explored above a given magnification, computed from the source plane. For each LAE, its corrected contribution to X_{LAE} is given by:

$$N(\mathrm{LAE})_{\mathrm{corr,i}} = \frac{V(> \mu_{\mathrm{lim,i}})}{C_i V_{\mathrm{max,i}}}. \quad (1)$$

The term $V(> mu\mathrm{lim, i})$ is the volume of observations above a given amplification (i.e. neglecting the effects of the spectral variations of noise across the layers of the cube) and is used to normalize the intrinsic numerical density of the LAE. The point of such a normalization is that the background volume explored varies strongly depending on the magnification regime considered as faint sources can only be detected within the highly magnified regions. The correction of all LAEs with $N(\mathrm{LAE_{corr,i}}) \geq> 10$ is neglected as it is estimated as untrustworthy. The fraction X_{LAE} is computed using both the corrected and uncorrected number of LAEs, and in both cases, no correction is performed for the UV selected population. Only the Poissonian uncertainties are considered for the error propagation of X_{LAE}.

The present results are compared to the ones derived by previous authors, namely Stark et al. (2011); Pentericci et al. (2011); Treu et al. (2013); Schenker et al. (2014); Tilvi et al. (2014); De Barros et al. (2017); Arrabal Haro et al. (2018). As expected, the present determination of X_{LAE} increases from z = 3.5 to z = 5.5 and drops for z >6, which can be interpreted as an increase in the neutral fraction of hydrogen. Our corrected points are most consistent with the determination of X_{LAE} from Arrabal Haro et al. (2018). Even though all of our corrected points are roughly

Table 1. Table summarizing the interrelation between the LAE and LBG populations. Numbers in boldface are absolute number of detections, and uncertainties correspond to the Poissonian error count.

	$2.9 \leq z \leq 6.7$	$2.9 \leq z \leq 4.0$	$4.0 \leq z \leq 5.0$	$5.0 \leq z \leq 6.7$
Effective Volume (Mpc^3)	13 361	4 546	3 638	5 177
Sample 1: LBG with LAE	**92±9.6**	**43±6.6**	**27±5.2**	**22±4.7**
	16.9±1.7%	13.2±2.0%	18.0±3.5%	32.8±7.0%
Sample 2: LBG only	**406±20.1**	**286±16.9**	**105±10.2**	**33±5.7**
	74.6±3.7%	81.9±5.2%	70.0±6.8%	49.2±8.5%
Sample 3: LAE only	**46±6.8**	**16±4.0**	**18±4.2**	**12±3.5**
	8.4±1.2%	4.9±1.2%	12.0±2.8%	17.9±5.2%
Total	**544±23.3**	**327±18.1**	**150±12.2**	**67±8.2**

consistent to 1σ level with the other values from the literature, it appears that the two lower redshift points tend to be below previous estimates. Several factors may explain this observed trend:

- Because of the lensing nature of the present sample, the volume probed is small, only $\sim$ 13 360 Mpc^3 are explored in the range $2.9 < z < 6.7$, and the cosmic variance has therefore a high impact on the observed statistics. This additional uncertainty is not shown in the error bars.
- There is clearly a difference in the selection processes with respect to previous studies. Here we use both broad-band photometry and IFU observations. The combination of these two methods ensures that we are as unbiased as possible in both the LBG and LAE selection in the same volume, range of magnitude and Lyα luminosity. All LAEs with a detected continuum are included in sample 1, event if this detected continuum has a lower S/N that would not have allowed it to pass the photometric selection required for the pure LBGs of sample 2. This is not the case in two-step surveys. For example, Stark et al. (2011) used multi-object spectroscopy to derive the prevalence of LAEs among the photometrically pre-selected LBG population (see Stark et al. 2010); therefore, they are likely missing all LAEs with the faintest continuum counterparts. On the contrary, Arrabal Haro et al. (2018) used the 25 medium bands of the SHARDS survey to select both the LBG and LAE populations. Theses observations have an average depth of m = 26.5 - 29 magnitude and an average spectral resolution of $R \sim 50$. They are therefore mostly sensitive to UV-brighter galaxies and higher $EW_{Ly\alpha}$, but are able to probe a much larger area. In this regard, this present study is complementary to their findings.
- Finally, we get $\sim$ 40% more objects using a photo-z selection compared to a more traditional colour-colour selection (see beginning of Sect. 3). This selection effect tends to lower our measurement of X_{LAE} compared to previous studies, but ensures that we have a more inclusive assessment of the high redshift SFGs.

4.2. Evolution with UV magnitude and Lyα luminosity

The main results of this study are summarized in Fig. 6 which shows the three samples on a plot presenting the Lyα luminosity in log-scale versus M_{1500}. The two values have been corrected for magnification but not for dust extinction. UV magnitude and Lyα luminosity histograms of the three samples are also provided on the side. Only galaxies in Sample 1 have both their Lyα luminosity and UV magnitude measured. For the pure LBGs,

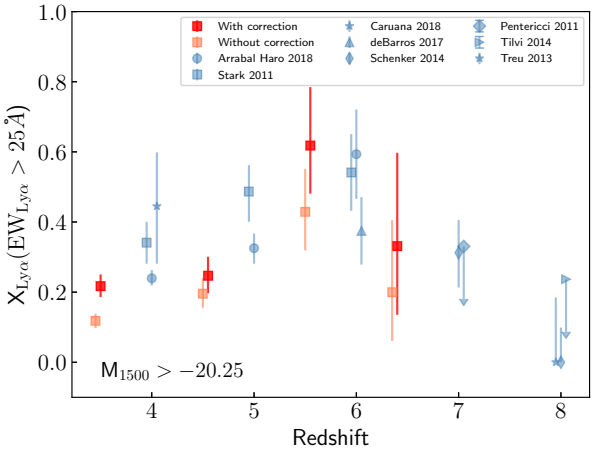

Fig. 5. Fraction of LAEs with $EW_{Ly\alpha} > 25$Å among the UV selected galaxies with $M_{1500} > -20.25$. This fraction is computed from galaxies in Samples 1 and 2. For clarity, a small redshift offset is applied to the points centered on the same redshift value.

the same limit of $F(Ly\alpha) = 1{\times}10^{-18}$ erg cm^{-2} s^{-1} already introduced for the $EW_{Ly\alpha}$ computation is used. The corresponding Lyα luminosity is obtained correcting for magnification and using the photometric redshifts. In a similar way, for pure LAEs of Sample 3, a (monochromatic) detection limit of $1.5{\times}10^{-21}$ erg cm^{-2} s^{-1} Å^{-1} is used for the continuum, assuming a flat spectrum, which is then transformed into absolute magnitude by taking into account the magnification and spectroscopic redshift. The detection limits used in the continuum correspond to a 3σ level for the best/deepest regions in *HST* data, that is, taking the maximum exposure time in a region free from BCG contamination. This simple scheme provides some interesting information about the position of galaxies in Sample 2 and 3 as compared to Sample 1 in Fig. 6.

Regarding the star formation rate (SFR), Fig. 6 also displays the locus of the $SFR_{Ly\alpha} = SFR_{uv}$ for a constant star-formation system. This relation was computed using the standard conversion in Kennicutt, Jr. (1998) for $SFR_{Ly\alpha}$, and the common conversion also given in Kennicutt, Jr. (1998) based on a Salpeter IMF for the SFR_{uv}. Since none of the values presented in Fig. 6 have been corrected for dust absorption, this constant star-formation line also represents the locus where the escape fraction for Lyα photons is the same as for UV photons ($f_{Ly\alpha} = f_{uv}$). Regarding the total ionizing flux density (or the Star Formation Rate density, SFRD), it means that objects along this line

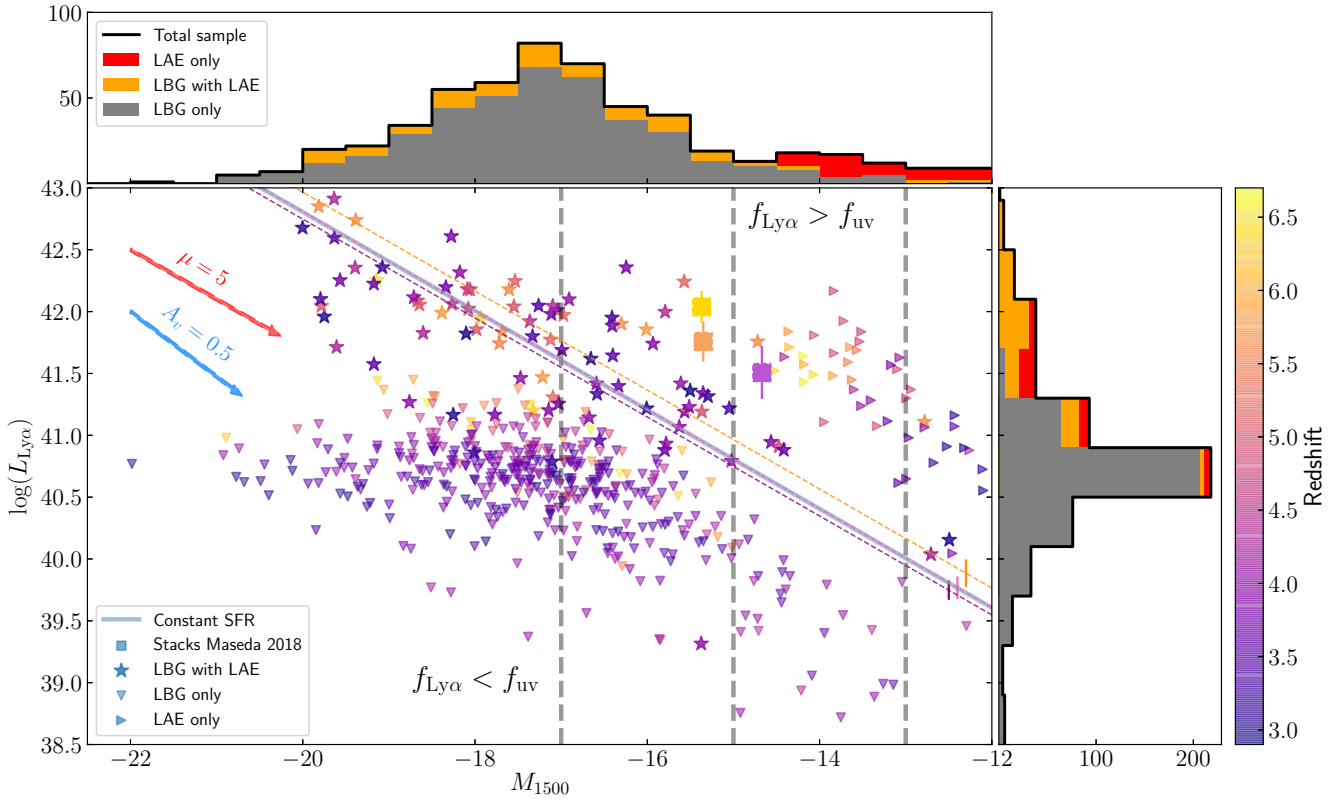

Fig. 6. Lyman α luminosity versus absolute UV magnitude, with redshift encoded in the color bar. On the top (right) are UV absolute magnitude (Lyα luminosity) histograms for the three samples, stacked on each other, using the same colors as in Fig. 4. Galaxies in Samples 2 and 3 have upper limit estimations of their Lyα and UV fluxes corresponding to 3σ detection limits respectively. All values have been corrected for magnification but not for possible dust extinction. The thick blue line displays the locus of the $SFR_{Ly\alpha} = SFR_{uv}$ for a constant star-formation system. The dashed violet, pink and orange lines correspond to the best-fit for the offset in this relation (with fixed slope) when the sample is split in the redshift bins: $2.9 < z < 4.0$, $4.0 < z < 5.0$ and $5.0 < z < 6.7$ respectively. Uncertainties on offset values are shown as vertical lines of the same color. The three vertical grey dashed lines correspond to $M_{1500} = -17$ $M_{1500} = -15$ $M_{1500} = -13$, which correspond roughly to the observational limit reached in blank fields, lensing fields, and the extrapolation needed to ensure that the UV LF provides enough ionizing flux for reionization (see Bouwens et al. 2015b). Red and blue arrows indicate the effect of a magnification factor of $\mu = 5$ and a reddening $A_V = 0.5$ magnitudes respectively.

yield the same values when measuring either the UV continuum or the Lyα line flux. Galaxies found above or below this line have respectively $f_{uv} < f_{Ly\alpha}$ or $f_{uv} > f_{Ly\alpha}$. In addition, the scatter can be easily understood given the variety of star-forming regimes that are not fairly represented by a stationary and constant star-formation regimes.

The three samples are each exploring different regions of Fig. 6. For bright galaxies with $M_{1500} < -15$, all SFGs in the present sample are selected as LBGs. However, for galaxies fainter than $M_{1500} = -15$ the proportion of SFGs only seen as LAEs progressively increases at lower UV luminosity. This result is in good agreement with the recent study of Maseda et al. (2018) which concluded that the LAE selection is better suited to identify and study intrinsically faint UV galaxies. This also suggests that the LAE Luminosity Function is a better proxy of the SFG population when focusing on the faint end. The observed trend depends on the relative depth between MUSE and *HST* observations: deeper *HST* observations would increase the number of faint LBGs detected. Needless to say that such observations are extremely expensive and the HFF data are currently the deepest observations available.

In addition to the theoretical $SFR_{Ly\alpha} = SFR_{uv}$ locus, the same relation has been adjusted with the offset as a free parameter, keeping a constant slope, for galaxies in Sample 1 split in the following redshift bins: $2.9 < z < 4.0$ (43 sources), $4.0 < z < 5.0$ (27 sources) and $5.0 < z < 6.7$ (22 sources). The results are presented respectively by the dashed violet, pink and orange lines in Fig. 6, where the derived uncertainties from the fit are represented as vertical error bars of the same color. Leaving this offset free means leaving the ratio f_{Ly_α}/f_{UV} free, in such a way that the fit can be seen as an average value of this ratio over the sample considered. For the two lower redshift bins, the adjusted line is fully consistent with the $SFR_{Ly\alpha} = SFR_{uv}$ locus within the 1σ level, whereas a $f_{Ly\alpha} > f_{uv}$ is observed for the higher redshift bin with a $\sim 1\sigma$ significance. When looking at all the galaxies of Sample 1, two regimes seem to appear. On average, bright galaxies with $M_{1500} < -17$ tend to be under the $SFR_{Ly\alpha} = SFR_{uv}$ locus, whereas the opposite trend is observed for faint galaxies with $M_{1500} > -17$. In addition, and following this observed trend, all galaxies of Sample 3 without exception are above the $SFR_{Ly\alpha} = SFR_{uv}$ locus, meaning that $f_{Ly\alpha}$ is much higher than f_{uv}. Such a behavior could be explained by the evolution of the dust content, and the relative distribution of dust and stars in star-forming regions, as discussed below. Also the large scatter observed for all the three redshift bins could be representative of individual variation on the f_{Ly_α}/f_{UV} ratio related to the star formation regime, the dust content, and the relative distribution

of stars and dust.

It is worth emphasizing that the LBG sample used throughout this work is NIR-selected (i.e. selected based on the rest frame continuum at $\sim$ 4000Å down to 2000Å for z $\sim$3 to 7 respectively). We expect a systematic trend in the sense that LBG galaxies with extremely blue continuum could have been preferentially missed at $z \sim$ 3-4 with respect to $z \sim$ 6-7. While this certainly impacts our statistics, this effect can hardly account for the systematic trends presented above.

The fact that all SFGs with $M_{1500} < -17$ in the present sample are selected as LBGs is particularly interesting since it roughly corresponds to the observational limit of the deepest *HST* blank fields (see e.g. Bouwens et al. 2015b). This limit can be pushed as faint $M_{1500} \sim -15$ in strong lensing fields before a correction is required to account for the contribution of LAEs with not continuum detection. This means that the UV LF derived from LBG selection can be safely integrated down to $M_{1500} \sim -15$ to derive the total ionizing flux without including the additional contribution of the (pure) LAE population. Reaching down to $M_{1500} \sim -15$ up to $z \sim 7$ is only possible in lensing fields, as shown by different studies (see e.g. Livermore et al. 2017; Bouwens et al. 2017; Atek et al. 2018). The situation is different for $M_{1500} > -15$, as the pure LAE fraction among SFGs increases towards the faintest UV luminosities. Since the M_{1500} values and associated luminosities for pure LAE galaxies are upper limits, it is not possible to determine individually whether they probe the same luminosity domain as (extremely faint) LBGs not detected as LAEs (Sample 2). Therefore, it is difficult to properly estimate the relative contribution to the ionizing flux for the ensemble of SFGs.

Stacking the galaxies of Sample 3 in redshift bins, following the technique adopted by Maseda et al. (2018) would allow us to know more on their average UV continuum. But this remains challenging because the strong variation of individual amplification makes it non trivial to give similar weight to all stacked LAEs and because of the small sample of pure LAEs. Therefore, based on the present results it is still difficult to quantify the missing contribution of LAE to the ionizing flux density with respect to the extrapolation of the LBG-based UV LF to $M_{1500} \sim -13$, if any, up to $z \sim 7$.

The fact that bright galaxies with $M_{1500} < -17$ tend to be under the $SFR_{Ly\alpha} = SFR_{uv}$ locus, whereas galaxies with $M_{1500} > -17$ lie above, including all galaxies in Sample 3, suggests an evolution in the f_{Ly_α}/f_{UV} ratio. The same trend is observed between galaxies at z <5 and z >5.

The simplest possible explanation for this trend is the age of the stellar population. Even in the case of a constant star formation rate, the ratio of UV to Lyα luminosity produced by a young stellar populations evolves and needs $\sim$ 100 Myr before reaching the Kennicut equilibrium (Verhamme et al. 2008). The same is true in the case of a non constant and evolving SFR: when a recent star-burst fades away, the UV emission turns off immediately while Lyα photons suffer a complex radiative transfer in the starburst halo.

As suggested by Atek et al. (2014), another possibility could be the existence of a multi-phase ISM with dust, where the Lyα emission is enhanced with respect to the non-resonant emission at similar wavelengths (i.e. Lyman continuum photons, or UV photons in the present case). Following this scenario, neutral gas and dust reside in clumps and they are surrounded by an ionized medium. The Lyα photons are scattered away when reaching the surface of these clumps while the UV photons can penetrate inside where they are more easily absorbed by the dust. Therefore even though $f_{Ly\alpha}$ decreases with increasing dust content or reddening, the ratio f_{Ly_α}/f_{UV} could increase since f_{uv} decreases faster than $f_{Ly\alpha}$ in presence of dust clumps (see e.g. Hayes et al. 2011, 2013; Atek et al. 2014; Matthee et al. 2016). Geometrical effects are also important and certainly contribute to the observed scatter; for instance, in galaxies observed edge-on, Lyα photons are able to scatter and go around the dust in the dust barrier, while the UV is strongly attenuated when passing directly through it. Atek et al. (2014) also observed a decrease in $SFR_{Ly\alpha}$ with SFR_{uv} (or, conversely, a decrease in $f_{Ly\alpha}$ with increasing UV luminosity). This trend is also predicted by models (see e.g. Garel et al. 2012) as a consequence of the old stellar populations found in UV bright galaxies, because these galaxies are more dusty and less clumpy than galaxies with younger stellar populations or star bursts. A more uniform dust distribution makes the absorption of Lyα photons more likely leading to $f_{uv} > f_{Ly\alpha}$, a systematic trend observed in the present sample for $M_{1500} < -17$ galaxies.

The increase of the f_{Ly_α}/f_{UV} with redshift is likely to trace the evolution of the dust distribution. As shown in Hayes et al. (2011), the amount of dust decreases with increasing redshift, as the stellar population become younger. Following this simple evolution and assuming a homogeneous distribution of dust, we would expect a similar increases in both $f_{Ly\alpha}$ and f_{uv}. This is not what is observed, meaning that an increased clumpiness in the distribution of dust and neutral hydrogen at higher redshift is also needed to explain the observed trend.

5. Conclusions

We have studied the intersection between the LAE and the LBG population behind the HFF cluster A2744. This has resulted in the following conclusions:

- For UV faint galaxies $M_{1500} \geq -20.25$, the fraction of LAE among SFGs increases with redshift up to z $\sim$6 and decreases at $z \gtrsim 6$, in agreement with previous findings (see e.g. Arrabal Haro et al. 2018).
- As faint as $M_{1500} \sim -15$, the LBG population seems to provide a good representation of the total SFG population, in particular when computing the total ionizing flux in the volume explored by current surveys.
- The selection of Lyα emitters seems to be more effective than the LBG technique to identify intrisically UV faint galaxies ($M_{1500} \geq -15$) that are missed in deep blank and lensing field photometric surveys. In this respect, our results are in good agreement with Maseda et al. (2018). This also shows that when assessing the faint part of the population of SFG with $M_{1500} \geq -15$ with the current deepest photometric data, a correction is needed to account for the contribution of the LAEs with no UV counterpart detection.
- There is no clear evidence, based on the present results, for an intrinsic difference on the properties of the two populations selected as LBG and/or LAE. However, further investigation will be needed. In particular, some systematic trends appear in the population selected as LBG and LAE, in the sense that the UV-brightest galaxies seem to exhibit a smaller f_{Ly_α}/f_{UV} ratio, increasing towards the faintest luminosities. This could be an indication for a different distribution of dust and stars depending on the luminosity. Measuring the UV-slopes of these galaxies could provide additional information in this respect.

Acknowledgements. Partially funded by the ERC starting grant CALENDS (JR), the Agence Nationale de la recherche bearing the reference ANR-13-BS05-

0010-02 (FOGHAR), and the “Programme National de Cosmologie and Galaxies" (PNCG) of CNRS/INSU with INP and IN2P3, co-funded by CEA and CNES, France. This work has been carried out thanks to the support of the OCEVU Labex (ANR-11-LABX-0060) and the A*MIDEX project (ANR-11-IDEX-0001-02) funded by the "Investissements d’Avenir" French government program managed by the ANR. This work also recieved support from the ECOS SUD Program C16U02. NL acknowledges financial support from European Research Council Advanced Grant FP7/669253. FEB acknowledges support from CONICYT grants CATA-Basal AFB-170002 (FEB), FONDECYT Regular 1190818 (FEB), and Programa de Cooperación Científica ECOS-CONICYT C16U02 the Chilean Ministry of Economy, Development, and Tourism’s Millennium Science Initiative through grant IC120009, awarded to The Millennium Institute of Astrophysics, MAS. TG acknowledges support from the European Research Council under grant agreement ERC-stg-757258 (TRIPLE). Based on observations made with ESO Telescopes at the La Silla Paranal Observatory under programme ID 094.A-0115.

References

Arrabal Haro, P., Rodríguez Espinosa, J. M., Muñoz-Tuñón, C., et al. 2018, Monthly Notices of the Royal Astronomical Society, 478, 3740
Atek, H., Kunth, D., Schaerer, D., et al. 2014, Astronomy & Astrophysics, 561, A89
Atek, H., Richard, J., Jauzac, M., et al. 2015, ApJ, 814, 69
Atek, H., Richard, J., Kneib, J.-p., & Schaerer, D. 2018, MNRAS, 479, 5184
Bacon, R., Accardo, M., Adjali, L., et al. 2010, in Ground-based and Airborne Instrumentation for Astronomy III, Vol. 7735, 773508
Bacon, R., Conseil, S., Mary, D., et al. 2017, A&A, 608, A1
Bertin, E. & Arnouts, S. 1996, A&A Supplement Series, 117, 393
Bolzonella, M., Miralles, J. M., & Pelló, R. 2000, A&A, 363, 476
Bouwens, R. J., Illingworth, G. D., Oesch, P. A., et al. 2015a, ApJ, 811, 140
Bouwens, R. J., Illingworth, G. D., Oesch, P. A., et al. 2015b, ApJ, 803, 34
Bouwens, R. J., Oesch, P. A., Illingworth, G. D., Ellis, R. S., & Stefanon, M. 2017, ApJ, 843, 129
Bouwens, R. J., Thompson, R. I., Illingworth, G. D., et al. 2004, ApJ, 616, L79
Bruzual, G. & Charlot, S. 2003, MNRAS, 344, 1000
Calzetti, D., Armus, L., Bohlin, R. C., et al. 2000, The Astrophysical Journal, 533, 682
Castellano, M., Amorín, R., Merlin, E., et al. 2016, Astronomy & Astrophysics, 590, A31
Chabrier, G. 2003, Publications of the Astronomical Society of the Pacific, 115, 763
Coleman, G. D., Wu, C.-C., & Weedman, D. W. 1980, The Astrophysical Journal Supplement Series, 43, 393
De Barros, S., Pentericci, L., Vanzella, E., et al. 2017, Astronomy & Astrophysics, 608, A123
de La Vieuville, G., Bina, D., Pello, R., et al. 2019, A&A, 628, A3
Finkelstein, S. L., Ryan Russell E., J., Papovich, C., et al. 2015, ApJ, 810, 71
Garel, T., Blaizot, J., Guiderdoni, B., et al. 2012, MNRAS, 422, 310
Hayes, M., Östlin, G., Schaerer, D., et al. 2013, ApJ Letters, 765, L27
Hayes, M., Schaerer, D., Stlin, G., et al. 2011, ApJ, 730, 8
Inami, H., Bacon, R., Brinchmann, J., et al. 2017, Astronomy & Astrophysics, 608, A2
Jullo, E. & Kneib, J. P. 2009, MNRAS, 395, 1319
Jullo, E., Kneib, J. P., Limousin, M., et al. 2007, New Journal of Physics, 9, 447
Kennicutt, Jr., R. C. 1998, ApJ, 498, 541
Kinney, A. L., Calzetti, D., Bohlin, R. C., et al. 1996, The Astrophysical Journal, 467, 38
Kneib, J.-P., Ellis, R. S., Smail, I., Couch, W. J., & Sharples, R. M. 1996, ApJ, 471, 643
Leclercq, F., Bacon, R., Wisotzki, L., et al. 2017, A&A, 608, A8
Leitherer, C., Schaerer, D., Goldader, J. D., et al. 1999, the Astrophysical Journal Supplement Series, 123, 3
Livermore, R. C., Finkelstein, S. L., & Lotz, J. M. 2017, ApJ, 835, 113
Lotz, J. M., Koekemoer, A., Coe, D., et al. 2017, ApJ, 97
Mahler, G., Richard, J., Clément, B., et al. 2018, MNRAS, 692, 663
Maseda, M. V., Bacon, R., Franx, M., et al. 2018, ApJ Letters, 865, L1
Matthee, J., Sobral, D., Oteo, I., et al. 2016, MNRAS, 458, 449
McLure, R. J., Dunlop, J. S., Bowler, R. A. A., et al. 2013, MNRAS, 432, 2696
Merlin, E., Amorín, R., Castellano, M., et al. 2016, Astronomy & Astrophysics, 590, A30
Oke, J. B. & Gunn, J. E. 1983, ApJ, 266, 713
Pentericci, L., Fontana, A., Vanzella, E., et al. 2011, ApJ, 743, 132
Piqueras, L., Conseil, S., Shepherd, M., et al. 2017, ArXiv e-prints, arXiv:1710.03554
Schenker, M. A., Ellis, R. S., Konidaris, N. P., & Stark, D. P. 2014, The Astrophysical Journal, 795, 20
Stark, D. P., Ellis, R. S., Chiu, K., Ouchi, M., & Bunker, A. 2010, MNRAS, 408, 1628
Stark, D. P., Ellis, R. S., & Ouchi, M. 2011, The Astrophysical Journal, 728, L2
Tilvi, V., Papovich, C., Finkelstein, S., et al. 2014, ApJ, 794, 5
Treu, T., Schmidt, K. B., Trenti, M., Bradley, L. D., & Stiavelli, M. 2013, The Astrophysical Journal, 775, L29
Verhamme, A., Schaerer, D., Atek, H., & Tapken, C. 2008, Astronomy & Astrophysics, 491, 89
Wisotzki, L., Bacon, R., Brinchmann, J., et al. 2018, Nature, 562, 229

D | Sample table

Table D.1: Table with the main characteristics of the 152 LAEs used to build the LFs. F_{Ly_α} is the detection flux of the LAE, expressed in 10^{-18} units, μ is the flux weightedmangification of the source and the error bars correspond to the 68% asymmetric errors computed from $P\mu$,$\log Ly_\alpha$ is the Lyman-alpha luminosity corrected for magnification. No error bars are associated to luminosity value, as this uncertainty is accounted for during the MC iterations needed to build the LFs. Comp is the completeness expressed in percentage. The $V_{\rm max}$ value given in this table are computed for $2.9 < z < 6.9$. An electronic version of this table is available at `http://cdsarc.u-strasbg.fr/viz-bin/qcat?J/A+A/628/A3`

Id	z	F_{Ly_α} erg s^{-1} cm^2	μ	$\log(Ly_\alpha)$ erg s^{-1}	Comp	$V_{\rm max}$ Mpc^3
A1689, 619	3.0446	102.06 ± 6.27	$7.95^{+0.60}_{-0.25}$	42.01	73.3 ± 1.7	16015.9
A1689, 1028	3.1109	119.36 ± 3.36	$26.83^{+2.80}_{-0.90}$	41.58	100.0 ± 0.0	15913.4
A1689, LN9	3.1789	44.72 ± 3.75	$7.69^{+0.55}_{-0.52}$	41.71	96.4 ± 0.7	15946.6
A1689, 1404	3.1800	11.99 ± 1.84	$5.90^{+0.22}_{-0.38}$	41.26	12.6 ± 1.5	15791.5
A1689, 835	3.1806	27.48 ± 2.48	$11.84^{+0.66}_{-1.23}$	41.31	93.2 ± 1.0	15835.8
A1689, LN10	3.4182	16.84 ± 1.36	$52.42^{+44.51}_{-10.64}$	40.53	99.4 ± 0.3	15698.1
A1689, LN26	4.0541	9.44 ± 1.29	$8.51^{+0.54}_{-0.40}$	41.25	62.2 ± 2.0	15805.0
A1689, LN13	4.0548	24.66 ± 1.82	$8.82^{+0.69}_{-0.66}$	41.65	98.1 ± 0.6	15943.8
A1689, LN14	4.1038	19.34 ± 2.37	$5.66^{+0.35}_{-0.21}$	41.75	98.9 ± 0.5	15930.8
A1689, LN25	4.8426	4.12 ± 0.66	$18.74^{+2.84}_{-1.65}$	40.73	38.9 ± 1.9	15509.8
A1689, LN15	4.8668	5.75 ± 0.92	$4.92^{+0.38}_{-0.32}$	41.46	68.9 ± 1.8	15851.1
A1689, 1379	4.8734	91.53 ± 2.22	$5.68^{+0.38}_{-0.18}$	42.60	99.9 ± 0.2	16352.6
A1689, LN17	5.0117	4.46 ± 0.56	$8.28^{+0.46}_{-0.45}$	41.15	84.5 ± 1.4	15818.2
A1689, LN18	5.7369	6.16 ± 0.83	$18.22^{+1.44}_{-1.22}$	41.08	50.1 ± 2.0	15711.5
A1689, LN19	6.1752	6.98 ± 1.00	$7.49^{+0.24}_{-0.56}$	41.60	97.8 ± 0.7	15835.2
A2390, L1	4.0454	207.18 ± 6.97	$19.81^{+1.22}_{-0.53}$	42.22	97.6 ± 0.9	15832.3
A2390, 96	4.0475	544.64 ± 6.51	$11.22^{+0.55}_{-0.33}$	42.89	99.2 ± 0.8	16246.7
A2390, 134	4.7210	16.75 ± 1.74	$24.27^{+3.28}_{-0.32}$	41.20	30.7 ± 2.5	15010.8
A2390, 71	4.8773	20.70 ± 1.97	$7.12^{+0.25}_{-0.24}$	41.85	99.4 ± 0.3	15810.7
A2390, 243	5.7574	2.69 ± 0.57	$21.33^{+1.26}_{-0.74}$	40.66	34.4 ± 2.5	13282.3
A2667, 24	3.7872	16.54 ± 1.52	$9.32^{+1.16}_{-0.34}$	41.38	99.2 ± 0.4	15732.7

Continued on next page

Table D.1 – continued from previous page

Id	z	F_{Ly_α}	μ	$\log(Ly_\alpha)$	Comp	$V_{\max}$
A2667, 25	3.7872	36.51 ± 2.85	$2.96^{+0.08}_{-0.06}$	42.22	89.4 ± 1.3	15869.4
A2667, 30	3.9743	59.56 ± 3.40	$46.08^{+24.71}_{-6.34}$	41.29	94.2 ± 0.9	14522.8
A2667, 33	4.0803	39.13 ± 3.63	$12.50^{+0.88}_{-0.49}$	41.70	96.1 ± 0.8	15696.9
A2667, 38	4.9467	30.77 ± 3.07	$16.22^{+2.42}_{-1.04}$	41.68	85.2 ± 1.5	15368.8
A2667, 41	5.1993	18.18 ± 1.30	$3.25^{+0.10}_{-0.07}$	42.20	99.9 ± 0.1	15939.4
A2667, 62	5.5003	6.52 ± 1.16	$43.08^{+10.58}_{-4.85}$	40.69	88.1 ± 1.4	2002.1
A2744, 8683	2.9315	25.86 ± 2.33	$3.22^{+0.12}_{-0.08}$	41.77	96.4 ± 0.8	15527.9
A2744, 11626	2.9422	4.59 ± 0.93	$1.75^{+0.06}_{-0.03}$	41.29	68.5 ± 1.7	13744.9
A2744, 5005	2.9513	9.71 ± 0.87	$18.10^{+1.63}_{-0.82}$	40.60	98.9 ± 0.5	11423.4
A2744, 4010	2.9986	4.15 ± 1.34	$2.17^{+0.04}_{-0.04}$	41.17	21.9 ± 1.7	12801.1
A2744, 10544	3.0211	2.41 ± 0.46	$2.95^{+0.10}_{-0.06}$	40.81	68.6 ± 1.9	13832.2
A2744, M10	3.0213	2.06 ± 0.53	$2.11^{+0.04}_{-0.05}$	40.88	21.1 ± 2.0	12606.1
A2744, M11	3.0234	1.34 ± 0.36	$3.48^{+0.07}_{-0.12}$	40.48	26.9 ± 2.1	13373.2
A2744, M12	3.0337	4.00 ± 0.91	$2.34^{+0.05}_{-0.04}$	41.13	11.6 ± 1.5	12826.9
A2744, 3424	3.0511	7.76 ± 1.00	$9.70^{+0.41}_{-0.55}$	40.81	95.4 ± 0.9	14816.9
A2744, M24	3.0532	14.55 ± 1.16	$12.90^{+0.92}_{-0.73}$	40.96	99.8 ± 0.2	15480.4
A2744, 11701	3.0543	18.54 ± 1.44	$4.80^{+0.12}_{-0.12}$	41.49	98.4 ± 0.5	15555.7
A2744, 7858	3.1291	82.08 ± 4.02	$3.47^{+0.11}_{-0.08}$	42.31	100.0 ± 0.1	15869.5
A2744, 7721	3.1295	138.50 ± 5.81	$2.78^{+0.10}_{-0.05}$	42.63	100.0 ± 0.0	15962.4
A2744, 11196	3.1508	6.72 ± 1.55	$3.31^{+0.12}_{-0.09}$	41.25	53.1 ± 2.2	13573.4
A2744, 6876	3.1900	1.68 ± 0.32	$2.21^{+0.05}_{-0.06}$	40.83	64.0 ± 2.3	13791.6
A2744, M13	3.2034	1.98 ± 0.40	$4.06^{+0.08}_{-0.12}$	40.64	56.8 ± 2.2	12840.3
A2744, M14	3.2034	1.32 ± 0.26	$2.32^{+0.04}_{-0.04}$	40.71	10.3 ± 1.6	10860.6
A2744, 2754	3.2075	6.29 ± 1.08	$8.53^{+0.47}_{-0.48}$	40.83	65.3 ± 2.2	11925.8
A2744, 11806	3.2356	3.92 ± 0.68	$1.97^{+0.06}_{-0.05}$	41.27	47.8 ± 2.2	12576.7
A2744, 4933	3.2466	21.69 ± 1.54	$2.46^{+0.05}_{-0.05}$	41.92	99.8 ± 0.2	15817.9
A2744, 3000	3.3161	17.87 ± 1.94	$1.68^{+0.02}_{-0.03}$	42.02	98.8 ± 0.5	15504.2
A2744, 3759	3.3576	2.64 ± 0.36	$1.72^{+0.03}_{-0.04}$	41.19	84.5 ± 1.6	14193.9
A2744, 11033	3.3788	25.15 ± 1.74	$2.64^{+0.10}_{-0.09}$	41.99	98.9 ± 0.5	15586.4
A2744, M7	3.4072	31.08 ± 1.14	$41.81^{+53.90}_{-3.16}$	40.89	100.0 ± 0.0	12532.9
A2744, M15	3.4337	0.62 ± 0.25	$1.91^{+0.07}_{-0.06}$	40.55	51.1 ± 2.1	12429.8
A2744, 10382	3.4750	8.59 ± 0.49	$1.66^{+0.03}_{-0.04}$	41.76	100.0 ± 0.1	15992.4
A2744, 10669	3.4757	59.29 ± 2.66	$1.90^{+0.04}_{-0.05}$	42.54	99.8 ± 0.2	15977.6
A2744, 9272	3.4758	6.50 ± 1.08	$1.78^{+0.04}_{-0.02}$	41.60	28.1 ± 1.8	11796.6
A2744, 10725	3.4759	6.67 ± 1.08	$2.40^{+0.06}_{-0.08}$	41.48	66.9 ± 2.2	13892.6
A2744, 3853	3.5415	24.46 ± 1.37	$2.97^{+0.08}_{-0.06}$	41.98	100.0 ± 0.0	15864.7
A2744, M16	3.5509	3.26 ± 0.61	$4.17^{+0.18}_{-0.08}$	40.96	55.7 ± 2.1	12487.1
A2744, 9731	3.5510	4.38 ± 0.69	$13.85^{+0.78}_{-0.77}$	40.56	23.5 ± 1.7	4748.5

Continued on next page

Table D.1 – continued from previous page

Id	z	F_{Ly_α}	μ	$\log(Ly_\alpha)$	Comp	$V_{\max}$
A2744, 5133	3.5733	75.75 ± 1.70	$9.53^{+2.40}_{-0.78}$	41.97	100.0 ± 0.1	15822.0
A2744, M17	3.5756	1.61 ± 0.24	$2.41^{+0.07}_{-0.07}$	40.90	61.3 ± 2.0	13434.5
A2744, 10174	3.5777	7.84 ± 0.90	$5.95^{+0.13}_{-0.15}$	41.19	98.2 ± 0.6	15075.2
A2744, 3423	3.5810	23.24 ± 1.82	$1.73^{+0.03}_{-0.03}$	42.20	86.1 ± 1.3	13721.1
A2744, 5922	3.5931	1.28 ± 0.25	$2.13^{+0.05}_{-0.04}$	40.85	35.5 ± 1.9	11881.1
A2744, 9672	3.6490	10.42 ± 1.15	$1.92^{+0.04}_{-0.04}$	41.83	99.4 ± 0.4	15536.7
A2744, 7737	3.6893	25.04 ± 1.68	$2.28^{+0.03}_{-0.04}$	42.14	100.0 ± 0.0	15879.7
A2744, 6374	3.6913	12.93 ± 0.74	$4.10^{+0.21}_{-0.09}$	41.60	100.0 ± 0.1	15768.8
A2744, 2951	3.7077	11.74 ± 1.28	$1.69^{+0.02}_{-0.03}$	41.95	97.6 ± 0.6	15061.7
A2744, 5625	3.7077	5.56 ± 0.60	$3.14^{+0.11}_{-0.06}$	41.36	97.3 ± 0.7	14886.1
A2744, M18	3.7247	5.17 ± 0.84	$1.95^{+0.03}_{-0.03}$	41.54	93.0 ± 1.2	14470.4
A2744, 5624	3.7794	64.92 ± 3.14	$2.30^{+0.05}_{-0.04}$	42.58	100.0 ± 0.1	15950.2
A2744, 10312	3.7866	53.38 ± 2.77	$3.96^{+0.22}_{-0.20}$	42.26	98.7 ± 0.5	14970.5
A2744, 2956	3.8123	26.26 ± 1.96	$2.26^{+0.03}_{-0.05}$	42.20	99.5 ± 0.3	15517.9
A2744, M19	3.8790	2.01 ± 0.42	$2.01^{+0.04}_{-0.03}$	41.16	30.9 ± 2.0	9352.5
A2744, 8357	3.9469	1.81 ± 0.35	$1.84^{+0.03}_{-0.03}$	41.17	72.1 ± 2.2	12209.1
A2744, 2104	3.9538	3.08 ± 0.30	$2.68^{+0.06}_{-0.02}$	41.24	85.1 ± 1.3	13596.4
A2744, 14684	3.9619	10.29 ± 1.01	$3.21^{+0.09}_{-0.14}$	41.68	98.4 ± 0.6	15003.1
A2744, 3210	3.9660	2.16 ± 0.91	$1.84^{+0.04}_{-0.02}$	41.25	51.1 ± 2.0	11563.0
A2744, 3986	3.9833	3.19 ± 0.58	$1.77^{+0.03}_{-0.03}$	41.44	22.2 ± 1.9	10007.8
A2744, 2736	4.0207	35.25 ± 1.66	$5.99^{+0.19}_{-0.18}$	41.96	100.0 ± 0.0	15787.9
A2744, 2407	4.0208	6.50 ± 0.82	$2.66^{+0.10}_{-0.04}$	41.58	80.9 ± 1.7	13299.4
A2744, 9303	4.0214	10.73 ± 1.16	$9.76^{+0.46}_{-0.33}$	41.23	36.9 ± 2.1	9066.9
A2744, 9440	4.0214	8.44 ± 1.13	$52.96^{+16.29}_{-3.18}$	40.40	74.2 ± 1.9	486.0
A2744, M41	4.0214	2.31 ± 0.44	$3.41^{+0.09}_{-0.08}$	41.02	13.3 ± 1.5	10475.7
A2744, 6510	4.0253	16.92 ± 1.45	$2.15^{+0.05}_{-0.05}$	42.09	94.6 ± 1.0	14159.5
A2744, M9	4.0280	0.78 ± 0.22	$44.55^{+8.97}_{-2.43}$	39.44	14.1 ± 1.7	124.7
A2744, 3672	4.0423	22.00 ± 1.66	$1.77^{+0.03}_{-0.03}$	42.29	100.0 ± 0.0	15893.3
A2744, 4378	4.0450	2.84 ± 0.55	$1.82^{+0.03}_{-0.04}$	41.39	68.9 ± 2.1	12832.3
A2744, 1903	4.0527	4.59 ± 0.55	$3.20^{+0.05}_{-0.04}$	41.36	71.1 ± 1.7	13441.5
A2744, M1	4.1924	13.76 ± 0.62	$40.04^{+8.00}_{-5.08}$	40.77	100.0 ± 0.1	9503.7
A2744, 10340	4.3006	19.82 ± 1.95	$8.13^{+0.39}_{-0.28}$	41.65	37.8 ± 2.0	6647.2
A2744, M23	4.3088	3.99 ± 0.60	$1.98^{+0.04}_{-0.05}$	41.57	87.5 ± 1.4	13547.6
A2744, 5574	4.3342	6.55 ± 0.73	$2.60^{+0.06}_{-0.05}$	41.67	98.6 ± 0.5	14004.8
A2744, 4926	4.3361	139.51 ± 1.82	$3.76^{+0.14}_{-0.09}$	42.84	99.7 ± 0.2	16215.6
A2744, 9683	4.3602	2.20 ± 0.43	$2.06^{+0.04}_{-0.05}$	41.30	93.5 ± 1.1	13105.2
A2744, M25	4.3663	2.44 ± 0.34	$15.25^{+0.37}_{-0.65}$	40.48	80.6 ± 1.7	5901.1
A2744, 9089	4.3748	10.24 ± 0.82	$1.95^{+0.04}_{-0.03}$	42.00	99.8 ± 0.2	15572.1

Continued on next page

Table D.1 – continued from previous page

Id	z	F_{Ly_α}	μ	$\log(Ly_\alpha)$	Comp	$V_{\max}$
A2744, 3837	4.3920	22.47 ± 0.91	$2.13^{+0.02}_{-0.06}$	42.31	100.0 ± 0.0	16051.1
A2744, 3275	4.4002	10.68 ± 0.94	$2.45^{+0.03}_{-0.06}$	41.92	99.2 ± 0.4	14908.4
A2744, 10305	4.4013	14.15 ± 1.34	$4.43^{+0.31}_{-0.21}$	41.79	99.4 ± 0.4	14890.4
A2744, 4321	4.6315	9.11 ± 0.71	$1.82^{+0.03}_{-0.04}$	42.04	99.7 ± 0.3	15121.9
A2744, 6505	4.6892	6.99 ± 0.55	$2.48^{+0.06}_{-0.05}$	41.80	99.8 ± 0.2	15501.0
A2744, 10644	4.6974	10.67 ± 0.90	$1.80^{+0.04}_{-0.05}$	42.12	99.9 ± 0.1	15751.0
A2744, M26	4.7026	3.28 ± 0.38	$4.77^{+0.15}_{-0.11}$	41.19	87.4 ± 1.5	12921.5
A2744, 10338	4.7125	16.12 ± 1.13	$4.46^{+0.20}_{-0.20}$	41.91	99.9 ± 0.1	15524.2
A2744, 2674	4.7283	11.13 ± 1.24	$1.86^{+0.03}_{-0.03}$	42.14	99.1 ± 0.4	14054.1
A2744, 2874	4.7283	5.70 ± 0.60	$2.61^{+0.04}_{-0.08}$	41.70	99.2 ± 0.4	14670.9
A2744, M27	4.7540	4.06 ± 0.64	$5.13^{+0.18}_{-0.09}$	41.26	25.2 ± 2.0	5747.2
A2744, 5488	4.7616	4.55 ± 0.85	$13.49^{+0.85}_{-0.51}$	40.89	15.4 ± 1.7	883.2
A2744, 2264	4.7786	5.11 ± 0.78	$4.45^{+0.11}_{-0.07}$	41.43	92.1 ± 1.1	11664.2
A2744, 2077	4.7804	13.95 ± 0.73	$4.63^{+0.16}_{-0.18}$	41.85	100.0 ± 0.0	15775.8
A2744, 11772	4.7984	7.07 ± 0.57	$2.40^{+0.08}_{-0.07}$	41.84	99.7 ± 0.2	15520.6
A2744, 10594	4.8018	27.00 ± 1.54	$5.42^{+0.16}_{-0.12}$	42.07	100.0 ± 0.1	15738.1
A2744, M28	4.8660	1.43 ± 0.19	$3.51^{+0.11}_{-0.10}$	41.00	90.6 ± 1.3	13656.0
A2744, 3492	4.8938	3.50 ± 0.53	$2.65^{+0.07}_{-0.13}$	41.51	86.1 ± 1.5	11999.3
A2744, M29	4.9020	0.87 ± 0.23	$2.03^{+0.08}_{-0.07}$	41.03	55.8 ± 2.0	10034.8
A2744, 10972	4.9116	1.88 ± 0.39	$3.58^{+0.12}_{-0.10}$	41.12	74.6 ± 1.8	11445.0
A2744, M40	4.9139	3.95 ± 0.50	$3.77^{+0.12}_{-0.26}$	41.42	99.5 ± 0.3	14741.6
A2744, 11629	4.9823	9.05 ± 0.88	$2.66^{+0.10}_{-0.07}$	41.95	98.9 ± 0.5	14720.8
A2744, 4946	5.0193	4.96 ± 0.69	$1.93^{+0.04}_{-0.04}$	41.83	52.9 ± 2.0	12336.5
A2744, 12026	5.0537	8.62 ± 1.04	$2.52^{+0.08}_{-0.07}$	41.96	11.3 ± 1.3	9808.2
A2744, 12404	5.0537	8.55 ± 1.03	$2.52^{+0.08}_{-0.07}$	41.96	59.1 ± 2.0	11332.7
A2744, 9377	5.1349	12.90 ± 1.33	$2.36^{+0.05}_{-0.04}$	42.18	94.5 ± 0.9	12386.3
A2744, 8885	5.1879	3.34 ± 0.65	$1.75^{+0.04}_{-0.03}$	41.73	90.2 ± 1.4	14584.2
A2744, 4213	5.1933	11.08 ± 0.87	$1.92^{+0.04}_{-0.03}$	42.22	99.4 ± 0.3	15508.4
A2744, 2821	5.2817	3.96 ± 0.61	$7.98^{+0.32}_{-0.38}$	41.17	52.0 ± 1.9	12204.9
A2744, 10004	5.2896	10.75 ± 1.21	$4.00^{+0.22}_{-0.12}$	41.90	98.3 ± 0.6	14947.1
A2744, M30	5.4316	4.73 ± 0.64	$3.53^{+0.16}_{-0.13}$	41.63	71.0 ± 2.1	12912.9
A2744, M31	5.5364	3.44 ± 0.73	$3.54^{+0.12}_{-0.08}$	41.51	29.2 ± 1.9	10209.6
A2744, 3306	5.5406	2.73 ± 0.70	$1.73^{+0.03}_{-0.03}$	41.72	39.3 ± 2.1	12351.3
A2744, M32	5.5601	2.58 ± 0.62	$3.32^{+0.09}_{-0.08}$	41.42	37.1 ± 2.0	9668.8
A2744, 11194	5.6094	9.10 ± 0.91	$2.53^{+0.08}_{-0.09}$	42.09	99.8 ± 0.2	15433.4
A2744, 10111	5.6218	6.23 ± 0.82	$4.99^{+0.24}_{-0.19}$	41.63	98.6 ± 0.5	14519.9
A2744, M3	5.6596	8.30 ± 0.62	$4.28^{+0.12}_{-0.15}$	41.83	99.2 ± 0.3	14785.7
A2744, M33	5.6608	12.41 ± 1.10	$149.96^{+797.40}_{-14.99}$	40.46	54.8 ± 1.8	126.2

Continued on next page

Table D.1 – continued from previous page

Id	z	F_{Ly_α}	μ	$\log(Ly_\alpha)$	Comp	$V_{\max}$
A2744, 8268	5.6618	160.30 ± 2.26	$8.50^{+0.42}_{-0.35}$	42.82	100.0 ± 0.0	15962.9
A2744, 5408	5.7219	32.37 ± 0.41	$28.01^{+3.18}_{-1.88}$	41.62	100.0 ± 0.0	15772.2
A2744, 11559	5.7637	4.65 ± 0.68	$3.56^{+0.17}_{-0.12}$	41.68	93.7 ± 1.1	13573.0
A2744, 3472	5.7648	3.22 ± 0.46	$1.80^{+0.03}_{-0.03}$	41.81	65.7 ± 1.9	12439.3
A2744, 11471	5.7668	3.80 ± 0.55	$2.30^{+0.08}_{-0.07}$	41.78	87.3 ± 1.3	13356.5
A2744, 7747	5.7709	4.66 ± 0.67	$1.89^{+0.04}_{-0.02}$	41.95	97.7 ± 0.7	13972.6
A2744, 8116	5.7751	1.35 ± 0.19	$1.82^{+0.03}_{-0.03}$	41.43	52.3 ± 2.4	10488.7
A2744, M34	5.8994	2.28 ± 0.37	$3.32^{+0.15}_{-0.14}$	41.42	92.6 ± 1.1	13712.5
vA2744, M35	5.9971	2.06 ± 0.29	$2.35^{+0.06}_{-0.06}$	41.54	38.9 ± 2.3	11330.8
A2744, M36	6.0938	2.43 ± 0.51	$2.13^{+0.04}_{-0.04}$	41.67	44.9 ± 2.3	14502.1
A2744, 2785	6.2737	0.57 ± 0.29	$1.68^{+0.03}_{-0.03}$	41.17	69.9 ± 1.8	12638.7
A2744, 5353	6.3271	6.58 ± 0.63	$3.73^{+0.12}_{-0.12}$	41.90	94.3 ± 1.1	14495.0
A2744, 10609	6.3755	1.34 ± 0.19	$2.28^{+0.07}_{-0.07}$	41.43	57.1 ± 2.2	12540.9
A2744, M37	6.5195	1.89 ± 0.43	$3.36^{+0.11}_{-0.11}$	41.44	20.9 ± 1.7	10376.5
A2744, M38	6.5565	1.48 ± 0.47	$3.45^{+0.09}_{-0.11}$	41.32	25.3 ± 1.8	12082.9
A2744, 2115	6.5876	12.30 ± 1.27	$4.12^{+0.10}_{-0.05}$	42.17	58.1 ± 2.2	12310.1
A2744, M39	6.6439	2.39 ± 0.35	$3.29^{+0.14}_{-0.08}$	41.57	68.5 ± 1.8	14415.0

Abstract — Reionization is the last change of state of the Universe which made its entire hydrogen content transition from a neutral to a completely ionized state. This rapid transition and heating of the gas content had major consequences on the formation and evolution of structures which makes of reionization a key element to understand the present day Universe. In our current understanding, reionization was mostly done by $z \sim 6$ and the sources responsible for this transition are likely faint, low mass and star-forming galaxies (SFGs). One way to study this population is to determine the Luminosity Function (LF) of galaxies selected from their Lyman-alpha emission and assess their ionizing flux density. However, most recent studies and their conclusions are in general limited by the lowest flux that can be reached with the current observational facilities. One of the major goals of the work presented in this manuscript is the study of the Lyman-alpha emitters (LAE) LF using deep observations of strong lensing clusters with the integral field unit (IFU) MUSE. The combined usage of large IFU data cubes and lensing fields makes this analysis computationally challenging. To get around this difficulty, we have developed new methods to account for the contribution of each individual LAE, including the effective-volume and completeness determinations. The LFs resulting form this analysis set an unprecedented level of constraint on the shape of the faint end. Making no assumption on the escape fraction of Lyα emission, we observe that the LAE population has a similar level of contribution to the total ionising emissivity as the UV-selected galaxies (LBGs) at $z \sim 6$. In the continuity of this work on the LAE LF, we investigate the effect of the selection method on this conclusion. The results have shown that the observed proportion of LAEs increases significantly among UV-faint galaxies and at increasing redshift.

Keywords: Astrophysics - Galaxies - Gravitational lensing - galaxy - clusters - Reionization

Résumé — La reionisation est le dernier changement d'état de l'Univers qui a fait passer l'ensemble de sa teneur en hydrogène d'un état neutre à un état ionisé. Cette transition rapide ainsi que le réchauffement du gaz ont eu des conséquences majeures sur la formation et l'évolution des structures, d'où l'importance de la reionisation pour comprendre l'Univers actuel. Dans notre compréhension actuelle, la réionisation s'est terminée à $z \sim 6$ et les sources responsables de cette transition sont probablement les galaxies de faible masse et à formation d'étoiles (SFG). Une des façons d'étudier cette population consiste à déterminer la fonction de luminosité (LF) des galaxies sélectionnées à partir de leur émission Lyman-alpha et à évaluer leur densité de flux ionisant. Toutefois, les études les plus récentes et leurs conclusions sont en général limitées par le flux le plus faible que l'on peut atteindre avec les instruments actuels. L'un des principaux objectifs du travail présenté dans ce manuscrit est l'étude de la LF des émetteurs Lyman-alpha (LAE) à l'aide d'observations profondes d'amas de galaxies avec l'IFU MUSE. L'utilisation combinée des cubes de données IFU et de champs lentillés rend cette analyse difficile sur le plan du temps de calcul. Pour contourner cette difficulté, nous avons mis au point de nouvelles méthodes pour tenir compte de la contribution de chaque LAE, y compris la détermination du volume effectif et de la complétude. Les LFs résultant de cette analyse ont établi un niveau de contrainte sans précédent sur la forme de la partie à très faible luminosité de la LF. En ne faisant aucune hypothèse sur la fraction d'échappement de l'émissions Lyα, nous observons que la population de LAE a un niveau de contribution à l'émissivité ionisante totale similaire à celui des galaxies sélectionnées par UV (LBG) à $z \sim 6$. Dans la continuité de ce travail sur la LAE LF, nous étudions l'effet de la méthode de sélection sur cette conclusion. Ces derniers résultats ont montré que la proportion observée de LAEs augmente de manière significative parmi les galaxies à faible continuum UV et à grand redshift.

Mots clés : Astrophysique - Galaxies - Lentilles gravitationelles - Amas de galaxies - Reionisation

Institut de Recherche en Astrophysique et Planétologie,
14 Avenue Edouard Belin, 31400 Toulouse